STUDIES OF LASER-TARGET INTERACTIONS IN PULSED EXCIMER LASER EVAPORATION OF SUPERCONDUCTING OXIDES AND OTHER METAL OXIDES

By

STEPHENS SIN-TSUN THÉ

A DISSERTATION PRESENTED TO THE GRADUATE SCHOOL
OF THE UNIVERSITY OF FLORIDA IN PARTIAL FULFILLMENT
OF THE REQUIREMENTS FOR THE DEGREE OF
DOCTOR OF PHILOSOPHY

UNIVERSITY OF FLORIDA

1993

UNIVERSITY OF FLORIDA LIBRARIES

Copyright 1993

by

Stephens Sin-Tsun Thé

To My Wife,
Jennifer

ACKNOWLEDGEMENTS

I would like to express my gratitude to Professor Tim Anderson, my thesis advisor, for his insight and effort have made this research possible. His numerous trips to Wilmington, DE, during the progress of this research were greatly appreciated.

I am grateful to Dr. Ken Keating, my mentor and thesis coadvisor. His patience and guidance during my internship at the Experimental Station were greatly appreciated. His insight and wisdom as as a research fellow at DuPont are invaluable in my industrial training. Also his efforts in maintaining funding supports during difficult times are greatly appreciated.

E.I. du Pont de Nemours and Co., especially Drs. Ken McKelvey, Bob Dorothy, Lew Goodrich, and Jim Trainham, are thanked for providing me with the research funding and the opportunity to work in this great research environment, while allowing me to learn the intricacy of industrial research.

The excimer laser group, Dr. Jim Hohman, Sandy Witman, Gerry Frost, and Don Wonchoba, are thanked for putting up with me for all these years and for kindly providing me with a lot of help and inspiration. This research would not have been possible without their expertise in optics and lasers.

The superconductivity group, especially Drs. Bill Holstein, Dean Face and Dan Laubacher, are thanked for providing me with constructive discussions and assistance in sample analysis.

John Pedrick is thanked for his SEM expertise and for providing me with all the SEM and EDAX analysis in this research; without his help this dissertation would have been deprived of pictures. Al Terzian is thanked for helping me with the design and construction of the laser deposition chamber. Dr. Raj Bordia, Rajesh Patel, and Phil Dye are thanked for the preparation of ceramic samples. Larry Harrison is thanked for the thermal analysis. Bert Diemer is thanked for providing some thermodynamic data. Larry Eichelberger is thanked for his photographical expertise. Dr. Rudy Enck at British Petroleum Research is thanked for the work on laser thermal diffusivity measurement. Carl Mueller from the University of Florida is thanked for the Auger analysis.

Researchers and staff initially in the Engineering Technology Laboratory, then in Central Research and Development, Science and Engineering, and lately in Corporate Science and Engineering, including Drs. Kurt Mikeska, Deepak Doraiswamy, Juan Figueroa, Mike Kelley, and many more, are thanked for providing me with valuable discussions and support.

Staff and colleagues at the Chemical Engineering Department, University of Florida, especially Shirley Kelly and Roger Aparicio, are thanked for helping me with paperwork and registration while I was off-campus.

My parents and family are thanked for their endless supports and encouragements; and for their financial support while I was working on my undergraduate degree. Also I am thankful to the Lord for His benediction.

I would like to give special thanks for my loving wife, Jennifer, for her infinite patience and understanding while I was completing my graduate study and for her assistance in the preparation of this manuscript.

TABLE OF CONTENTS

Page

ACKNOWLEDGEMENTS iv

LIST OF TABLES xiii

LIST OF FIGURES xiv

ABSTRACTS xxii

CHAPTERS

1. INTRODUCTION 1

1.1 Overview of High Tc Superconductor Thin Film 3
1.1.1 Status and Applications 3
1.1.1.1 Superconductor and its properties 3
1.1.1.2 Passive microwave devices 7
1.1.1.3 Active microwave devices 9
1.1.1.4 Integrated Systems 11
1.1.2 HTSC Thin Films 13
1.1.2.1 Ideal film properties 13
1.1.2.2 Characterization techniques 13
1.1.2.3 Substrates 15
1.1.2.4 Technological challenges 16
1.1.3 Comparison of Techniques for Deposition of YBCO 16
1.1.3.1 Electron-beam evaporation 16
1.1.3.2 Sputtering 17
1.1.3.3 Metallorganic chemical vapor deposition (MOCVD) 17
1.1.3.4 Pulsed-laser deposition (PLD) 18
1.2 Overview of Pulsed-Laser Evaporation 18
1.2.1 Hardware Configurations 18
1.2.2 Operational Procedures 20
1.2.3 Typical Results 22

1.2.4 Overview of Laser-Target Interactions 23
1.2.4.1 Photon absorption and phase transformation 24
1.2.4.2 Plasma expansion 25
1.2.5 Some Outstanding Problems for PLD Technique 26
1.2.5.1 Boulder generation 26
1.2.5.2 Target stoichiometry and texturing 26
1.2.5.3 Process scale-up 27
1.2.5.4 Substrate-film interface reactions 27
1.3 Overview of This Work 28
1.3.1 Target Surface Morphology 28
1.3.2 Particulate Reduction 28
1.3.3 Target and Film Stoichiometry 29

2. EQUILIBRIUM ANALYSIS OF THE YBCO SYSTEM 30

2.1 Introduction 30
2.1.1 Chemical Equilibrium Analysis 32
2.1.2 Fundamental Assumptions 33
2.1.2.1 System temperature 33
2.1.2.2 Local equilibria 34
2.1.2.3 Charge neutrality 35
2.1.2.4 Electronic excitation 36
2.1.3 Theoretical Backgrounds 37
2.1.4 Outline of the Computer Program 38
2.1.5 Statement of Purpose 40
2.2 Thermodynamic Calculations 40
2.2.1 Data Fitting Functions 40
2.2.2 Condensed Phases 41
2.2.3 Gas Phase 47
2.2.4 Oxygen System 47
2.2.5 Yttrium-Oxygen System 50
2.2.6 Barium-Oxygen System 52
2.2.7 Copper-Oxygen System 52
2.3 Complex Reaction Equilibria at Elevated Temperature 55
2.3.1 Effect of Temperature 55
2.3.2 Effect of Pressure 56

2.3.3 Effect of Oxygen Pressure 59
2.3.4 Effect of Inert Gas 68
2.3.5 Analysis of PLD Plasma 68
2.4 Conclusion 70

3. SELECTED THERMOCHEMICAL AND THERMOPHYSICAL PROPERTIES STUDIES 71

3.1 Introduction 71
3.2 Sample Preparation 72
3.3 Differential Thermal Analysis 73
3.3.1 Introduction 73
3.3.2 Experimental 73
3.3.3 Result and Discussion. 74
3.4 Thermal Gravimetric Analysis 78
3.4.1 Introduction 78
3.4.2 Experimental 78
3.4.3 Result and Discussion 79
3.5 Differential Scanning Calorimetry 79
3.5.1 Introduction 79
3.5.2 Experimental 81
3.5.3 Result and Discussion 81
3.6 Laser Flash Thermal Diffusivity Measurement 81
3.6.1 Introduction 81
3.6.2 Experimental 84
3.6.3 Result and Discussion 84
3.7 Thermal Mechanical Analyzer 85
3.7.1 Introduction 85
3.7.2 Experimental 90
3.7.3 Result and Discussion 90
3.8 Conclusion 90

4. THERMAL MODELS 92

4.1 Introduction 92
4.2 Important Phenomena and Process Description 94
4.2.1 Surface Morphology 95

4.2.2 Thermal Penetration Depth 95
4.2.3 Plasma Kinetic Energy 96
4.2.4 Physical Definition of Process to be Modeled 97
4.3 Review of Laser Heating Model 98
4.3.1 Theory of Electromagnetic Radiation 98
4.3.1.1 Electromagnetic radiation 98
4.3.1.2 Surface and absorption 99
4.3.2 Laser Activated Heat Transfer Models 101
4.3.2.1 Fundamental models 101
4.3.2.2 Surface temperature 104
4.3.2.3 Subsurface heating 105
4.3.2.4 Heating and cooling rates 106
4.3.2.5 Heat transfer with material ejection 106
4.4 Macroscopic Energy Balance 107
4.4.1 Photon Absorption 108
4.4.2 Phase Transformation 108
4.4.3 Radiation, Convection and Thermal Conduction Losses 110
4.4.4 Plasma Kinetic Energy 112
4.5 Conclusion 112

5. PARTICLE PRODUCTION STUDIES 114

5.1 Overview of Particulate Formation 114
5.1.1 Introduction 114
5.1.2 Surface Roughness 115
5.1.3 Formation of Clusters 116
5.1.4 Formation of Particulates 117
5.2 Effect of Deposition Parameter Film Deposition 119
5.2.1 Effect of Laser Parameter 119
5.2.2 Effect of Deposition Parameter 121
5.2.3 Effect of Target Quality 122
5.3 Techniques of Particulate Reduction 122
5.3.1 Secondary Laser 122
5.3.2 Mechanical Velocity Filter 123
5.3.3 Surface Heating 123
5.3.4 High-Velocity Target and Plasma Spray 124

5.3.5 Ag-Doped Target 124
5.3.6 Off-Axis Deposition 124
5.3.7 Substrate Negative Voltage Bias 124
5.4 Particulate Reduction via Target Heating 125
5.4.1 Introduction 125
5.4.2 Experimental Procedure 126
5.4.3 Results and Discussion 128
5.4.3.1 Droplet temperature and liquid molten pool 136
5.4.3.2 Surface morphology and droplet formations 144
5.4.3.3 Hydrodynamic sputtering and particle size 145
5.5 Conclusion 147

6. TARGET MORPHOLOGY OF YBCO SUPERCONDUCTOR 148

6.1 Review of Literature 148
6.1.1 Introduction 148
6.1.2 Surface Modification 149
6.1.3 Target Morphology in YBCO 149
6.1.4 Statement of Purpose 150
6.2 Target Morphology Studies of YBCO Systems 150
6.2.1 Experimental Setup 151
6.2.2 Effects of Laser Fluence 154
6.2.2.1 Porous 159
6.2.2.2 Cones 169
6.2.2.3 Melts 176
6.2.3 Effect of Pulse Number 183
6.2.3.1 Melting of surface: less than 20 pulses 183
6.2.3.2 Formation of columns: 20 to 100 pulses 186
6.2.3.3 Formation of tables: higher than 100 pulses. 186
6.2.4 Effect of Phase Impurities 192
6.2.5 Effects of Repetition Rate and Beam Size 201
6.2.6 Effects of Environments 201
6.2.7 Effects of Target Density 207
6.3 Target Morphology Studies of Other Materials 212
6.3.1 Ceramics 212
6.3.1.1 $LaAlO_3$ 212

6.3.1.2 Al_2O_3 214
6.3.2 Metals 214
6.3.2.1 Titanium 214
6.3.2.2 Gold and copper 218
6.3.3 Polymers 222
6.4 Modelling on Target Morphology 222
6.4.1 Surface Morphology at Low and Medium Fluences 224
6.4.1.1 Radiation heating and suface asperties 227
6.4.1.2 Shielding of porous and cones 228
6.4.2 Surface Morphology at High Fluence 229
6.4.2.1 Surface cracks due to self-stress 231
6.4.2.2 Surface tension induced ripples 235
6.4.2.3 Fluence-dependent optical analysis 236
6.5 Conclusions 239

7. PLUME EXPANSION STUDIES 244

7.1. Overview of Laser Induced Shock Wave 244
7.1.1 Photon Absorption and Induction Period 245
7.1.2 Fundamental of Shock Wave Formation 245
7.1.3 Laser-Induced Shock Wave 247
7.1.4 Recoil Pressure and Plume Redeposition 249
7.2 Plume Expansion Studies of YBCO Systems 249
7.2.1 Statement of Problem 249
7.2.2 Experimental Details 250
7.2.3 Effect of Fluence 250
7.2.4 Effect of Geometry 250
7.2.5 Effect of Ambient Pressure 258
7.3 Conclusions 258

8. MASS SPECTROSCOPIC INVESTIGATION 259

8.1 Review of Literature 259
8.1.1 Plasma Characterization 259
8.1.2 Mass Spectroscopy Fundamentals 261
8.1.3 Mass Spectroscopic Plasma Analysis 262
8.1.3.1 Atoms and molecules 263

8.1.3.2 Clusters 263
8.1.3.3 Quantitative determination 264
8.1.3.4 Kinetic energy 264
8.1.3.5 Photochemistry 264
8.2 Mass Spectroscopic Analysis of YBCO 265
8.2.1 Experimental 265
8.2.2 Effect of Fluence 268
8.2.3 Effect of Ambient Gas and Pressure 272
8.2.4 Effect of Repetition Rate 276
8.2.5 Effect of Pulse Number 278
8.2.6 Effect of Target Density 278
8.3 Comparison with Complex Equilibrium Reactions 278
8.3.1 Effect of Temperature 279
8.3.2 Effect of Pressure 279
8.3.3 Effect of Background Gas 280
8.4 Conclusion 280

9. CONCLUSION 281

9.1 Reduction of Film Particulate 281
9.2 Development of Target Morphology 282
9.3 Chemical Equilibrium Analysis 283
9.4 Recommendation for Future Studies 284

REFERENCE LIST 286

BIOGRAPHICAL SKETCH 301

LIST OF TABLES

Table		page
2-1	Thermodynamic coefficients of the species in YBCO chemical equilibria	43
2-2	Solid phases of YBCO system	44
2-3	List of vapor species detected in laser induced YBCO plasma	48
2-4	Pressure dependence on the boiling point temperature of copper element	58
2-5	Equilibrium composition of YBCO vapor phase at 8000 K and 1 atm with various initial conditions	67
3-1	Temperature rise time and thermal diffusivity of high density pellets (94 % theoretical density) irradiated using a CO_2 laser. Temperature was measured at the rear surface.	87
3-2	Temperature rise time and thermal diffusivity of low-density pellets (65% theoretical density) irradiated using a CO_2 laser. Temperature was measured at the rear surface.	88
5-1	Comparison of the number of particulates generated by laser deposition taken from this work and literature	131
6-1	Morphology of YBCO target evaporated using a KrF laser at fluence of 0.1 to 2.0 J.cm^2 for 2000 pulses in 1 atm air. Evaporation size of 100 μm x 100 μm	156
6-2	Surface morphological development of high- and low-density YBCO target evaporated using a KrF laser in 100 mTorr oxygen.	208
8-1	Atomic species detected using mass spectroscopy at fluence of 0.3 - 3.0 J/cm^2.	271
8-2	Effect of pressure on the composition of YBCO plasma species	275
8-3	Effect of fluence on the composition of YBCO plasma species	277

LIST OF FIGURES

Figure		page
1-1	$YBa_2Cu_3O_7$ superconductor (a) atomic structure; (b) temperature dependent resistivity.	6
1-2	Schematic view a stripline resonator. (a) cross section showing conductor and dielectric; (b) top view.	8
1-3	Schematic view a HTSC Josephson Junction circuit.	10
1-4	Cross sectional view a integrated SQUID magnetometer (a) on LaAlO3 substrate; (b) on YSZ substrate.	12
1-5	Schematic diagram a pulsed laser deposition chamber. Bottom view shows zones of laser-target interactions.	19
2-1	Temperature dependent heat capacity of O^+. Comparison of three different fitting functions.	42
2-2	Gibbs free energy yttrium element as a function of temperature.	46
2-3	Oxygen phase equilibria at 1 atm.	49
2-4	Yttrium-oxygen vapor phase chemical equilibria at 1 atm.	51
2-5	Barium-oxygen vapor phase chemical equilibria at 1 atm.	53
2-6	Copper-oxygen vapor phase chemical equilbria at 1 atm.	54
2-7	YBCO vapor phase equilibria at temperatures from 2500 to 20000 ^oK and presure 1 atm.	57
2-8	YBCO vapor phase equilibria at temperatures from 5000 to 10000 ^oK and pressure 0.2 atm.	60
2-9	YBCO vapor phase equilibria at temperatures from 5000 to 10000 ^oK and pressure 0.5 atm	61
2-10	YBCO vapor phase equilibria at temperatures from 5000 to 10000 ^oK and pressure 1 atm	62
2-11	YBCO vapor phase equilibria at temperatures from 5000 to 10000 ^oK and pressure 10 atm.	63

2-12 YBCO vapor phase equilibria at temperatures from 5000 to 10000 °K and pressure 50 atm. 64

2-13 Mole fraction and number density of electron in YBCO plasma at a temperature of 8000 K and pressures up to 50 atm. 65

2-14 Electron density of YBCO plasma at temperatures of 5000, 8000 and 10000 K at pressures up to 50 atm. 66

2-15 Composition of YBCO plasma at temperatures between 5000 and 10000 K and pressures up to 50 atm. Note the formation of oxides at low temperature and high pressure and the formation of ions at low pressure and high temperature. 69

3-1 Differential Thermal Analysis of YBCO powder. Heating rate: 20 °C/min. Sample size: 39.2 mg. Temperature range: 30 to 1600 °C. Atmosphere: air. 75

3-2 Differential Thermal Analysis YBCO pellet (wt. 99.9 mg), YBCO powder (wt. 39.2 mg) and gold powder (wt. 86.9 mg) at temperatures around the melting point. Heating rate: 20 °C/min. Atmosphere: air. 76

3-3 Resolidified sample of YBCO powder after undergoing DTA analysis to 1100 °C. Magnification (a) 30x; (b) 600x 77

3-4 Thermal Gravimetric Analysis of YBCO powder. Heating rate: 10 °C/min. Sample size: 44.9 mg. Atmosphere: N_2. 80

3-5 Differential Scanning Calorimetry YBCO. Heating rate: 10 °C/min. Temperature range: 30 to 600 °C. Atmosphere: N_2. Peak at 270 °C is probably due to organic impurity. 82

3-6 Temperature rise during laser flash technique used in determining thermal diffusivity. 86

3-7 Thermal diffusivity YBCO as a function temperature, measured up to 400 °C. 89

3-8 Thermal Mechanical Analysis YBCO. Initial dimension: 10.93 mm. Heating rate: 20 °C/min. Top curve: heating cycle. Bottom curve: cooling cycle. 91

4-1 Enthalpy of $YBa_2Cu_3O_7$ as a function temperature. Charged species not considered. 111

4-2 Energy distribution for the evaporation YBCO target using KrF laser 113

5-1 YBCO film on $LaAlO_3$ substrate produced by pulsed laser deposition. Target heated to 700 °C. 129

5-2 YBCO film on MgO substrate produced by pulsed laser deposition. Target at room temperature. 130

5-3 Surface morphology a heated target surface evaporated using KrF excimer laser at 1.2 J/cm^2. Magnification (a) 70 x, and (b) 1000 x. 132

5-4 YBCO film on $LaAlO_3$ substrate produced by pulsed laser deposition. (a) 10000x magnification (b) 30000x magnification. Note the absence of large particles. 133

5-5 YBCO film on $LaAlO_3$ substrate produced by pulsed laser deposition using heated target at 700 °C. Note the absent of large spherical particles. 134

5-6 YBCO film on $LaAlO_3$ substrate produced by pulsed laser deposition using heated target at 25 °C. Note the present of large spherical particles. 135

5-7 Surface morphology a heated target surface evaporated using KrF excimer laser at 2.5 J/cm^2. Number pulses: 3000. Atmosphere: 100 mtorr O_2. (a) magnification 50x and 250x , and (b) maginfication 600x and 3000x. Note the absence of surface morphology. 137

5-8 Surface morphology a target surface evaporated using KrF excimer laser at 2.5 J/cm^2. Number pulses: 3000. Atmosphere: 100 mtorr O_2. (a) magnification 50x and 250x , and (b) maginfication 600x and 3000x. Note the presence of surface morphology. 138

5-9 Surface morphology YBCO target surfaces evaporated using KrF excimer laser at 2.5 J/cm^2. Number pulses: 3000. Atmosphere: 100 mtorr O_2. Magnification: 40x. (a) target at 25 °C, and (b) target at 600 °C. 139

5-10 XRD YBCO target after heating at 600 °C for 2 hours. Loss of oxygen can be noticed. 140

5-11 Typical temperature dependent surface resistivity. 141

5-12 Typical XRD of laser deposited thin film on MgO substate, showing c-axis orientation. 142

6-1 High density superconductor pellet target. (a) nonpolished surface, (b) polished surface. 152

6-2 Schematic diagram of the microfabrication stage used in the evaporation YBCO target. 153

6-3 YBCO target evaporated at fluence (a) 0.1 to 0.6 J/cm^2, (b) 0.6 to 1.1 J/cm^2, and (c) above 1.1 J/cm^2. Corresponding to the formation of pores, cones and melts surface morphology. 155

6-4 Etch rate YBCO as a function laser fluence. Inset graph is in linear scale. 157

6-5 EDAX analysis YBCO target evaporated at fluence from 0.1 to 2.0 J/cm^2. The fraction of yttrium is high at fluence less than 1 J/cm^2. 158

6-6 YBCO target evaporated using KrF laser at fluence between 0.1 to 0.6 J/cm^2. Formation of pores surface morphology. Atmosphere: air. Pulse number (a) 50 pulses; (b) 200 pulses; (c) 1000pulses. 160

6-7 YBCO target evaporated using KrF laser. Atmosphere: air. Pulse number: 50 pulses. Fluence: 0.6 J/cm^2. Repetition rate: 10 pps. (a) top view; (b) cross-sectional view. 161

6-8 YBCO target evaporated using KrF laser. Atmosphere: air. Pulse number: 200 pulses. Fluence: 0.6 J/cm^2. Repetition rate: 10 pps. Top view. 162

6-9 YBCO target evaporated using KrF laser. Atmosphere: air. Pulse number: 500 pulses. Fluence: 0.6 J/cm^2. Repetition rate: 10 pps. (a) top view; (b) cross-sectional view. 163

6-10 YBCO target evaporated using KrF laser. Atmosphere: air. Pulse number: 1000 pulses. Fluence: 0.6 J/cm^2. Repetition rate: 10 pps. (a) top view; (b) cross-sectional view. 164

6-11 Cartoon for the evolution surface shielding due to formation yttrium rich phase. (a) initial absorption; (b) formation of yttrium-rich phase; (c) material shielding. 166

6-12 XRD YBCO (a) virgin material; (b) laser scanned at low fluence. Note the presence of Y_2O_3 phase. 167

6-13 Experimental and calculated phase diagrams for the Y-Ba-Cu-O system. 168

6-14 YBCO target evaporated using KrF laser at fluence between 0.6 to 1.1 J/cm^2. Formation of cones surface morphology. Atmosphere: air. Pulse number (a) 50 pulses; (b) 200 pulses; (c) 1000pulses. 170

6-15 YBCO target evaporated using KrF laser. Atmosphere: air. Pulse number: 50 pulses. Fluence: 0.9 J/cm^2. Repetition rate: 10 pps. (a) top view; (b) cross-sectional view. 172

6-16 YBCO target evaporated using KrF laser. Atmosphere: air. Pulse number: 200 pulses. Fluence: 0.9 J/cm^2. Repetition rate: 10 pps. Top view. Note the formation of "nipples". 173

6-17 YBCO target evaporated using KrF laser. Atmosphere: air. Pulse number: 500 pulses. Fluence: 0.9 J/cm^2. Repetition rate: 10 pps. (a) top view; (b) cross-sectional view. 174

6-18 YBCO target evaporated using KrF laser. Atmosphere: air. Pulse number: 1000 pulses. Fluence: 0.9 J/cm^2. Repetition rate: 10 pps. (a) top view; (b) cross-sectional view. 175

6-19 YBCO target evaporated using KrF laser at fluence above 1.1 J/cm^2. Formation of melts surface morphology. Atmosphere: air. Pulse number (a) 50 pulses; (b) 200 pulses; (c) 1000pulses. 177

6-20 YBCO target evaporated using KrF laser. Atmosphere: air. Pulse number: 50 pulses. Fluence: 2.0 J/cm^2. Repetition rate: 10 pps. (a) top view; (b) cross-sectional view. 179

6-21 YBCO target evaporated using KrF laser. Atmosphere: air. Pulse number: 200 pulses. Fluence: 2.0 J/cm^2. Repetition rate: 10 pps. (a) top view; (b) cross-sectional view. 180

6-22 YBCO target evaporated using KrF laser. Atmosphere: air. Pulse number: 500 pulses. Fluence: 2.0 J/cm^2. Repetition rate: 10 pps. (a) top view; (b) cross-sectional view. 181

6-23 YBCO target evaporated using KrF laser. Atmosphere: air. Pulse number: 1000 pulses. Fluence: 2.0 J/cm^2. Repetition rate: 10 pps. (a) top view; (b) cross-sectional view. 182

6-24 Polished YBCO surface. 184

6-25 Polished YBCO target evaporated using KrF laser. Fluence: 2.0 J/cm^2. Atmosphere: air. Pulse number: (a) 1 pulse; (b) 2 pulses. Note that at 2 pulses, some of the holes are filled. 185

6-26 Polished YBCO target evaporated using KrF laser. The same surface area as 6-25. Fluence: 2.0 J/cm^2. Atmosphere: air. Pulse number: (a) 5 pulses; (b) 8 pulses. 187

6-27 Polished YBCO target evaporated using KrF laser. Fluence: 2.0 J/cm^2. Atmosphere: air. Pulse number: (a) 10 pulses; (b) 20 pulses. 188

6-28 Polished YBCO target evaporated using KrF laser. The same surface area as 6-27. Fluence: 2.0 J/cm^2. Atmosphere: air. Pulse number: (a) 50 pulses; (b) 80 pulses. 189

6-29 Polished YBCO target evaporated using KrF laser. Fluence: 2.0 J/cm^2. Atmosphere: air. Pulse number: (a) 100 pulses; (b) 200 pulses. 190

6-30 Polished YBCO target evaporated using KrF laser. The same surface area as 6-29. Fluence: 2.0 J/cm^2. Atmosphere: air. Pulse number: (a) 500 pulses; (b) 800 pulses. 191

6-31 Y_2BaCuO_5 target evaporated using KrF laser. Atmosphere: air. Condition: (a) Virgin material; (b) 0.4 J/cm^2,1000 pulses 193

6-32 Y_2BaCuO_5 target evaporated using KrF laser. Atmosphere: air. Condition: (a) 0.7 J/cm^2, 1000 pulses, 10 pps; (b) 1.1 J/cm^2, 1000 pulses, 10 pps 195

6-33 Y_2BaCuO_5 target evaporated using KrF laser. Atmosphere: air. Condition: (a) 2.1 J/cm^2, 1000 pulses, 10 pps; (b) 3.5 J/cm^2, 1000 pulses, 10 pps 196

6-34 Comparison between the etch rates of $YBa_2Cu_3O_7$ and Y_2BaCuO_5 materials as a function fluence. 197

6-35 Etch depth Y_2BaCuO_5 as a function fluence and pulse number, evaluated at fluences from 1.7 to 3.5 J/cm^2. 198

6-36 Etch depth of $YBa_2Cu_3O_7$ as a function fluence and pulse number. 199

6-37 Y_2O_3 target evaporated using KrF laser. Atmosphere: air. Fluence: 3.0 J/cm^2. Pulse number: 200 pulses. 200

6-38 YBCO target evaporated using KrF laser. Atmosphere: air. Fluence: 0.5 J/cm^2. Repetition rates: (a) 10 pps (b) 100 pps. 202

6-39 YBCO target evaporated using KrF laser. Atmosphere: air. Fluence: 0.8 J/cm^2. Repetition rates: (a) 5 pps; (b) 100 pps. Note that surface (b) is smoother. 203

6-40 YBCO target evaporated using KrF laser. Atmosphere: air. Fluence: 1.1 J/cm^2. Pulse rates: (a) 5 pps; (b) 10 pps. 204

6-41 YBCO target evaporated using KrF laser. Atmosphere: air. Fluence: 0.4 J/cm^2 Size: 200 μm x 200 μm. Pulse number: 1000. Repetition rate: 10 pps. Top view. 205

6-42 YBCO target evaporated using KrF laser. Atmosphere: air. Size: 200 μm x 200 μm. Pulse number: 1000. Repetition rate: 10 pps. Fluence: (a) 0.9 J/cm^2; (b) 1.4 J/cm^2 206

6-43 YBCO target evaporated using KrF laser. Atmosphere: air. Fluence: 2 J/cm^2. Pulse number: 20. Repetion rate: 1pps. Target density: (a) low density; (b) high density 209

6-44 YBCO target evaporated using KrF laser. Atmosphere: air. Fluence: 2 J/cm^2. Pulse number: 50. Repetition rate: 1pps. Target density: (a) low density; (b) high density 210

6-45 YBCO target evaporated using KrF laser. Atmosphere: air. Fluence: 2 J/cm^2. Pulse number: 100. Repetition rate: 1pps. Target density: (a) low density; (b) high density 211

6-46 $LaAlO_3$ target evaporated using KrF laser. Atmosphere: air. Pulse number: 1000. Repetition rate: 10 pps. Fluence: (a) 0.6 J/cm^2; (b) 0.8 J/cm^2 213

6-47 $LaAlO_3$ target evaporated using KrF laser. Atmosphere: air. Pulse number: 1000. Repetition rate: 10 pps. Fluence: (a) 1.0 J/cm^2; (b) 1.3 J/cm^2 215

6-48 $LaAlO_3$ target evaporated using KrF laser. Atmosphere: air. Fluence: 2.1 J/cm^2. Repetition rate: 10 pps. Pulse number: (a) 200; b) 1000 216

6-49 Al_2O_3 target evaporated using KrF laser. Atmosphere: air. Fluence: 15 J/cm^2 217

6-50 Titanium target evaporated using KrF laser. Atmosphere: air. Pulse number: 500 pulses. Repetition rate: 50 pps. Fluence: (a) 0.2 J/cm^2; (b) 0.4 J/cm^2 219

6-51 Titanium target evaporated using KrF laser. Atmosphere: air. Pulse number: 500 pulses. Repetition rate: 50 pps. Fluence: (a) 0.8 J/cm^2; (b) 1.6 J/cm^2 220

6-52 Gold target evaporated using KrF laser. Atmosphere: air. Fluence: 2.0 J/cm^2. Note the formation of surface ripples. 221

6-53 Polyimide Kapton® target evaporated using KrF laser. Atmosphere: air. Fluence: 25 mJ/cm^2. The surface morphology showed the presence of debris. 223

6-54 Cross sectional view YBCO target evaporated using KrF laser. Fluence: 2.0 J/cm2. Pulse number: 1000. Note the formation of melt on the crater wall. (a) cross sectional view of the crater; (b) close up of the deposit on the left wall. 225

6-55 Cross sectional view YBCO target evaporated using KrF laser. Fluence: 1.5 J/cm2. Pulse number: 500. Note the formation of column on the crater bottom. (a) cross sectional view of the crater; (b) close up of the deposit on the column. 226

6-56 Cross sectional view YBCO-gold powder target evaporated using KrF laser. Notice the formation gold spheres at the tip of the columns. 230

6-57 Cartoon of ultra thin surface crack model. 233

6-58 Ray tracing model used in the development surface morphology. As the pulse number increases, the etch depth becomes deeper and the broader. 238

6-59 Surface absorbance as a function wavelength. Wavelength from 220 to 750 nm. 240

6-60 Surface reflectivity as a function of incident angles. 241

6-61 Evolution of YBCO suface morphology at fluence of 2J/cm^2 as a function of pulse number for both polished and non-polished targets 242

7-1 Redeposited YBCO plume as a function fluence. 251

7-2 Redeposited plume area as a function of fluence. Linear dependency observed for both 10 pps and 100 pps. 252

7-3 YBCO target evaporated using KrF laser. Pulse number: 500. Repetition rates (top to bottom): 100, 10 and 5 pps. Fluences: (a) 1.7, 0.1, 0.2, 0.3, 0.4, and 0.5 J/cm^2; (b) 0.5, 0.6, 0.7, 0.8, 0.9, and 1.0 J/cm^2. 253

7-4 YBCO target evaporated using KrF laser. Pulse number: 500. Repetition rates (top to bottom): 100, 10 and 5 pps. Fluences: (a) 1.0, 1.1, 1.2, 1.3, 1.7 and 2.0 J/cm^2; (b) 1.0, 1.1 and 1.2 J/cm^2, 10 and 5 pps. 255

7-5 Redeposited plume as a function of fluence for different evaporation sizes for YBCO target. 256

7-6 Titanium target evaporated using KrF laser. Fluence from 0.1 to 2.0 J/cm^2. 257

8-1 Schematic diagram a differentially pumped mass spectrometer. 266

8-2 Detail the orifice design at the differentially pumped mass spectrometer. Orifice diameter: 100 μm. Orifice length: 100 μm. 267

8-3 Mass spectrometer (MID) as a function fluence. (a) with ionizer, detecting both neutral and ionic species; (b) without ionizer, detecting only ionic species. 269

8-4 A representative mass spectra for YBCO plume. Note the presence of atomic species. 273

Abstract of Dissertation Presented to the Graduate School
of the University of Florida in Partial Fulfillment of the
Requirements for the Degree of Doctor of Philosophy

STUDIES OF LASER-TARGET INTERACTIONS IN PULSED EXCIMER LASER EVAPORATION OF SUPERCONDUCTING OXIDES AND OTHER METAL OXIDES

By

Stephens Sin-Tsun Thé

August 1993

Chairman : Professor Timothy J. Anderson
Major Department : Chemical Engineering

A detailed study of the interaction of a KrF beam with a Y-Ba-Cu-O high-temperature superconductor target was performed to address two principal problems associated with thin film deposition via pulsed laser evaporation: (1) formation of film surface particulates and (2) development of irregular target surface morphology. Thermodynamic chemical equilibrium and mass spectroscopic analysis were performed to determine the composition of the plasma generated by laser irradiation of Y-Ba-Cu-O during the formation and expansion stages.

The formation of film particulates was suppressed by maintaining the target bulk temperature greater than 700 ^{o}C. Such target heating eliminated the formation of spherical film particulates greater than one micron and suppressed the evolution of target surface morphology (i.e., pores, cones, and melts).

The development of surface morphology entailing the distribution of laser power via optical and conventional thermal analysis was investigated. A detailed fluence-dependent optical analysis was used to describe the surface morphology evolution which

was found to be a strong function of laser fluence and pulse number. An overall energy balance showed that the phase transformation consumed one-third of the absorbed laser energy with the remainder converted to plasma kinetic energy. This kinetic energy was manifested in the redeposited plume area formed during ambient pressure evaporation; plume area was a linear function of fluence. The physical properties used in calculations were determined using thermal methods (heat capacity, transition temperatures, and thermal expansion coefficient) and laser flash technique (thermal diffusivity).

A thermodynamic equilibrium calculation (stoichiometric algorithm) was performed on a high-temperature, high-pressure, adiabatically expanding system to determine the chemical equilibrium as a function of temperature, pressure, and inert gas concentration. Ion formation was favored at high temperatures, low pressures, and high inert gas concentrations. Oxide formation was favored at high oxygen pressures and low temperatures. Chemical characterization of the plasma plume using a differentially pumped quadrupole mass spectrometer ($P \leq 30$ mtorr) showed the presence of mainly neutral and ionic atomic species. The result was consistent with the thermodynamic equilibrium calculation.

For comparison, the effect of KrF laser irradiation on other materials, including refractory ceramics, biocompatible materials, and polymer films, was also investigated.

CHAPTER 1
INTRODUCTION

The recent discovery of high T_c superconductors (HTSC) has prompted considerable interest in new fields of superconductor applications, including electronics. However, this application requires smooth, high-quality film, and the quality of film depends largely on the deposition technique. Pulsed laser deposition (PLD) has emerged as a very versatile technique for thin film deposition. PLD is effective for depositing multicomponent materials while maintaining the stoichiometry of the film with respect to the laser target.[1] More than a hundred different materials [2] containing up to six elements,[3] such as superconductors,[4] semiconductors,[5] metals,[1] dielectrics,[1] and bioceramics,[6] have been deposited using PLD. Some of the highest quality HTSC thin films have also been produced by this technique.[4]

PLD is an experimentally simple, thin-film deposition technique, although the detailed process mechanisms are complex and not well understood. In this deposition process, photon energy is absorbed by target materials to produce volatile species that are subsequently deposited as thin films on a substrate. The process phenomena, however, are complex, involving absorption of the photon energy by the target, followed by the conversion of photon energy into electronic, thermal, chemical, and mechanical energies,[7] and finally evaporation, excitation, plasma free-expansion, and film deposition. Specific subprocesses can involve near equilibrium mixtures as well as highly nonequilibrium reacting systems. In a recent review, Hubler described PLD as a simple method, the effectiveness of which no one exactly understands.[3]

Studies of laser-material interaction were pioneered by Ready in 1963 [8] after the invention of the laser in 1960.[9] Early work on laser-assisted thin-film deposition was

initiated in 1965 by Smith and Turner,[10] using a ruby laser to deposit semiconductors and dielectrics. Although this work was conducted early in the development of the laser deposition technique, two fundamental observations were made: 1) the interaction between the laser beam and the target material produces a high-velocity plasma plume, and 2) the stoichiometry of the deposited film is preserved. Limited by the availability of high-energy lasers and suitable materials, this deposition technique was largely ignored until the invention of the high-energy pulsed excimer laser around 1975 and the recent discovery of HTSC.[11] Bellcore/Rutgers University [4] pioneered the use of pulsed laser deposition of HTSC thin films by successfully making the first high-quality $YBa_2Cu_3O_7$ thin film in 1987. Presently, PLD is one of the most rapidly developing thin-film deposition techniques for growing thin films of advanced materials.

PLD has several positive attributes. Its intrinsic capacity to preserve stoichiometry during deposition of multicomponent materials makes it especially suited for materials that evaporate incongruently.[5] In addition, the formation of a highly directional plume,[12] perpendicular to the target surface, makes PLD very efficient for transferring target materials. The highly energetic plasma plume imparts significant species surface mobility on the substrate surface,[3] permitting deposition at a lower substrate temperature.[1, 13] Because the evaporation is induced by an external laser source, in contrast to a sputtering process that uses accelerated background gases, the PLD chamber pressure is decoupled from the evaporation mechanism and can be independently adjusted.[14] Moreover, multilayered structures can be grown by simply switching the target materials during the deposition process.[15]

Compared to the widely used sputtering process, PLD is still an immature technology, with the underlying physics and chemistry still largely unknown. As a result, several practical issues need to be addressed before PLD can become a dependable deposition technique. These issues include the generation of micron-sized particles, which lead to poor film surface morphology; the formation of irregular target surface

morphologies, which affect the deposition efficiency; and the production of a limited plume cross section, which restricts the use of PLD for small areas. Solving these problems is crucial to the broad adoption of this process by the electronic industry, which traditionally demands high process efficiency and adaptability.

This dissertation addresses some of the key issues associated with the deposition of Y-Ba-Cu-O high-temperature, superconducting thin films. In particular, attention is given to understanding the mechanism by which different target morphologies are developed, understanding the composition of the plasma plume, and investigating methods to reduce the formation of particulates. This introduction presents an overview of HTSC materials and their applications, discusses the general features of the PLD process and provides a perspective of the work included in this dissertation.

1.1 Overview of High Tc Superconductor Thin Film

This section deals with the basic properties of superconductors and their applications, especially as they pertain to thin films used for microwave devices. The criteria for high-quality thin films, film characterization techniques, and various thin-film deposition techniques are discussed.

1.1.1 Status and Applications

Superconductor is an ideal material in the fabrication of electronic components because it exhibits zero-resistance properties. To understand the current status of superconductors and their applications in research, the use of superconductors in passive and active microwave devices, as well as integrated systems, is examined.

1.1.1.1 Superconductor and its properties

One of the most important characteristics of a superconductor is its ability to carry current without any resistance. This departure from normal electrical behavior allows electrons to be conducted through a superconductor without energy loss or Joule heating.

Superconductivity was discovered and investigated by Onnes in 1911 in his study of solid mercury (Hg) at low temperature.[16] The abrupt transition from an ordinary conductor to a superconductor occurs at the critical temperature, T_c. In the case of Hg, this transition occurs at 4 K, the boiling point of helium at zero field. Two other important characteristics of this transition are the critical current density, J_c, and the critical magnetic field, H_c, which specify the upper limit of the applied current and magnetic field for superconducting behavior. A superconductor is not only a perfect electrical conductor, it also is a perfect diamagnet, with the capability to expel a magnetic field. This characteristic, which renders a superconductor capable of magnetic levitation, is known as the Meissner effect. If a magnetic field greater than H_c is applied, however, it will abruptly penetrate the superconductor material and destroy the superconductivity. In a similar manner, superconductivity will abruptly vanish beyond the critical current level, J_c.

There are two classes of superconductors based on the transition temperature range: low- and high-temperature superconductors. A low-temperature superconductor becomes a superconductor in the liquid helium temperature range. Common examples are niobium-based metal superconductors, such as pure niobium with a critical transition temperature, T_c, of 9 K. A high-temperature superconductor, on the other hand, becomes a superconductor in the liquid nitrogen temperature range; rare-earth oxide-superconductors are examples. Based on operating cost, high-temperature superconductors are more economical than metal superconductors because the required cooling can be supplied by liquid nitrogen instead of the more expensive liquid helium, which reduces the cooling cost by four orders of magnitude.[16]

In spite of their higher operating cost, low-temperature superconductors have broader applications than high-temperature superconductors. Low-temperature superconductors, because they are more malleable, can be more easily shaped into useful forms such as superconducting magnetic coils and cables. Applications include the superconducting supercollider, the magnetically levitated train, and magnetic resonant

imaging, as well as applications in superconducting circuits. In contrast, the high-temperature superconductor is brittle, currently restricting applications to superconducting circuits.

High-temperature superconductors are ceramic materials with an oxygen-depleted, layered perovskite structure. A perovskite structure consists of a framework of a cubic structure with three distinct elements with a chemical formula ABO_3, where A and B are cations, which occupy the center and the corners of the cube, respectively; the oxygen anions occupy the centers of the edges of the cube.

The most common high T_c superconductor is $YBa_2Cu_3O_{7-x}$, first reported by Chu et al.[11] This superconductor is also known as the 123 compound or YBCO superconductor with a T_c value near 95 K (Figure 1-1).[17] The general formula for this class of material is $REBa_2Cu_3O_{7-x}$, where RE comprises the rare earths Y, La, Nd, Sm, Eu, Gd, Dy, Ho, Er, Tm, Yb, and Lu, and x is between 0.095 and 0.3.[18]

In $YBa_2Cu_3O_7$, Y and Ba atoms occupy the A cation sites; whereas, Cu ions occupy the B cation sites (Figure 1-1). It is believed that the current is transported in the copper-oxygen plane of this unit cell, which is parallel to the substrate in c-axis oriented film.[16] Vertical-device structure applications require a-axis oriented film with the Cu-O plane normal to the substrate.

Because of the differences in the relative sizes of the ions, a variety of distortions from the cubic structure can take place. As the result, a YBaCuO superconductor has two crystalline forms: orthorhombic and tetragonal. The orthorhombic state is the superconducting state with the oxygen stoichiometric in the range of 6.5 to 7. The tetragonal state has an oxygen stoichiometry less than 6.5 and a T_c value of 66 K. The unit cell dimensions of orthorhombic YBaCuO superconductor are a=3.8 ‹, b=3.9 ‹, and c=13.0 or 27.2 ‹.[16] An excellent review of the properties and processing of this material is available.[19]

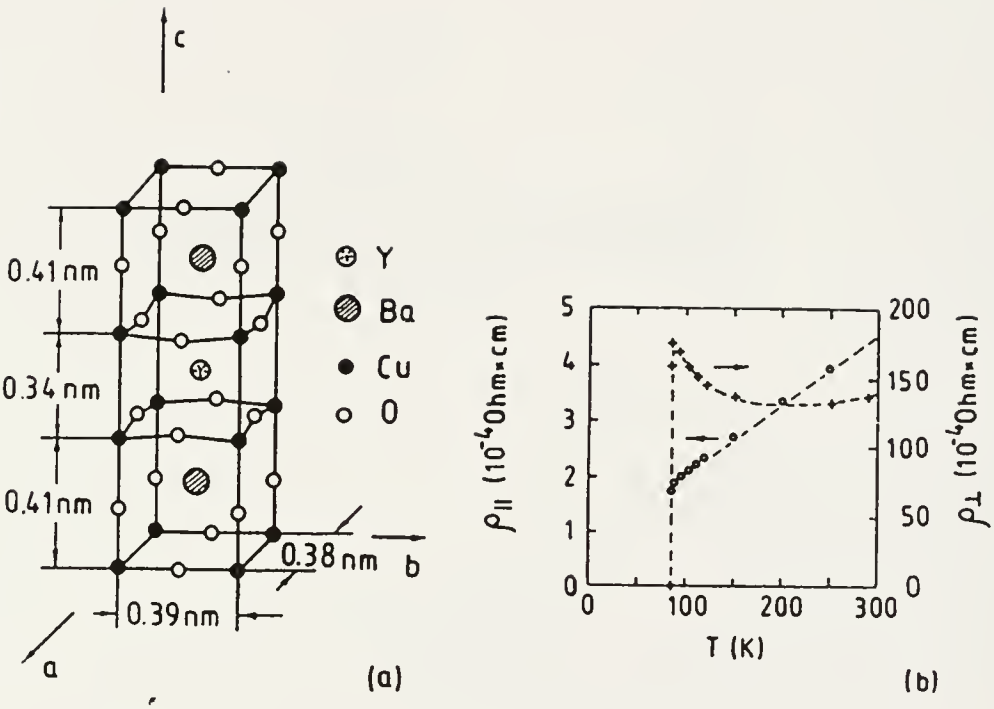

Figure 1-1 $YBa_2Cu_3O_7$ superconductor (a) atomic structure; (b) temperature dependent resistivity. Reference 17.

Other technologically important classes of superconductors include the thallium-based compounds, e.g., Tl-Ba-Ca-Cu-O (T_c=125 K) and Tl-Pb-Sr-Ca-Cu-O (T_c=125 K), and bismuth-based compounds, e.g., Bi-Sr-Ca-Cu-O (T_c=110 K). The general formula of these compounds is $(A^{III}O)_xA_2^{II}Ca_{n-1}Cu_nO_{2n+2}$, where A^{III} = thallium, bismuth, bismuth+lead, bismuth+thallium, RE or thallium+lead; A^{II}= barium or strontium; and n = number of copper-oxygen $(CuO_2)^{2-}$ layers.[18] Because these superconductors have more elements than YBCO, more secondary phases are present, which makes it difficult to produce high-quality and stoichiometric films. A problem with thallium-based films is that the high vapor pressure of thallium makes it difficult to control the stoichiometry. An advantage of this material, however, is that the grain boundaries have less influence on the surface resistivity than in YBCO films.

The qualities of high-temperature superconducting thin films make them suitable for a variety of applications including passive microwave devices (e.g., passive interconnects) and active microwave devices (e.g., quantum interference devices and tunneling junction switches).[20] It is important to consider the potential dynamic application in determining how the film should be optimized and in understanding the quality of film to be made. These device applications are discussed in detail below.

1.1.1.2 Passive microwave devices

Passive devices are constructed from a patterned, single-layer superconducting film. Passive microwave devices change the input signals in a linear fashion,[21] that is, the output varies linearly with the input. Applications of this type of device are microwave filters, resonators, switches, and delay lines. A schematic view of a stripline resonator is shown in Figure 1-2.[21] With these devices, only the surface properties of the superconducting film are important, mainly, the superconducting zero resistance property. The device is primarily used as the signal transfer media in which the signals travel at the surface.

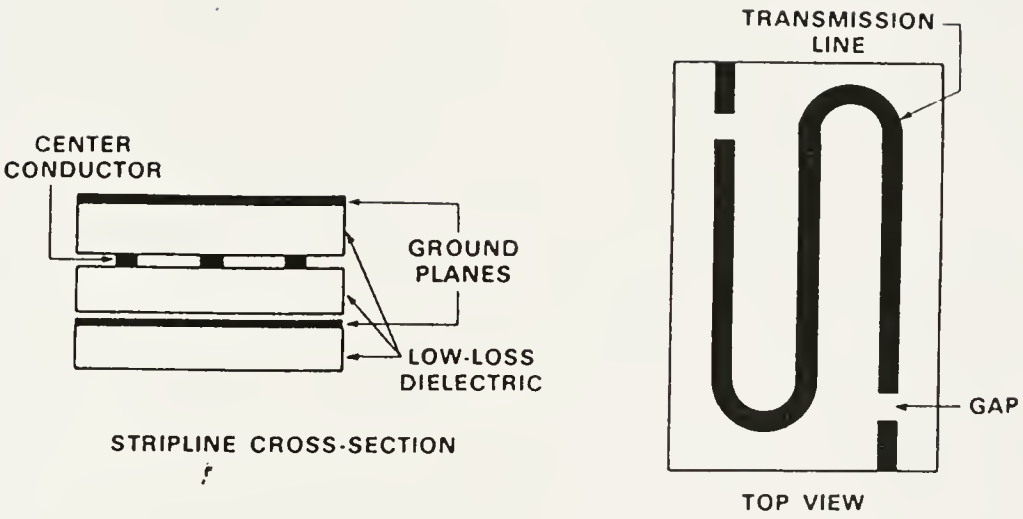

Figure 1-2 Schematic view a stripline resonator. (a) cross section showing conductor and dielectric; (b) top view. Reference 21.

Devices fabricated of superconductor material are superior to those that use a metal (e.g., copper) since the superconductor surface resistance value is a few orders of magnitude lower. The microwave surface resistance of copper at 77 K and 10 GHz is typically 10 mΩ, whereas for an HTSC, the value is 200 μΩ.[22]

The main application for passive microwave devices is in signal processors, which accept signals from analog sources and extract the essential information by improving the signal-to-noise ratio. Radar is an example of signal processing used to produce a map of target intensity as a function of range and velocity.

1.1.1.3 Active microwave devices

Active devices have more complex structures than passive devices and process signals nonlinearly.[21] The best example is the Josephson junction. The intrinsic speed of superconductive electronics comes from the rapid switching ability of Josephson junctions. A cross section of a circuit containing Josephson junctions is shown in Figure 1-3.[23]

Constructing a Josephson junction involves complex, multilayered superconductor film formation with critical control of the interface and thickness. A typical Josephson junction consists of two layers of superconductor separated by a thin insulator. The thickness of the insulator is of the same order as the coherence length; that is, the thickness for "tunneling" to take place, which, depending on the crystal orientation, is from 3 to 35 Å for YBCO material.[24]

In principle, Josephson switches use a tunnel junction that operates between the superconducting state and the voltage state, corresponding to the logical "0" and "1" states. The device switching time from the zero-resistant state to the finite-voltage state is in the range of picoseconds. This rapid switching allows an electronic signal to be controlled in the same time frame, which is much faster than current computers with time constants on the order of nanoseconds. Since light travels a foot in a nanosecond, the future fast superconducting computer has to be small, about the size of a calculator, to minimize distance; otherwise the fast switching time is useless.

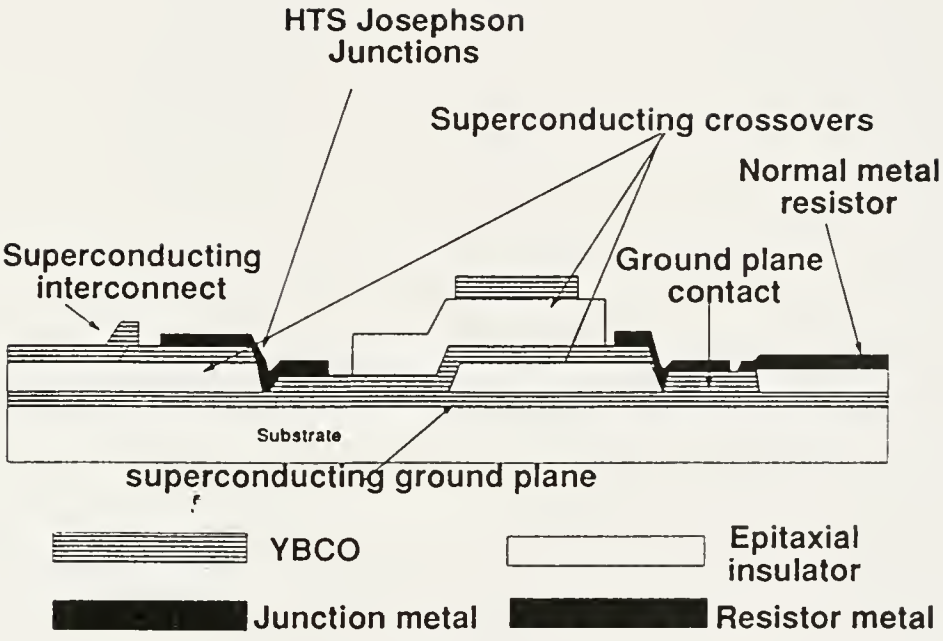

Figure 1-3 Schematic view a HTSC Josephson Junction circuit. Reference 23.

1.1.1.4 Integrated systems

Beyond active and passive devices, there are integrated systems, which consist of several devices. Examples are superconducting quantum interference devices (SQUIDs), Josephson arrays, microwave detectors, digital signal processors, and analog signal processors.[20] A cross section of an integrated SQUID is shown in Figure 1-4.[23]

A SQUID, in principle, is a flux-to-voltage transducer, which was developed at Ford Motor in 1960. It combines two physical phenomena: flux quantization and Josephson tunneling. Fundamentally, it is a superconductor ring that acts as a storage device for magnetic fields, and was intentionally made to contain weak links of Josephson junctions. Its main function is to serve as a magnetic flux gate. A superconductor ring will oppose an applied magnetic field by generating superconducting current. If the field is large, the current will also be large and beyond the Josephson junction capacity, causing the junction to fail. This breaks continuity and allows more "quanta" of magnet to pass. If a known and variable current is applied to the ring to balance this effect, the field can be detected using a feedback method.

Since SQUIDs have quantum-level sensitivity to magnetic flux, they are used as ultra-sensitive magnetic-field detectors, capable of detecting fields less than a billionth of the naturally occurring earth field. Applications of SQUIDs include passive devices for medical diagnostics, mineral surveying, earth mapping, submarine detection, relative motion detection, and scientific instruments; and active devices for low-noise, high-frequency mixers, high-speed oscilloscopes, and A/D converters.

The development of the Josephson junction and SQUIDs is currently limited by the lack of high-quality thin films. The film must be smooth and uniform at a length scale less than the smallest circuit feature in the order of a few nanometers; so far, no film deposition technique can meet this criterion. Fabrication of the Josephson junction is further complicated by the requirement of high substrate temperature during deposition, which

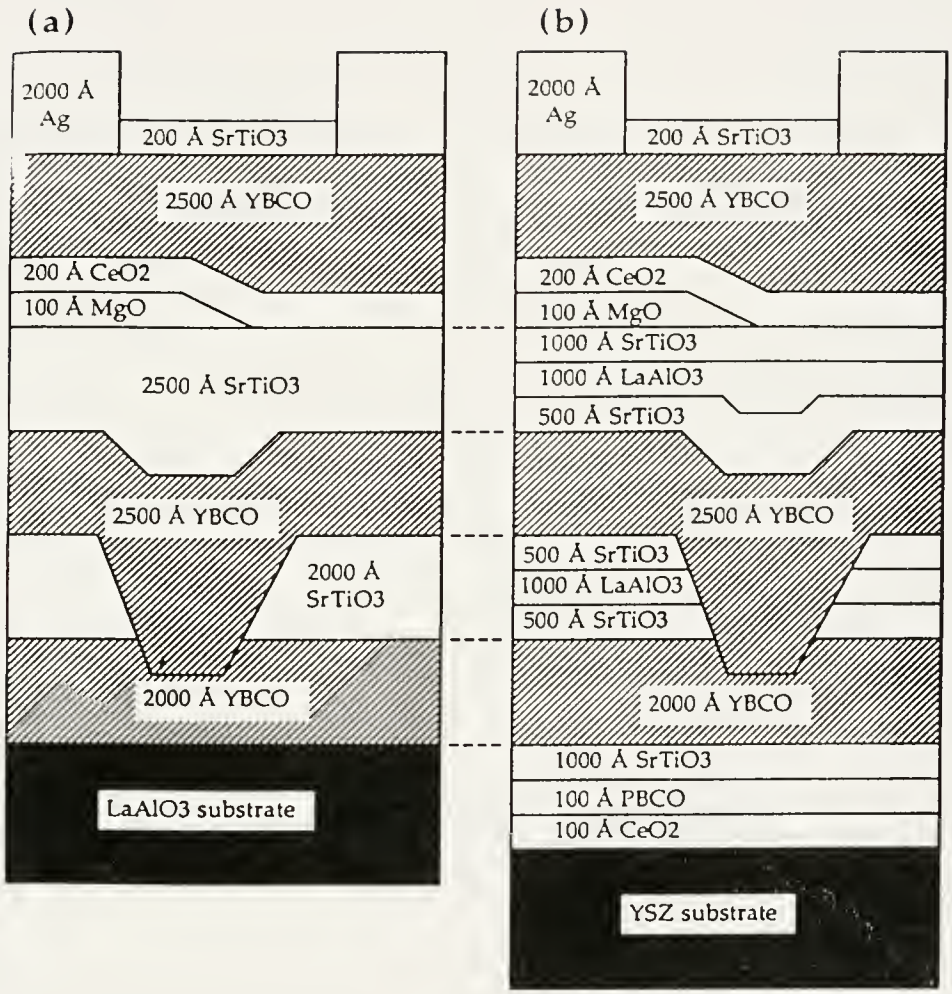

Figure 1-4 Cross sectional view a integrated SQUID magnetometer (a) on $LaAlO_3$ substrate; (b) on YSZ substrate. Reference 23.

makes it almost impossible to fabricate two superconducting layers sandwiched through an insulating barrier without encountering interdiffusion problems.

1.1.2 HTSC Thin Films

The quality of the superconducting film is the key to a high-performance microwave device. This section deals with the selection and testing criteria for an ideal thin film, selection of the substrate, and the technological challenges in producing the superconducting thin film.

1.1.2.1 Ideal film properties

Ideally, a high-quality HTSC thin film possesses good stoichiometry, high phase purity, perfect crystalline structure, high T_c, small transition width, high J_c, low surface resistance, and smooth surface morphology. These are, in fact, the characteristics of a single, perfect superconductor crystal. In reality, however, films only have some of these properties. At a minimum, a useful high T_c film should be epitaxially grown on a lattice-matched substrate with the correct crystalline structure and be relatively smooth; i.e., have only a few boulders and pinhole defects. It is important to point out that high T_c film does not necessarily have a high J_c, since only one direct superconductive path is required to give good T_c, in contrast to J_c, which is determined by the bulk surface resistance. The presence of in-plane misorientation and grain boundaries strongly affects the film's high-frequency surface resistance, which is important in microwave applications.

1.1.2.2 Characterization techniques

Many analytical techniques are available to evaluate the performance and quality of thin films. They are specifically used to determine the film composition, T_c, J_c, and crystal orientation. The techniques used in this dissertation are briefly described below. This thesis focuses on the laser target and plasma plume interaction, and the deposited film provides a record of this interaction.

Composition.

Rutherford backscattering (RBS), used to determine the thin-film composition, is based on the elastic collisions between accelerated $^{2}He_{4}$ atoms and the atom constituents in the film. Atomic weights and distributions of elements in the film can be determined from the measured momentum of the reflected helium atoms momentums.

Electron micro probe analysis (EMPA), which was used to determine composition, was based on the x-ray produced when the outer-shell electrons drop to the inner-shell vacancies. The element can be identified from the x-ray energy released.

Auger electron spectroscopy (AES), used to determine composition, was based on the Auger electron produced when electrons from the outer shell drop to the vacancies in the inner shell. An Auger electron has a kinetic energy characteristic of the host atom.

T_c.

Eddy current measurement was used to determine the T_c onset and transition width. It works by detecting the inductive current generated by the film's superconducting magnetic fields. As the film undergoes a zero resistance transition, the inductive current sharply increases.

J_c.

Four-point DC current probes and AC surface current measurements were used to determine the J_c value and surface resistance of the film. DC current measurements are simply contact probe resistance measurements, while AC current measurement are used to determine the surface inductance.

Crystal structure.

X-ray diffraction (XRD) was used to determine the phase purity and crystal orientation of the film. Based on the diffracted x-ray beam by the crystal lattice, the crystal spacing and coherence of each phase can be determined.

Surface morphology

The scanning electron microscope (SEM) is used to determine the film surface morphology. The surface image can be constructed from the reflected electrons. Most units are equipped with EDAX (energy dispersive x-ray analysis), which determines surface composition based on the electron kinetic energy.

1.1.2.3 Substrates

Success in making high-quality HTSC thin film depends on the substrate chosen. The substrate influences the film quality through the following properties: thermal expansion mismatch, which can cause cracks in the film; interface reaction, which changes the film composition; and, most importantly, substrate lattice mismatch, which affects the film crystallographic orientation.[25] The ideal substrate for depositing YBCO film is lattice-matched with the perovskite structure (e.g., $SrTiO_3$, $LaAlO_3$, and $LiNbO_3$) and has a reasonable thermal expansion match and minimum interface reactivity.

In addition to the lattice matching, thermal stability, and reactivity properties, the substrate dielectric characteristic should be carefully considered for microwave applications. Many of the available substrates (such as $LiNbO_3$, MgO, ZrO_2, $LaAlO_3$, and $SrTiO_3$) have some, but not all, of these desired properties. For example, $LiNbO_3$ has good dielectric and crystalline matches, but is very reactive, permitting Ba and Cu migration through the interface. MgO and ZrO_2 have ideal dielectric characteristic for microwave applications. They are chemically inert with superconducting material, but show poor crystal matching properties. $LaAlO_3$ and $SrTiO_3$, on the other hand, are perfect in crystal match, but have high dielectric constants, which are poor for microwave circuits. Similarly, $SrTiO_3$ has an extremely high dielectric constant, which results in considerable high-frequency losses in microwave applications. $LaGaO_3$ has the lowest dielectric constant and a lattice constant comparable to YBaCuO (orthorhombic, a=3.820 Å, b=3.892 Å, c/3=3.896 Å). It is, however, susceptible to a phase transition at 140 C, which is below the temperature range required for film annealing.[26]

Other choices for substrate are glass, quartz, sapphire, Sr_2TiO_4, $BaTiO_3$, and BaF_2. Recent technology combines the characteristics of two or more materials in forming buffer layers between a substrate and the high T_c film. Two examples are $SrTiO_3$-buffered MgO and cerium-oxide buffered zirconia.

1.1.2.4 Technological challenges

A quality HTSC is defined as having good crystalline structure and a smooth surface. The crystalline structure determines the thin film performance, while the surface smoothness determines the circuit resolution. High deposition temperatures are required to enhance surface mobility during film growth, which results in proper crystalline structure.

However, imperfections arise in the film quality since superconductor materials are inherently reactive [27] and the crystalline structure is sensitive to oxygen stoichiometry. High temperatures exacerbate these problems, especially in multilayer thin films.

The above constraints pose many technological challenges in producing good HTSC thin film. Some of these challenges are directly related to deposition techniques used to produce thin film. Various deposition techniques and their merits are discussed below.

1.1.3 Comparison of Techniques for Deposition of YBCO

The deposition of epitaxial thin films has been demonstrated using a number of techniques,[28,29] including electron-beam evaporation, sputtering, chemical vapor deposition, laser deposition, spray pyrolysis, molecular-beam epitaxy, and activated reactive evaporation. Although pulsed-laser deposition was the only technique used in this research, a brief comparison of the four most common techniques is presented below. An expanded discussion of pulsed-laser deposition follows this comparison.

1.1.3.1 Electron-beam evaporation

This was the first technique used for depositing HTSC thin films. This process involves the evaporation of a solid target via electron-beam heating. Since the 123 material

does not melt congruently, separate sources are used. Early work was performed in laboratories at IBM, Stanford, Cornell, and later at Kyoto University and AT&T. In order to achieve a stoichiometric film, it is necessary to control the fluxes from the individual sources, which can be elemental or compound. Some of the best films have been made by the three-electron-gun evaporation technique. This technique is the most sophisticated in terms of complexity and expense, and it is not favored when a large number of elements must be deposited.

1.1.3.2 Sputtering

Sputtering works by the momentum transfer between the sputtering ions and the atoms or molecules in the target. There are several types of sputtering systems, including diode source, conventional magnetron, ion beam, and novel cathodes. The oxides can be sputtered from multiple or single sources. This method was developed by Stanford, Westinghouse, and Argonne. TRW has developed a three-target technique. The target may be in a machined form or a powder. The composition of the film is altered by the negative ion bombardment on the deposited film during the deposition. Off-stoichiometry targets, correct geometry, or high pressure are used to correct the problem. This technique is widely used for commercial applications and has no scale-up problem. Thin films as large as several inches in diameter have been deposited. The drawback of this technique is the slow deposition rate.

1.1.3.3 Metallorganic chemical vapor deposition (MOCVD)

This method is capable of epitaxial growth of multielement crystalline materials on large-area substrates and is widely used to deposit compound semiconductors. This technique uses volatile metallorganic precursors to transport the elements. The challenge is to identify, produce, and handle precursors with suitable properties, especially for the transport of barium, since volatile barium precursors are limited. The chemical complexity of this method and the limited selection of volatile precursors have caused the slow development of this technique.

1.1.3.4 Pulsed-laser deposition (PLD)

The pulsed-laser deposition technique utilizes photon energy to evaporate a target material at low pressures and to deposit the resulting plasma as a thin film. Since the irradiated surface temperature can reach several thousand degrees, a multicomponent target can be evaporated stoichiometrically. Various laser sources can be used, including those that emit in the far IR wavelength (e.g., a CO_2 laser) and in the near UV wavelength (e.g., the KrF excimer laser). This technique was broadly applied to HTSC deposition by Bellcore and Rutgers University. Although the deposition rate is relatively high, it is limited by the optical properties of the evaporated target material and the formation of particulates on the film.

1.2 Overview of Pulsed-Laser Evaporation

Pulsed-laser deposition can be adapted for depositing a variety of materials, including the high-temperature superconductors. It is the technique used in this study, and a broad overview of the hardware, deposition parameters, laser-target interactions, and current challenges is presented below. Particular attention is given to the formation of film particulates and the development of target morphology for deposition of YBCO.

1.2.1 Hardware Configurations

Compared to other thin-film deposition techniques, a PLD growth system is a relatively simple experimental design, with minimum hardware requirements inside the vacuum chamber.[30] A PLD system has two main components, a vacuum chamber and a laser system.

A schematic diagram of the system used in this study is shown in Figure 1-5.

The basic vacuum chamber is configured with a target holder, a substrate holder, a gas nozzle, and a glass window. The target holder is generally designed to allow rotation in order to present new target areas to the laser during the evaporation. The substrate is

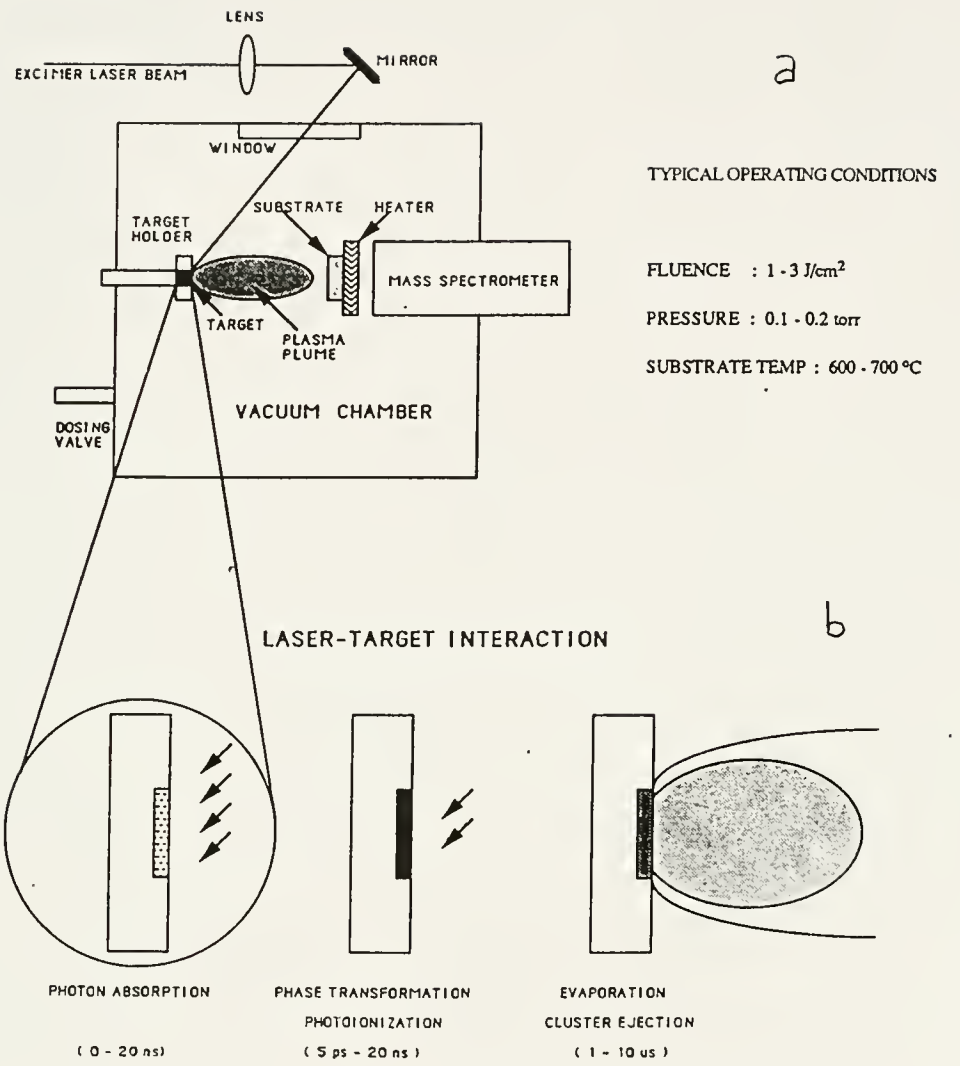

Figure 1-5 Schematic diagram a pulsed laser deposition chamber. Bottom view shows zones of laser-target interactions.

heated (≥ 700 ^{o}C) to allow optimum crystalline growth. The nozzle, placed at a location away from the pump in the chamber, is used to establish a gas ambient, typically oxygen, during deposition. The background pressure is typically adjusted in the range of 100 to 200 mTorr, requiring a flow rate in the range 50 to 100 sccm. For optional plasma in situ monitoring, a PLD growth system can be equipped with a variety of diagnostic instruments such as a mass spectrometer, optical spectrometer, or ion probe.

The laser system consists of a high-power laser, coupled to an appropriate beam delivery system. Lasers are operated in continuous and pulsed modes. A continuous laser produces a steady output of laser power. Pulsed laser, on the other hand, discharges the laser energy periodically at high intensity in a short duration. Various types of lasers have been used, including short wavelength UV pulsed excimer lasers, e.g., ArF (193 nm), KrF (248 nm), XeCl (308 nm), and long wavelength IR lasers, e.g., CO_2 laser (10.6 μm), Nd:YAG lasers, both pulsed (1.064 μm), and Q-switched (532, 355 nm). The peak power of these lasers can be as high as 10^8 W/cm^2, with a pulse width that varies between nanoseconds and milliseconds. The selection of a particular laser depends on the material to be deposited. An excimer laser, having a high absorption coefficient, requires a lower evaporation threshold; however, the repetition rate is low, typically less than 250 pulse per second (pps). In contrast, a Nd:YAG laser has a higher evaporation threshold because the absorption coefficient is low; however, the repetition rate can be as high as 2000 pps [31] Both an excimer laser and a Nd:YAG laser are capable of producing high-performance films, although it is argued that the longer wavelength lasers may be better since the higher penetration depth produces a deeper molten layer. Thus, the material removal is dominated by nonequilibrium molten droplets, instead of equilibrium vapor.[31, 32]

1.2.2 Operational Procedures

The two key sets of design and operational parameters in PLD are associated with the laser and the deposition chamber. The parameters associated with the laser operation

are external and consist of laser wavelength, laser fluence, repetition rate, number of pulses and the incident angle. The parameters associated with the deposition chamber include the deposition geometry (e.g., the distance and orientation between the target and the substrate), and the deposition environment (e.g., the ambient gas species, background pressure, substrate temperature, and the annealing cycle). The results from several different laboratories indicate that similar operational parameters will yield high-quality $YBa_2Cu_3O_7$ films [4, 33-36] The optimal values of these operational parameters have been largely determined by empirical methods.

A typical deposition run begins with the placement of a pellet of YBCO superconductor into a target holder inside the vacuum chamber. The pellet is produced using a sintering technique that is discussed in Chapter 3. The pellet mounted in the holder rotates at speeds up to 10 rpm to ensure that the laser beam encounters a new area on successive evaporations. The pulsed laser beam is directed into the chamber through a quartz or fused silica window and focused onto the target surface. Typical laser pulse energy densities varies from 1 to 3 J/cm^2, with repetition rates of 1 to 10 pps and incident angles from 30 to approaching 90^o from the target normal. The target area impacted by the laser beam produces a brilliant, elongated plasma plume, which is then deposited on a substrate located at 1 to 5 cm from the target surface.[4] The optimum distance for film deposition depends on the background oxygen pressure.[37] Though the typical target etch rates are 70 nm per pulse, deposition rates are on the order of 1 to 4 A/pulse due to the large ratio of substrate to ablated area.[4] The deposited film has a thickness variation of about 20% across the substrate of an area of 0.25 cm^2.[4] In early studies, the substrate temperature was maintained at a low value ($\approx$ 400 ^oC), and the chamber pressure was regulated at low value ($\approx 10^{-5}$ Torr). In this high-vacuum process, the film is in an amorphous state and requires annealing in oxygen at a temperature over 800 ^oC. Because of the susceptibility of this amorphous film to moisture uptake during transfer, the procedure was improved by increasing the background pressure to the range of 100 to 200

mTorr of oxygen to maintain the correct film oxygen content. Following film deposition, the film is annealed by increasing the oxygen chamber pressure close to atmospheric pressure, while cooling the substrate temperature at a prescribed rate.[38, 39] With these growth conditions, the resulting $YBa_2Cu_3O_7$ film is black, shiny, and superconducting.

The substrate temperature and the oxygen pressure have been found to strongly influence the superconducting properties of the films. It is known that the activation energy required for in-diffusion oxygen increases from 0.5 to 1.5 eV for $YBa_2Cu_3O_{6.7}$ and $YBa_2Cu_3O_7$ respectively,[40] therefore the higher deposition temperature is preferred in obtaining superconducting film. PLD films that are deposited at room temperature are insulating, yellow-brown, and exhibit poor adhesion to the substrate; subsequent annealing does not improve the conductivity.[4] In contrast, heating the substrate to 450 °C during deposition produces a shiny, brown film with good adhesion properties. Upon annealing in oxygen at elevated temperature (≈900 °C) and then cooling slowly, the film becomes superconducting. This film, however, is rough and phase-segregated. *In situ* growth eliminates the need for this annealing procedure; therefore, the phase-segregation is minimized. At low deposition temperatures, films are typically a-axis orientated,[41] while film deposited at optimal conditions (≈700 to 800 °C in 100 to 200 mTorr oxygen) are oriented along the c-axis.

1.2.3 Typical Results

The YBCO films deposited by laser deposition have been measured to have T_c values as high as 95 K [4] and J_c values as high as $5x10^6$ A/cm^2 at 77 K and $4x10^7$ A/cm^2 at 4 K. The surface resistances at 10 GHz have been measured to be as low as 10 μohm at 4 K and below 300 μohm at 77 K.

XRD measurements have shown that film performance depends on the substrate-film crystalline match. If the film is deposited on a perovskite substrate, such as (100) $SrTiO_3$, XRD has shown that the film has a high degree of c-axis orientation. On the other

hand, a film that is deposited on a cubic sapphire [4] has fewer degrees of orientation. This mismatch is reflected in the value of T_c with measured values of 95 K on (100) $SrTiO_3$ [4] and 75 K on sapphire.[4]

The critical grain size required for high-quality superconducting properties has been found to depend on the substrate selection. Typical grain sizes, as determined by SEM, is 500 nm on $SrTiO_3$ and 150 nm on Al_2O_3.[4] Small particles are always observed on the film surface with diameter of 0.5 to 2 μm as detected by SEM. These particulates are seen regardless the type of laser used.

Laser fluence has been found to affect the film composition, especially if a laser other than an excimer laser is used. At low fluence (0.6-0.8 J/cm^2), Y-deficient films are obtained. At medium fluence (1-2 J/cm^2), excess Y and Ba and deficient Cu films are obtained. At high fluence (> 2 J/cm^2), excess Ba and deficient Cu films are obtained.[33] Venkatesan reported that stoichiometric films could be produced using a KrF excimer laser at fluences greater than 0.9 J/cm^2 at an incident angle greater relative to the target normal than 20°. With an XeCl laser, improved stoichiometry was found at a higher angle and at an energy density of 4 J/cm^2.

Another factor affecting film quality is reaction with the substrate,[27] especially at high deposition or annealing temperature. Films grown on sapphire and annealed at 800 °C gave a Ba-rich interfacial layer and, consequently, a Y-rich remaining layer.[42] These films had poor superconductivity characteristics, although a Rutherford backscattering showed that these films were highly stoichiometric with composition within 1% of the target.

1.2.4 Overview of Laser-Target Interactions

The sequential processes involved in laser evaporation are as follows. The photon beam is absorbed in the outer layer of the target ($\alpha = 10^5$ cm^{-1} at 248 nm),[43] causing the surface temperature to increase, which produces surface melting and evaporation (Figure

1-5). The rapid evaporation can develop a recoil pressure, which expels the molten pool and produces droplet ejection. The plasma, therefore, consists of both liquid and vapor phases. If the pulse duration is sufficiently long, absorption of the photon by the plasma becomes more important. The solid-liquid-vapor-phase transformations take place in several picoseconds, whereas the plasma ejection process takes place in several nanoseconds, possibly because it is limited by Knudsen flow.

Model development can be simplified by dividing the process into two steps based on the characteristic time constants. The first step involves the absorption of photons by the target, causing the target to heat, melt, and ionize while spatially localized in the picoseconds. The second step is the expansion of the resulting high-temperature, high-pressure plasma into the free space during the subsequent several microseconds.

1.2.4.1 Photon absorption and phase transformation

Photons are absorbed by the electrons and phonons in the target lattice, by the molten carrier through surface absorption, and by the emitted plasma. The initial stage of the evaporation process is surface heating due to the absorption of the laser energy in a short period of time. During the evaporation of the ceramic target, the laser power density can be as high as 10^7 to $10^8 W/cm^2$. The surface temperature is determined by the wavelength and flux of the incoming radiation, the thermal diffusivity, heat capacity, and the absorption coefficient of the target. In general, a one-dimensional heat transfer model involving surface melting is used.[44]

In a condition suitable for material removal, the surface temperature of the ceramic must exceed the melting point. For example, with YBCO this corresponds to a threshold energy density of 0.11 J/cm^2 at wavelength of 248 nm (KrF laser).[43] The corresponding etch rate varies logarithmically with energy density with a reported inverse absorption length of $2.3 \times 10^5/cm$ or a penetration depth of 500 Å.[43] As evaporation progresses, texturing of the target surface is taking place, which lowers the evaporation rate.

1.2.4.2 Plasma expansion

The shape of the expanding plume is characterized by a high order cosine distribution function, as high as twelfth order. In comparison, a normal Langmuir or Knudsen evaporation exhibits a first order cosine function.[45] It has been suggested that the cosine distribution function in pulse-laser deposition contains both the high order and the first cosine functions due to the contributions of both the high-velocity and the low-velocity components of the plasma. In addition to the total mass distribution, a composition variation is also observed.[46] This composition variation is negligible for the center portion of the plume in the high cosine region, but becomes nonstoichiometric in the outer region. The plasma velocity was measured to be in the order of 10^6 cm/sec.[12]

Various techniques have been used in an attempt to analyze the composition of the plasma phase, including emission, fluorescence, and absorption spectroscopy. Although widely used, emission spectroscopy does not give a representative composition of the plasma. First ,this technique only detects species that have detectable quantum yields for fluorescence, and second, not all the species in the plasma fluoresce. Another method, which more accurately detects the plasma phase, is mass spectroscopy.

Mass spectroscopy has revealed that the plasma contains mostly neutral and charged atomic species.[47-51] Although most results showed that the plasma consists mainly of atomic species, high molecular weight clusters have also been detected under enhanced conditions with secondary radiation. Quantitative determination of the ion content using an ion probe has shown that charged species constitute less than 10 percent of the total species,[52] with a minimum charge concentration at fluence of 3 J/cm^2. At low fluence, the mechanism of material ejection is dominated by electronic excitation of the solid, producing mainly charged species.[47]

1.2.5 Some Outstanding Problems for PLD Technique

There are several practical issues that still need to be addressed to make PLD a reliable technique. The main problems are the generation of micron-sized boulders and the development of target texturing, which affect the deposited film quality and deposition efficiency. Furthermore, PLD is currently used only in laboratory-scale and has not been developed fully to process scale. Lastly, a problem common to all deposition techniques is the required high deposition temperature, which causes substrate-film interface reaction.

1.2.5.1 Boulder generation

The main drawback of the PLD technique is the production of boulders or particulates on the substrate. It has been suggested that the boulder formation is caused by surface texturing, plume condensation, or subsurface explosions at the target, which produces fragments that transport to the substrate. Targets that have been polished smooth produce fewer boulders;[53] however, it is impractical to polish the target surface repeatedly during the deposition, once the target texturing takes place. Several schemes have been used to destroy the particles in mid-air, such as secondary lasers and plasma rings, but particle densities on the substrate remain greater than $10^4/cm^2$. Other schemes used mechanical filters, which selectively remove the low-velocity components, based on the concept that the larger mass particles have a lower velocity than the lower mass plasma.

1.2.5.2 Target stoichiometry and texturing

Since laser evaporation is a photon-activated evaporation process, the nature of the evaporation depends on the optical characteristics of the target surface. As the target surface becomes highly textured, the photon efficiency for material removal is affected by factors such as surface reflectivity, surface scattering, and absorption nonuniformity. As a result, the surface texturing leads to a decrease in the deposition rate.[53] In addition, the plasma direction changes towards the direction of the incident laser beam as the target becomes more morphologically uneven. Several techniques have been tried to limit the

texturing problem, including rotating the target to increase the evaporated surface area. The fundamental problem, however, remains unsolved.

1.2.5.3 Process scale-up

Although a highly directional laser-induced plasma plume is advantageous for small area deposition, it poses a problem when process scale-up is attempted. Given the limitation on the maximum beam size with a sufficient fluence that can be generated from a laser (few mm^2), the area for film deposition is limited to only a few centimeters. In contrast, the maximum target diameter in sputter deposition is on the order of several cm, and therefore capable of producing a comparable size film. The deposition rate of sputtering, on the other hand, is several orders of magnitude lower than that of laser evaporation. It has been demonstrated that deposition rates as high as 150Å/sec are possible with PLD, using a high repetition rate.[54] Although beam scanning, in combination with substrate scanning and rotation, has been demonstrated to produce relatively large deposition areas (2 inches in diameter), a great deal of work is still needed to produce the desired film and compositional uniformities due to the inherent super-cosine distribution of the plume.

1.2.5.4 Substrate-film interface reactions

As the result of high deposition temperatures, as high as 800 °C, substrate-film interface reactions can become significant. For some applications, such as one that involves silicon substrate, this problem becomes more pronounced. In addition, there is the inherent difficulty of maintaining a uniform temperature as substrate radiation losses become important at high temperature. The laser deposition technique, having a highly energetic plasma plume, could potentially be adopted to produce films at much lower substrate temperatures.

1.3 Overview of This Work

This dissertation addresses several of the problems associated with the PLD technique. Though most of the studies reported in the literature address issues related to processes occurring at the substrate and the properties of the deposited film, this work focuses on interactions between the laser beam, the target, and plasma plume. It is thought that a better understanding of the processes that occur at the target will lead to solutions to some of the important problems. In general, the research reported in this dissertation is divided into three main topics, each of which is summarized below.

1.3.1 Target Surface Morphology

The fundamental mechanisms of the development YBCO target surface features were investigated. The effect of fluence, repetition rate, pulse number, target density, surface roughness, and background pressure were studied. The formation of surface features on the YBCO targets was compared to other ceramic, metal, and polymer targets. A detailed fluence-dependent optical analysis was used to investigate the mechanism for the surface evolution. The effect of bulk target temperature on surface morphology development was also investigated. The physical and chemical properties of the target, such as thermal conductivity, heat capacity, and phase transition temperatures, were measured and related to the development of target surface morphology.

1.3.2 Particulate Reduction

The fundamental mechanism of the formation of particulates during the evaporation of YBCO superconductors was investigated. The target temperature was found to have a strong influence on the production of particulates. The particulate size was estimated using a model based on the ejection of liquid droplets from the molten layer. The patterns

generated by the plume redeposited on the surface during the evaporation at atmospheric pressure were used to provide the extent of shock wave formation.

1.3.3 Target and Film Stoichiometry

The composition of the plasma plume was examined using a mass spectrometer at an intermediate pressure typical to most film deposition processes. The composition of the plasma phase, including neutrals and ions, was studied as a function of pulse number, fluence, and pressure. The ideal plasma composition under equilibrium conditions was determined using complex chemical equilibrium analysis of the plasma phase based on a stoichiometric algorithm. The effects of the temperature and pressure of the plasma on the composition were investigated with this thermodynamic model and related to the experimental results.

CHAPTER 2
EQUILIBRIUM ANALYSIS OF THE YBCO SYSTEM

2.1 Introduction

One of the advantages of pulsed laser deposition (PLD) is that the process is highly nonequilibrium, so a multielement compound can be deposited with the same stoichiometry as the target. This process is ideal for a compound that melts incongruently, since the intermediate phases are not formed. In essence, since the evaporation process is highly energetic, the solid phase is completely transformed at the target into a vapor phase with the same composition as the target and transported to the substrate where it often condenses as a stoichiometric compound. Because of the instantaneous absorption of the high-energy beam, the material is superheated and becomes a one-phase plasma system.

The degree of equilibrium in a laser-induced evaporation process, however, depends on the type of laser used in the evaporation, as well as the applied energy density. For example, the evaporative mechanism using a pulsed UV laser with high peak energy at a very short duration is believed to be highly nonequilibrium.[4] In this case, the rapid heating in a confined to a small volume, due to the shallow optical penetration depth of UV light, allowing the irradiated target temperature to increase rapidly causing evaporation. On the other hand, for a continuous infrared (IR) laser with lower peak energy, the process is closer to equilibrium or, in principle, is similar to a thermal evaporation process. With IR heating, the heated target volume is large due to the deep optical penetration depth, which can be several orders of magnitude greater than that of the UV. As the result, the temperature increase is sluggish. In the near equilibrium process, the composition of the solid and the vapor phases change with time.

It has been experimentally demonstrated that with PLD stoichiometry can be preserved with up to six elements under certain conditions.[3] This is only possible at a very high fluence and at a deposition temperature low enough to yield high sticking coefficients. At lower fluence, the stoichiometry is not preserved. For the evaporation of a YBCO material, a lower fluence is known to produce a yttrium-deficient film. This behavior suggests that the process is not totally physical even under the conditions of energetic UV vaporization, and may be connected to the target surface temperature or the temperature of the plasma.

The PLD process can be broken into two connected processes, one occurring during irradiation at the target vapor interface and one occurring after the pulse, primarily with vapor phases. The first process is a high-temperature, high-pressure vapor system. This superheated vapor may be in partial chemical equilibrium, since the laser pulse duration is very short (i.e., in nanoseconds), although the temperature is high, a condition that favors rapid chemical reaction. Such rapid thermal increase causes superheating such that there is no distinction between superheated solid and highly condensed gas.[8] A simple calculation of the resulting dense plasma, assuming all the photon energy is absorbed to cause solid-vapor phase transformation, shows that the temperature could easily reach a few thousand degrees, with pressure as high as thousands of atmospheres. This superheated gas is more appropriately called a plasma, since a fraction of them is ionized. At a temperature of 10,000 K every gas is ionized.[55]

In the second process, the plasma expands during or following the laser pulse. This process may be closer to chemical equilibrium than the first, depending on the number of collisions. As the hot, expanding plasma leaves the target surface, it undergoes adiabatic expansion. A simple calculation involving a plasma that expands adiabatically shows that, within the expansion distance, typically approximately 3 cm between the target and the surface, the plasma could reach ambient pressure and temperature. Because of the long transit time (as the plasma expands prior to being deposited on a substrate), which can

reach several microseconds, and the collisions with the background gas, it is likely that chemical equilibrium can be reached.

2.1.1 Chemical Equilibrium Analysis

Chemical equilibrium analysis can be used to understand the characteristics of the plasma generated from pulsed laser evaporation as it forms and expands. This analysis can predict the composition of the vapor phase as a function of temperature and pressure. Because thermodynamic constraints are insensitive to a certain dynamical variables, a thermodynamic approach cannot be expected to give a detailed answer; however, it helps in representing the ideal condition. A detailed discussion of thermodynamic of unstable plasma is available.[56]

In addition to simple analysis, equilibrium analysis can be used to bound the problem, namely, the extreme high-temperature, high-pressure process of the plasma formation, and the low-temperature, low-pressure process of the plasma expansion. Moreover, the direction in which the deposition characteristics may turn out, for example, as the target composition is changed or as the temperature or pressure is varied, is often predicted by an equilibrium analysis, making this analysis an easy probe tool. The equilibrium composition can be used to predict optimum plasma temperature and pressure for the deposition, determine physical and transport properties used in process analysis, determine the effect of oxygen pressure and the inert gas, and to predict the species available for the deposition process.

The author is not aware of any previous attempts to apply equilibrium analysis to PLD. Baldwin examined laser evaporation of a binary compound and related the results to an equilibrium analysis.[57] Using a Q-switched Nd:glass laser, it was found that the composition of deposits collected from the evaporation corresponds to the equilibrium composition of liquid in equilibrium with the solid. A more complex thermodynamic equilibrium simulation has been performed in the YBCO-Cl,I system as applied to chemical

vapor deposition (CVD) of YBCO.[58] However, the chemical species involved were different, since metallo-organic precursors were used, and the typical temperature range for CVD is much lower than that of the target-vapor interface during laser evaporation.

The results of the analysis presented in this chapter will be used to help interpret the result presented in Chapter 8, where the plasma composition predicted by the computer simulation and the experimental measurements will be compared. The equilibrium composition is determined from the relative free energy of the possible components in the system. The key assumptions used in the equilibrium calculations will be discussed below.

2.1.2 Fundamental Assumptions

The basic assumptions necessary to calculate plasma thermodynamic equilibrium are local thermodynamic equilibria, electrical charge neutrality, and ideal gas. This calculation assumed that the evaporation process is strictly thermal; therefore, the effect of photochemistry, both photon absorption and emission, is ignored. It is further assumed that the plasma has a uniform pressure and density. This section describes a selection of fundamental concepts pertinent to the assumptions made above. Local equilibria and electrical charge neutrality, the concept of temperature and its significance in the partial or near equilibrium condition, and the significance of plasma electronic excitation in the laser-induced plasma will be briefly discussed.

2.1.2.1 System temperature

In thermodynamic equilibrium, the distribution of translational, rotational, vibrational, and electronic energies, as well as the distribution of energy in the spectral radiation depend on a single parameter—the system temperature. Although the rate and the type of energy transfer from one form to another may vary, or through which the dissociations are achieved, the final energy distribution is strictly determined by the temperature. The equilibrium distribution does not depend on the interactions between the individual species, it depends only on the temperature and molecular properties of each

species.[59] Once the system temperature is determined, the degree of thermal equilibrium can be determined.

A system achieves thermodynamic equilibrium if sufficient time is allowed for it to reach a uniform temperature in a heat bath. In the case of the vapor species produced by laser evaporation, each vapor species, in principle, is surrounded by the plasma plume, which acts as the heat bath. At very high temperatures, chemical reactions can proceed very rapidly, so that the time required to approach chemical equilibrium is short, even compared to the dynamics of the plasma transport. As a result, chemical equilibrium may be achieved at the target surface, the highest temperature region in the process.

If the heat transfer rate in the plasma is slow, the reaction temperature is different from the process temperature and a thermal equilibrium is not met. Where the reaction temperature conforms to the process temperature, all species are in a state of thermal ionization, and the plume is said to be in a state of Saha equilibrium.[59]

2.1.2.2 Local equilibria

Local thermodynamic equilibria in laser-induced vapor is analogous to that in metal vapor in flame.[59] Ideally, a system having thermodynamic equilibria must be adiabatic (i.e., absence of material and energy exchange with the surroundings), while at the same time being allowed to relax toward the state of equilibrium. Real flames are not really adiabatic. In addition to the energy loss due to radiation and convection, fresh supplies of combustion material are continuously added. As a result, the system consists of temperature and concentration gradients, and therefore it is not possible for a single temperature to represent the system. If, however, the rate of energy loss is slow compared to the rate of energy is partition to the various degree of freedom, a concept of local thermodynamic equilibrium may be introduced.[59] The system of interest in PLD can be assumed to be in local equilibria, since the pulse duration is short, and the transient nature of the evaporation may prevent true equilibria from being achieved. At high temperature,

however, an equilibrium condition is more likely because the electron-ion thermalization time varies inversely to the cubic of the temperature.[60]

2.1.2.3 Charge neutrality

A plasma can be defined as a collection of free-charged and neutral particles such that the net uncompensated charge is small compared with the charge of either sign, i.e., plasma is electrically neutral.[61] A system may be classified as plasma if the electron density exceeds 10^8 cm^{-3}.[59] In a charge-neutral system, the density of electrons and the charge density of all negative ions balance the charge density of all positive ions.

It is also possible that electrical neutrality can be achieved locally, especially in the case where the Debye shielding distance is small, lower than 10^{-2} cm at an electron concentration above 10^8 cm^{-3}.[55] The positive and negative charges are constrained to move together, otherwise the electrostatic forces caused by the charge separation prevent the movement of the charged ions.

At low temperature, the composition of ions can generally be neglected, especially at temperatures much lower than 5000 K.[55] However, at higher temperatures, especially when oxygen is involved, ionization becomes important, and a significant concentration of free electrons exists as the result of the equilibrium of

$$M_xO_y \leftrightarrow x\,M^+ + y\,O^+ + (x+y)\,e^- \qquad (2\text{-}1)$$

where M and O represent the constituents of a neutral molecule with stoichiometric coefficients x and y, M^+ and O^+ are the ions, with e^- as the electron. The equilibrium constant, K, can be given by the Saha equation, which is expressed as a function of ionization potential, temperature, and the statistical weight of the products and reactants. It is important to point out that treating ionization as a chemical equilibrium with the electron as the product, implies that the degree of ionization of a metal depends on the presence of other ions in the plume. Determining the degree of ionization of a species requires a calculation involving the dissociation constant of other ions and the mass balance equation of

$$\Sigma M^+ + \Sigma O^+ = \Sigma e^- \quad (2\text{-}2)$$

As the result of atoms-ions equilibria, the composition of the ions varies in a complex manner.

2.1.2.4 Electronic excitation

One factor that may affect the equilibrium calculation is the presence of other reaction paths, such as photochemistry, which may coexist with the thermal process. The transition between two electronic states involves the gain and loss of energy in a species from the ground state to the excited state. If the energy difference between these transition states is small, the transition is thermal and involves a change in vibrational and rotational states. If the energy difference is greater, the absorption and emission of radiation is involved. The absorption of light in the visible and ultraviolet region involves the transition between ground singlet states and some excited states of the molecules. In this energy range, the absorption is comparable to the atomic bond strength in a molecule, which leads to electronic excitation, bond rearrangement, and chemical reaction. The difference between the ground state and the first excited state of a molecule is typically 150 to 600 kJ/mole.[62] The transition from a singlet state to the triplet state is quantum-mechanically forbidden since it requires spin transition. If this transition takes place, the transition from the triplet to singlet emits photons, known as phosphorescence and has a lifetime of 10^{-5} sec. The travel time from the target surface to the substrate, in comparison, is approximately 3×10^{-6} sec. The transition from singlet excited state to ground state also emits photons, known as fluorescence, and has a lifetime of 10^{-8} sec. Due to the long lifetime of the triplet state, the transition from the triplet to singlet states takes place without the radiation of light. The energy, instead, is degraded into heat. The increase in temperature, according to the Boltzman relationship, should increase the concentration of excited atoms. However, as a result of this ionization, the number of neutral species also decreases. Therefore, the emissions may be decreased with a hotter flame. The absorption of photon energy by the solid and vapor during PLD involves the change of the species

from the ground state to the excited state, followed by photon emission. This emission, however, is small and will be ignored in the simulation. The dissociation reaction involving metal oxides plays an important part in the emission spectra of this element.

2.1.3 Theoretical Backgrounds

The chemical equilibrium condition in this study was formulated in terms of the chemical potential. The potential function was defined as state function; that is, the functions between the two states is independent of the path. Depending on the appropriate constraints, entropy is at a local maximum, whereas the Gibbs function is at a local minimum.

There are two formulations for the equilibrium conditions: stoichiometric and nonstoichiometric formulations.[63] The stoichiometric formulation is one in which the closed-system constraint is treated by the stoichiometric technique; for the nonstoichiometric formulation, it is treated by the Lagrange multipliers. The formulation of the stoichiometric matrix as well as the stoichiometric restrictions have been discussed in detail.[63] Both of these formulations work by minimizing the Gibbs free energy, G, as a function of the temperature and pressure.

$$\left(\frac{\partial G}{\partial \xi}\right)_{T,P} = 0 \qquad (2\text{-}3)$$

where ξ is the extent of reaction.

The free-energy information can be presented in several ways, regardless of the methods to be used in determining the equilibrium composition. They are the free energy based on the Raoult and Henry conventions, the free-energy function, the conventional absolute entropy in combination with the enthalpy of formation, and the standard electrode potentials. In this calculation, the free-energy based on the conventional absolute entropies (S^o), together with the enthalpies of formation (ΔH_f^o) was used.

The value of ΔG^o can be determined by

$$\Delta G^o = \Delta H^o - T\Delta S^o \tag{2-4}$$

where

$$\Delta S^o = \Sigma \upsilon_i S_i^o \tag{2-5}$$

and

$$\Delta H^o = \Sigma \upsilon_i H_i^o \tag{2-6}$$

and S_i^o is the absolute entropy of species i, and υ_i is the stoichiometric coefficient i.

From all the above equations, it follows that

$$\mu_i^o = \Delta H_{fi}^o - TS_i^o \tag{2-7}$$

If, however, the ΔS^o and ΔH^o are expressed in terms of the standard heat capacity at constant pressure, Cp(T), the standard enthalpy of formation at 298 K, $\Delta H_{fi,298}$, and the standard absolute entropy at 298 K, $S_{i,298}$, such that

$$\Delta H_{f,T}^o = \Delta H_{f,298}^o + \int_{298}^{T} Cp\,(T)\,dT \tag{2-8}$$

and

$$S_T^o = S_{298}^o + \int_{298}^{T} \frac{Cp\,(T)}{T}\,dT \tag{2-9}$$

then from 2-7, 2-8 and 2-9, the following expression can be obtained

$$\mu_T^o = \Delta H_{f,298}^o + \int_{298}^{T} Cp(T)\,dT - T\left(S_{298}^o + \int_{298}^{T} \frac{Cp(T)}{T}\,dT\right) \tag{2-10}$$

The database of all the species in this simulation consist of $\Delta H^o_{f,298}$, S^o_{298}, and Cp(T), which are obtained from various sources.

2.1.4 Outline of the Computer Program

The computer program used in this calculation was originally developed at the University of Florida.[64] Some modifications were made to make the program more

adaptable with the database available in this research. A brief summary of the program algorithms is presented below.

The computer program takes the input in the form of $\Delta H^{o}_{f,298}$, S^{o}_{298}, and Cp(T), together with the initial moles of each species and the elemental composition. The temperature and pressure for the simulation can be set arbitrarily. Distinctions are made for the vapor, liquid, solid, condense phase, and solution.

The program begins by calculating the standard chemical potentials for all the species and by making an initial estimate of the equilibrium compositions. The standard chemical potentials are calculated using Equation 2-10 above. The equilibrium composition based on the initial composition is determined after the optimum basis species and activity coefficients are calculated. The optimum basis species matrix is tested for linear dependency using the Gram-Schmid orthogonal algorithm, while the activity coefficients are calculated using ideal solution theory. The extent of reactions are adjusted using nonnegativity constraints. Next, a comparison is made between these equilibrium constants and the equilibrium constants calculated from the Gibbs free energy. If the error is greater than the error set for the convergence criteria, the calculations are repeated until convergence criteria are met. The details of these programs are available.[64]

The programs used to generate $\Delta H^{o}_{f,298}$, S^{o}_{298}, and Cp(T) are mainly multiple linear regression techniques. Since all the references are available in tabular form, the multiple linear regression technique is used to generate the coefficients, which can be used with the equilibrium program.

Since this simulation involves the presence of ions, the elemental basis used are ions and electrons. The basis species are chosen to be those that represent the highest ionization level, which are Y^{2+}, Ba^{2+}, Cu^{2+}, O^{2+} and e^{-}. A neutral species is, therefore, considered as a combination of a cation and two electrons, while a negative ion is considered as a combination of a cation with three electrons.

2.1.5 Statement of Purpose

The purpose of this study was to determine the composition of the plasma generated from pulsed laser evaporation during the formation and expansion stages. The chemical equilibrium calculations were performed for conditions bounded by the high-temperature high-pressure and the low-temperature low-pressure systems. The effect of excess oxygen pressure and inert gas concentration on the equilibrium composition was also studied. It should be noted that the effect of photochemistry due to the laser photon was neglected.

2.2 Thermodynamic Calculations

The thermodynamic properties used in the simulations were taken from a number of sources. The Journal of Physical and Chemical Reference Data and IVTAN Thermo provided most of the thermophysical properties used in this calculation. Additional thermophysical properties searches were done through STN International® network, which further searches BEILSTEIN, CA, DETHERM, GMELIN, JANAF, NISTTHERMO, TRCTHERMO, and DIPPR.

The following thermodynamic properties, $\Delta H^{o}_{f,298}$, S^{o}_{298}, and Cp(T), were extracted from the sources. The thermodynamic data were checked for internal consistency. If only partial information was available, an estimate was made. The species of interest are grouped into each basic element, Y, Ba, Cu, and O, with the corresponding states, solid, liquid, and vapor. Each entry in the table contained one to several references.

2.2.1 Data Fitting Functions

Three types of fitting functions were used for the heat of capacity at constant pressure. These functions were chosen because, given any set of heat capacity values with their corresponding temperature, at least one of them could give a good fit. These functions are

$$Cp(T) = A_0 + A_1.T + A_2T^{-2} + A_3.\ln T \quad (2\text{-}11)$$

$$Cp(T) = A_0 + A_1.T + A_2.T^2 + A_3.T^3 \quad (2\text{-}12)$$

$$Cp(T) = A_0 + A_1.T + A_2.T^2 + A_3.T^{-2} \quad (2\text{-}13)$$

The effectiveness of these functions is illustrated in Figure 2-1 for the heat capacity fitting of O^+. A fit using Equation 2-12 gave a correlation coefficient value of 0.98, whereas for the other two the value was only 0.80.

Each of the initial set of heat capacity data at each temperature was fitted to these functions, and the one with the highest correlation coefficient was chosen. The heat capacity coefficients, $\Delta H^o_{f,298}$, S^o_{298}, the reference source, and the fit standard deviations are summarized in Table 2-1.[65-82] All the data in this table have an accuracy better than 100 K, determine from the temperature difference between the calculated and the literature Gibbs free energy of the same value.

Where the heat capacity function did not produce an accurate fit, the calculated Gibbs free energy may have been too far from the literature value. If the standard deviation was greater than 100 K, new extrapolated values of $\Delta H^o_{f,298}$ and S^o_{298}, which minimized the error, were used. In this case, the standard deviation was denoted by a symbol "d". In the case of an ion for which only the $\Delta H^o_{f,298}$ value was available, the S^o_{298} and Cp(T) were estimated to be the same as those of the neutral species, and the standard deviation is denoted with a symbol "e."

To evaluate the accuracy of these coefficients and the others, simulations of the solid-liquid-vapor phase equilibria were performed for elemental yttrium, barium, and copper (Sections 2.2.5, 2.2.6 and 2.2.7). The phase transition temperatures were then compared with the literature values.

2.2.2 Condensed Phases

The solid phases containing at least one of the elements in YBCO are tabulated in Table 2-2.[83] All these solid phases have been identified and formed at temperatures

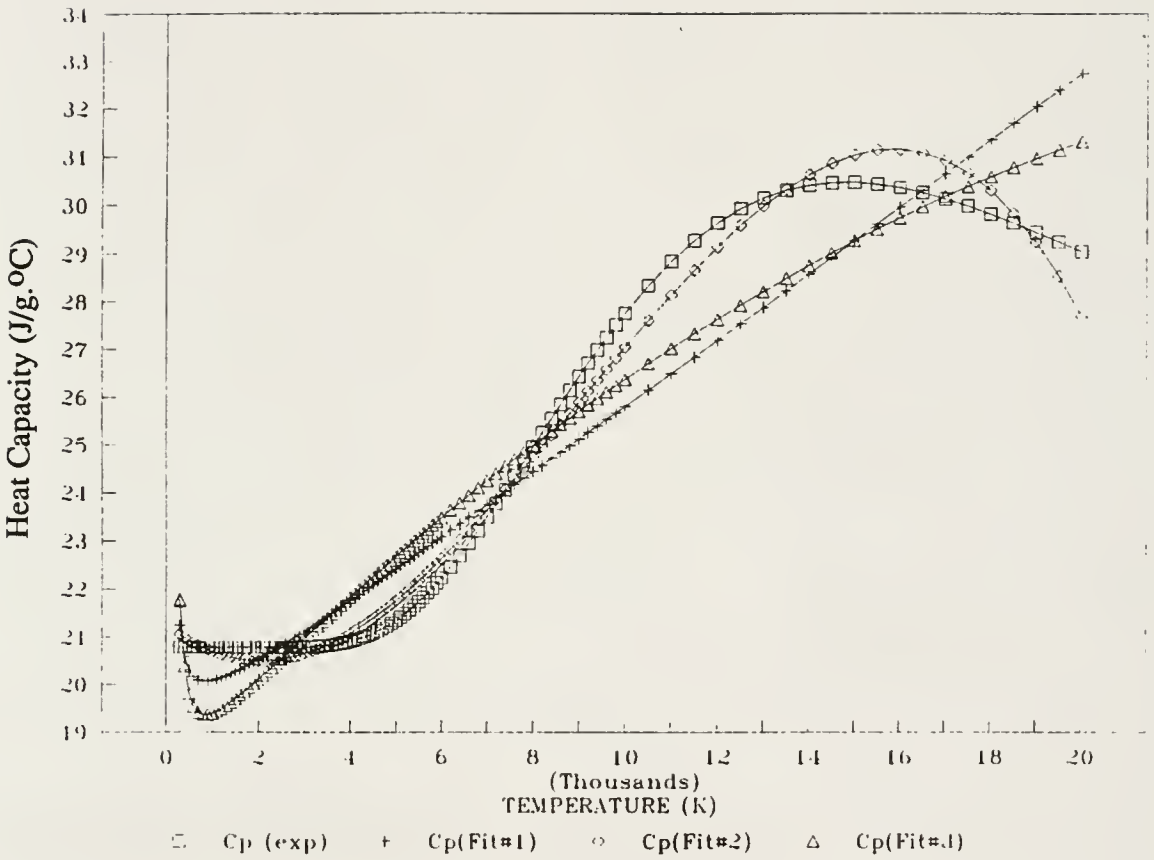

Figure 2-1 Temperature dependent heat capacity of O^+. Comparison of three different fitting functions.

Table 2-1 Thermodynamic Coefficients of the Species in the YBCO Chemical Equilibria

SPECIES	$\Delta H_{f,298}$ (kcal/mole)	S^o_{298} (kcal/mole°K)	A_0	A_1	A_2	A_3	Fits	Ref.	Note
Ba (s)	0.00000E+00	1.49390E-02	5.60108E-03	-1.90805E-06	-3.17626E+02	9.00407E-04	2-11	65-68	a
Ba (l)	1.19201E+00	1.58604E-02	1.89038E-02	-1.03272E-05	2.86804E-09	-9.03101E+02	2-13	65,66	c
Ba (g)	4.28204E+01	4.07090E-02	4.50495E-03	-4.65545E-07	1.39974E-09	-1.98165E-13	2-12	65,66	a
Ba^+ (g)	1.64545E+02	4.20870E-02	-2.63591E-02	-1.68347E-06	4.08322E+02	4.84064E-03	2-11	65,69	b
Ba^{2+}(g)	3.96860E+02	4.20870E-02	-2.63591E-02	-1.68347E-06	4.08322E+02	4.84064E-03	2-11	65,70	e
BaO (s)	-1.31063E+02	1.72331E-02	9.16463E-03	1.34519E-06	-8.30147E+01	4.66540E-04	2-11	65,71	b
BaO (l)	-1.17558E+02	2.38051E-02	9.83678E-03	5.40625E-06	-1.51091E-09	1.35875E-13	2-12	65,72	d
BaO (g)	-2.82037E+01	5.62764E-02	4.49375E-02	3.98870E-06	-5.05254E+02	-5.76722E-03	2-11	65,73,80	c
BaO^+ (g)	1.22359E+02	5.84763E-02	2.04991E-02	5.27892E-07	-2.35541E+02	-1.57789E-03	2-11	73,74,81	b
BaO_2 (s)	-1.51672E+02	2.22605E-02	1.41060E-02	6.69592E-06	1.24130E-11	-6.35853E-15	2-12	72	d
Cu (s)	0.00000E+00	7.93018E-03	6.44572E-03	-1.49983E-06	1.98729E-09	-2.53983E+01	2-13	65,67,75	b
Cu (l)	2.83525E+00	9.95218E-03	4.64409E-03	4.15329E-06	-1.65357E-09	2.06336E-13	2-12	65,67	b
Cu (g)	8.07269E+01	3.97626E-02	5.42674E-03	-1.18703E-06	6.59858E-10	-6.48923E-14	2-12	65,73	b
Cu^+ (g)	2.60469E+02	3.83845E-02	4.97961E-03	9.03273E-08	-1.40443E-10	4.02391E-14	2-12	65,73	a
Cu^{2+} (g)	7.29930E+02	3.83845E-02	4.97961E-03	9.03273E-08	-1.40443E-10	4.02391E-14	2-12	73,76	e
Cu^- (g)	5.09134E+01	3.84108E-02	4.97000E-03	0.00000E+00	0.00000E+00	0.00000E+00	2-11	65	a
Cu_2 (g)	1.16055E+02	5.78003E-02	9.08461E-03	1.28676E-08	4.01306E-11	-3.27938E+01	2-13	65,74	a
Cu_2^+ (g)	2.96030E+02	5.78003E-02	9.08461E-03	1.28676E-08	4.01306E-11	-3.27938E+01	2-13	65,74	e
CuO (s)	-3.73178E+01	1.01851E-02	1.15973E-02	1.77285E-06	-1.81827E+02	3.72076E-06	2-11	65,67	a
CuO (g)	7.49878E+01	5.60789E-02	8.96267E-03	-4.99690E-07	4.49139E-10	-4.22352E-14	2-12	65,73	b
CuO^+ (g)	2.55000E+02	5.60789E-02	8.96267E-03	-4.99690E-07	4.49139E-10	-4.22352E-14	2-12	73	e
Cu_2O (s)	-4.08195E+01	2.20851E-02	1.75347E-02	-6.61984E-07	2.87208E-09	-2.35673E+02	2-13	65,67	b
Cu_2O (l)	-2.67802E+01	3.10753E-02	-5.42559E-02	-3.83687E-06	4.88611E+02	1.14032E-02	2-11	65,67	b
e^- (g)	0.00000E+00	5.01650E-03	4.97000E-03	0.00000E+00	0.00000E+00	0.00000E+00	2-11	65,82	a
O (g)	5.96251E+01	3.85965E-02	4.75399E-03	1.18743E-07	-4.49053E-12	4.63720E+01	2-13	65,72,82	d
O^+ (g)	3.75130E+02	3.70538E-02	5.08662E-03	-1.88197E-07	5.19815E-11	-1.93666E-15	2-12	65,82	b
O^{2+} (g)	1.18726E+03	3.70538E-02	5.08662E-03	-1.88197E-07	5.19815E-11	-1.93666E-15	2-12	77,82	e
O^- (g)	2.43015E+01	3.77319E-02	5.03059E-03	8.12100E-10	1.79628E+01	-7.51902E-06	2-11	65,82	b
O_2 (g)	0.00000E+00	4.90548E-02	7.03297E-03	1.19695E-06	-1.21454E-10	3.04348E-15	2-12	65,78,82	a
O_2^+ (g)	2.80208E+02	4.91129E-02	7.65328E-03	2.45797E-07	6.08848E-11	-3.72326E-15	2-12	65,82	b
O_2^- (g)	-1.14904E+01	5.00564E-02	7.73116E-03	8.66153E-07	-1.11548E-10	3.22342E-15	2-12	65,82	b
O_3 (g)	3.40259E+01	5.75435E-02	8.46102E-03	3.62353E-06	1.06165E-09	-2.34939E-13	2-12	65,67,82	d
Y (s)	0.00000E+00	1.06251E-02	5.81244E-03	1.62982E-06	8.50022E-11	3.13799E+00	2-13	67,68,72	a
Y (l)	-1.15864E-01	7.32637E-03	1.03050E-02	-1.91355E-13	7.64557E-04	7.48732E-10	2-11	72,79	d
Y (g)	1.01339E+02	4.28895E-02	7.31717E-03	-3.61055E-06	1.56677E-09	-1.42223E-13	2-12	72,73	a
Y^+ (g)	2.46327E+02	4.03216E-02	9.95620E-03	-4.21214E-06	1.30167E-09	-1.16956E-13	2-12	73,74	c
Y^{2+} (g)	5.29383E+02	4.03216E-02	9.95620E-03	-4.21214E-06	1.30167E-09	-1.16956E-13	2-12	73,74	e
YO (g)	-1.09445E+01	5.59027E-02	9.08767E-03	-3.95467E-07	1.69535E-10	-1.37948E+02	2-13	73,74,80	b
YO^+ (g)	1.29222E+02	5.43967E-02	7.54216E-03	1.41692E-06	-5.13830E-10	8.20905E-14	2-12	73,81	b
Y_2O_3 (s)	-4.55598E+02	2.36923E-02	2.81389E-02	3.79680E-06	-1.01445E-09	-4.11308E+02	2-13	72	a

Note : a) Std. dev. 10 °K; b) Std. dev. 50 °K; c) Std. dev. 100 °K; d) $\Delta H_{f,298}$ and S^o_{298} extrapolated; e) Estimated

Table 2-2 Solid Phases of Y-Ba-Cu-O System

No.	Chemical Name	Y:Ba:Cu	Physical Properties
1	$YBa_2Cu_3O_{7-x}$	123	black, opaque, superconducting, orthorombic, stable to 500 °C
2	$YBa_3Cu_2O_{7-x}$	132	--
3	Y_2BaCuO_5	211	green, orthorombic, stable at high temperature
4	Y_2BaO_4	210	dissociates at 1400 °C
5	$Y_2Ba_2O_5$	220	occurs at 900 - 1000 °C
6	$Y_2Ba_4O_7$	240	occurs at 900 - 1000 °C
7	$Y_3Ba_4O_9$	340	melts congruently at 2160 °C
8	$Y_4Ba_2O_7$	420	--
9	$YCuO_2$	102	--
10	$Y_2Cu_2O_5$	202	orthorhombic, melt incongruently at 1100 to 1150 °C
11	Y_2O_3	200	white, raw material, melt at 2410 °C
12	$Y_4Ba_3O_9$	430	--
13	$BaCuO_2$	011	opaque, cubic, melt congruently between 1000 to 1010 °C
14	$BaCuO_4$	011	--
15	$BaCu_2O_2$	012	not stable at 1 atm
16	BaO	010	white, raw material, melt at 1918 °C
17	Ba_2CuO_3	021	decompose above 850 °C
18	Ba_3CuO_4	031	decompose above 850 °C
19	CuO	001	black, raw material, melt at 1326 °C

between 950 and 1010 °C, the temperature of interest for the formation of the 123 phase. The phase diagram generated from the experiments and from theoretical calculations is available.[84] It is important to control the stoichiometry in the formation of the 123 phase since a small change in the composition changes the stable species that may form, such as the 132 and 211, which normally occurs as phase impurities. A detailed analysis of the 123 phase is available.[83, 85]

Heating $YBa_2Cu_3O_7$ has been shown to produce Y_2BaCuO_5 and liquid phase.[86] The temperature required is at least 900 °C for the barium-copper-rich phase and up to 1500 °C for the barium-rich phases.[84] Since the 123 phase melts incongruently, the composition of the liquid phase is different from that of the liquid phase, making melt processing difficult.

For the pure yttrium system, the equilibrium condition between the solid, liquid, and vapor phase were accurately predicted, indicating that the database used in the simulation was accurate. Below the melting point, 1800 K, the chemical potential of the solid was lower than that of the liquid, indicating that the solid phase was more stable (Figure 2-2). On the other hand, above the melting point, the chemical potential of the liquid was lower, indicating that the liquid phase is more stable at this condition. Similarly, the chemical potential of the liquid phase was lower than that of the vapor below the boiling point of 3600 K, and higher above the boiling point. The literature values are 1800 K for the melting point and 3607 K for the boiling point.[72]

Phase-transformation simulation of barium metal showed a melting point of 935 K and a boiling point of 2115 K. The reference values are 1002 K and 2167 K, respectively.[72]

The phase transition temperatures for a copper element were calculated. The melting point was calculated at 1325 K, whereas the boiling point was at 2825 K. The literature values for the melting and boiling point temperatures of the copper element are 1358 and 2800 K, respectively.[72]

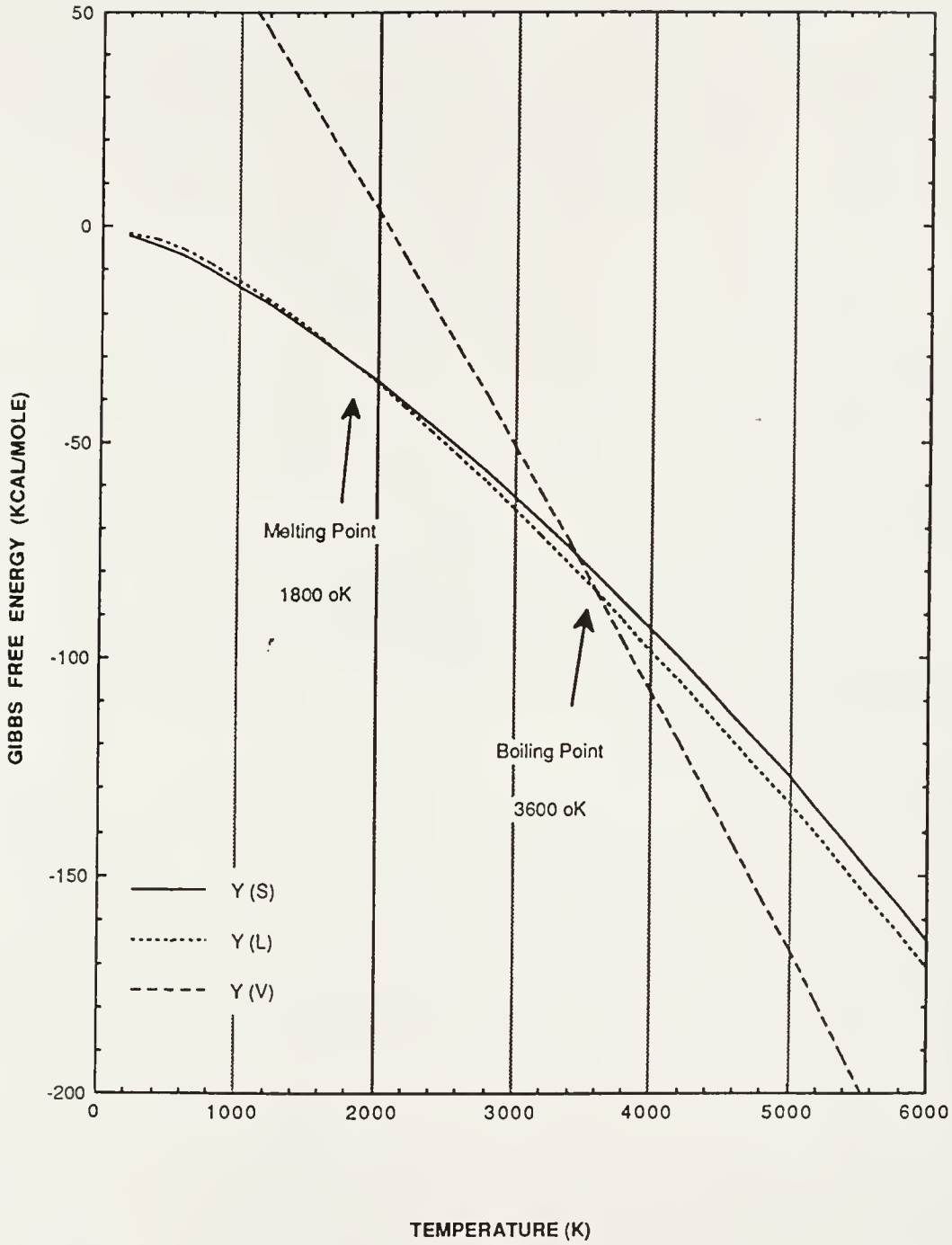

Figure 2-2 Gibbs free energy yttrium element as a function of temperature.

2.2.3 Gas Phase

The gas species that contain at least one of the elements in YBCO and have been reported in the literature are presented at Table 2-3. Most of these species are atoms and oxides, both as neutral or charged species. Since the temperature was very high, beyond the boiling points of all the species, only the gas-phase reactions were considered in the simulation. The system pressure was chosen to be 1 atm, since this was an intermediate pressure that may best represent the plasma. The plasma pressure varies from tens of atmospheres on the target surface to fractions of an atmosphere as the plasma expands. The general equilibrium reactions in the vapor phase can be summarized using the following equations:

$$MO \leftrightarrow M + O \qquad \Delta H^{o}_{rxn} = 3\text{-}7 \text{ eV} \qquad (2\text{-}14)$$

$$MO \leftrightarrow MO^{+} + e^{-} \qquad \Delta H^{o}_{rxn} = 5\text{-}7 \text{ eV} \qquad (2\text{-}15)$$

$$M \leftrightarrow M^{+} + e^{-} \qquad \Delta H^{o}_{rxn} = 5\text{-}8 \text{ eV} \qquad (2\text{-}16)$$

$$M^{+} \leftrightarrow M^{2+} + e^{-} \qquad \Delta H^{o}_{rxn} = 10\text{-}20 \text{ eV} \qquad (2\text{-}17)$$

$$O \leftrightarrow O^{+} + e^{-} \qquad \Delta H^{o}_{rxn} = 14 \text{ eV} \qquad (2\text{-}18)$$

$$O^{+} \leftrightarrow O^{2+} + e^{-} \qquad \Delta H^{o}_{rxn} = 35 \text{ eV} \qquad (2\text{-}19)$$

where M is Y, Ba, or Cu. The heat of reaction values were determined to be 298 K. All of the lower and upper limits on the heat of reaction values are for the Ba and Cu, respectively, except for Equation 2-14, which correspond to Cu and Y, respectively.

2.2.4 Oxygen System

Simulation of the oxygen system, consisted of the following vapor species: O, O_2, O_3, O^+, O^{2+}, O^-, O_2^+, and O_2^-. The pressure was kept at 1 atm, whereas the temperature was varied from 298 to 20,000 K (Figure 2-3). The four dominant species in this phase equilibria, which exist with mole fractions greater than 10^{-2}, are O_2, O, O^+ and e^-. At a temperature below 3500 K, O_2 is the majority species in the plasma. At temperatures

Table 2-3 List of vapor species detected in laser induced YBCO plasma

NO	SPECIES	DETECTION METHOD
1	Y	MS, PL, FS
2	Y^+	PL, FS
3	Y^{2+}	ES
4	Y^{3+}	ES
5	YO	MS, PL, FS
6	YO^+	FS
7	YO^{2+}	MS
8	YO_2^{2+}	MS
9	Y_2O	MS
10	Ba	MS, PL, FS
11	Ba^+	PL, FS
12	Ba^{2+}	ES
13	BaO	MS, PL
14	BaO^+	ES
15	Ba_2O	MS
16	Ba_2O_2	MS
17	Cu	MS, PL
18	Cu^+	PL
19	Cu^{2+}	ES
20	CuO	MS, PL
21	CuO^+	ES
22	CuO^{2+}	MS
23	O	MS, PL
24	O^+	PL, FS
25	O_2^+	PL, FS

Note: MS=mass spectroscopy; ES=emission spectroscopy; PL=photoluminesence spectroscopy; FS=fluoresence spectroscopy.

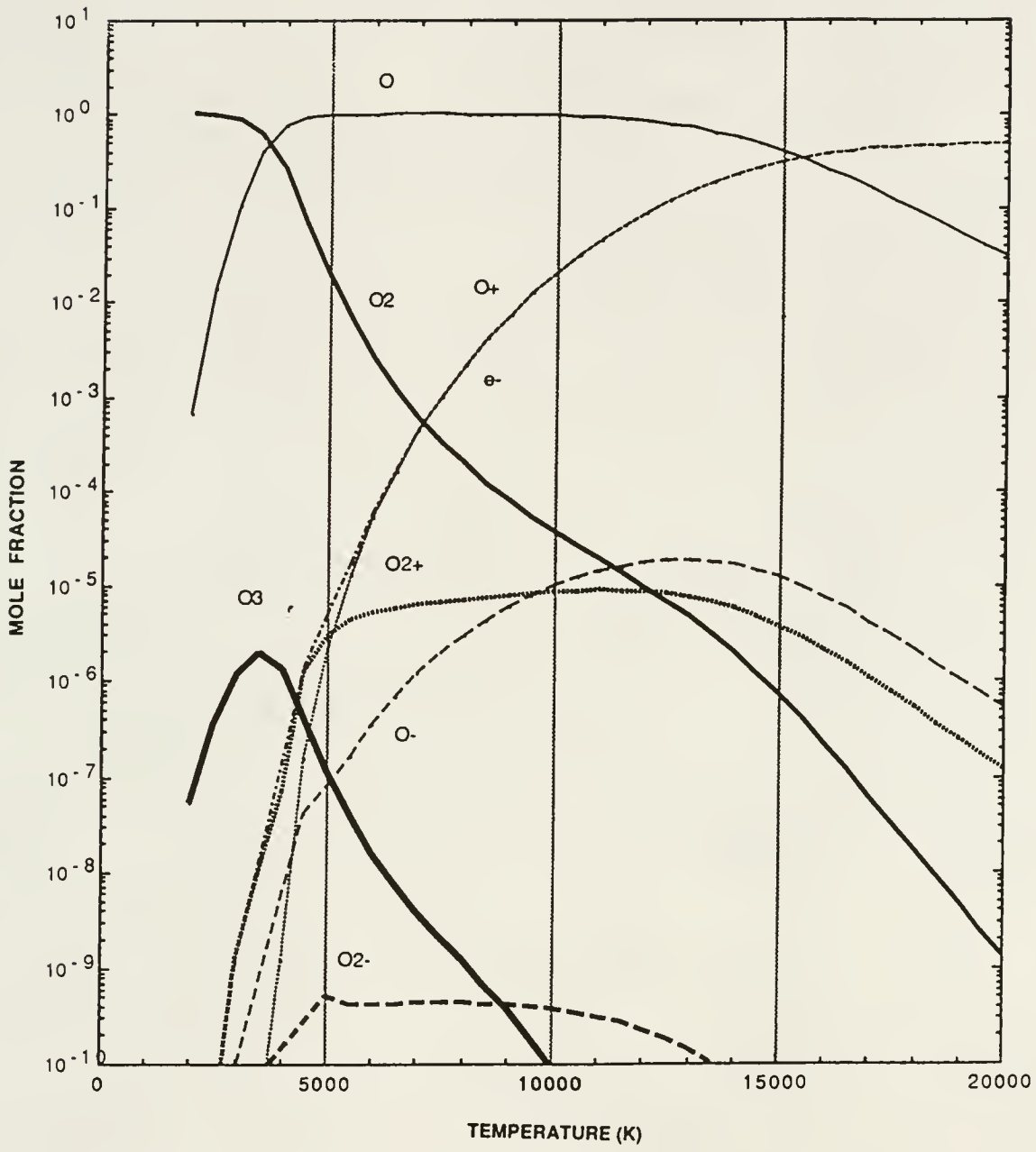

Figure 2-3 Oxygen phase equilibria at 1 atm.

between 3500 and 16,000 K, O species predominates, whereas beyond 16,000 K, O^+ and e^- ions predominate. The concentration of O_3 species reaches a maximum at 3000 K, then disappears with increasing temperature. O_2^+ and O^- are comparable in concentration at temperatures beyond 5000 K. While the concentration of O_2^- is negligible, in the ppb range, O^{2+} is practically nonexistent due to its high ionization potential (35 eV).

If the plasma temperature generated from laser evaporation is indeed around 8000 K, as commonly stated in the literature, then the equilibrium plasma consists mainly of O atoms, with decreasing O_2 and increasing O^+, two to three orders of magnitude lower than that of the O atoms. A higher concentration of ions, if detected, therefore can only be attributed to the photochemistry process.

2.2.5 Yttrium-Oxygen System

The yttrium-oxygen system equilibrium diagram with excess oxygen is presented in Figure 2-4. All the species in this figure have mole fractions greater than 10^{-2} at some temperature. The oxygen species, O_2, O, and O^+, the dominant species shown in Figure 2-3, showed temperature-dependent concentration profiles identical to those of a pure oxygen system. The values of entropy and heat capacity of Y^{2+} was assumed to be the same as those of Y^+ since only the enthalpy value was available. Both Y and YO species exist at high concentration at temperatures below 13,000 and 9000 K respectively. It has been reported that YO transfer is the main path for oxygen transfer to the film.[87] The YO^+ cation exists only in the temperature range of 3000 to 11,000 K, with a maximum at 7000 K. The Y^+ exists at temperatures beyond 4000 K with a maximum at 10000 K, while the Y^{2+} only exists at temperatures beyond 10000 K. In the temperature range of interest in laser deposition, around 8000 K, the major species are Y, Y^+, YO and YO^+, with minimum concentration Y^{2+}, consistent with the composition of plasma observed using emission spectra.[88] The thermodynamic properties of yttrium-oxygen system, including YO^+ up to 3000 K has been studied.[89, 90]

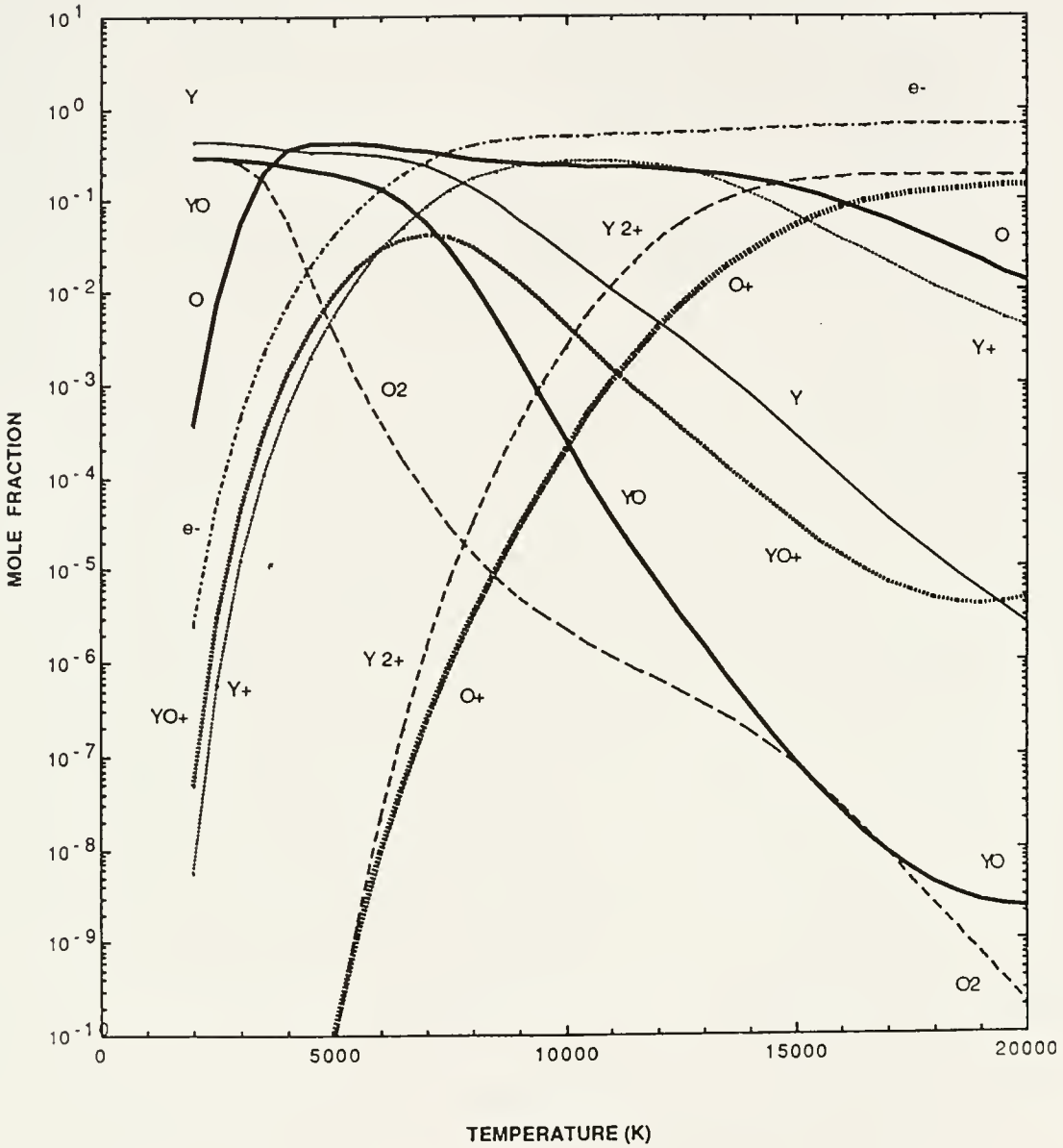

Figure 2-4 Yttrium-oxygen vapor phase chemical equilibria at 1 atm.

2.2.6 Barium-Oxygen System

The equilibrium composition of a barium-oxygen system with excess oxygen is presented in Figure 2-5. The composition of the oxygen species, O_2, O, and O^+, is identical to the one in Figure 2-3. The BaO species dominates the vapor phase until 6000 K because, compared to the other species, it has the lowest heat of formation. It had been experimentally shown that the concentration of higher gaseous barium oxides, Ba_2O, Ba_2O_2, Ba_2O_3 and Ba_2O_4 were negligible in comparison to BaO,[91] therefore they were ignored in this calculation. The concentration of Ba vapor increases with increasing temperature beyond its boiling point temperature (2000 K) until it reaches a maximum at 5000 K. At temperatures beyond 4000 K, an increasing number of the Ba atoms are converted to Ba^+ ion. The Ba^{2+} ion concentration increases at 7000 K until it saturates the plasma at 10000 K. The Ba^+ ion, in comparison, reaches a maximum at 7000 K and starts to decrease at 10000 K. At the temperature of interest in laser evaporation, around 8000 K, Ba^+ is at its maximum, while the Ba^{2+} is reaching a saturation point. Both the BaO and BaO^+ are rapidly disappearing at the same point.

2.2.7 Copper-Oxygen System

The equilibrium composition of a copper-oxygen system with excess oxygen is presented at Figure 2-6. The composition of the oxygen species, O_2, O, and O^+, was identical to the one in Figure 2-3. Beyond the boiling point temperature of 2800 K, the composition of Cu and Cu_2 vapor decreases with increasing temperature, whereas the concentration of Cu^+ increases. The entropy value for Cu^+ reported in JANAF table [65] was significantly larger than others, therefore it was not used. Because only enthalpy value was available, [76] the entropy and heat capacity for Cu^{2+} were assumed to be the same as those of Cu^+. The concentration of Cu^-, although very low, reaches a maximum at 5500 K. The Cu^{2+} ion concentration becomes significant at temperatures beyond 15000 K.

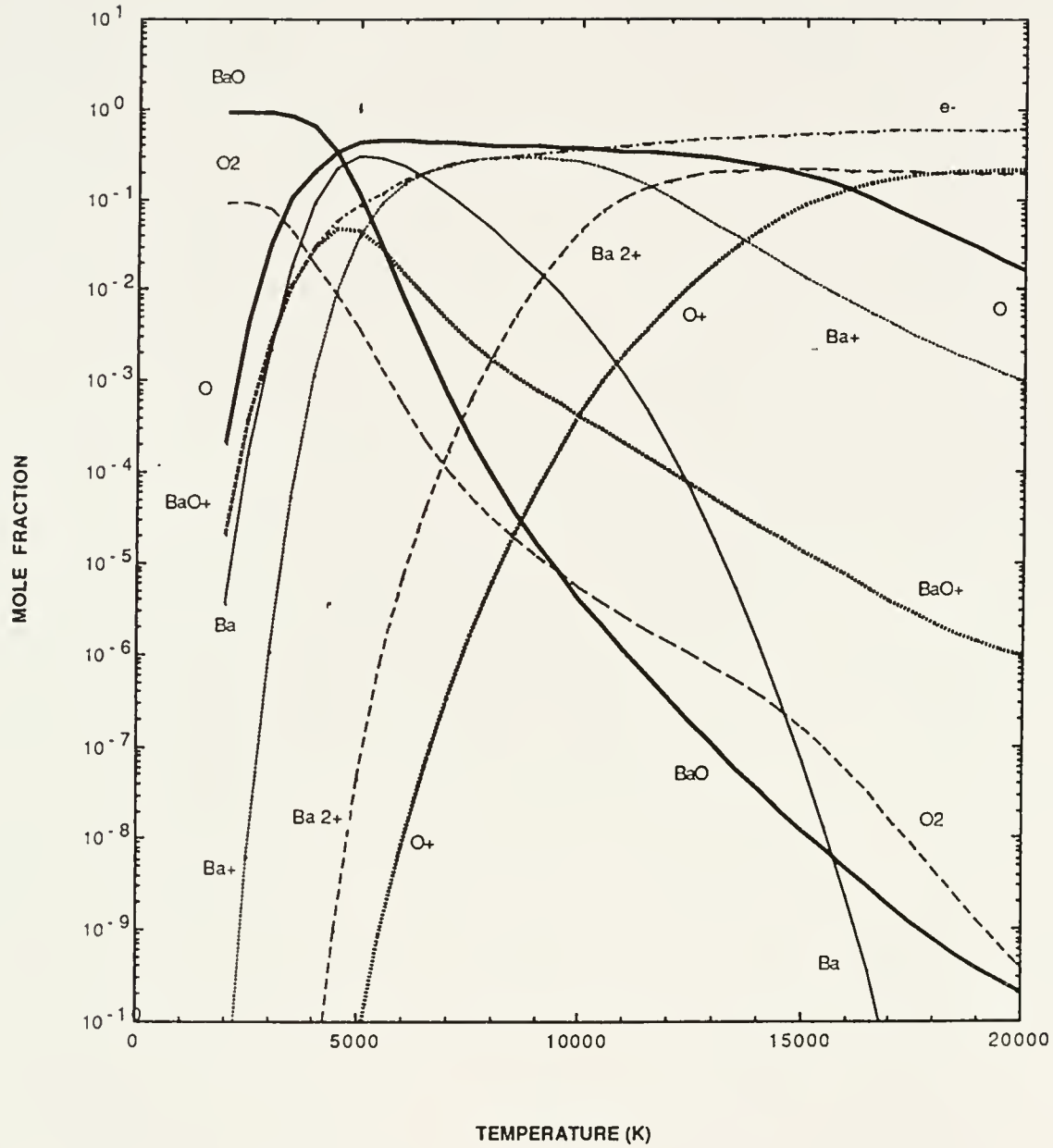

Figure 2-5 Barium-oxygen vapor phase chemical equilibria at 1 atm.

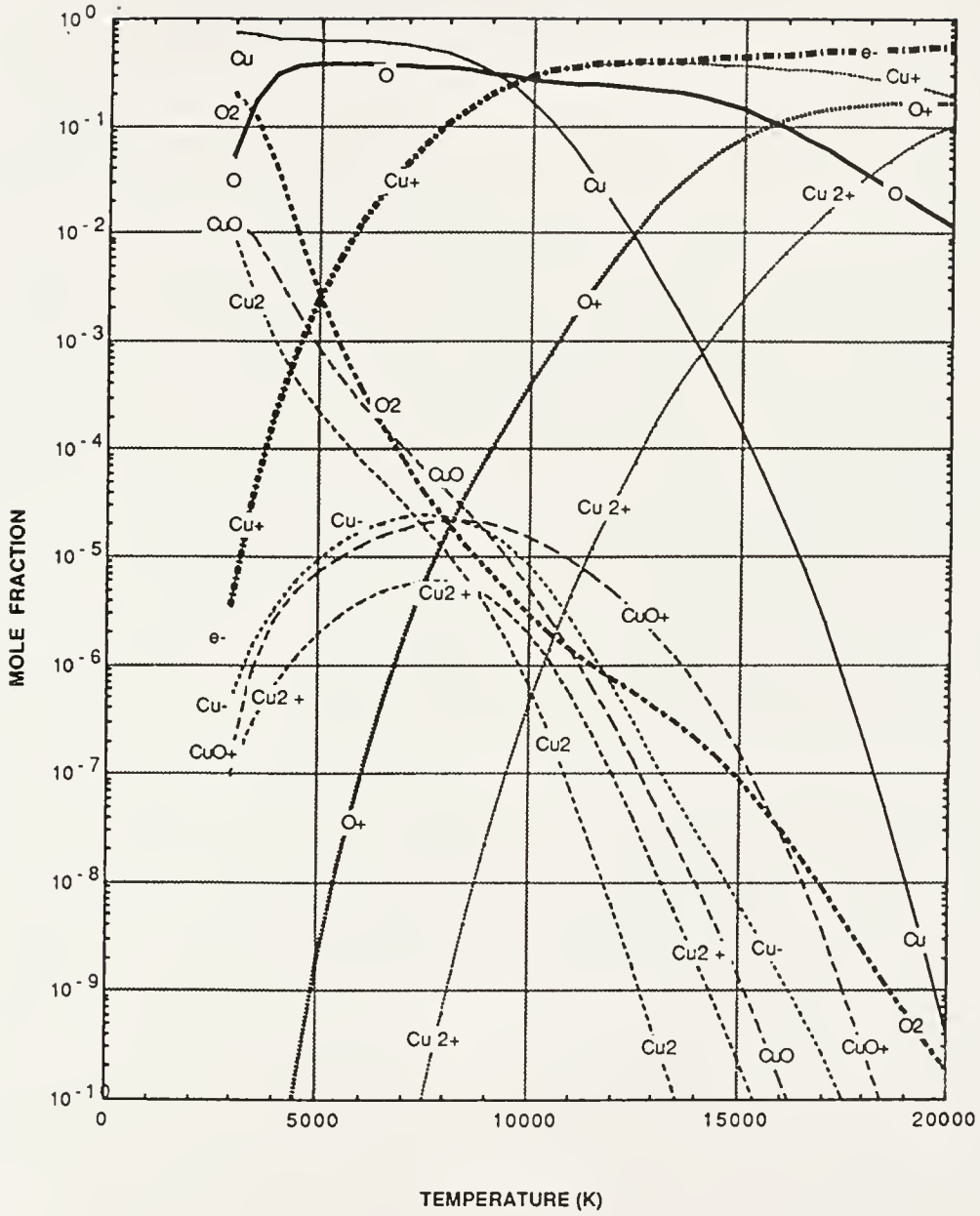

Figure 2-6 Copper-oxygen vapor phase chemical equilbria at 1 atm.

Because of their high heat of formation values, both CuO and CuO^+ only occur in small concentration and disappear at temperatures beyond 5000 K, consistent with experimental result.[92] The ionization potential for CuO was estimated to be the same of that of Cu since none of the thermophysical property for the CuO^+ is not available. This estimate can be justified since the ionization potentials of all of the oxides shown in Table 2-1 or similarly, Equations 2-15 and 2-16, are comparable to those of the elements. This high ionization potential value is reflected in the mole fraction of CuO^+ is only in the ppm range at its maximum. In the temperature range of interest in laser evaporation, the Cu^+ ion dominates the vapor phase. The concentrations of CuO, CuO^+, Cu^-, Cu_2 and Cu_2^+ have decreased to below one ppm. The concentration of Cu^{2+} is increasing but it will not become significant until 15000 K.

2.3 Complex Reaction Equilibria at Elevated Temperature

The database used to simulate the YBCO system is presented at Table 2-1. The initial concentration of the chemical species adds up to the concentration of the stoichiometric YBCO. Some oxygen and inert gas were added to study the effects of the environments. The calculation for the YBCO system, in principle, is a composite of the calculations of the Y-O, Ba-O,and Cu-O systems presented above, since all the elements, with the exception of oxygen, do not interact. The difference, however, is that the oxygen concentration was kept at stoichiometric YBCO. For graphical clarity, only the significant species that exist at mole fractions greater than 10^{-3} will be presented.

2.3.1 Effect of Temperature

The effect of temperature on the composition of Y, Ba, Cu and O system was investigated. The process simulation was a solid YBCO superconductor, which transforms to the vapor phase by maintaining the material balance. The pressure of the system was maintained at 1 atm, whereas the temperatures were varied from 3000 to 20,000 K. The

result of the simulation for the species present at mole fractions higher than 10^{-3} is presented at Figure 2-7.

In general, all the oxide species, both neutral and charged, have disappeared within the first 6000 K. The CuO species, in particular, only exist up to 3000 K. Beyond 6000 K, an increasing number of charged elemental species dominate the vapor phase. Correspondingly, the electron concentration also increases. Only about one-tenth of all the species are charged at 5000 K, whereas at 16000 K, almost half of all the species are charged.

All the neutral elements transform to ionic species at temperatures beyond 6000 K. For the Y element, the transformation from Y to Y^+ and from Y^+ to Y^{2+} take place at 8000 and 13000 K, respectively. For the Ba element, the transformation of Ba to Ba^+ and Ba^+ to Ba^{2+} takes place at 6500 and 11500 K, respectively. And lastly, for the Cu element, the transformation of Cu to Cu^+ and Cu^+ to Cu^{2+} takes place at 9500 and a temperature higher than 20,000 K, respectively. The concentration of the ionic species increases and reaches a saturation value at high temperatures.

For the deposition of thin film, it is desirable to have the temperature below 6000 K,where the concentration of oxides is still abundant. It can be concluded that in most deposition processes, where only ionic species are found, the temperature of the plasma is greater than 7500 K.

2.3.2 Effect of Pressure

The pressure dependence of the copper boiling points was studied from the range of 1 Torr to 10 atm to test the accuracy of the program and the database (Table 2-4 [69]). The result was found to be consistent with the literature, even under very low and very high pressures. The deviation at the very high pressure is caused by the system nonideality.

The effect of system pressure on the equilibrium composition of a YBCO system was investigated. The results for the pressure of 0.2, 0.5, 1, 10 and 50 atm are presented

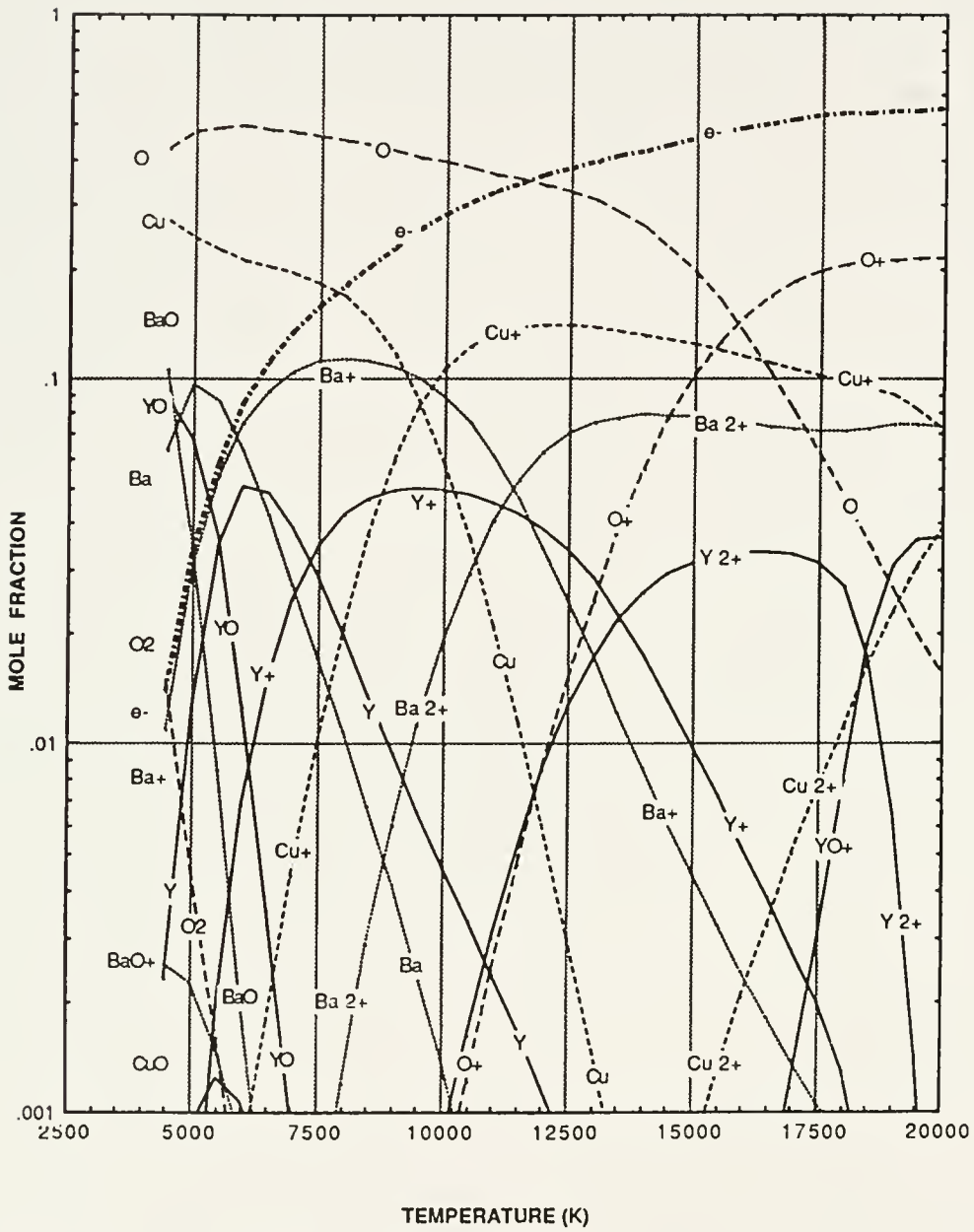

Figure 2-7 YBCO vapor phase equilibria at temperatures from 2500 to 20000 ^{o}K and presure 1 atm.

Table 2-4 Pressure dependence on the boiling point temperature of the copper element

Pressure (torr)	Tb Experimental (°K)	Tb Calculated (°K)
1	--	1685
10	2143	2130
100	2463	2448
400	2713	2712
760	2873	2837
7600	3773	3450

at Figures 2-8 to 2-12. Note that at pressure greater than 10 atm, the computational accuracy decreases as the system becomes less ideal. As predicted from the Le Chatelier principle, as the pressure decreases, the concentration of the large molecule increases, while the concentration of atoms decreases.

The mole fraction of electron, indicative of the total charges, decreases as the pressure increases because the formation of neutral atom is preferred. The electron mole fractions for a plasma at 8000 K with pressures up to 50 atm are presented in Figure 2-13. The corresponding electron density, calculated using ideal gas law, varies from 10^{16} to 10^{18} cm^{-3} at temperatures between 5000 and 10000 K (Figure 2-14). The ion concentration reached a limiting value beyond 8000 K.

2.3.3 Effect of Oxygen Pressure

The effect of oxygen pressure on the equilibrium composition of a YBCO system was investigated. The addition of 100% excess oxygen increases the concentration of oxides and ions, and decreases the concentration of the elements. This result is presented in Table 2-5. Note that the underlined values indicate the reduction in concentration from the stoichiometric composition.

In the formation of the oxides, the reaction reverse of eq. 2-15, for which M and O are the reactant and MO is the product, the extent of reaction to form MO depends on the product of the equilibrium constant, K, and the initial concentration of both reactants; therefore, with the increase in the initial oxygen concentration, the formation of the oxide increases. Accordingly, the concentration of the oxide ions increases with the increase in oxide concentrations. As an illustration, at 8000 K, the presence of 100% excess oxygen increases the concentration of the ion oxides by an average of 50%. The increase of the neutral oxides, however, is only about 10 %, due to further conversions to ionic oxides.

In Equations 2-16 and 2-17, where the right-hand side of the equation is the products, cations, and electrons, the increase in the extent of reaction can be expressed in

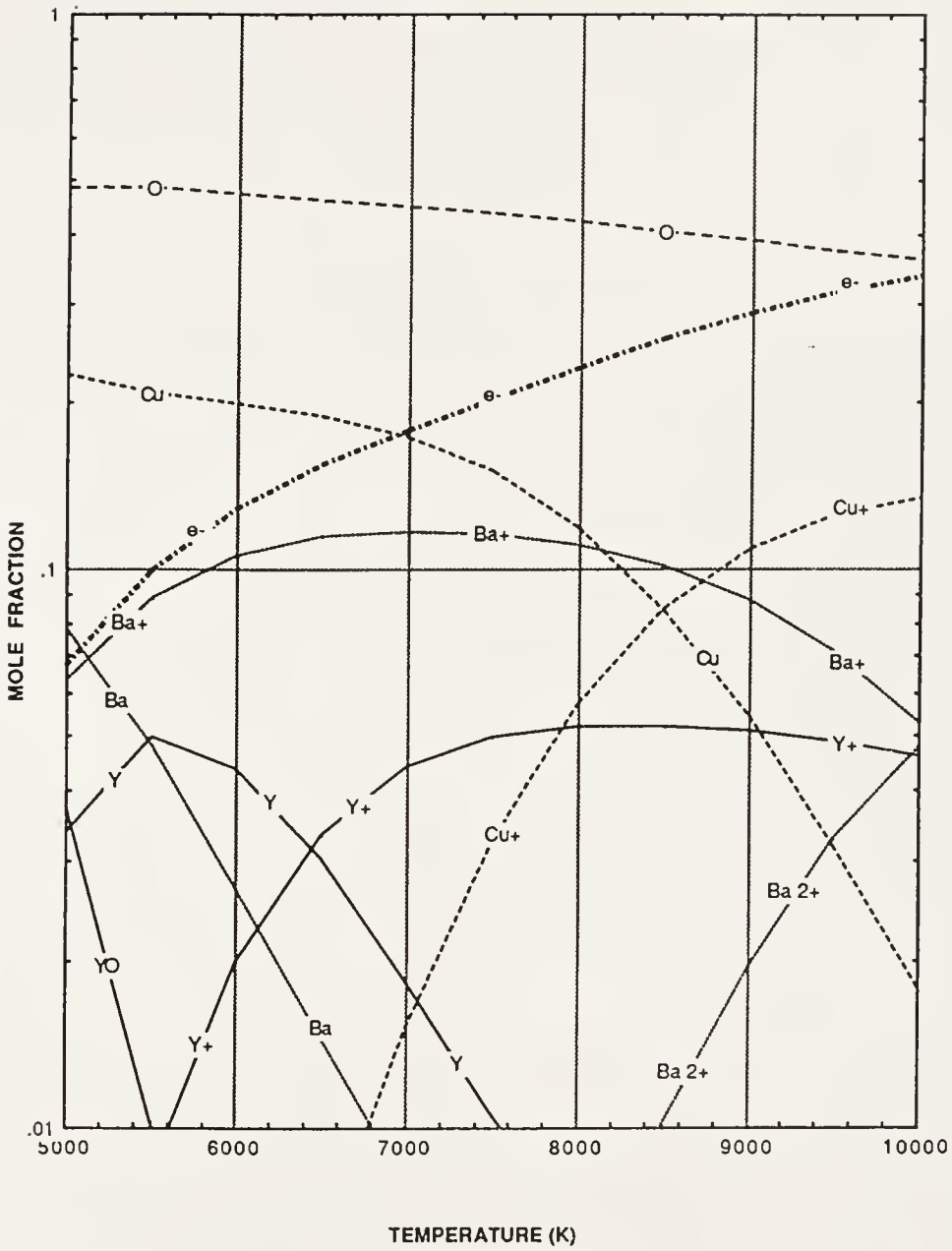

Figure 2-8 YBCO vapor phase equilibria at temperatures from 5000 to 10000 ^{o}K and pressure 0.2 atm.

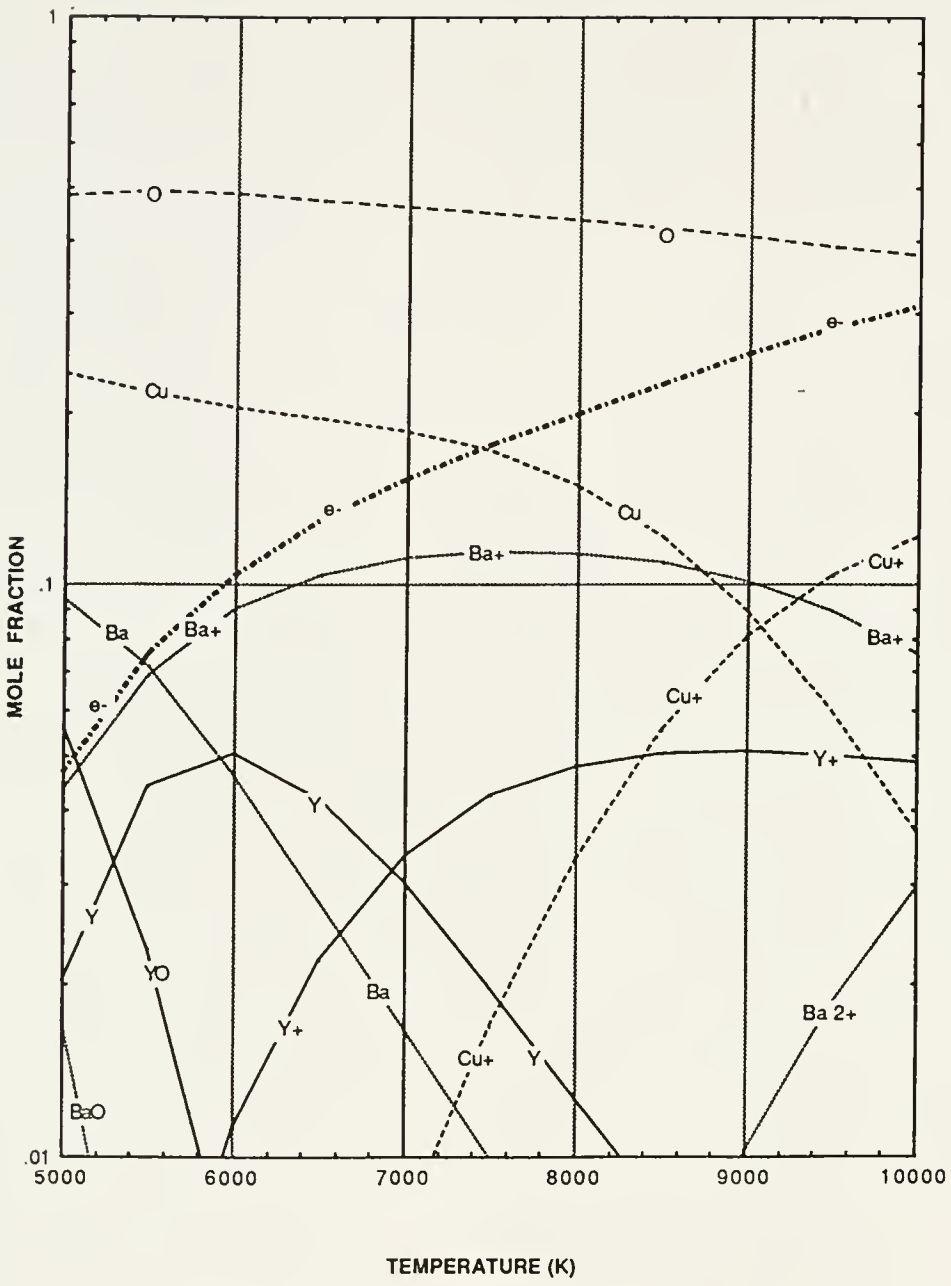

Figure 2-9 YBCO vapor phase equilibria at temperatures from 5000 to 10000 ^{o}K and pressure 0.5 atm

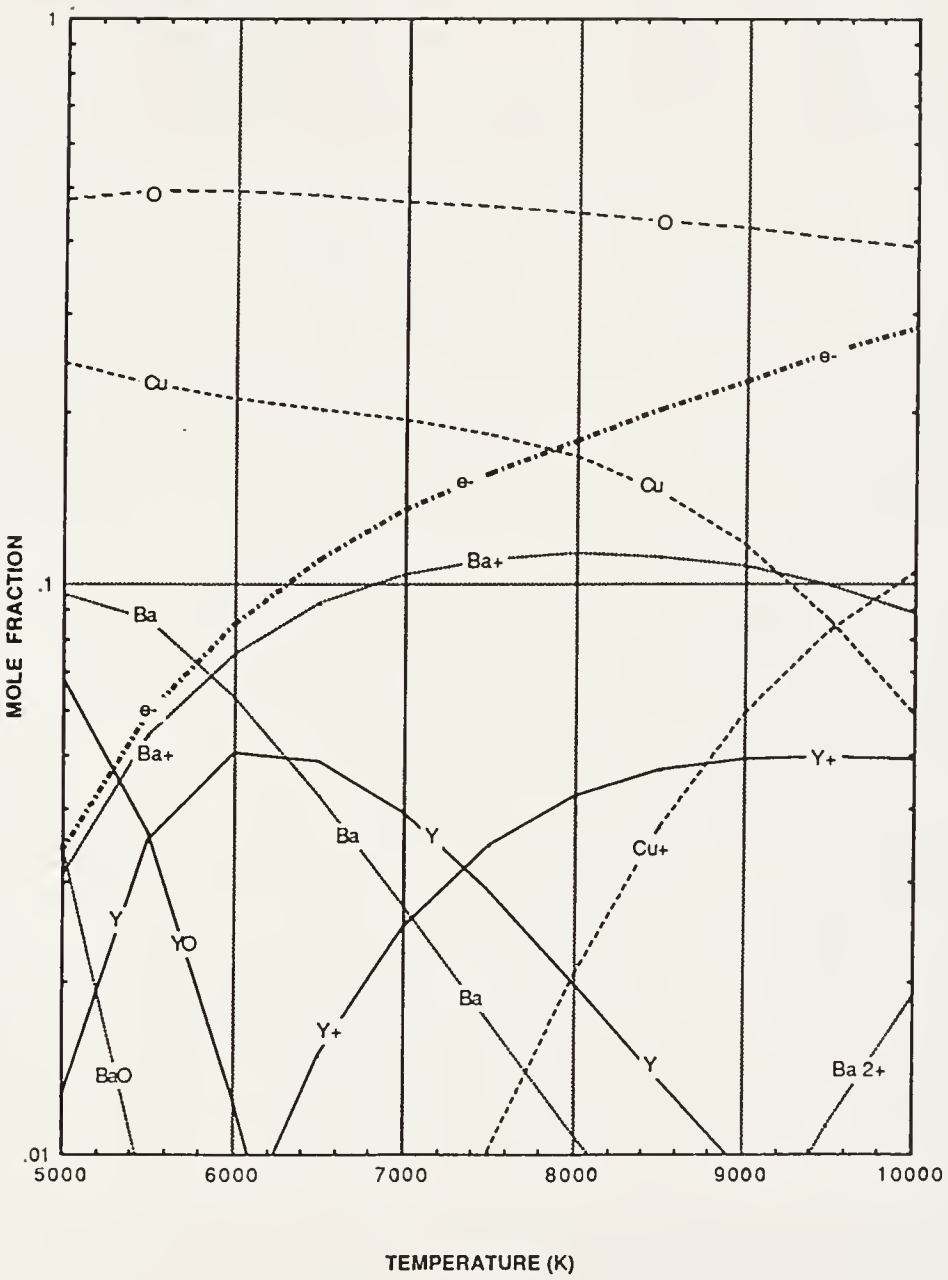

Figure 2-10 YBCO vapor phase equilibria at temperatures from 5000 to 10000 ^{o}K and pressure 1 atm

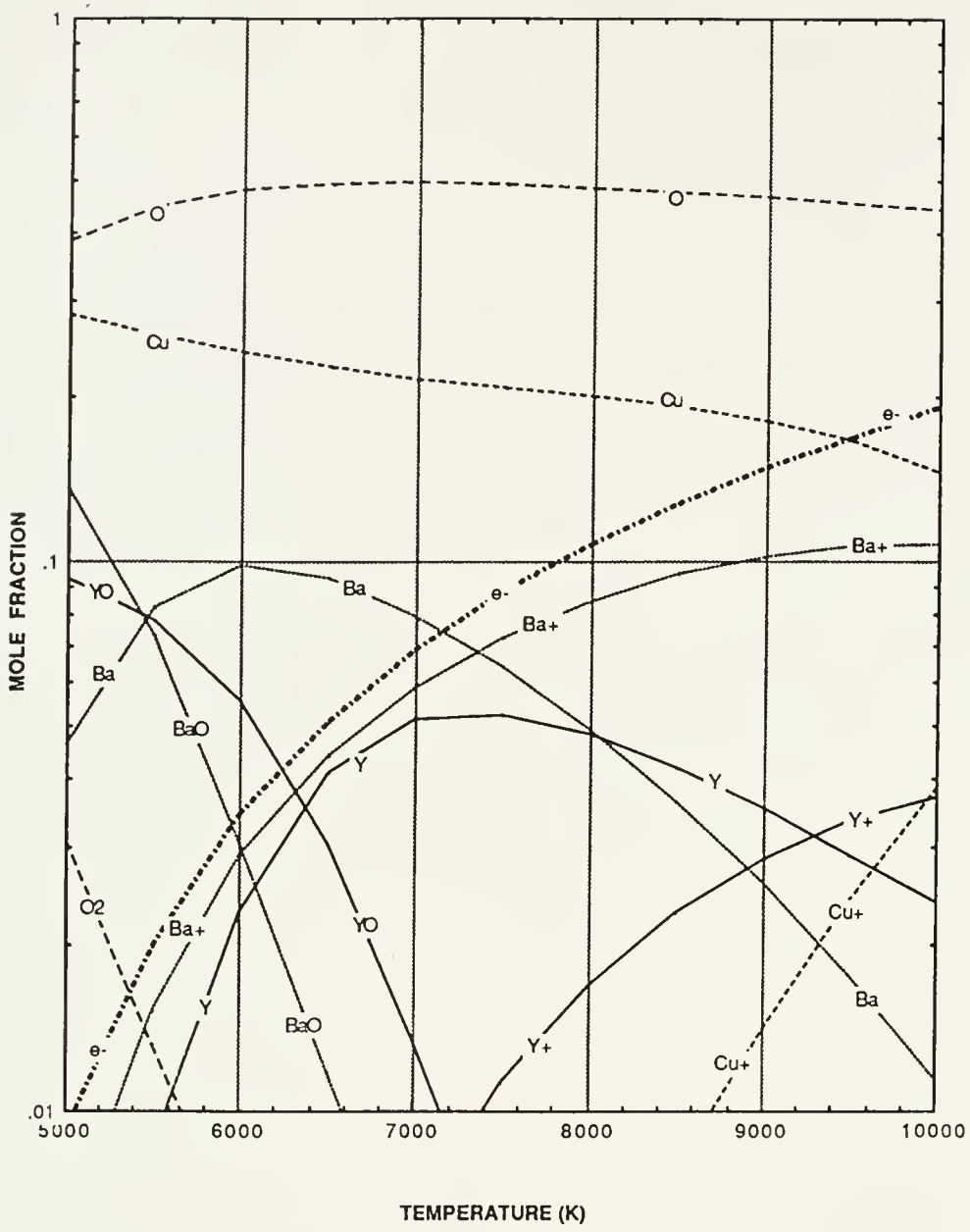

Figure 2-11 YBCO vapor phase equilibria at temperatures from 5000 to 10000 ^{o}K and pressure 10 atm.

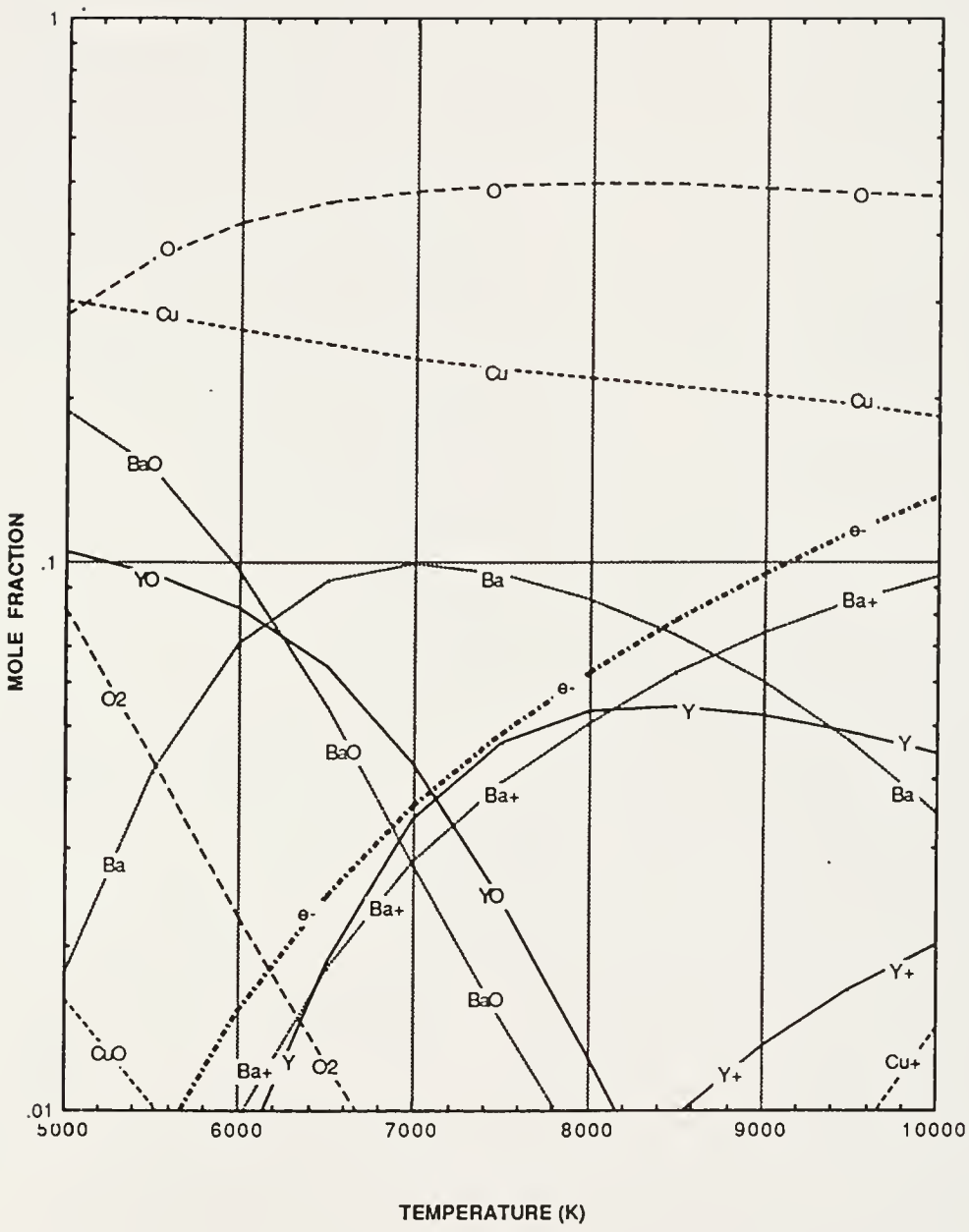

Figure 2-12 YBCO vapor phase equilibria at temperatures from 5000 to 10000 ^{o}K and pressure 50 atm.

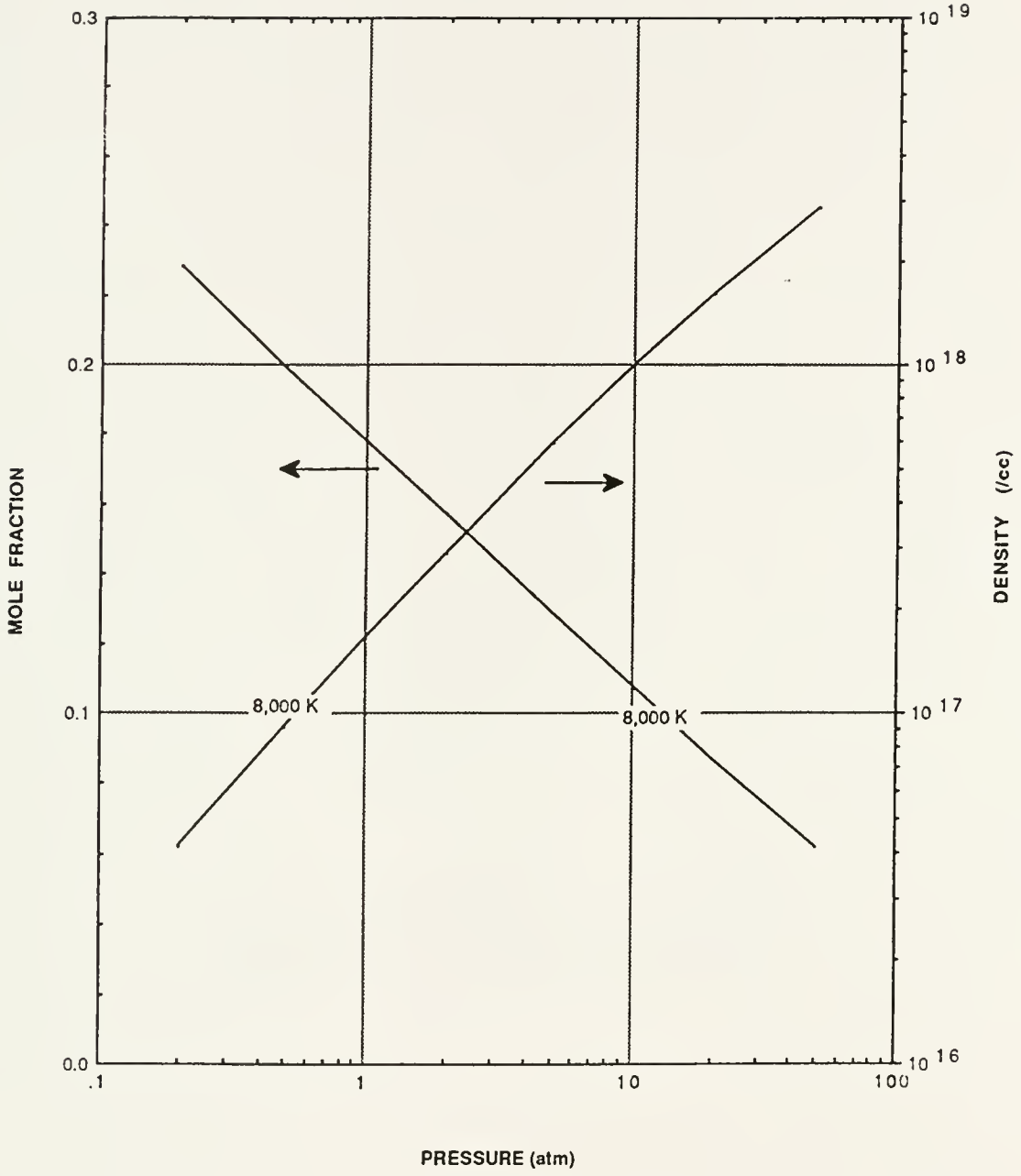

Figure 2-13 Mole fraction and number density of electron in YBCO plasma at a temperature of 8000 K and pressures up to 50 atm.

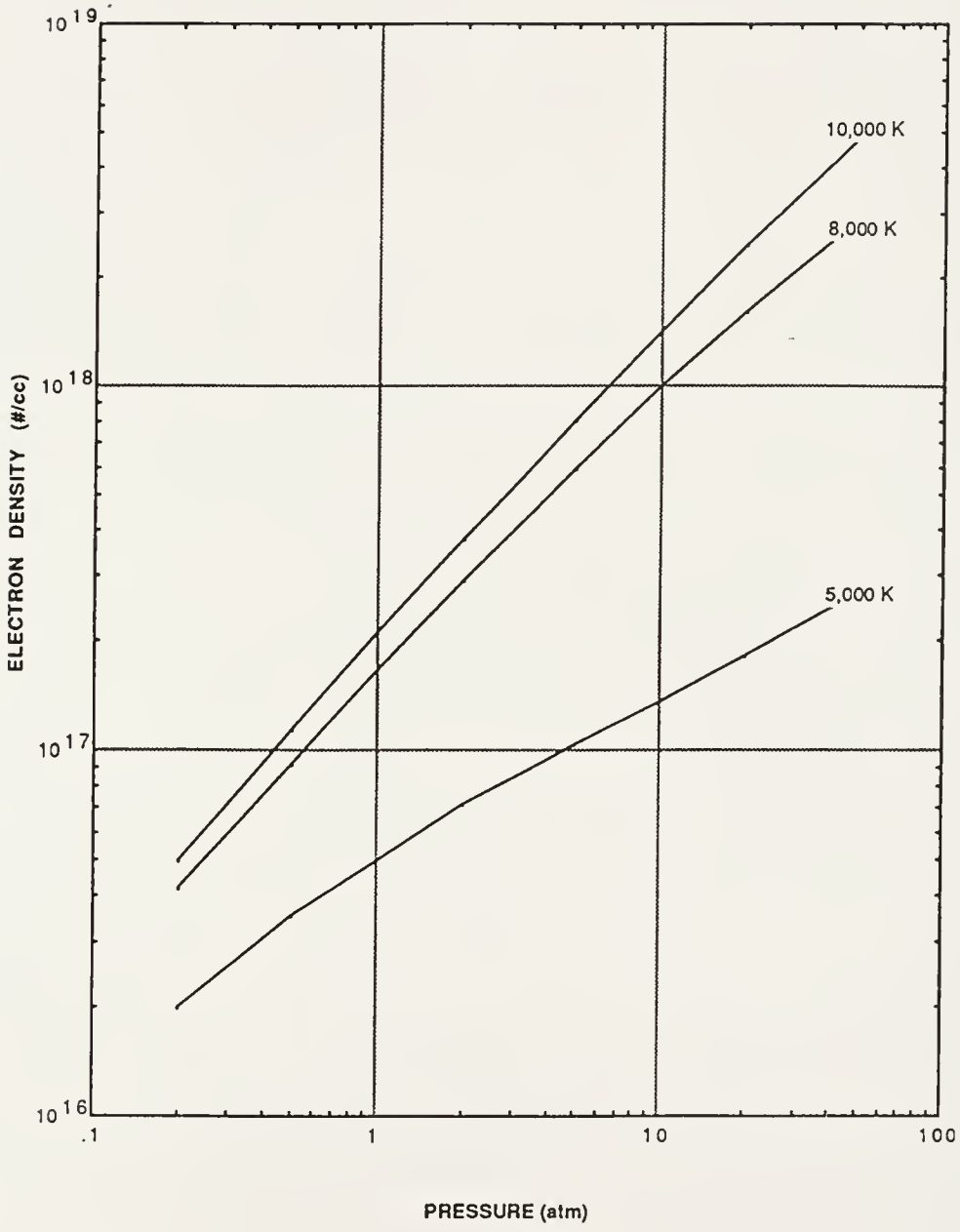

Figure 2-14 Electron density of YBCO plasma at temperatures of 5000, 8000 and 10000 K at pressures up to 50 atm.

Table 2-5 Equilibrium composition of YBCO vapor phase at 8000 K and 1 atm with various initial conditions

SPECIES	Initial Comp. (moles)	Stoichiometric (moles)	With excess O_2 (moles)	With inert gas (moles)
Y	0.10000E-01	0.15966E-01	0.12815E-01	0.11133E-01
Y^+	0.10000E-01	0.33834E-01	0.36913E-01	0.38741E-01
Y^{2+}	0.10000E-01	0.14800E-04	0.21948E-04	0.27829E-04
YO	0.10000E-01	0.68193E-04	0.74899E-04	0.25789E-04
YO^+	0.10000E-01	0.11680E-03	0.17438E-03	0.72538E-04
Ba	0.20000E-01	0.86638E-02	0.64981E-02	0.54290E-02
Ba^+	0.20000E-01	0.90273E-01	0.92033E-01	0.92894E-01
Ba^{2+}	0.20000E-01	0.96078E-03	0.13314E-02	0.16235E-02
BaO	0.20000E-01	0.14605E-04	0.14990E-04	0.49639E-05
BaO^+	0.20000E-01	0.87674E-04	0.12231E-03	0.48931E-04
Cu	0.30000E-01	0.13349E+00	0.12841E+00	0.12469E+00
Cu^+	0.30000E-01	0.16489E-01	0.21560E-01	0.25293E-01
Cu^{2+}	0.30000E-01	0.58327E-10	0.10366E-09	0.14697E-09
CuO	0.30000E-01	0.16374E-04	0.21553E-04	0.82955E-05
CuO^+	0.30000E-01	0.46778E-05	0.83695E-05	0.38917E-05
O	0.40000E-01[a]	0.35962E+00	0.71939E+00	0.35979E+00
O^+	0.40000E-01[a]	0.89915E-05	0.24449E-04	0.14772E-04
O_2	0.40000E-01[a]	0.31323E-04	0.85742E-04	0.16996E-04
O_2^+	0.40000E-01[a]	0.13561E-07	0.50459E-07	0.12084E-07
e^-	0.32000E+00	0.14277E+00	0.15354E+00	0.16037E+00
inert	0.00000E+00[b]	0.00000E+00	0.00000E+00	0.66000E+00

Note : [a] With 100 % excess oxygen, this initial value is 1.0000E-00 moles
[b] With 50% inert gas by volume, this initial value is 6.6000E-01 moles
[c] Underlined values indicate decrease in concentration from normal

terms of diluent effect.[93] The addition of oxygen, which is considered an inert gas in Equations 2-16 and 2-17, increases the total volume of the system. Since the extent of reaction is expressed in terms of the product of the equilibrium constant and the total volume, additional oxygen favors the formation of the products. As an illustration, at 8000 K, the concentrations of M^+ and M^{2+} increase by approximately 10 and 40% respectively.

2.3.4 Effect of Inert Gas

The effect of inert gas on the equilibrium composition of a YBCO system was investigated. The equilibrium composition is also presented at Table 2-5. The underlined values indicate the reduction in composition compared to the stoichiometric composition. This result, which is similar to that for the system with excess oxygen, causes the increase in the ion concentrations by the dilution effect.[93] The addition of inert species increases the total volume of the system and increases the extent of reaction proportional to the square root of the total volume. In this process, the reactants are the neutral elements and oxides. The products, are all the ionic species. With the additional inert gas, which constitutes half of the total moles, the concentrations of the neutral oxides and ionic oxides at 8000 K decreased by about 40 and 20%, respectively, whereas for the charged elements, both the M^+ and M^{2+}, the concentrations increased by 20 and 40%, respectively.

2.3.5 Analysis of PLD Plasma

The equilibrium condition for oxides, elements and ions in stoichiometric YBCO are presented in Figures 2-15. In general, at high pressure and low temperature, the formation of oxides is preferred, except for copper-oxygen where only a small concentration of CuO was formed at pressures greater than 100 atm. At high temperature and low pressure, the formation of ions is preferred. Because of the low ionization potential, Ba^{2+} can be observed at high temperature and low pressure, whereas other ions only exist as single charged species.

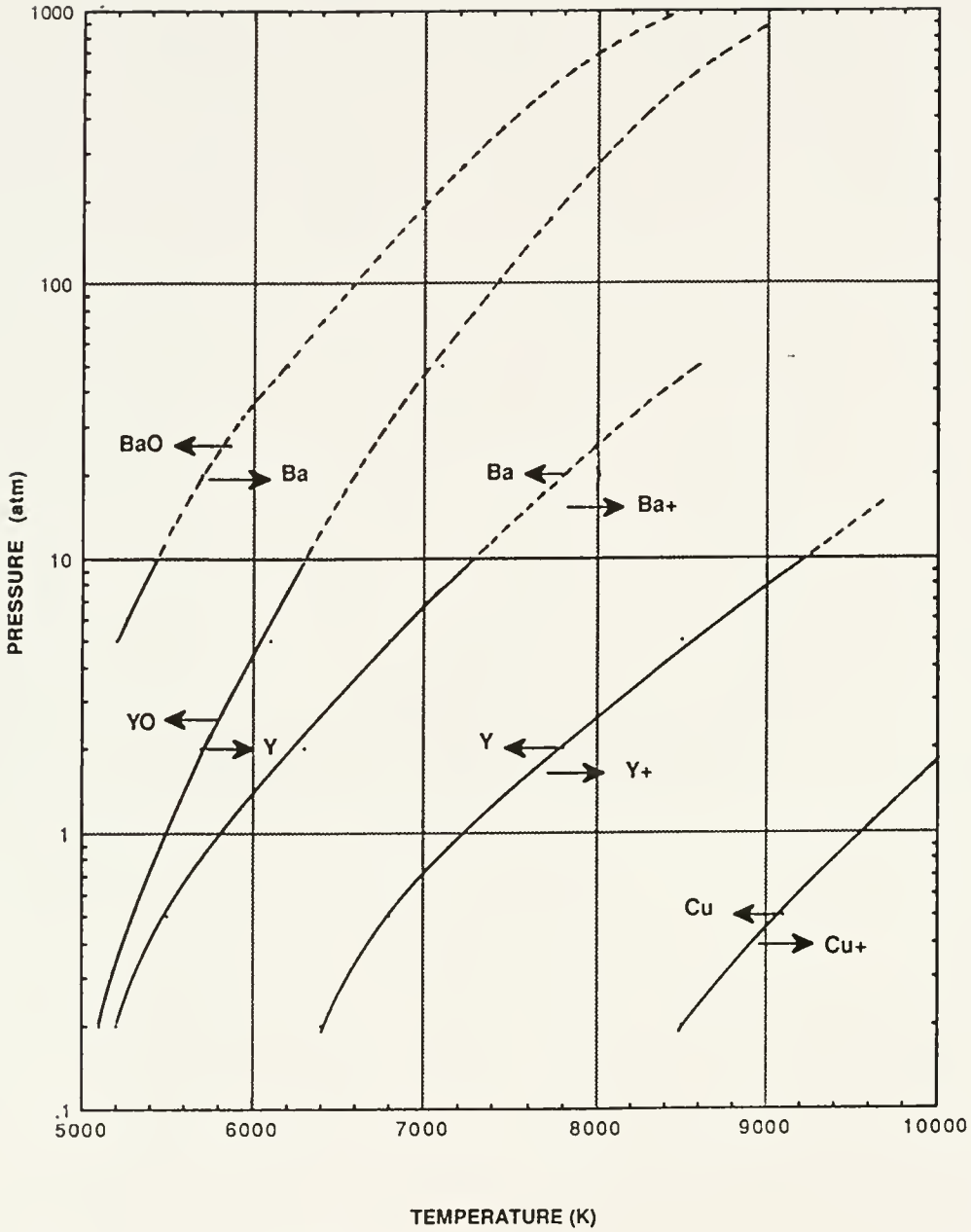

Figure 2-15 Composition of YBCO plasma at temperatures between 5000 and 10000 K and pressures up to 50 atm. Note the formation of oxides at low temperature and high pressure and the formation of ions at low pressure and high temperature.

In the adiabatic expansion of plasma, from high-temperature high-pressure to low-temperature low-pressure system, it is likely that initially the plasma consist of atomic charged species and some oxides. As the plasma expands, depending on the heat capacity ratio, both the temperature and the pressure drops with the temperature drops faster than the pressure, favoring the formation of oxides.

2.4 Conclusion

Chemical equilibrium analysis has been shown to be useful in predicting the composition of the gas phase during the irradiation of the YBCO target. The calculations can predict the composition of the vapor phase, consistent with the composition as predicted from the plasma diagnostic. The analysis shows that the formation of oxide species is limited to the first 6000 K. The absence of CuO species is caused by the relatively high heat of formation. Beyond 6000 K, the vapor phase is dominated by elements, both neutral and charged species. The change in pressure affects the equilibrium composition, consistent with the Le Chatelier principle, which increases the transition temperature with the increase in pressure. The addition of oxygen increases the formation of both the oxides and the charged species, while the addition of an inert gas only increases the production of the charged elements, and reduces both the neutral elements and the oxides. If during the laser deposition, high concentrations of oxides are desired in order to preserve the target film oxygen stoichiometry, it is desirable to perform the deposition at high oxygen pressure.

In the treatment of a high-temperature high-pressure plasma which expands adiabatically, it can be expected that initially, the plasma contains a high concentration of neutral atoms and oxides since the concentration of neutral atoms and oxides is favored at high pressure. As the plasma expands, both the temperature and pressure drops, favoring the formation of ions, until the temperature drops significantly that oxide and neutral species are again formed.

CHAPTER 3
SELECTED THERMOCHEMICAL AND THERMOPHYSICAL PROPERTIES STUDIES

3.1 Introduction

To describe the state of an initially solid superconductor during laser evaporation, its thermochemical and physical properties must be accurately known. Various characterization techniques have been used to determine the physical as well as the superconducting properties of YBCO. Most characterization, however, has been limited to the physical properties at cryogenic temperatures, typically near the superconducting transition temperature. In previous modelling work, the available data at cryogenic temperatures were extrapolated to establish the physical properties at the high temperatures required for the heat-transfer modeling of bulk superconductor and thin film preparation. To minimize the error associated with the extrapolation of physical properties from the cryogenic range to the melting temperature, a series of measurements at high temperature were performed to determine the heat capacity and thermal conductivity.

This work focuses on determining these physical properties of YBCO superconductor at temperatures close to the melting point. The measurements were performed using Differential Thermal Analysis (DTA), Thermal Gravimetric Analysis (TGA), Differential Scanning Calorimetry (DSC), and the Thermal Conductivity Laser Flash Method.

3.2 Sample preparation

Samples were prepared from a ceramic powder obtained from Rhone-Poulenc. The powder was grounded in a ball mill using 7 mm diameter zirconia beads in Freon until the particle size was about a micron. Since the rate of sintering is inversely proportional to the cube of the particle diameter, it is desired to have the smallest particle diameter possible. The powder was initially pressed in a 3/4 inch diameter die at 2500 psi to produce its initial form. The loose pellet was then isostatically pressed at 50,000 psi. This process decreased the pellet dimensions by about 10%. Next, the pellet was sintered in dry oxygen. A series of desicator, containing Ascarite (NaOH fine particle in silica) and anhydrous $MgClO_4$ were used to remove CO_2 and moisture from the flowing oxygen. The pellet was then placed in a gold lined ceramic crucible to prevent a reaction with the container materials. During the sintering process, the oven temperature was increased at a rate of 10 °C/min to 450 °C, where it was held for 1 hr to evaporate possible organic contaminants. The temperature was then increased to 960 °C and held there for 2 hours. After sintering, the sample temperature was lowered at a rate of 10 °C/min to room temperature.[94]

After the sintering, the pellet dimensions were further reduced by 15 %. The sintered pellet was black and had a density of 6.0 g/cm^3 or 96% of the theoretical density. Low-density targets, 65% of the theoretical density, were made using the same procedure, except that the powder was uniaxially pressed at 5000 psi instead of isostatically pressed at 50,000 psi. XRD analysis of this sample showed that the target was pure YBCO with the correct oxygen stoichiometry.

3.3 Differential Thermal Analysis

3.3.1 Introduction

Differential thermal analysis (DTA) measures the heat absorbed or released by a chemical system by measuring the temperature difference between the sample and a known inert standard as the temperatures of both are increased at a constant rate.[95] A minima in the differential thermogram, a plot of temperature difference versus temperature, indicates that the sample is colder than the reference sample as a consequence of an endothermic process; a maxima indicates an exothermic process. Using a known sample as a standard, the magnitude of the heat effect may also be determined from the peak area. It was intended to use this technique to determine the number of reactions or phase transformations that occur during the heating of a YBCO sample and the magnitude of the heat of fusion.

3.3.2 Experimental

The DTA scan for the YBCO sample was performed using a DuPont 9900 General V2.2 differential thermal analyzer. The temperature scan was from 25 to 1200 °C at the rate of 20 °C/min. During measurement, the alumina reference crucible was left empty, while the alumina sample crucible was filled with the sample of interest. The equipment was initially calibrated using a gold powder sample. The superconductor powder sample was obtained from a ground, sintered pellet. The weight of the samples used was approximately 40 mg. The temperature was monitored during the heating and cooling cycles.

The heat of fusion can be calculated from the area under the peak of the differential thermogram. The peak area, A, is a function of the sample mass, m, thermal conductivity, k, and the enthalpy of fusion, ΔH_f, by the following relationship[95]

$$A = -(G/k)\, m\, \Delta H \qquad (3\text{-}1)$$

where G is the geometric constant. The value of G was determined from measurements with the gold sample. The heat of fusion for gold is 15.3 cal/g at 1336 K.[69] The thermal conductivities of the Au and YBCO at 400 °C are 300[69] and 2.4 W/m.K, respectively.

3.3.3 Result and Discussion

Figure 3-1 shows a typical scan for YBCO powder in the temperature range of 25 to 1600 °C performed in air. A typical DTA scan available in the literature for YBCO sample was from 25 to 1250 °C.[96] In the low temperature range, the scan shows a broad and shallow minimum, possibly due to volatilization of residual water or organics. A broad maximum is also observed near 500 °C and is possibly related to oxygen uptake by the sample. Three sharper peaks are observed at 950, 1040 and 1260 °C. The high temperature region near these first two peaks is shown in greater detail in Figure 3-2 for both the powder and pellet samples. These thermal arrests are seen in both the pellet and powder samples indicating that the pellet formation process is not responsible for the occurrence of these arrests. The heat effect in the pellet is somewhat larger due to the larger mass of the pellet, though the thermal conductivity is higher. For comparison, the scan for the gold sample is also shown in Figure 3-2.

SEM of the YBCO sample following the analysis showed that the sample had melted and resolidified (Figure 3-3). A glassy surface and solid that had not yet melted were observed. From the phase diagram it was expected that YBCO superconductor melt incongruently at 1277 K[84]; therefore, it was possible that only a small part of the solid underwent a phase transformation. The cooling curve showed an exothermic reaction at 1075 K.

Based on the calibration using the gold sample, the heat of fusion of YBCO was measured to be 0.24 cal/g or 160 cal/mole. Although the area under the curve for the YBCO sample is twice that of the gold (Figure 3-2), the thermal conductivity of the gold is

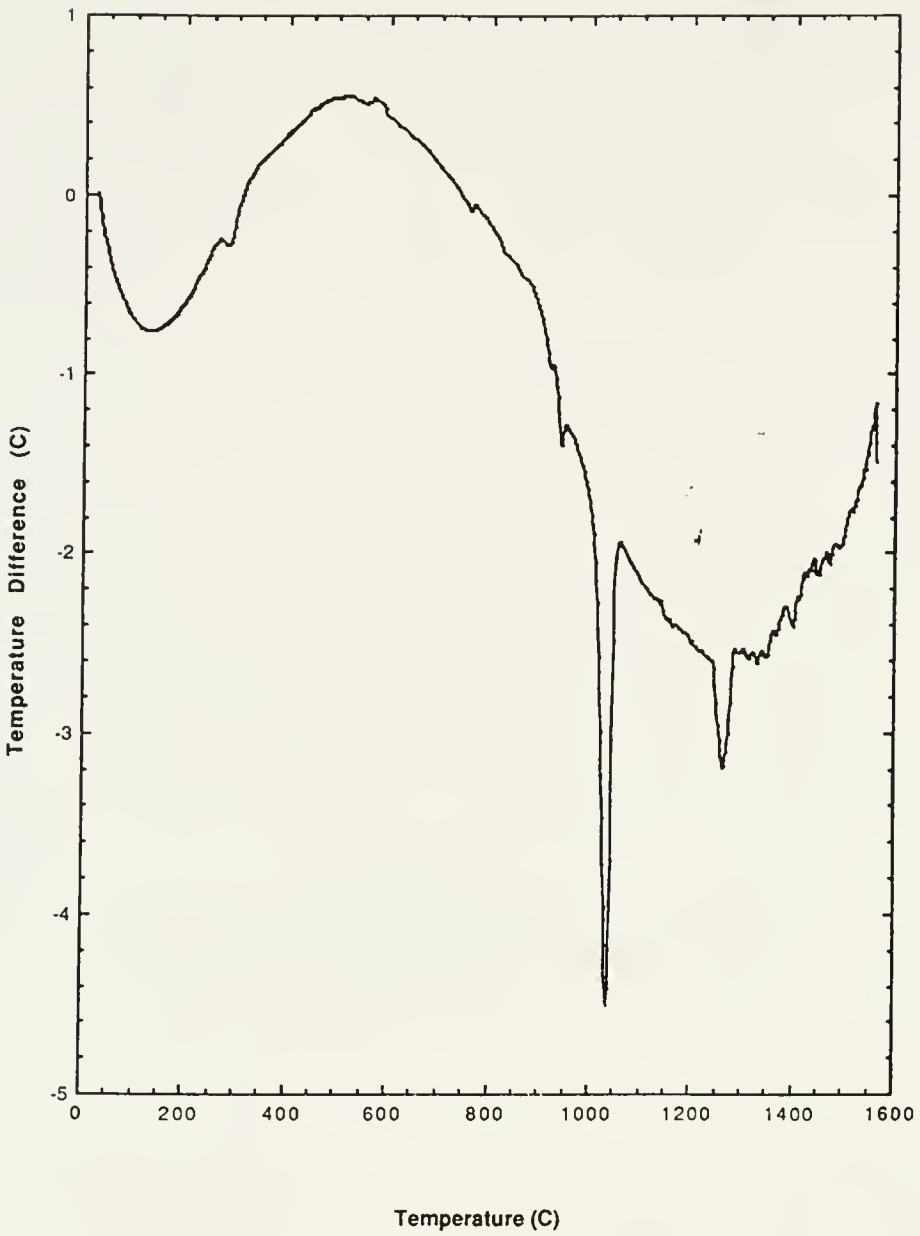

Figure 3-1 Differential Thermal Analysis of YBCO powder. Heating rate: 20 °C/min. Sample size: 39.2 mg. Temperature range: 30 to 1600 °C. Atmosphere: air.

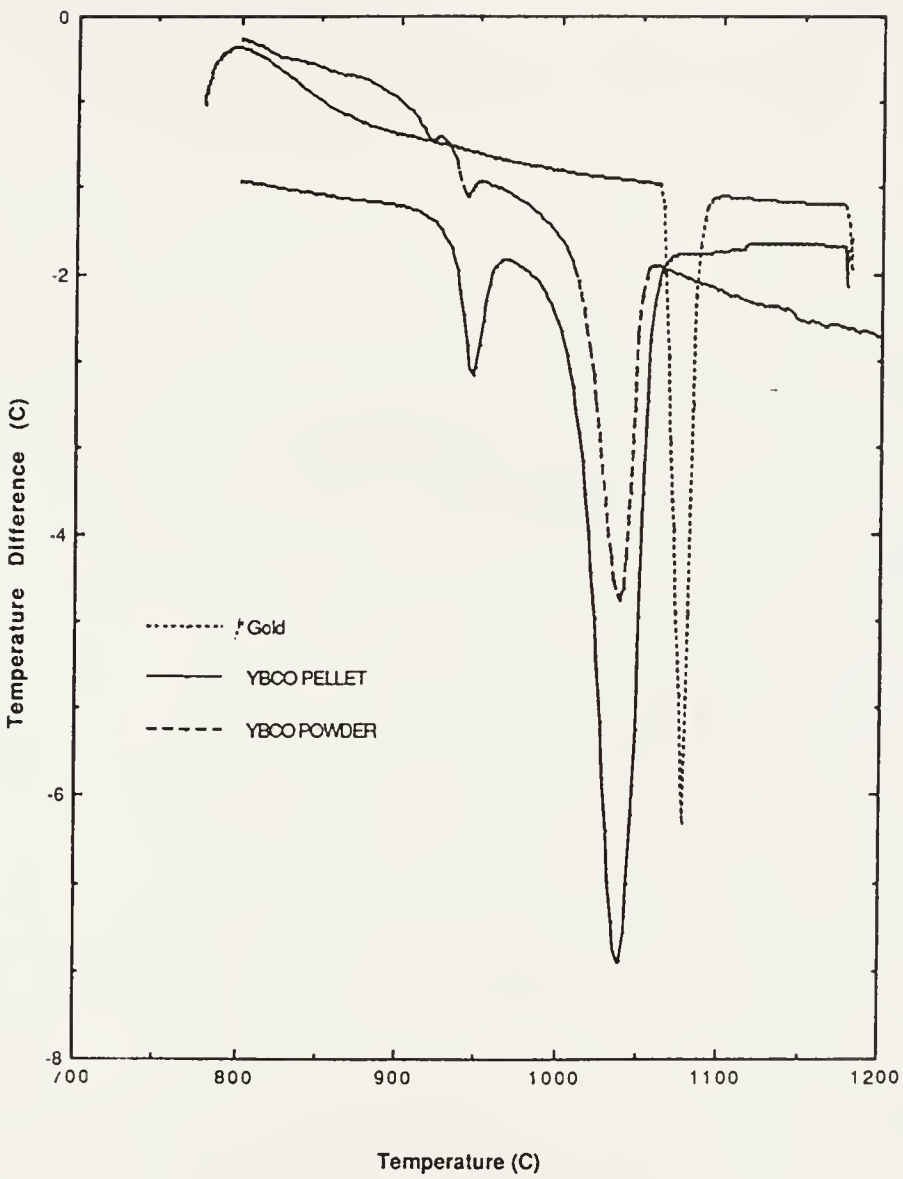

Figure 3-2 Differential Thermal Analysis YBCO pellet (wt. 99.9 mg), YBCO powder (wt. 39.2 mg) and gold powder (wt. 86.9 mg) at temperatures around the melting point. Heating rate: 20 °C/min. Atmosphere: air.

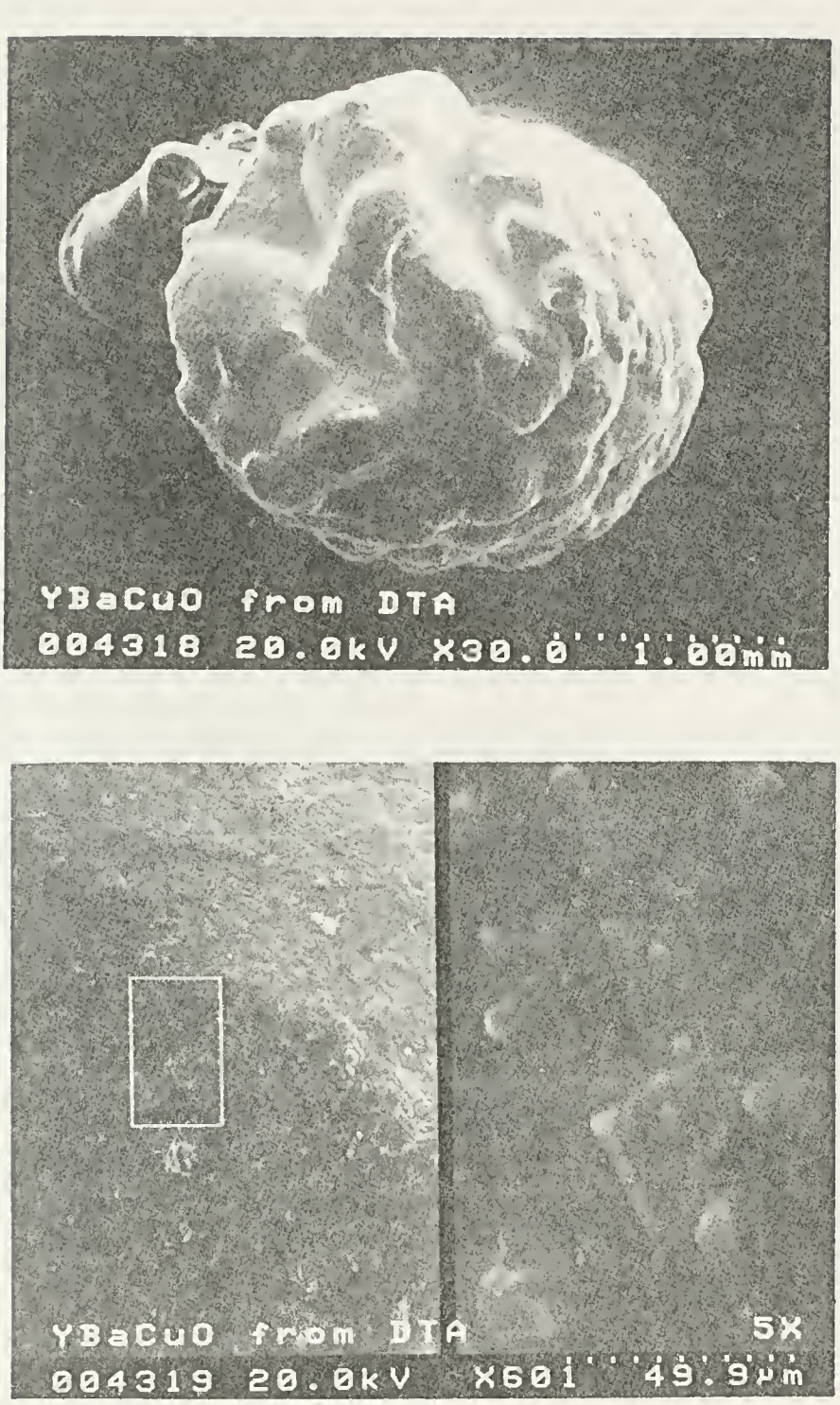

Figure 3-3 Resolidified sample of YBCO powder after undergoing DTA analysis to 1100 °C. Magnification (a) 30x; (b) 600x.

two orders of magnitude higher. As a result, the calculated heat of fusion of the YBCO is very small. The measured heat of fusion for the YBCO sample is much smaller then the expected value. Assuming that YBCO solid consists of stoichiometric mixture of Y_2O_3, BaO, and CuO, the heat of fusion is calculated to be 73 cal/g or 49 kcal/mole. The literature value of heat of fusion at 1020 °C was reported to be 90.9 cal/g,[97] while the latent heat of evaporation at 2200 °C, in comparison, was 454 cal/g.[98]

3.4 Thermal Gravimetric Analysis

3.4.1 Introduction

Thermogravimetric analysis (TGA) measures the mass of a sample as a function of temperature in order to determine the weight loss associated with volitilization of initial material or reaction products or weight gain due to reaction with the ambient air that occurs at a particular temperature. In order to help interpret the unexpected DTA results, YBCO samples were scanned from room temperature to 1200 °C. To study the phase transitions in this temperature range, the gas species and the solid residue were analyzed. One method of analysis is TGA/MS, in which the volatile gas components are analyzed as the sample is heated. The problem with this technique is that the vapor pressure is low making detection difficult. Another method available is GC/IR, in which the volatile gases are analyzed using IR spectroscopy. This method is more sensitive than the mass spectroscopy method, but species identification is more difficult. The results of TGA/MS studies are described below.

3.4.2 Experimental

The TGA was performed using a DuPont 2100 TGA Unit V5.1A. A 75-mg YBCO Superamic Y123 sample was analyzed under a 50 ml/min flowing N_2 atmosphere, at a heating rate of 10 °C/min. The maximum operation temperature of this system is 1200 °C.

Using a TGA/MS setup, the composition of the gas released was investigated to 400 °C, the operating limit of the system.

3.4.3 Result and Discussion

As shown in Figure 3-4, four weight losses were detected at 270, 780, 960 and 1150 °C during the scan to 1200 °C. The first three of these peaks were also observed in the DTA scan, suggesting volatization of an impurity. The total weight loss accompanying these transitions was 7%. During this run, the sample continuously lost weight at the rate of 0.005 %/°C. This continuous weight loss could be attributed to the loss of oxygen, which took about 2.5% weight loss per mole of oxygen. To understand the reactions that took place during the phase transition, the sample was analyzed using TGA/MS. The result showed that the onset of mass release started at 120 °C and continued on to 400 °C, with a maximum at 270 °C. This result is consistent with the weight loss transition on the TGA and exothermic peak observed during DTA (Figure 3-1). The chemical species detected had a molecular weight around 500; the observed fragments indicate it could have been a hydrocarbon from the binder in the powder. Unfortunately, the MS results could not be obtained above 400 °C.

3.5 Differential Scanning Calorimetry

3.5.1 Introduction

Differential scanning calorimetry (DSC) measures the difference in energy added to or removed from a sample, relative to a reference material, in order to maintain an identical temperature in both samples. The amount of heat added or removed depends on the enthalpy changes associated with exothermic or endothermic chemical processes. In the absence of chemical reactions and phase transformations, heat capacity can be obtained for the sample as a function of temperature.

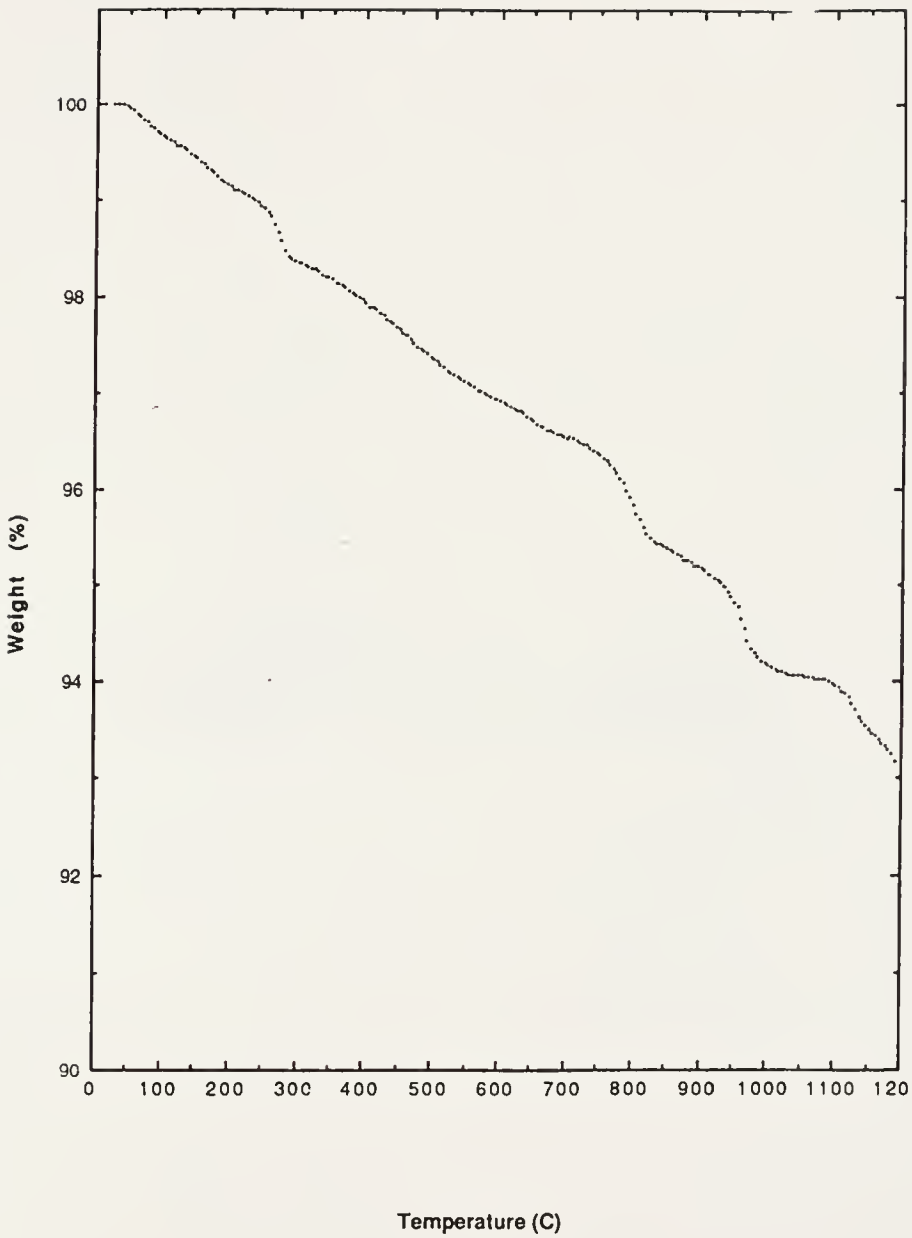

Figure 3-4 Thermal Gravimetric Analysis of YBCO powder. Heating rate: 10 ^{o}C/min. Sample size: 44.9 mg. Atmosphere: N_2.

3.5.2 Experimental

The DSC was performed using a DuPont 2100 General V4.1C unit. A 13-mg YBCO Superamic Y123 sample was analyzed under 30 ml/min flowing N_2 atmosphere at the rate of 20 °C/min. Sapphire was used as the standard for this measurement. Although this technique is more accurate than TGA, it unfortunately can only be scanned up to 400 °C, considerably below the melting point of YBCO material.

3.5.3 Result and Discussion

The DSC measurement measured heat capacity is shown in Figure 3-5. The literature value is 0.425 J/g K.[99] An exothermic reaction took place at 300 °C, possibly due to the evaporation of polymer binder, consistent with the DTA/MS analysis. It appeared that beyond 100 °C, the heat capacity decreased linearly with temperature.

3.6 Laser Flash Thermal Diffusivity Measurement

3.6.1 Introduction

Thermal conductivity of the YBCO has been determined using several methods, including theoretical calculation from the photon and electron scattering [100] and experimentally by the four-probe technique.[101] The thermal conductivity in this study was measured using the laser flash thermal diffusivity technique.[102, 103] This technique involves uniform pulse heating of the sample front surface using a long-wavelength laser and monitoring the evolution of the sample back surface temperature with an optical pyrometer. By fitting the temperature rise to a simple one-dimensional heat transfer model, the thermal diffusivity, α, can be calculated. This method is accurate, rapid, and non-destructive.

The equation used in the determination of α is derived from the equation for temperature distribution in solid sheet of finite thickness,[104] which is given by

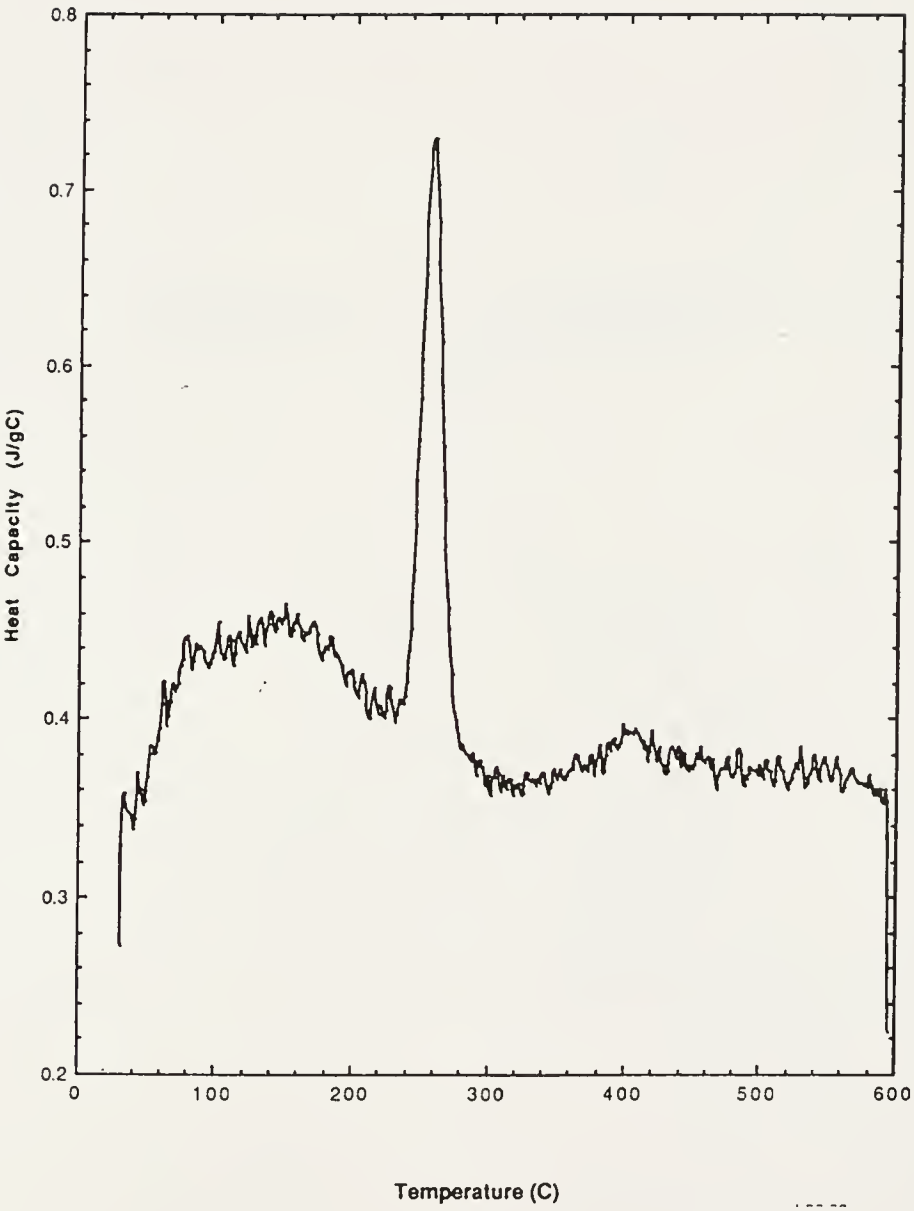

Figure 3-5 Differential Scanning Calorimetry YBCO. Heating rate: 10 °C/min. Temperature range: 30 to 600 °C. Atmosphere: N_2. Peak at 270 °C is probably due to organic impurity.

$$\frac{T(t) - T(0)}{T_m - T(0)} = 1 + 2 \sum_{n=1}^{\infty} (-1)^n \exp(-n^2 \pi^2 \alpha t / L^2) \qquad (3\text{-}2)$$

where t is the time after the laser pulse, T(t) is the time dependent back surface temperature, T(0) is the initial rear temperature, T_m is the maximum front surface temperature, and L is the sample thickness. At the time when the temperature T(t) is equal to half of T_m, the value of α can be simplified to a single value by [105]

$$\alpha = 0.1388 \, L^2 / t_{1/2} \qquad (3\text{-}3)$$

where $t_{1/2}$ is the time at which the temperature rise reached its half of the maximum value. The advantage of this method is that the value of $t_{1/2}$ is independent of the applied fluence at the surface as long as the temperature increase is not too significant.

Unlike a conventional laser flash thermal diffusivity measurement, which typically relied on the measurement of surface temperature using a thermocouple.[97], the method used in this experiment had several advantages. First, a short pulse length laser was used to heat the front surface, therefore producing an unambiguous rear surface temperature response. Second, an optical pyrometer was used instead of a thermocouple a the back surface. The wavelengths detected by the pyrometer were also different than the incident laser to improve the accuracy of the temperature measurement.

An initial attempt was made to determine the thermal conductivity using steady-state condition; however, the error was too great, and no useful information was obtained.

In order to obtain an accurate measurement, the following criteria must be met. First, the sample must strongly absorbed the incident laser. Second, the heat absorbed must be small to avoid non-linear effects. And finally, the laser pulse width must be small compared to the rear temperature rise time. In essence, the incident laser should produce a surface spike in temperature.

3.6.2 Experimental

The thermal conductivity measurements were made using thin superconductor pellets of 65 and 95% theoretical density with pellet sample thickness of 1.35 and 1.48 mm, respectively. The sample was radiated using a TEA CO_2 laser at a wavelength of 10.8 μm with a pulse width of 0.5 μs. The rear pellet temperature was monitored by imaging the rear surface of the pellet onto a HgCdTe detector which is sensitive to wavelength shorter than 14 μm. This detector unit has a response time less than 1 μsec (from 10 to 90% of rise time). To reduce signal interference from the incident laser, a filter was used to pass photons of only wavelength greater than 10.8 μm. A calibration was made using a 3.95 mm thick piece of iron provided by NIST with a known thermal conductivity value of 76.8 W/m K. For the measurement at high temperatures, the sample was placed in an oven. The temperature rise signal was digitized and the data was processed for non-linear least square fit. A typical repeatability value for the thermal diffusivity was within 1%. From the correlation of the temperature evolution into a one-dimensional heat transfer model, the thermal diffusivity and later the thermal conductivity were obtained. If the ERR_Q value, a value associated with the curve fitting, was greater than 0.40, the data was rejected.

3.6.3 Result and Discussion

The thermal diffusivity of superconductor pellets of two different densities (65% and 94%) was measured as a function of temperature in the temperature range 25 to 400 °C for the denser pellet and 25 to 200 °C for the less dense material. This method measures the temperature response of the back surface produced by a temperature pulse on the front surface. Solution of the one-dimensional equation of change for energy allows the thermal diffusivity to be easily determined from the measured values of pellet thickness and $t_{1/2}$ by Equation 3-3. A representation plot of normalized back temperature as a function of time is

shown in Figure 3-6. This data was fitted to a function derived from Equation 3-2 and values of $t_{1/2}$ were extracted. These values of $t_{1/2}$ and the calculated values of the thermal diffusivity for the sample of 95% and 65% theoretical densities are displayed in Table 3-1 and 3-2 at several measurement temperatures. The values of $t_{1/2}$ listed are the averages of multiple runs at each temperature. The thermal diffusivity of the low density pellet is a combination of both the solid diffusivity and the air between the solid. As the result, its value is lower than that of the high density pellet.

As shown in Figure 3-7, the thermal diffusivity decreased with increasing temperature. These data were fitted to a power law function with the result:

$$\alpha = 1.92 \times 10^{-2} T^{-0.175} \quad (3\text{-}4)$$

The room temperature value of α is 0.0103 cm^2/sec.

Given the value of heat capacity of 0.4 J/g·K obtained from Figure 3-5, density of 5.9 g/cm^3, and thermal diffusivity of 6.46×10^{-3} cm^2/sec, the thermal conductivity at 400 °C is calculated to be 1.5 W/m·K. The extrapolated thermal diffusivity at 1000 °C, in the vicinity of the melting temperature, is 0.0057 cm^2/sec, about half of the thermal diffusivity at room temperature. The literature values for thermal diffusivity and thermal conductivity at 77 K are 0.013 cm^2/sec and 1.55 W/m·K, respectively.[99] Using laser flash method, the thermal diffusivity was measured to be 0.0014 cm^2/sec at 400 °C.[97] The thermal diffusivity measured at 77 K is 0.012 cm^2/sec. The thermal conductivity of the YBCO was measured to be 2.5-3.1 W/m·K [106] and 4 W/m·K [107] at 300 K. The measured thermal conductivity of YBCO using the four-probe technique was 3 W/m·K at 100 K.[101]

3.7 Thermal Mechanical Analysis

3.7.1 Introduction

Thermal mechanical analysis measures the dimensional change of a sample as a function of temperature in order to determine the thermal expansion coefficient. This

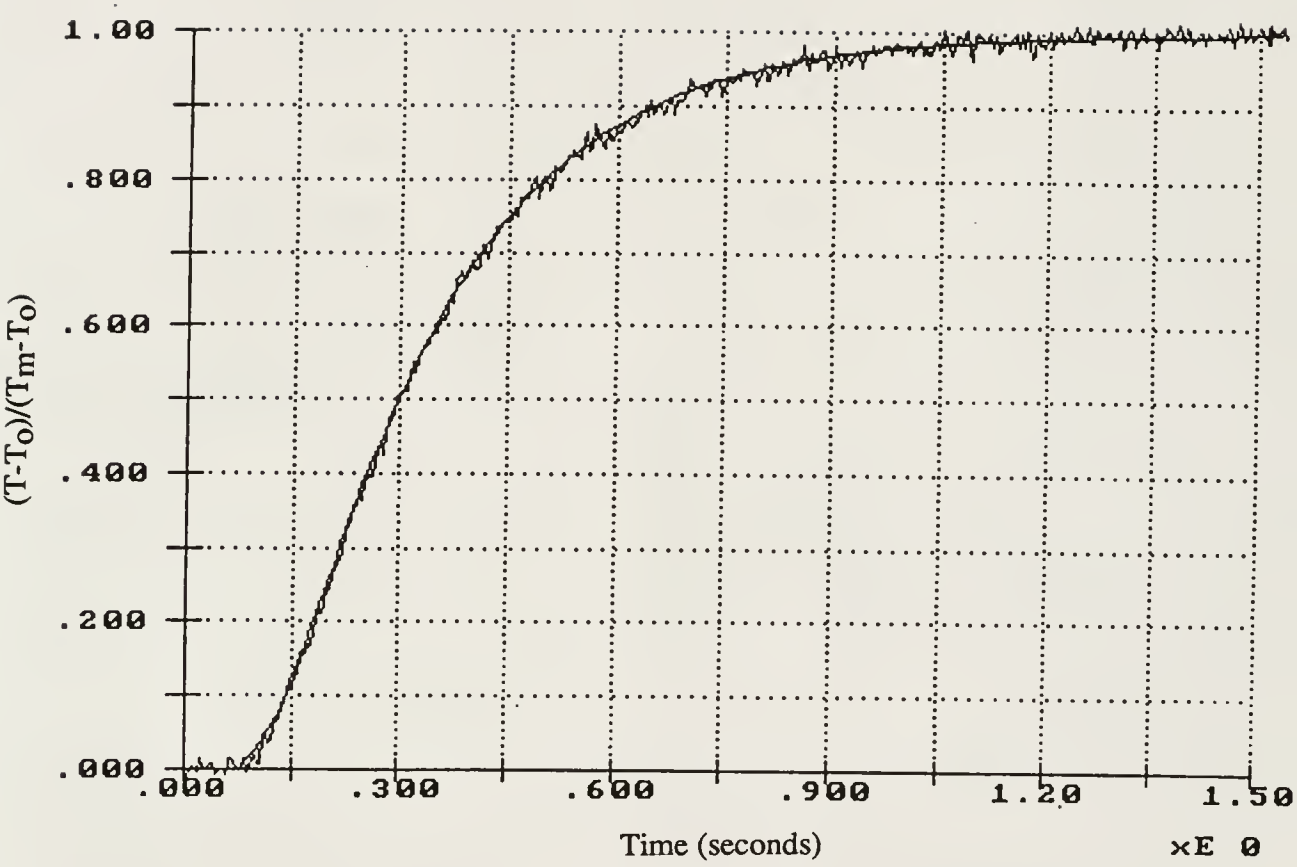

Figure 3-6 Temperature rise during laser flash technique used in determining thermal diffusivity.

Table 3-1 Temperature rise time and thermal diffusivity of high density pellets (94 % theoretical density) irradiated using a CO_2 laser. Temperature was measured at the rear surface.

TEMPERATURE (°C)	$TIME_{1/2}$ (msec)	THERMAL DIFFUSIVITY (cm^2/sec)
25	295	0.01031
50	284	0.01071
100	307	0.00900
150	351	0.00865
200	384	0.00791
250	413	0.00735
300	434	0.00700
350	456	0.00666
400	470	0.00646

Table 3-2 Temperature rise time and thermal diffusivity of low-density pellets (65% theoretical density) irradiated using a CO_2 laser. Temperature was measured at the rear surface.

TEMPERATURE (°C)	$TIME_{1/2}$ (msec)	THERMAL DIFFUSIVITY (cm^2/sec)
25	721	0.00351
50	765	0.00331
100	785	0.00320
150	816	0.00310
200	808	0.00313

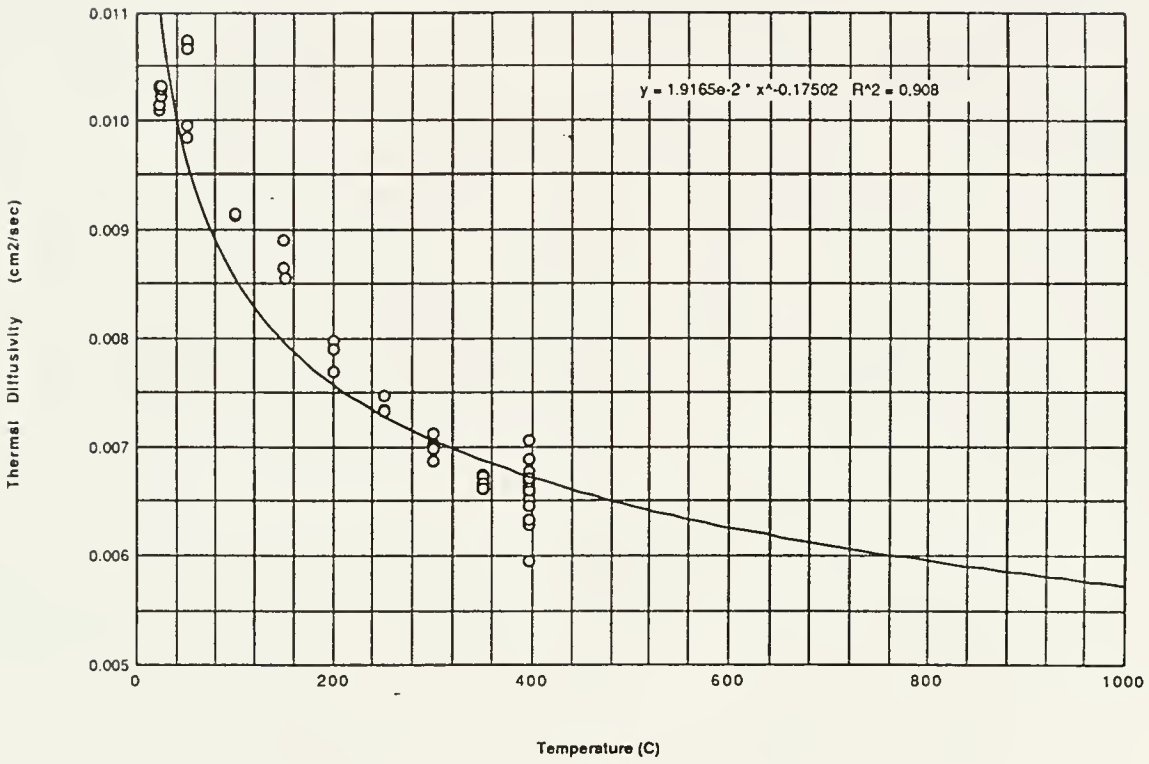

Figure 3-7 Thermal diffusivity YBCO as a function temperature, measured up to 400 °C.

information is needed in predicting the dimensional change as the YBCO solid is laser heated.

3.7.2 Experimental

The thermal mechanical analysis (TMA) was performed using a DuPont 2100 TMA Unit V5.1A. A YBCO high-density (95% theoretical density) pellet sample was heated from 25 to 1200 °C at the rate of 25 °C/min. The initial sample length was 10.93 mm, and the change of dimension reached a maximum of 250 μm at 900 °C.

3.7.3 Result and Discussion

Results from the TMA of a solid YBCO pellet are shown at Figure 3-8. During the heating cycle, the sample underwent phase transitions at 270, 400, and 550 °C, which is consistent with the results from DTA and TGA. The average measured thermal expansion coefficient was 28.5×10^{-6}/°C. For the cooling cycle, the thermal expansion coefficient was 13.8×10^{-6}/°C. The literature value at cryogenic temperature was 11×10^{-6}/°C.[99, 108] This range is typical for the thermal expansion coefficient for perovskites.[109]

3.8 Conclusion

Some thermal physical properties of a high-density YBCO superconducting ceramic were investigated. The thermal gravimetric analysis showed that a 7% weight loss accompanied the heating of this ceramic to 1200 °C. The continuous weight loss could be attributed to the loss of oxygen. The differential scanning calorimetry showed that an exothermic phase transition occurred at 270 °C, and the heat capacity of this ceramic is, on average, 0.4 J/g°C. The thermal conductivity values measured using a laser flash method were 1.5 W/m·K and 0.6 W/m·K for the high- and low-density pellets, respectively. The thermal expansion coefficient value during the heating and cooling cycles cycle were measured to be 28.5×10^{-6}/°C and 13.8×10^{-6}/°C respectively.

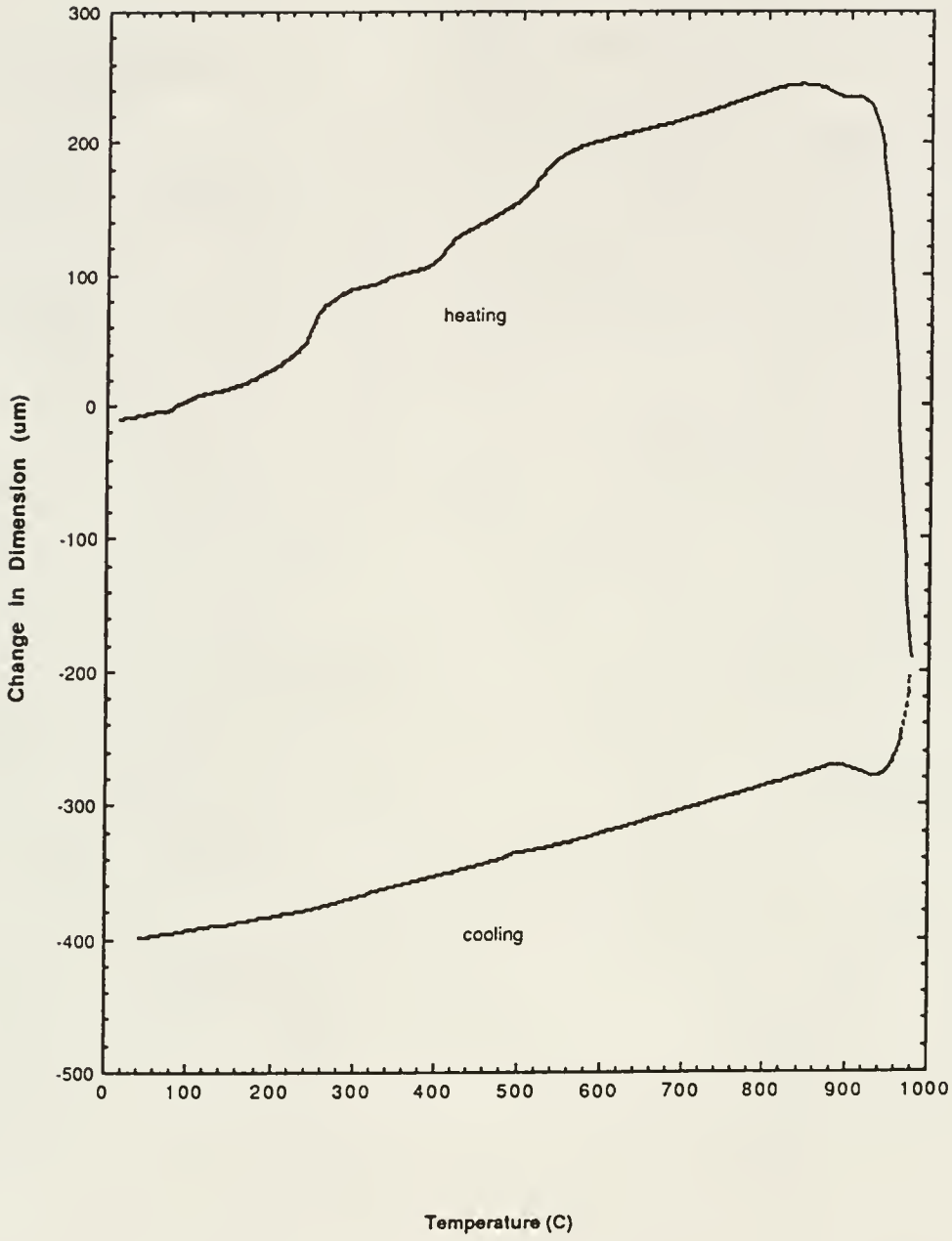

Figure 3-8 Thermal Mechanical Analysis YBCO. Initial dimension: 10.93 mm. Heating rate: 20 °C/min. Top curve: heating cycle. Bottom curve: cooling cycle.

CHAPTER 4
THERMAL MODELS

4.1 Introduction

The evaporation of solid material using laser irradiation, is often treated as a thermal process, although in some cases, such as in the evaporation of polymer material, a photochemical treatment may also be preferred. With the thermal treatment, photons are treated simply as a thermal source, and the chemical interactions that take place between the photon and the irradiated surface are ignored. The process, therefore, deals with the absorption of photon energy, surface heating, subsequent phase transformations, and, finally, material ejection, either as vapor or droplets.

A great deal of thermal modeling of laser heating has been performed, including one- to three-dimensional heat transfer models for both stationary and moving heat sources. The most common application for the laser heating model is for laser welding processes and, to some extent, for material etching. Excellent reviews of the one-dimensional models are available.[110, 111]

When using a high-intensity laser to evaporate material, the temperature gradient in the solid surface could be quite large, and the evaporation process can be initiated within only several nanoseconds.[8] This type of evaporation results in the formation of a high kinetic energy plasma. If the laser interacts with the plasma, such as in the cases where long laser pulse or continuous laser sources are used, photon absorption by the plasma via inverse Bremstrahlung [112] takes place and reduces the effective laser fluence at the target surface. As the surface cools, a rapid surface temperature change could introduce great surface stress, causing cracking at the target surface.

In the development of a material-photon interaction thermal model, both the beam characteristics and material properties must be considered. The beam characteristics consist of the beam spatial distribution as well as the time-dependent beam intensity. The material properties can be further divided into the optical properties (e.g., surface reflectivity, optical penetration depth), physical properties (e.g., density, heat capacity, thermal conductivity), and thermodynamic properties (e.g., enthalpy of transformation, phase equilibria, vapor pressure). If the peak power is low (10^4 to 10^5 W/cm^2), the evaporization process can be adequately described by the conventional description of boiling; however, at a high peak power (10^7 to 10^8 W/cm^2), a more complex thermal description is needed.[113]

Although in laser evaporation the energy input is provided only by radiative heating, energy loss can take place by: radiation, conduction, and convection. The solutions for some common radiation heat transfer problems are available in the literature for various geometries[114] and boundary conditions.[104] If the surface is heated using short laser pulse radiation, especially in the initial stages of the heating, a treatment using the radiative and conductive heat transfer is generally sufficient. On the other hand, if the heating is performed using a continuous laser, the analysis would also include the convective term.

One of the earliest models on heat transfer during laser evaporation was developed by Ready.[113] This model is a one-dimensional heat transfer model, incorporating both heat loss due to conduction and the latent heat of evaporation. This work has since been improved by including the liquid expulsion,[115] momentum transfer [116, 117] and discontinuity across the Knudsen layer.[117, 118]

Because of the application in laser welding, which uses a continuous laser, most of the laser heating problems are solved for the steady-state case,[119, 120] including both for stationary or moving beam. In most cases, the models assumed that the Beer's absorption law was followed and that reflectivity was independent of temperature. For models

involving time-dependent laser irradiation heating, solutions have been achieved by methods such as the Fourier series expansion technique [121] and by the implicit finite difference method.[122]

Many phenomena observed in the evaporation of solid material can be understood through consideration of the surface temperature and thermal profile. While it may be difficult to explain the development of target surface morphology using only a thermal modeling (since the process also depends on the optical properties of the irradiated surface), a thermal model could be used to predict the rate of evaporation as well as the rate of surface cooling.

This study will review some of the work on laser heating models. After the physical descriptions of the evaporation of solid material using a KrF laser are presented, an appropriate model for this particular process will be used to describe the observed physical phenomena. Specifically, thermal models will be used to determine the surface temperature, temperature distribution in the solid, and heating and cooling rates. This information will be used to predict the phase transformations, material evaporation, crystallization rate, and the development of surface morphology that accompany the pulsed laser deposition process. A radiative, one-dimensional heat transfer will be used to predict the maximum surface temperature. While the thermal modelling is used to answer some practical questions, the thermal model will also be used to provide input to the overall energy balance calculation.

4.2 Important Phenomena and Process Description

In this section, the phenomena observed in the evaporation of YBCO material using KrF laser are discussed. These phenomena will be used as the basis for the development of a heat transfer model. In particular, details will be discussed on the topics of surface morphology, penetration depth, and kinetic energy, as well as on the description of the process to be modelled.

4.2.1 Surface Morphology

It has been seen that different types of surface morphology develop as a function of laser fluence and pulse number during the laser evaporation of a YBCO superconducting target using a KrF excimer laser. One important observation is that a periodicity exists in the surface. At low fluence, the amount of material removed per pulse is small, leaving behind a rough, porous surface. As the fluence increases, more material is removed per pulse and the remaining evaporated surface appears smooth. The different types of surface morphology are discussed in detail in Chapter 6. The surface morphology also depends on the number of pulses. At low pulse number and high fluence, the surface is flat and smooth. As the pulse number increases, although the surface is still smooth, the formation of periodic structures can be clearly seen in the length scale of 10 μm or greater. This periodic structure becomes more pronounced with increasing pulse number. Although a thermal model may directly explain how the etch depth varies with fluence, it is not clear that it can be used to explain the surface periodicity. As discussed in Chapter 6, it is conceivable that this surface periodicity may be attributed to the formation of surface cracks resulting from rapid cooling. An estimate on the target surface cooling rate may be useful in estimating the magnitude of surface stress on the target surface.

4.2.2 Thermal Penetration Depth

The analysis of cross-sectional SEM micrograph of the evaporated target (presented in detail at Chapter 6) showed that the thermal penetration depth is short. Although it can be shown that the etch depth per pulse (i.e., quantity removed per pulse) increases with fluence, the thermal penetration depth on the material underneath the evaporated surface is constant. It is reasonable to estimate that the penetration depth at all fluences is less than 0.1 μm. The evaporated target surface appears smooth, a strong indication that melting has taken place. However, heat penetration below this top layer is minimal. There is no

physical indication that the microstructure of the target has changed in the bulk material at a depth greater than 0.1 μm. During evaporation at high fluence and high pulse number, the formation of frozen droplets can be seen. The smaller droplets, with a diameter less than 10 μm, consist of previously molten material, and are smooth and amorphous with no grain boundary. The larger droplets, however, contain virgin material in the center portion. The top smooth layer, previously molten, is less than 0.1 μm thick. These frozen droplets are oriented in the direction of laser beam. It would be useful if the heat transfer calculation could demonstrate that the observed penetration depth is consistent with the observed depth.

To further evaluate the penetration depth, a target made of a sintered mixture of fine, 1 μm diameter, porous gold powder and the superconductor powder were prepared (discussed in Chapter 6). After evaporation, it was found that the porous gold powder had not melted beyond 0.1 mm from the target surface, consistent with the previous observations.

4.2.3 Plasma Kinetic Energy

In this section, the development of a thermal heating model as it relates to laser heating is discussed. The concept of radiation heating, followed by the development of a simple one dimensional heat transfer model, and finally a more complex two phase heat transfer model with material ejection are reviewed. This result will later be used to determine the overall energy balance which will involve the heat conduction as well as detailed phase transformation calculation.

An advantage of the pulsed laser evaporation process is that the generated plasma has a high kinetic energy. The plasma velocity has been measured to be as high as 10^4 m/sec, with a corresponding kinetic energy as high as 100 eV.[13] Even at these high plasma energies, the pulsed laser evaporation process is still energetic enough to remove a significant amount of material with each pulse. One would wonder how this pulsed laser

energy is distributed in the evaporation process. An overall energy balance calculation of the evaporation process, taking into account the target surface properties, energy required for phase transformations, and finally the plasma kinetic energy is useful in understanding how the photon energy is being distributed.

4.2.4 Physical Definition of Process to be Modeled

The following physical descriptions were used in the evaporation of YBCO superconductor using an excimer laser: (1) The laser beam has a uniform power density and well-defined rectangular shape and strikes the target surface. The assumption of a uniform power distribution is justified since only the center portion of the flat-top horizontal axis and gaussian vertical axis was used; (2) The target surface is opaque with a uniform reflectivity value of 0.05; (3) The beam and the target are assumed to be stationary, even if the target is rotated. In a typical pulsed laser evaporation, where the pulse width is 20 nanoseconds and the 0.5 inch diameter target is rotated at 10 rpm with a tangential velocity of 6 mm/sec, the target is essentially stationary since during the pulse duration, the target only moves by 0.1 nm. The three-dimensional energy equation of change is solved for the nonsteady state condition.

To simplify the solution, the following assumptions were made. The reflectivity was assumed to be zero when the temperature exceeded the boiling point, commonly referred to as the keyhole assumption.[120] When the temperature exceeded the boiling point, it was assumed that the material had evaporated. Some of the laser energy was lost due to radiation and convection if the pressure was high, while the rest of the energy was lost to the bulk phase by conduction. The radiation was assumed to follow the Beer Lambert's law ($P = P_o e^{-ad}$, where P and P_o are the power at a certain depth and at the surface, respectively, a is the absorptivity and d is the penetration depth).

4.3 Review of Laser Heating Model

In this section, various models on laser heating are reviewed. Since most of the models are based on solution of the one-dimensional energy equation of change for energy, the results of these models are discussed in detail. The variations in model approaches included the application of different boundary conditions as well as assumptions on the physical properties. Because of the importance of electromagnetic radiation and surface properties in the formulation of a radiative heating model, this topic is briefly discussed. The relevant topics on surface temperature, subsurface heating, and heating and cooling rates indirectly derived from the one dimensional heat transfer model are also presented.

4.3.1 Elements of Electromagnetic Radiation

The basis of laser evaporation is energy exchange by thermal radiation. This section will discuss thermal radiation and its properties, focusing primarily on electromagnetic energy, surface radiation, and absorption theory.

4.3.1.1 Electromagnetic radiation

Radiant energy can be described either in terms of electromagnetic waves or photons.[114] In predicting the radiation properties of a certain class of surfaces, electromagnetic theory can be used, whereas, the properties of the absorbing and emitting media can be predicted in terms of quantum theory.

From the second law of thermodynamics, it can be demonstrated that the maximum radiation energy transfer from a radiating surface depends on its temperature and wavelength. A surface that is capable of emitting this maximum radiation energy is termed a black body. The explicit form of this thermal and wavelength relationship is given by Planck's law. Since not all bodies are black bodies, a factor called the emissivity, $\varepsilon(\lambda,\theta,\varphi)$ is interjected. The emissivity is the ratio of energy emitted to that emitted by a black body. This emissivity value depends on the wavelength, λ, and the polar angle coordinates, θ and

φ. For black bodies in equilibrium, the energy absorbed is the same as the energy emitted, and the total energy emitted from a black body, E_b, depends only on the temperature, as given by

$$E_b = \sigma T^4 \qquad (4\text{-}1)$$

where σ is the Steffan-Boltzmann constant which has a value of 5.668×10^{-5} erg/sec·cm^2·K^4. For a constant refractive index solid, Planck's law can be simplified, and the relationship for the wavelength which gives the maximum emissive power, λ_{max}, is given by

$$\lambda_{max}.T = 2884\ \mu m \cdot K \qquad (4\text{-}2)$$

which is also known as the Wien's displacement law. An often cited peak surface temperature during PLD is 8000 K. At this temperature the λ_{max}. value is 360.5 nm.

The incident laser radiation is of higher energy. The energy associated with each photon is equal to hυ, where h the Planck's constant which has a value of 6.625×10^{-27} erg·sec, and υ is the frequency of radiation. Inserting Planck's constant, this relationship is

$$E_p = 1240/\lambda \qquad (4\text{-}3)$$

where E_p is the photon energy in eV and λ is wavelength in nm. Therefore, the energy of a 248 nm photon (KrF excimer laser used in this study) is equal to 5 eV, sufficiently high to break most chemical bonds.

4.3.1.2 Irradiation of material

In the radiation of a surface or medium, three processes can occur: absorption, reflection, and transmission.[123] The absorptance, $\alpha(\lambda,\theta,\varphi)$, is defined by the ratio of the energy absorbed divided by the total incident energy. This absorptance is both wavelength, λ, and direction, (θ,φ), dependent. For a uniformly diffuse, spectrally selective surface, $\alpha(\lambda,\theta,\varphi)$ is equal to $\alpha(\lambda)$. For a black body in thermal equilibrium, according to Kirchoff's law, the absorptance is equal to the emissivity, $\varepsilon(\lambda)$. The reflectance of a medium, $\rho(\lambda,\theta,\varphi)$, is defined as a fraction of the incident energy that is reflected. A

uniformly diffuse reflectance, which is irradiated from a single direction, will reflect the light in all direction. A secular or mirror-like reflectance, on the other hand has a one-to-one correspondence between the incident and the reflected light. If the reflectance is directionally uniform, but spectrally selective, $\rho(\lambda,\theta,\varphi)$ is equal to $\rho(\lambda)$. Transmission is a process by which an incident light enters a medium from one side and leaves from the opposite side. The transmittance of a medium, $\tau(\lambda,\theta,\varphi)$, is defined as the ratio of the transmitted over the incident energy. If the transmission is independent of the direction of incident, $\tau(\lambda,\theta,\varphi)$ is equal to $\tau(\lambda)$. For the irradiation of a semitransparent, directionally uniform and diffuse surface using a beam with a wavelength λ, the following relationship can be applied, $\alpha + \rho + \tau = 1$.

Most materials absorb UV and visible radiation via the production of excited species by electronic excitation. These excited species have a lifetime on the order of 10^{-8} to 10^{-9} sec.[95] As the excited species relax, the radiation energy absorbed by the material is dissipated in the form of heat, fluorescence, or chemical reactions inside the material. The principle mechanism for photon absorption in metals is the excitation of electrons to higher energy states in the conduction band.[113] Since the average time between electron-electron and electron-phonon collisions is in the order of 10^{-14} to 10^{-13} sec, many collisions take place during a typical nanosecond laser pulse. For nonradiative relaxation, the excitation energy is converted into kinetic energy by collisions with other molecules, which increases temperature.

The intensity of electromagnetic radiation passing through a homogeneous and absorbing material is reduced as a function of the material thickness. For a solid material, the relationship between the absorption and the thickness is known as the Bouguer's and Lambert's law, whereas for a liquid solution, it is known as the Beer's law.[123] These laws assume the same logarithmic form as

$$I/I_0 = 10^{-\alpha t} \qquad (4\text{-}4)$$

where I and I_0 are the intensity after and before absorption, respectively; α is the absorptivity; and t can either be a thickness for a solid or a concentration for a liquid solution. In the absorption of photons by a solid material, the thickness corresponding to the inverse of absorptivity is referred to as the optical penetration depth. For the YBCO material, the reported value of α is 2.3×10^5/cm, which corresponds to a penetration depth of 500 Å.[43]

4.3.2 Laser Activated Heat Transfer Models

Research in laser-material interactions can be divided into two categories:[110] solid and liquid phase heat transfer involving thermal conduction, vaporization, and liquid expulsion;[113, 115, 124] and vapor-phase kinetics involving shock wave and Knudsen layer formation.[117, 118, 125] Previous work ranges from analytical solutions to one-dimensional models to numerical solutions of a three-dimensional description.[126] The temperature-time history of a solid surface irradiated with a laser pulse may be calculated by solving the transient heat conduction equation, while the temperature profile of a target bombarded with electron beams has been predicted using a Green's function approach and Kirchoff transformation for both linear and nonlinear thermal conductivity.[127] Several excellent reviews of one-dimensional heat transfer during laser heating are available in the literature.[110, 111]

In this section, the developments of heat transfer models from the simplest 1-D thermal model to the more complex heat transfer and material expulsion model are discussed. The predictions of these models for surface temperature, subsurface heating, heating and cooling rates will be discussed.

4.3.2.1 Fundamental models

Perhaps the simplest approach to formulating a heat transfer model for laser evaporation is to use one-dimensional heating of a semi-infinite solid with a constant heat flux.[104, 128, 129] It is assumed that the heat flux, in this case the laser beam, is spatially

uniform, and that the physical properties (i.e., k, C_p, ρ) are temperature independent. While it is easy to produce a spatially uniform beam, it can be seen from Section 3.6 that the measured thermal diffusivity value of YBCO drops by 40% when the sample is heated from room temperature to 400 °C. It is further assumed that no phase transformations take place, while the thermal analysis in Chapter 3 indicates that YBCO has a complex phase behavior.

The temperature profile across the solid for a semi-infinite solid is given by

$$\partial\Theta/\partial t = \alpha\, \partial^2\Theta/\partial z^2 \qquad (4\text{-}5)$$

where $\Theta = (T-T_0)/(T_1-T_0)$, a dimensionless number, z is depth, T_1 and T_0 are the surface and initial temperature, t is radiation time, and α is the thermal diffusivity, $k/\rho C_p$, where k, ρ, and C_p are the thermal conductivity, density and heat capacity, respectively. The initial and boundary conditions are

I.C.	$\Theta = 0$	for all z	at $t \leq 0$	(4-6)
B.C. 1:	$\Theta = 1$	at $z = 0$	for $t > 0$	(4-7)
B.C. 2:	$\Theta = 0$	at $z = \infty$	for $t > 0$	(4-8)

Solving for 4-5 using the conditions for 4-6 to 4-8 gives

$$(T-T_0)/(T_1-T_0) = 1 - \mathrm{erf}(z/\sqrt{4\alpha t}) \qquad (4\text{-}9)$$

In this model, the thermal penetration depth, δ, as defined as the depth where 99% of the energy is absorbed, is given by

$$\delta = \sqrt{4\alpha t} \qquad (4\text{-}10)$$

For a constant heat flux, the surface temperature can be expressed by

$$(T_1-T_0) = q|_{z=0}\sqrt{4\alpha t}/k \qquad (4\text{-}11)$$

where $q|_{z=0}$ is the heat flux at the surface which in this case equal to the laser fluence. This model illustrates that, to maximize the surface temperature, T_1, for a given material, a pulsed laser with high pulse energy and long pulse duration gives the best result. For the YBCO material at 1000 °C, using a thermal diffusivity of 5.7×10^{-3} cm^2/sec extrapolated from Figure 3-7, a pulse duration of 20 nsec, fluence of 2 J/cm^2 (or 1×10^8 W/cm^2) and

heat capacity of 0.3 J/g·°C extrapolated from Figure 3-5, the penetration depth and the surface temperature are calculated to be 0.2 μm and $2x10^5$ K respectively. For the laser heating of a material with finite thickness, such as a thin film on a substrate, the solution includes the film thickness as well as the physical properties of the substrate material.[104]

The problem formulation has also been solved for materials with temperature-dependent optical and physical properties,[126, 130] as well as for a beam with a gaussian distribution.[131]

In pulsed laser evaporation the heat flux varies with time. An analytical solution can be obtained for heating of a semi-infinite solid with a uniformly distributed heat flux by applying the Duhamel's theorem [104]

$$T(z,t) = \int_0^t f(t)\, \partial/\partial t\, F(z,t-\tau)\, dt \qquad (4\text{-}12)$$

where f(t) is the heat flux function, τ is the pulse width, and F(z,t) is the solution for constant heat flux. The solution of the above equation shows that the maximum temperature is inversely proportional to the square root of the pulse width, therefore a shorter pulse width gives a higher maximum temperature.

When a phase transformation takes place as the result of laser heating, the problem formulation must be modified. The one-dimensional equation of change for energy at the solid-liquid vapor interface can be described as [132]

$$\rho C_p\, \partial T/\partial t = \partial/\partial z\, (k\, \partial T/\partial z) + I(1-R)/\rho C_p\, \alpha\, e^{-\alpha z} \qquad (4\text{-}13)$$

where α is the absorption coefficient, I is the laser intensity and R is the surface reflectivity. Motion of the solid-liquid interface involves a latent heat effect, ΔH. An energy balance a the interface can be written as

$$v\, \rho\, \Delta H = k_s\, (\partial T/\partial z)_{solid} - k_l\, (\partial T/\partial z)_{liquid} \qquad (4\text{-}14)$$

where v is the interface velocity, and k_s and k_l are the thermal conductivity of the solid and liquid, respectively. This problem has been solved for many different boundary conditions.[111]

For one-dimensional heat transfer involving convective heat transfer, the temperature profile can be expressed by the following equation

$$k\,(\partial T/\partial z) = I(1-R) - (h_c+h_r)(T_1-T_a) \qquad (4\text{-}15)$$

where h_c and h_r are the convective and the radiation heat transfer coefficients, respectively; T_1 and T_a are the surface and the ambient temperature, respectively. The convective heat transfer for vertically impinging jets, which may be assumed as the energy removed from the surface of the heated target surface a few microseconds after the laser pulses, can be calculated by [120]

$$h_c = 13Re^{0.5}Pr^{0.33}k_{gas}/B \qquad (4\text{-}16)$$

where Re, Pr, and B are Reynolds number, Prandl number and jet plate distance, respectively. The radiative loss can be expressed by

$$h_r = \sigma(1-R)(T_1^2-T_a^2)(T_1-T_a) \qquad (4\text{-}17)$$

where σ is the Steffan-Boltzman constant. The convection term is negligible for molten ceramics in the 18 ns time frame of a laser pulse; however, the thermal diffusion contribution is significant, and the relationship as a function of temperature has been developed.[133]

4.3.2.2 Surface temperature

Thermal model based on the one dimensional heat transfer could be used to determine the surface temperature. A commonly used equation to determine surface temperature is [44]

$$\Delta T \propto (1-R)\,(M/k\rho C_p)^{1/2} \qquad (4\text{-}18)$$

where ΔT is the temperature rise, M is the molecular weight, ρ is the density and C_p is the heat capacity. Unlike the assumption commonly used in thermal modeling, which is that the target surface melts at T_m and evaporates at T_b,[134] the above model assumes that the evaporation can take place at any temperature, and that the evaporation rate increases with temperature. This estimate was reasonably accurate in predicting the surface temperatures of metals. Ready found that during the evaporation of tungsten using a ruby laser, the

calculated surface temperature was underestimated by 20% of theoretical.[113] For YBCO, the temperature of the target surface has been estimated from 1243 K [135] to 3000 K.[136]

4.3.2.3 Subsurface heating

The concept of subsurface heating was initially suggested by Ready while investigating the laser evaporation of a carbon surface.[8] Subsurface heating is a term used to describe the situation when the temperature profile shows a maximum in the interior of the solid. The phenomena can be understood by considering the absorption of energy that decreases exponentially below the surface, the evaporation of material that provides an energy sink at the surface, and the conduction of energy into the bulk that decreases the extent of subsurface heating. When the temperature of the material underneath the surface exceeds the vaporization temperature (i.e., becomes superheated) though the surface temperature is in equilibrium, the superheated interior of the solid can explode.

Ready investigated the temperature distribution during the irradiation of a metal using a high-energy laser.[137] A typical laser power density before subsurface heating is $5x10^8$ W/cm^2,[14] corresponding to a fluence of 1 J/cm^2 if an excimer laser with 20 ns pulse width is used. The time required for surface melting to begin, t_m, is given by [111]

$$t_m = (\pi/\alpha)\,(T_m\, k/2I)^2 \qquad (4\text{-}19)$$

where T_m is the melting temperature, and I is the energy flux; the depth of melting, d_m, for metals can be empirically given by[111]

$$d_m = 0.16\, I\, (t\text{-}t_m)/\rho\Delta H \qquad (4\text{-}20)$$

For the YBCO material at 1000 ^oC evaporated at fluence of 2 J/cm^2 (or 10^8 W/cm^2), the valuel of t_m is calculated to be $1.5x10^{-12}$ sec.

The likelihood that subsurface heating can take place was predicted by Gagliano using a dimensionless absorption parameter, B, which is defined by [138]

$$B = k\,\alpha\,\Delta H/I\,C_p \qquad (4\text{-}21)$$

If the value of B is high, such as for metals, material removal is by evaporation. On the other hand, if the value of B is small (<<1), such as for ceramics, the material removal

mechanism favors subsurface explosion. The value of B for YBCO is calculated to much less than unity, indicating that a subsurface heating is highly probable.

4.3.2.4 Heating and cooling rates

In the beam processing of silicon,[139] the heat transfer model is constructed by assuming that the system is adiabatic because radiation is short (< 200 ns) and that little heat is lost by diffusion. As the result, the temperature profile is steep within the top 2 μm from the surface. If the thermal flux is applied continuously, the thermal penetration depth can go as high as 100 μm. For an even longer heating time, a uniform steady-state profile can be obtained. The temperature profile calculated by assuming that one-dimensional heat transfer with melting is constant at 0.2 μm.[140] The heating rate of the surface temperature of YBCO irradiated using KrF laser at 0.15 J/cm^2 was calculated to be 10^{11} C/sec.[140] As a comparison, the molten surface layer of laser irradiated semiconductor could remain molten up to 100 nsec.[141]

4.3.2.5 Heat transfer with material ejection

Above a critical value of fluence, the irradiation of solid gives rise to material ejection. There are two mechanisms for material removal: evaporation and liquid ejection. The total material removed is the sum of these two mechanisms. The proportion contributed by each mechanism depends on the fluence and the properties of the materials. The rate of evaporation increases with increasing fluence since the surface temperature increases with increasing fluence. The rate of liquid expulsion, however, shows a maximum with fluence variation. At low fluence, the temperature and recoil pressure are both low, resulting in low liquid expulsion rates. At high fluence, the surface temperature and recoil pressure are high, however, the liquid layer is thinner, resulting in low liquid expulsion rates. It is assumed that the liquid layer is thin and that the vapor is optically thin. The surface temperature increases with increasing fluence. A metal with low vapor pressure has higher superheating since a certain superheating pressure is required for material removal. The thickness of the liquid layer decreases with increasing fluence due to higher recoil pressure.

The Mach number increases with fluence due to higher recoil pressure. The laser drilling efficiency of copper using Nd:YAG laser was investigated for three stability ranges.[142] At low intensity, the rate for material removal was limited by normal evaporation. At intermediate intensity , an unstable region developed. The intensity was sufficiently high to overcome the surface tension of the liquid layer but insufficient to compensate for the energy loss associated with the expulsion of the melts, resulting in an oscillatory behavior. At high intensity, a steady-state condition for material removal was achieved. This chapter deals primarily with the temperature distribution during the initial stages of heating. The ejection of material will be further discussed at Chapters 5, 6 and 7.

4.4 Macroscopic Energy Balance

It is instructive to consider a macroscopic energy balance in order to determine the plasma velocity during the evaporation of YBCO with a KrF laser. This evaporation process is divided into three stages: (1) absorption of laser energy by the target, (2) equilibrium conversion of the target from solid or liquid to the plasma state, and (3) ejection of the plasma from the target surface. The energy requirements for each of these process was determined.

A typical condition for film deposition was considered in the overall energy balance calculation. A high-density pellet of YBCO with a density of 96% was evaporated using a pulsed KrF laser with a fluence of 2.0 J/cm^2. An evaporation area of 1mm x 1mm was assumed in this calculation. The average experimental value of the depth of material removal under these conditions is 0.07 μm/pulse. The thermal penetration depth, defined as the depth where 99% of the energy is absorbed, is 0.1 μm as determined by experimentation. This intense heating produced a plasma at a temperature near 8000 K, which expanded at a velocity of 10^6 cm/sec.[12] The plasma composition was assumed to be equal to the equilibrium composition calculated from thermodynamic equilibrium.

A complete energy balance of the above process was performed. It was assumed that all the nonreflected beam was absorbed by the solid. The solid material then transformed to plasma state with a composition equal to that calculated from thermodynamic equilibrium at 8000 K. The energy required to form the plasma state and impart the observed kinetic energy was calculated.

4.4.1 Photon Absorption

The total energy absorbed by the target was calculated from the laser fluence and target surface reflectivity. Spectroscopic reflectivity measurement of a high-density target showed that at an incident radiation wavelength of 248 nm, 95% of the energy was absorbed. The total energy absorbed by the target is

$$E = I\,A\,(1-R) \tag{4-22}$$

where E is the absorbed energy (2×10^{-4} J/pulse or 5×10^{4} J/g), A is surface area (1 mm^2), I is the laser fluence (2 J/cm^2), and R is surface reflectivity (0.05). Because an excimer laser on a YBCO target has a penetration depth of only 50 nm, no light was transmitted for a typical sample thickness, and therefore all the nonreflected laser energy was absorbed by the solid.

The total energy absorbed by the solid is used to form the plasma phase, import kinetic energy to the ejected plasma (isentropic expansion), or is lost by radiation, conduction into the bulk, convection to the surrounding low pressure ambient. Each of these terms is addressed in the discussion below.

4.4.2 Phase Transformation

A fraction of the energy absorbed by the target is used to convert the solid target to liquid and then to the plasma state at an elevated temperature. Since the initial and final conditions, along with the thermodynamic properties were known, the energy required for the conversion could be calculated.

The initial condition was a YBCO target at room temperature. The final condition was a plasma gas mixture at 8000 K at 1 atm with a composition calculated from the equilibrium analysis given in Chapter 3. A temperature of 8000 K was selected since this temperature was reported in the literature as determined from emission spectroscopy[143] and constant with the mass spectroscopic measurements to be discussed in Chapter 8. The pressure of 1 atm was taken because at the end of the 20 ns laser pulse, the hot dense plasma has expanded slightly. At higher pressure the gas composition would contain more oxide and neutral species.

At 8000 K and 1 atm the composition of the plasma consists only of neutral and ionic atomic species as shown in Figure 2-7. At this condition, 40% of yttrium exists as neutral species, whereas the remainder as charged Y^+ species. Only 10% of barium exists as neutral Ba, the remainder as charged Ba^+ ion. Copper at this condition exists only as Cu^+ ion with all the neutral Cu disappearing at 7000 K. In contrast, oxygen which exists only as neutral O with O^+ not forming until 12,000 K. At a higher pressure of 10 atm, the vapor composition would be mostly Y with equal concentrations of Ba and Ba^+, Cu^+, and O.

Given the final composition, the energy required to produce this composition can be calculated from the following set of equations.

$$YBa_2Cu_3O_7(s,298K) \rightarrow 1/2\ Y_2O_3(s,298K) + 2\ BaO(s,298K) + 3\ CuO(s,298K) + 1/4\ O_2(v,298K) \quad (4\text{-}23)$$

$$Y_2O_3(s,298K) \rightarrow 2\ Y(v,298K) + 3\ O(v,298K) \quad (4\text{-}24)$$

$$BaO(s,298K) \rightarrow Ba(v,298K) + O(v,298K) \quad (4\text{-}25)$$

$$CuO(s,298K) \rightarrow Cu(v,298K) + O(v,298K) \quad (4\text{-}26)$$

$$O_2(v,298K) \rightarrow 2\ O(v,298K) \quad (4\text{-}27)$$

$$Y(v,298K) \rightarrow Y^+(v,298K) \quad (4\text{-}28)$$

$$Ba(v,298K) \rightarrow Ba^+(v,298K) \quad (4\text{-}29)$$

$$Cu(v,298K) \rightarrow Cu^+(v,298K) \quad (4\text{-}30)$$

$Y(v,298K) \rightarrow Y(v,8000K)$ (4-31)

$Ba(v,298K) \rightarrow Ba(v,8000K)$ (4-32)

$Cu(v,298K) \rightarrow Cu(v,8000K)$ (4-33)

$Y^{+}(v,298K) \rightarrow Y^{+}(v,8000K)$ (4-34)

$Ba^{+}(v,298K) \rightarrow Ba^{+}(v,8000K)$ (4-35)

$Cu^{+}(v,298K) \rightarrow Cu^{+}(v,8000K)$ (4-36)

The energy change for each reaction was calculated using the available thermodynamic data and the composition presented in Table 2-6. The enthalpy of formations for each plasma species listed in Table 2-6 at 8000 K was calculated. From these values, the enthalpy of the overall reaction was determined to be 1.4×10^{4} J/g. The calculated enthalpy as a function of temperature assuming only neutral species are formed is presented in Figure 4-1. A sharp increase between temperatures of 2000 and 4000 K was caused by the phase transformations from solid-liquid to vapor phase. At 4000 K, all the elements had been converted into gaseous phase.

The calculation shows that the total energy required to convert solid target to the plasma state at 8000 K and 1 atm is equal to 29% of the total beam energy. At higher pressures, the composition of the plasma changes, however, the energy required was almost identical since more oxide species are present (requires less energy to form than atomic species) but less ionic species are present (requires more energy to form).

4.4.3 Radiation, Convection and Thermal Conduction Losses

The radiation loss during this process is negligible, even by assuming that the emissivity is unity. Using a surface temperature value of 8000 K, the energy loss due to radiation within the 20 nsec pulse length is calculated from Equation 4-1 to be 5×10^{-8} J/pulse, which is 0.02% of the total energy.

Assuming that the heat conduction can be described by a one dimensional heat transfer model, the thermal penetration depth was calculated to be 0.2 μm, consistent with

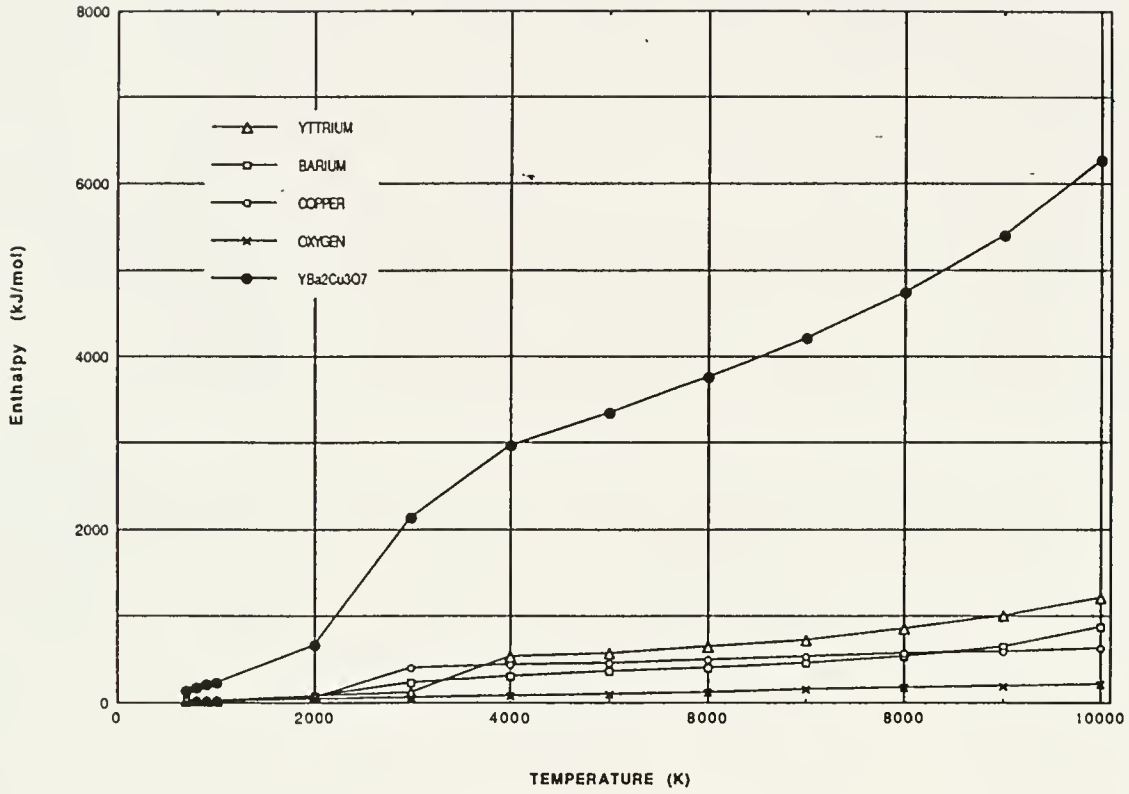

Figure 4-1 Enthalpy of $YBa_2Cu_3O_7$ as a function temperature. Charged species not considered.

the experimental value (see Chapter 6). The calculated energy contribution of the solid is equivalent to 0.25% of the total energy.

4.4.4 Plasma Kinetic Energy

The remaining energy from the phase transformation was used to estimate the velocity of the plasma. This energy amounts to 68% of the total energy. Using the plasma composition as calculated from the equilibrium analysis, the velocity each plasma species was calculated. This calculation assumes that the kinetic energy of all particles are the same, therefore, the velocity depends on the molecular weight. It is noted that the neutral and ionic states of the same species have the same velocity since the MW remains the same. The calculated average velocity was 8.2 km/sec, consistent with experimental values as measured from time-of-flight measurement.[144]

4.5 Conclusion

The result of the energy balance calculation showed that most of the energy absorbed by the target is converted to kinetic energy (Figure 4-2). The formation of the plasma state, surprisingly, only consumed 27% of the total energy. This energy is required to bring the solid target at room temperature to a plasma at 8000 K. The radiation loss, even assuming that the surface has an emissivity value equal to unity only contributes to 0.02% of the absorbed energy. The contribution due to the energy absorbed by thermal conduction only contributes 0.25% of the total energy. The remainder of the energy, which account for more than 68% of the total energy is converted to plasma kinetic energy. The laser evaporation process is categorically an efficient process with most of the energy converted to kinetic energy.

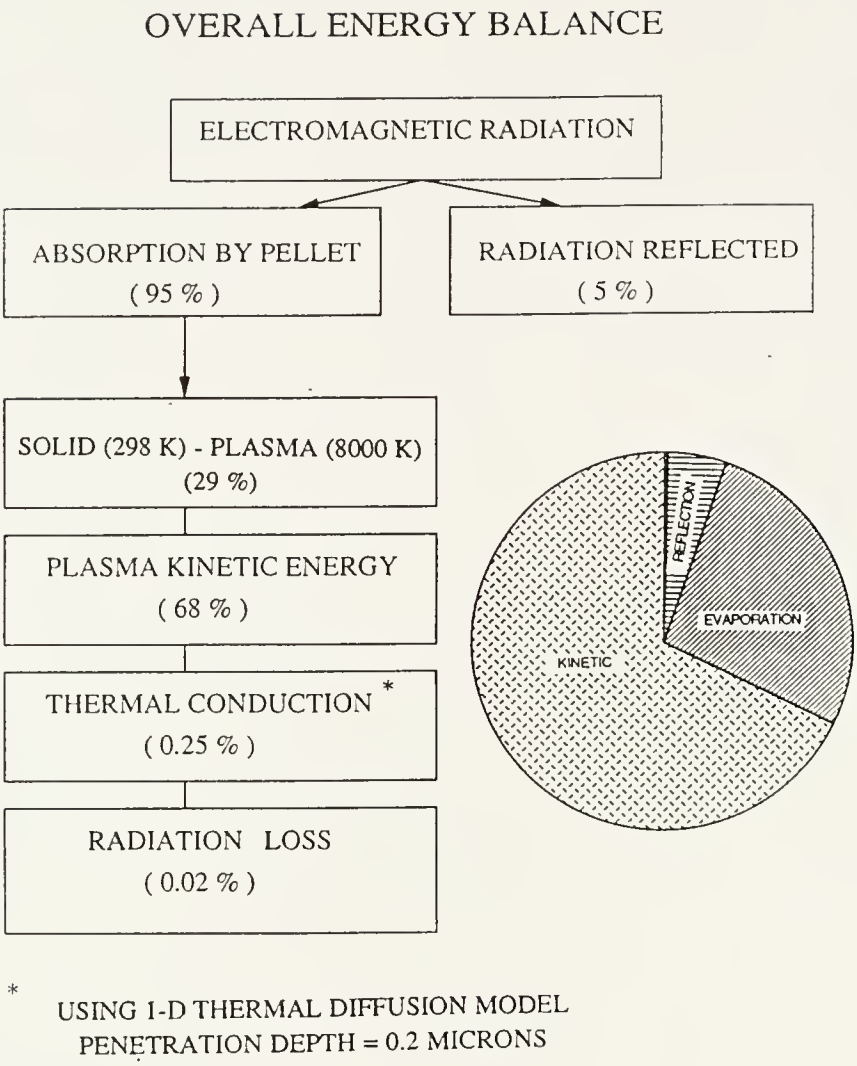

Figure 4-2 Energy distribution for the evaporation YBCO target using KrF laser.

CHAPTER 5
PARTICLE PRODUCTION STUDIES

5.1 Overview of Particulate Formation

This chapter discusses the formation of particulates, a common problem associated with the deposition of thin films by laser evaporation. The fundamentals of particulate formation are discussed. A detailed study of the method particulate reduction via target heating is also presented.

5.1.1 Introduction

The presence of film particulates has been a long-standing problem in pulsed laser deposition, especially in the deposition of superconducting thin film.[1, 25, 38, 145] These particulates are largely spherical, on the order of 1 μm in diameter, or irregularly shaped submicron sized particulates. Particulates on the film are undesirable, since they limit the spatial and thickness resolutions of features that can be patterned on the film. It has been shown that the size, shape and number density of these particulates depends on the material characteristics as well as the fluence and wavelength of the laser.[1]

Film particulates have also been observed in the laser deposition of other materials such as semiconductors, [5, 30, 146] dielectrics, [5, 147] ferrites, [148] polymers, [149] and diamond.[150]

The primary source of particulate formation is believed to be derived from laser-target interactions. Several mechanisms for particulate production have been suggested, including the ejection of loosely packed target particles, [30, 151] splashing of molten target, [33, 152] subsurface heating [8, 14, 138, 153] rapid expansion of trapped gas bubbles in the

target, [1] and, in particular, material ejection associated with the development of target surface morphology.[30] Laser fluence and pulse number have been shown to strongly texture the target surface.[53, 154] Particulate formation as the result of homogeneous plume condensation has also been suggested.[25, 145]

The number density of particulates, deposited under normal conditions, is on the order of $2x10^5$ to $4x10^6$ particles/cm^2.[39, 54, 155] In a multilayer device, with each layer thickness typically on the order of 200 nm, or in a fine line resolution circuit with line width in the order of a micron, the presence of micron sized particulates is highly undesirable.

Although undesirable as surface defects, the formation of surface particulates could be fundamental in preserving the stoichiometry in PLD. It has been suggested that the splashing of target or direct ejections of clusters [4, 32, 33, 156] is the main mechanism for preserving stoichiometry for materials that melt incongruently. In addition, it is reported that the best performance films with high T_c and J_c have rough surfaces, [41] which could indicate that a great deal of splashing has taken place.

In this chapter, the development of film particulates during laser evaporation and the methods currently available to reduce particulates will be discussed. This discussion is primarily focused on the formation of film particulates during the laser deposition of YBCO. A new method of particulate reduction via target heating and its relation to the proposed mechanisms, unique to this thesis, will be discussed.

5.1.2 Surface Roughness

The surface roughness on a deposited film can be attributed to several factors. For example, depending on the choice of the deposition technique, droplet-like particulates can be produced in PLD or homogeneously nucleated particulates can be formed in CVD. The other factors are the physical properties of the film and substrate, for example, thermal

expansion compatibility, film growth mechanism and substrate-film interface reactions. In most cases, film surface roughness results from a combination of these factors.

Film particulates observed in laser deposition consist of two types: (1) melted spherical particles with a diameter less than 1 μm and, (2) irregular crystalline particles with diameter larger than 1 μm. For deposition of YBCO, most particulates are stoichiometric, though evidence of particulates that are Cu-rich [25] and contain aggregates with the wrong composition [41] has also been reported. The irregular particles are believed to have been dislodged from the target without evaporation, but could become spherical after annealing, whereas the spherical particles are deposited throughout the growth duration.[25]

If the substrate and film thermal expansion are not compatible, the film tends to crack or buckle.[25] It has been shown that $LaGaO_3$ undergoes a phase transformation at 140 °C and causes surface roughening, [26] while the random plate-like morphology has been attributed to random crystal orientations.[157]

Outgrowth formations also contribute to the film roughness and have been commonly mistaken for particulates.[41] This outgrowth exists in the form of pinholes, lenses, and needle-shaped outgrowths, [41] which exist even in the absence of particulates. Outgrowths are more predominant at higher growth temperatures.[158]

The above evidence and the fact that surface roughening is found not only in laser deposited films, but also with other techniques (sputtering, CVD, and plasma evaporation), suggest that laser evaporation may be more particle-free than previously believed. Nevertheless, it is still important to study the fundamentals of particulate formation and the development of a better method of particulate reduction.

5.1.3 Formation of Clusters

Cluster formations has been identified during laser evaporation of metals and semiconductors.[159-162] Clusters, which may contribute to the formation of particulates, are formed at the region near the target, while the expanding plasma is still very dense.[151]

Clustering is less likely at locations away from the target. Clusters can be created by the adiabatic expansion of high-pressure gas into a small orifice.[163, 164]

A cluster is defined as a nonrigid assembly of components bound together by chemical bonds, [165] with the upper limit of 10^5 [166] to 10^6 units.[167] The cluster size is inversely related to the melting point.[167] Cluster formation has been observed during evaporation, forming as high as 110 carbon [160] and 148 argon [168] atoms. Attempts have been made to quantify the cluster distribution using the liquid drop approximation.[169]

If the photon energy colliding with a gas-phase cluster is higher than the critical energy corresponding to the ionization cross section, the cluster can be ionized.[165] Given the surface tension and droplet radius, the maximum number of charges allowed can be determined from the Rayleigh charging limit.[170] The stability of a metastable ion cluster induced by a photon was shown to be dependent on the excess energy released following the ionization.[171]

Although clusters are present during laser evaporation, [12] it is unlikely that the particulates are in the form of clusters. A simple calculation demonstrates that a particle is simply too large to be a cluster, although it is possible that a cluster can nucleate a particle that grows on the surface. Assuming that the particulate density is 80% of the theoretical density, a droplet with a diameter of 1 μm will have a molecular weight of 1.6×10^{12} g/mole, or equivalent to 2.4×10^9 molecules of YBCO. The upper limit of a cluster, as previously defined, is only 10^6 molecules.[167] In addition, molecules of YBCO are much too complex compared to atoms and simple molecules, the typical constituent of a cluster. It is more likely that a particulate is a result of droplet formation or other mechanisms.

5.1.4 Formation of Particulates

As previously stated, it has been suggested that the formation of particulates is related to the laser-target interaction. The target related mechanisms include explosion of target, such as the ejection of loosely packed target, splashing within molten target areas,

subsurface heating, and rapid expansion of trapped gas bubbles in the target. Other mechanisms include plume condensation and target surface morphology development.

An explosion within target produces atomic and molecular ions, molten phases and fractured solid particles.[25] The ejected particles consist of two different components, one has a velocity of $5x10^6$ cm/s, and the other is much slower at $6x10^5$ cm/s as determined by fast photography technique.[12] Films with particle problems always contain spheres, possibly produced by melting and recrystallization of small particles at reduced temperature (lowered because of the small diameter).[41] If the deposition rate is kept at or below 1 pulse per second, nuclei ripening occurs and the film contains no boulders.[41]

The nature and stability of the particulates depend on the viscosity of the melt and velocity of the particulates [172] as they are deposited on the film. During the transit, if the particulate temperature drops much below the melting point, the droplet will remain solid and be observed as particulates on the surface. On the other hand, if the droplet remains molten, therefore having a lower viscosity, it is probable that the droplet will either be absorbed by the film due to high surface mobility at high surface temperature, or will form a "splat," a compressed sphere.[173] Evidence from the boulder formation on the surface commonly observed on films indicates that the droplets arrive at the substrate surface as solids with high kinetic energy since the particulates appears to be spherical and partly buried in the film.

The theoretical droplet temperature can be determined by assuming that the initial temperature is between the melting and boiling points. In the case of YBCO, the temperature is higher than 1060 °C, but the upper limit is not known, since no literature boiling point was found. Equilibrium calculations at Chapter 2, however, suggest that beyond 3000 K only vapor species could exist. The temperature history of a droplet leaving the target surface in a plasma that expands adiabatically should be higher than the thermal history of the bulk plasma, since additional cooling time is required to cool a spherical droplet. The liquid-to-solid droplet transformation can take place only if

sufficient heat can be removed from the droplet during the travel time from the target to the substrate, approximately 3 to 5 μsec, so that the droplet temperature drops below the melting point. At a minimum, the heat removal should be equivalent to the enthalpy of fusion. The initial temperature of the plasma estimated from the expansion velocity and emission spectroscopy was estimated from 1400 K [174] to 8000 K.[143]

The ejection of the particulate can be explained by momentum transfer. Since the time constant is small, only 20 nsec, comparable to the relaxation time of the molten target, a standard fluid flow model such as the Navier-Stokes equation does not apply. It is analogous to water that behaves as a solid when the impact velocity is very high. A model based on momentum transfer was derived. This model assumed that there are surface imperfections.[44]

5.2 Effect of Deposition Parameter Film Deposition

The investigation of the YBCO evaporation reveals that the particulate formation depends strongly on the wavelength and fluence being applied. The best conditions for minimization of the particulate density is at low wavelength at low fluence.

5.2.1 Effect of Laser Parameter

Comparisons among YBCO thin films made using wavelengths varying from 193 nm to 1064 nm showed that films made with shorter wavelengths were smoother and contained fewer particulates.[151] It was suggested that the improvement in the film smoothness was attributed to the shorter penetration depth of the UV lasers and the higher absorption of the ablated fragments. Films depostited at 1064 nm were the roughest and about three times thicker than films deposited at shorter wavelengths for the same fluence and number of pulses.[151] Rougher films also have poorer superconducting properties due to poorer connections between the grain boundaries.

The production of particulates is a strong function of fluence as seen from the work on YBCO and other systems. At high fluence, the particulates are spherical or disk shaped with a smooth surface, indicating melt solidification. At lower fluence, the particulates have an irregular shape.[1] A mass spectrometer has been used to correlate the presence of particulates on the film with the presence of clusters.[1]

The deposition of YBCO films using a near IR laser at low fluence, 0.6 to 0.8 J/cm^2, produced fewer particulates than the deposition at fluences of 1.0 J/cm^2 or higher.[33] The film deposited at low fluence was Ba and Cu rich; however, at higher fluence, the film was more stoichiometeric. It was suggested that at high fluence the volume of the target melt increases, producing liquid droplets and giving stoichiometric but rougher films. At low fluence, the heating is confined to a thin layer and emits clusters. Quenching of liquid droplets, unfortunately, produced stable nonsuperconductive phases, such as $BaCuO_2$.[33] Evidence from streak camera studies suggests that, as the fluence increases, the contribution of the slow-moving components increases.[12] This can be interpreted as meaning that more large particles are produced at higher fluence.

A higher incidence of droplet formation at higher fluence was also observed during the evaporation of ZrO_2 thin films by CO_2 pulsed laser.[152] Laser fluence was found not only to affect the number of particulates but also the particulate shapes. At high fluences (>100J/cm^2), spherical or disk-shaped particulates (3-5 μm), with particle density of 3-10/mm^2 indicative of molten droplets, were observed. At medium fluences (50-100 J/cm^2) a low particulate density is observed. However, at low fluence (<50 J/cm^2), irregularly shaped submicron particles were found at high density (100-1000/mm^2). These small particulates probably come from the fractured solid surface. A possible explanation is that, at intermediate fluence, the small particulates are evaporated, and the energy is still not sufficient to produce a pool of molten surface, which causes the formation of droplets.[152]

A model that correlates the laser intensity with the tendency of splashing to occur was developed.[14] Given the time for the electrons on the surface to reach the Debye

temperature, laser surface penetration, solid density and heat of vaporization, the maximum fluence allowed to avoid splashing can be calculated.[14] The temperature of the plasma can be higher than that of the target surface due to inverse bremsstrahlung.[175] Based on a laser subsurface heating model, which postulates that splashing will occur if the rate of laser energy input to the target is higher than the rate of energy dissipated by the target, the maximum laser power allowed before splashing takes place is $P_{max} = \alpha\rho\Delta H_v/t_r$, where α is the light penetration depth, ρ is the solid density, ΔH_v is the heat of evaporation, and t_r is the relaxation time of hot electrons in the surface layer.[1, 14]

During the evaporation of silicon, at low energy density, large clusters and droplets are emitted. At higher fluence, ions are emitted by a repulsive coulombic force; however, within tens of nanoseconds, recombination takes place forming small clusters.[176] The mechanism of plasma absorption was believed to be inverse bremsstrahlung if the energy is low.[175] During the deposition of diamond, doubling the power density from $3x10^8$ W/cm^2, increases the particulate density ten times from $1x10^5/cm^2$.[150]

5.2.2 Effect of Deposition Parameter

If the film is grown within the narrow temperature range (700-800 °C), [177] the film is rough, but has good superconducting properties. Below the optimum temperature range, the film is smoother, but has poor electron transport properties. In general, a higher deposition temperature increases film performance, but contributes to surface roughness.[41]

The maximum pressure allowed before the formation of a shock wave is 0.25 mbar.[178] At high pressures, shock waves are formed, and the fragments remain near the target surface.[174, 179] It is speculated, therefore, that at higher pressure the film is less likely to contain particulates.

The use of an oxidizing atmosphere was found to be helpful in reducing the number of particulates during the evaporation of polymers.[149] Large organic particles were

oxidized to CO_2. It is doubtful that this will drastically effect in the evaporation of YBCO since the vapor pressure of the oxide and the elements in vapor are similar.

5.2.3 Effect of Target Quality

Reductions of particulates have been observed using high density [151, 180] or highly polished [30, 41] targets. Commonly, as the evaporation progresses, the rapid heating and cooling causes the top surface to be filled with cracks, craters, bumps, and loose particles. Scanning the target generates fewer boulders.[181] The disintegration of this mechanically weak structure causes the formation of particles.[1] Similarly, this effect applies to structurally weak, low-density targets.

5.3 Techniques for Particulate Reduction

A number of efforts have been made to reduce the number of particulates. The work includes preventive approaches such as utilizing a homogeneous, dense, and polished target, [53] or utilizing an Ag-doped target [182] to prevent the formation of particulates. Counteractive approaches, such as a mechanical velocity filter, [183] secondary beam, [151] and plasma spray [184] designed to remove or to evaporate particulates in transit have also been used. Some of the available methods for particulate reductions will be briefly discussed.

5.3.1 Secondary Laser

An experiment designed to produce smoother films was performed using a secondary laser, KrF excimer laser (30 ns), to irradiate the plume generated by the primary laser, a Nd:YAG infrared laser (1.64 um, 10 ns).[151] A UV secondary laser was chosen instead of the IR laser because it has a higher electronic state absorption for particles and molecules in the plasma. The pulse duration was synchronized with a 1 μs delay such that only the larger particles, with lower velocity, were affected by the second radiation. The

use of the secondary laser failed to reduce the number of particulates, although it was shown to increase the film density by 40%.[151] It was suggested that the presence of the second radiation further breaks down the larger particles, as indicated by the doubling of the plume size. This technique could be improved by optimizing the secondary laser intensity, wavelength, location, and time delay.[145]

5.3.2 Mechanical Velocity Filter

The mechanical velocity filter was developed based on the concept that larger particles in the plasma plume move slower than smaller atoms or molecules.[185] This method was proven to be reliable in reducing particles in the film. Recently, however, this velocity filter was improved.[183] The equipment, in concept, is similar to a turbomolecular pump, and consists of a vane located axially in the direction of the plume and rotated at 3000 rpm. Depending on the filter's vane length, number of vanes and rotational speed, large particles with a certain velocity can be separated by colliding with the rotating vane. The number of particles has been reduced by an order of magnitude using this technique. A similar method using an electronically actuated shutter synchronized with the laser firing was successfully used to filter particles with a velocity less than 1.2×10^4 cm/sec.[30]

5.3.3 Surface Heating

For an element with low vapor pressure at its melting point, such as germanium, the splashing that occurs during the laser evaporation can be completely eliminated.[186] This technique, however, is not applicable for the evaporation of a multicomponent target. It has been recently suggested that direct laser heating is not desirable since it will always produce more particulates.[145]

5.3.4 High-Velocity Target and Plasma Spray

A high-velocity target material moving at a velocity comparable to that of the fragments, in combination with a plasma arc spray, synchronized with the laser pulse, are used to eject the fragments that travel perpendicular to the plasma.[184] This method is capable of reducing the particle density by an order of magnitude.

5.3.5 Ag-Doped Target

A reduction of particulate density by an order of magnitude using Ag-doped YBCO target was demonstrated.[182] It was suggested that the incorporation of Ag improves the target's thermal conductivity, optical absorption coefficient, and bulk density, making subsurface heating, and thus particulate formation, less likely to take place.

5.3.6 Off-Axis Deposition

Off-axis deposition is performed with the substrate parallel to the direction of the plume.[187] Brownian-like motion changes the trajectory of the light particles, allowing them to be deposited off-axis. The heavy particles, on the other hand, are not affected and pass the substrate without being deposited. The deposition rate, however, is very low.

5.3.7 Substrate Negative Voltage Bias

A negative voltage bias applied to the substrate has reduced the density of particles in the as-deposited film of Ge by as much as a factor of five.[30] The macroscopic particles have negative charges and are repelled by the bias. Typical boulder density during the deposition of Ge is $10^6/cm^2$.[30]

5.4 Particulate Reduction via Target Heating

The method of particulate reduction via target heating is based on the principle that, if the development of target surface morphology during the evaporation can be surpressed, the formation of film particulates can be avoided. Studies have shown that the formation of film particulates could be linked with the formation of surface morphology.[30]

5.4.1 Introduction

As described in Chapter 6, the formation of target morphology during the evaporation of YBCO is initiated by the development of surface cracks, possibly due to the surface stress induced during rapid cooling of the target surface. If the formation of this surface crack can be prevented, the formation of surface morphogy, and therefore film particulates could be avoided.

A direct method of minimizing the surface cooling rate is to maintain the area surrounding the evaporation area at an elevated temperature. The use of a long wavelength laser as the primary laser could be considered since a long wavelength laser has a long penetration depth, and therefore a thicker molten layer can be formed on the target surface. This thick, hot layer will, in principle, help reduce the cooling rate of the target surface. The problem, however, is that a thick molten layer is known to cause splashing and therefore will increase the particulate formation. A shorter wavelength, with a shorter penetration depth, does not provide a radiated target surface with enough bulk heating to reduce the cooling rate.

The use of molten target material to reduce splashing, believed to be responsible for the production of film particulate, has been studied.[186] This method, however, is limited to simple target material such as the Ge used in the experiment. Further evidence, however, suggests that the use of molten material, such as by direct laser heating, should be avoided since it will always produce more particulates.[145] In the case of laser

deposition of YBCO, the use of molten target material is impractical since the material is complex, containing four elements, and melts incongruently. As the result of melting, it is possible that the high vapor pressure element, such as barium, will be depleted in addition to the phase transformations that might occur.

A method was developed to heat the target surface to a temperature below the melting point during the evaporation using a short wavelength laser.[188] Although it may sound similar to the method previously described, which uses molten target to reduce splashing, the principle behind the heating is completely different. In this approach, the target will be heated at temperatures close to the melting point in order to avoid the surface crack formation. At an elevated temperature, the surface relaxation can still take place without significantly affecting the phase composition of a complex multicomponent system such as in the case of high-temperature superconducting oxides. It was found that heating of the target to temperatures above 600 °C helps to maintain a smooth target surface and to reduce the number of boulders. The details of the experiments and results are discussed below.

5.4.2 Experimental Procedure

In this experiment, the experimental condition was similar to the procedure described in Chapter 1, with the exception that the target was kept at high temperature instead of the normal room temperature. The laser deposition setup was modified by adding a target heater behind the target holder.

A high-density, superconducting pellet was mounted on a modified automobile cigarette lighter. The target temperature was controlled by adjusting the voltage supplied to the lighter to a Variac. In order to produce a target surface temperature around 800 °C, the voltage was set at 8 volts AC. The maximum surface temperature that can be achieved is only 900 °C, since the target melts beyond this point. The surface temperature was

measured using a small 0.05 in thermocouple wire attached to the target surface using a silver paste.

In the first set of experiments, the evaporation was done at three different spots on the target with evaporation area of 1400 μm x 1400 μm using a 248 nm laser beam. The pulse energy was 295 mJ/pulse at 10 pps, giving an effective fluence at the target of 1.2 J/cm^2. The first target area was evaporated for 10 minutes (or 6000 pulses). The second target area was also evaporated for 10 minutes, the last area for 1 minute. Three separate evaporation locations were selected in order to increase the evaporation efficiency and also to allow later SEM studies. Due to the difficulty in maintaining a good thermal contact between the target and the heating filament, the voltage to the target heater was periodically adjusted. A total of 12,000 pulses was delivered.

In the subsequent experiment, the laser fluence from a KrF laser was kept at 2.5 J/cm^2 using Powerlok™ at 470 mJ/pulse. A total of 12000 pulses, four sites of 3000 pulses each, at 10 pulses per second was utilized for each experiment. The evaporation size was 1200 μm x 1200 μm imaged from an aperture near the laser source. The pressure was kept at 100 mTorr in pure oxygen. The substrates were single crystal $LaAlO_3$, heated at 860 °C during the deposition, and kept 3 cm from the target. The target temperature was maintained at between 500 to 900 °C throughout the experiment. Above 500 °C temperature, the target glowed red. After the deposition, the substrates were annealed in 760 Torr oxygen at 400 °C for 30 minutes, followed by slow cooling to room temperature.

The deposited film was analyzed using SEM to determine the surface morphology and the particulate number density. The films were later analyzed for elemental composition by RBS and phase composition by XRD. The T_c of the films was analyzed using eddy current measurement.

5.4.3 Results and Discussion

Comparison between films deposited from a room temperature target and heated target showed that the film from the heated target contained smaller and fewer boulders. Boulders as large as 2 μm could be seen on films deposited using the nonheated target in addition to a rough background appearance. In comparison, films deposited from the heated target showed only submicron particles with a smoother background. Drastic morphological differences could be seen in the ablated target, as the nonheated target showed a frozen droplet surface, whereas the heated target showed a smooth surface.

The SEM analysis of the film from the first experiment showed that the film made using the heated target was very smooth with a minimal number of particulates, approximately $5x10^3$ to $6x10^3$ particulates/mm^2 (Figure 5-1). In comparison, deposition with the target at room temperature under similar conditions produced more particulates (Figure 5-2 and Table 5-1). Table 5-1 compares the number of film particulates from this experiment with the literature values.[151, 189, 190] The SEM analysis of the target showed that the target had melted, and the cone and melted-type morphology was observed (Figure 5-3). The cone shape, however, was very irregular and thin, compared to the previously observed cones on the room temperature target (see Chapter 6). Further evaluation of the film revealed that the film background contained small triangular particles, possibly from the crystal growth (Figure 5-4), while the particulates appeared to be spherical. RBS analysis of the film shows a composition that is close to the ideal stoichiometry, with Y, Ba, and Cu ratios of 0.95 ± 0.05, 2.00 ± 0.14, and 3.05 ± 0.13.

For the second set of experiments, a higher fluence was used. The result showed that, although the number of particulates on this film is higher than on the film made at low fluence, a drastic improvement can be seen between the film made using a heated target and using a target at room temperature (Figure 5-5 and 5-6). Not only did the film made with a heated target contain less particulates, it also had no very large and very small spherical

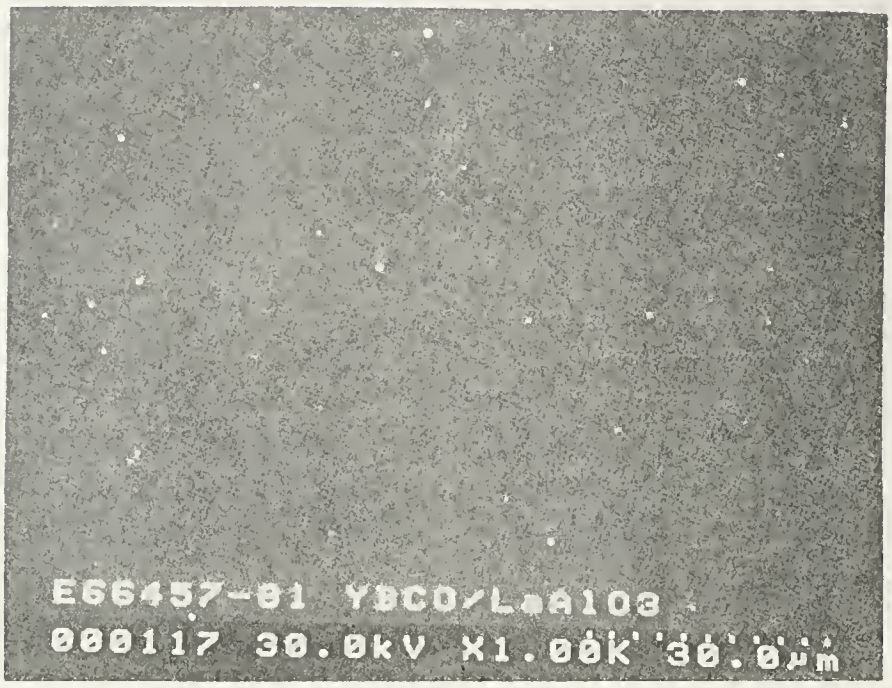

Figure 5-1 YBCO film on $LaAlO_3$ substrate produced by pulsed laser deposition. Target heatedto 700 °C.

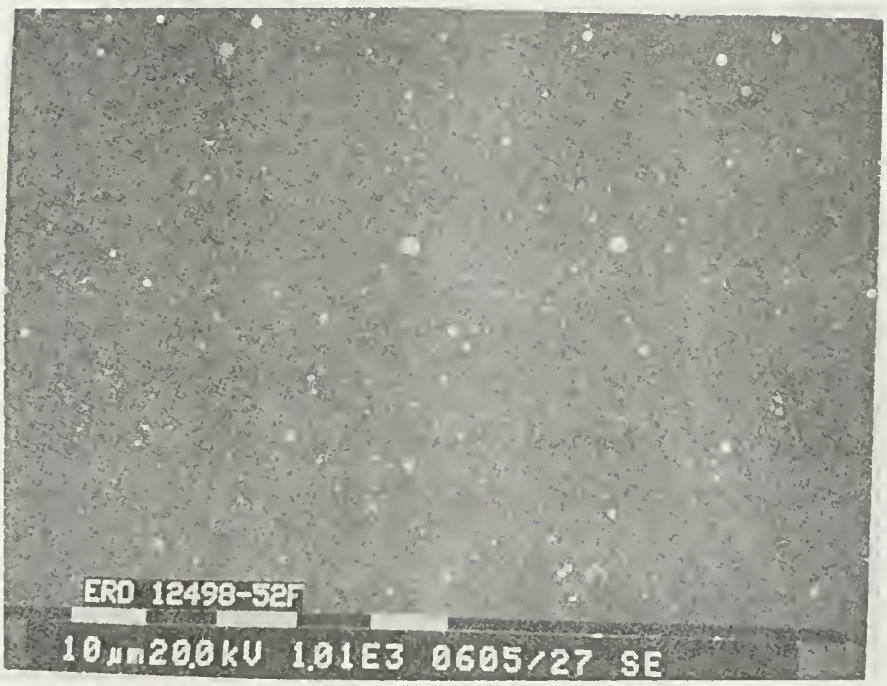

Figure 5-2 YBCO film on MgO substrate produced by pulsed laser deposition. Target at room temperature.

Table 5-1 Comparison of the number of particulates generated by laser deposition taken from this work and from literature.

Method	Particulate Number Density (particulate/mm^2)	Reference
Heated Target	$5x10^3$	this work
Normal Deposition	$2x10^5$	this work
Normal Deposition	$8x10^4$	151
Normal Deposition	$3x10^6$	189
Plasma Ring	$1x10^4$	190

Note: Films are approximately 200 nm thick.

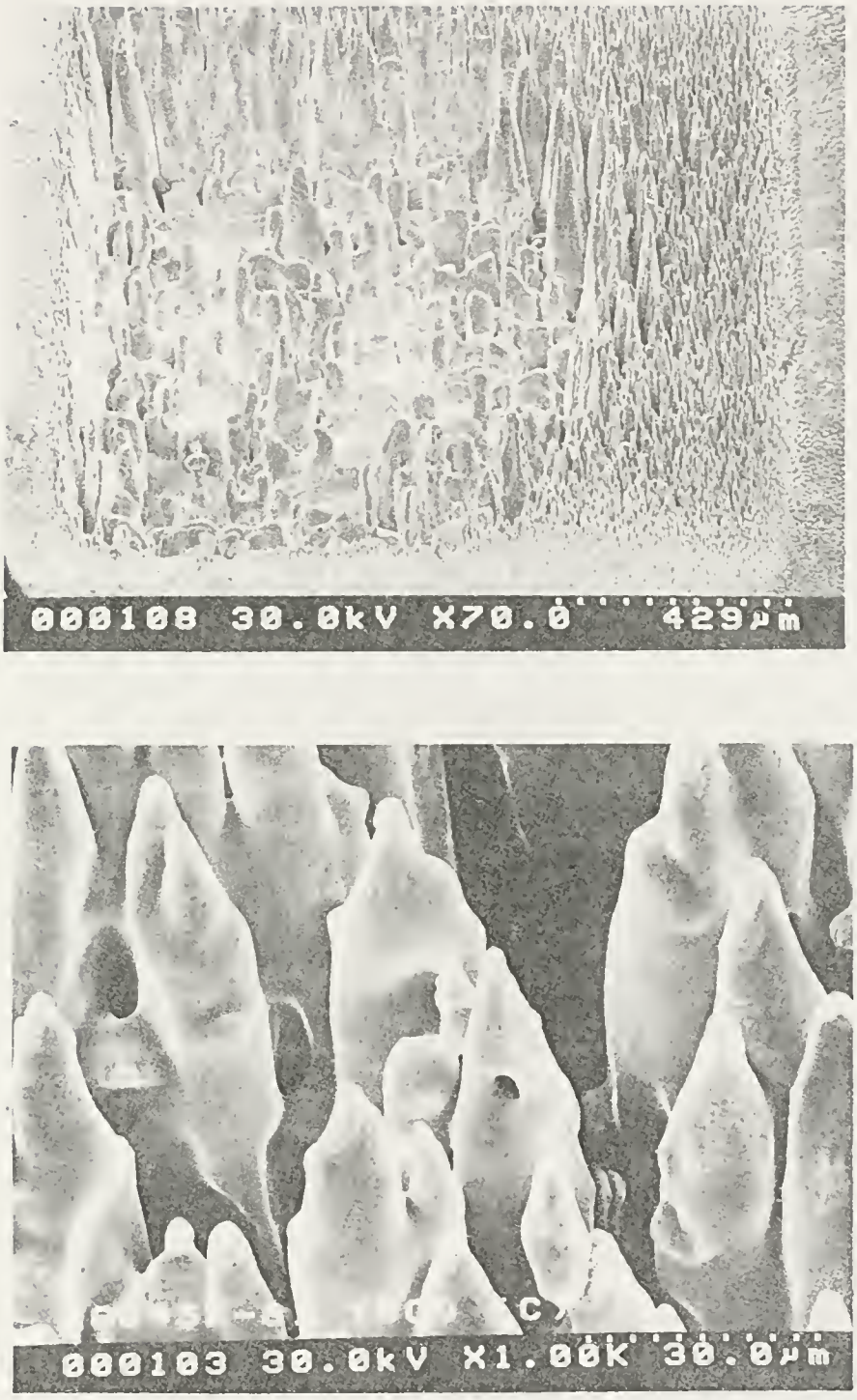

Figure 5-3 Surface morphology a heated target surface evaporated using KrF excimer laser at 1.2 J/cm^2. Magnification (a) 70 x, and (b) 1000 x.

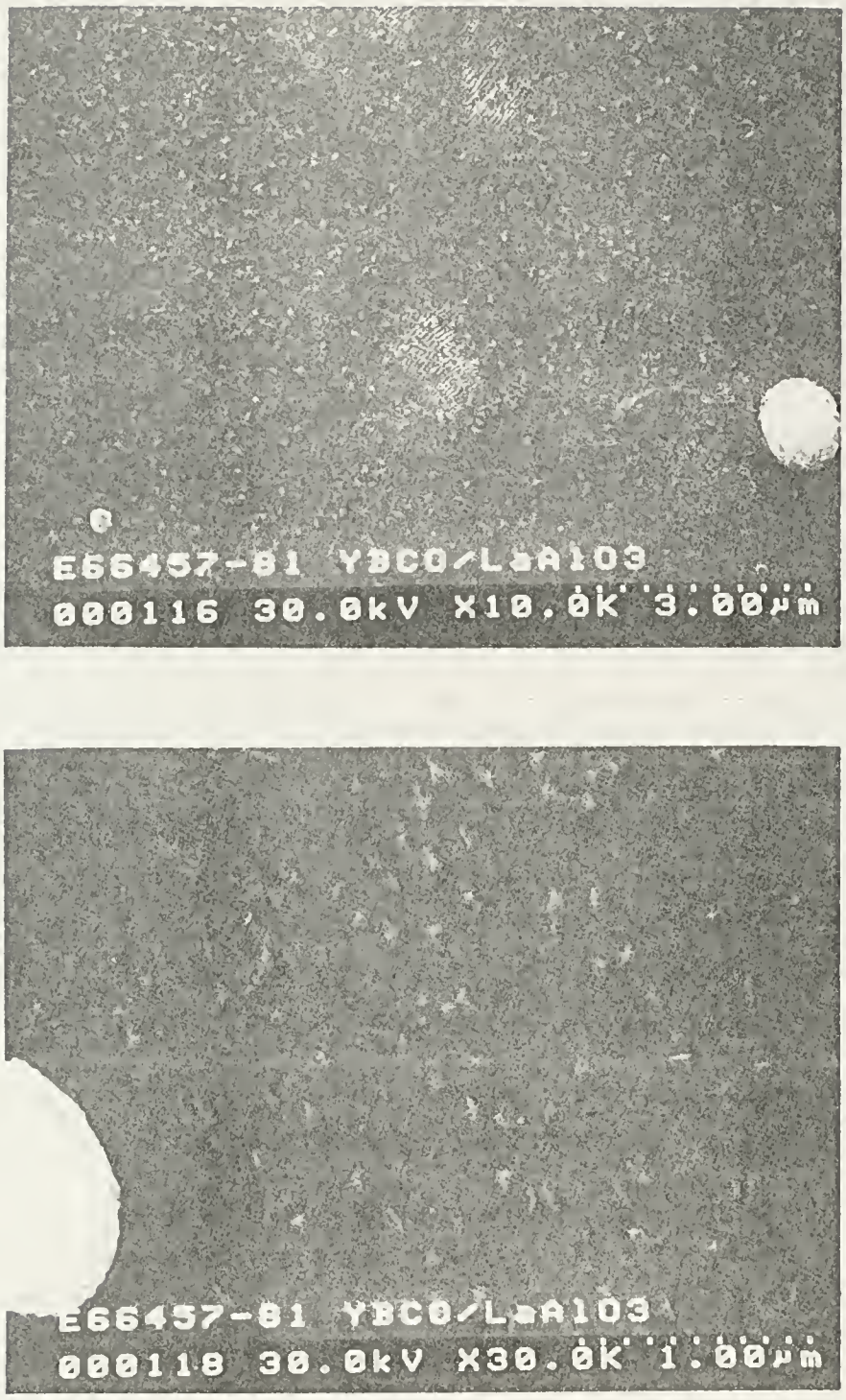

Figure 5-4 YBCO film on $LaAlO_3$ substrate produced by pulsed laser deposition. (a) 10000x magnification (b) 30000x magnification. Note the absence of large particles.

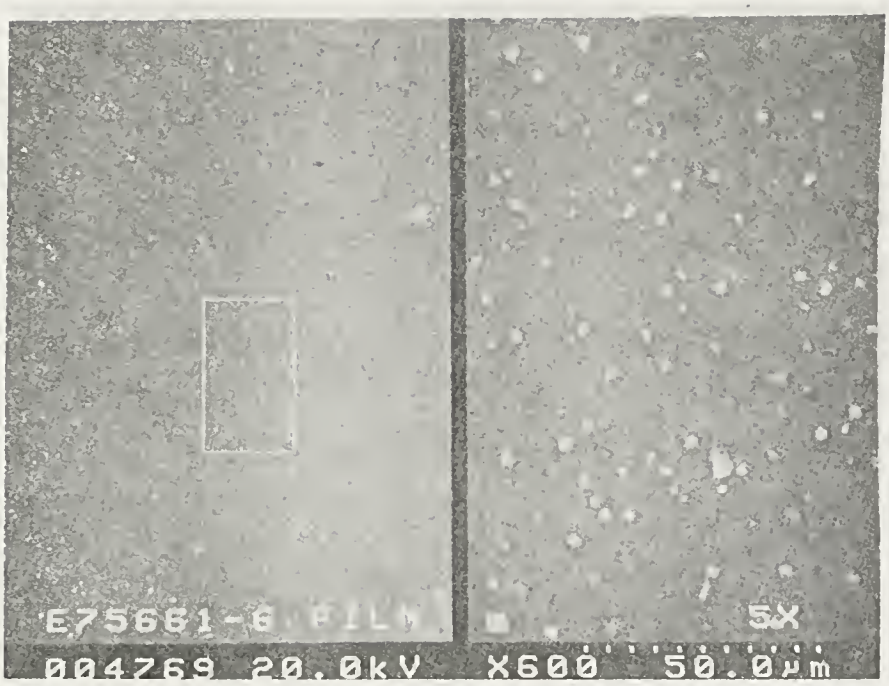

Figure 5-5 YBCO film on $LaAlO_3$ substrate produced by pulsed laser deposition using heated target at 700 °C. Note the absent of large spherical particles.

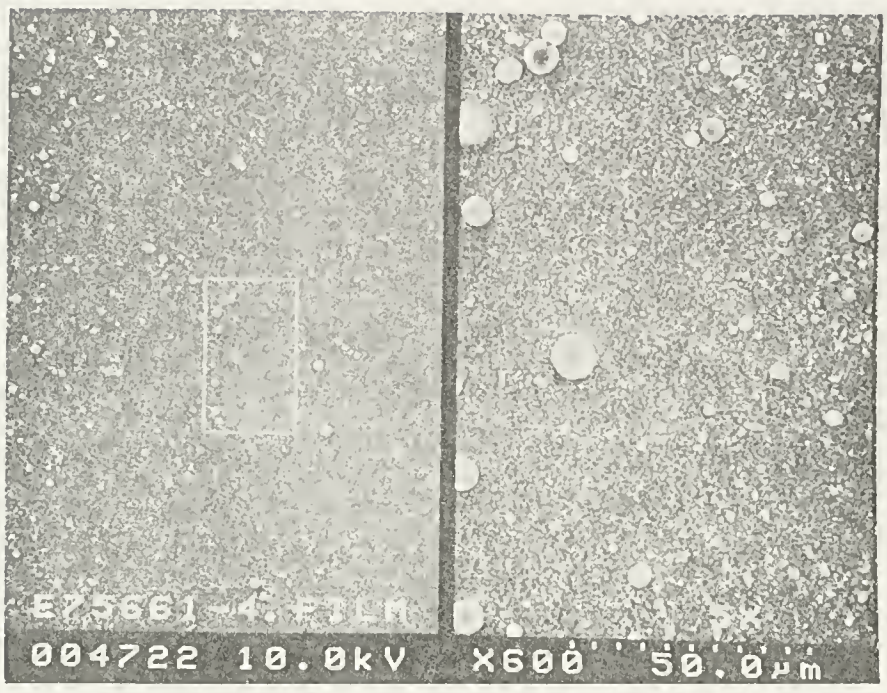

Figure 5-6 YBCO film on $LaAlO_3$ substrate produced by pulsed laser deposition using heated target at 25 °C. Note the present of large spherical particles.

particulates. Only irregular particulates, which existed on both the heated and nonheated target, could be seen. The micrograph of the target morphology for the heated (Figure 5-7) and the nonheated target (Figure 5-8) showed drastic differences. The heated target did not develop any surface morphology, while the target at room temperature developed a typical molten morphology. The 45 degree views of both heated and nonheated targets are presented in Figure 5-9. Although the target was heated close to its melting point, the target composition remained stoichiometric for its major elements. An XRD analysis of the targets showed that the heated target lost some of its oxygen and was converted from $YBa_2Cu_3O_7$ to $YBa_2Cu_3O_6$ (Figure 5-10). No other phases were present as the result of heating. This temperature condition is lower than the condition for target sintering, normally performed at 960 °C.[94] The RBS analysis of the film showed an atomic composition of the Y, Ba and Cu to be 0.92 ± 0.08, 2.00 ± 0.10, and 3.08 ± 0.11. The Tc values of the films were typically 88 K, with a transition width less than 5 K (Figure 5-11). The XRD analysis showed a c-axis film film formation (Figure 5-12).

Three possible mechanisms could be responsible for the reduction of particulates and the smoothing of the target surface. The first mechanism is the prevention of surface morphology formation by crack relief, as described in Chapter 6. The second possibility is that the heated target remains molten during the evaporation and relaxes after each pulse to form a smooth surface, whereas the nonheated target immediately solidifies. The third possibility is that the ejected particulates are hotter, and therefore they remain molten during the deposition and disappear on the film surface. Each of this mechanisms will be discussed.

5.4.3.1 Droplet temperature and liquid molten pool

For the third mechanism, using the heat transfer model for the cooling of a sphere,[104, 129, 172, 191, 192] the surface temperature of the particles prior to deposition on the substrate can be estimated. It is known that, in the evaporated plasma, the particulates have a lower velocity than the bulk of the plasma. In effect, during the expansion it appears as if

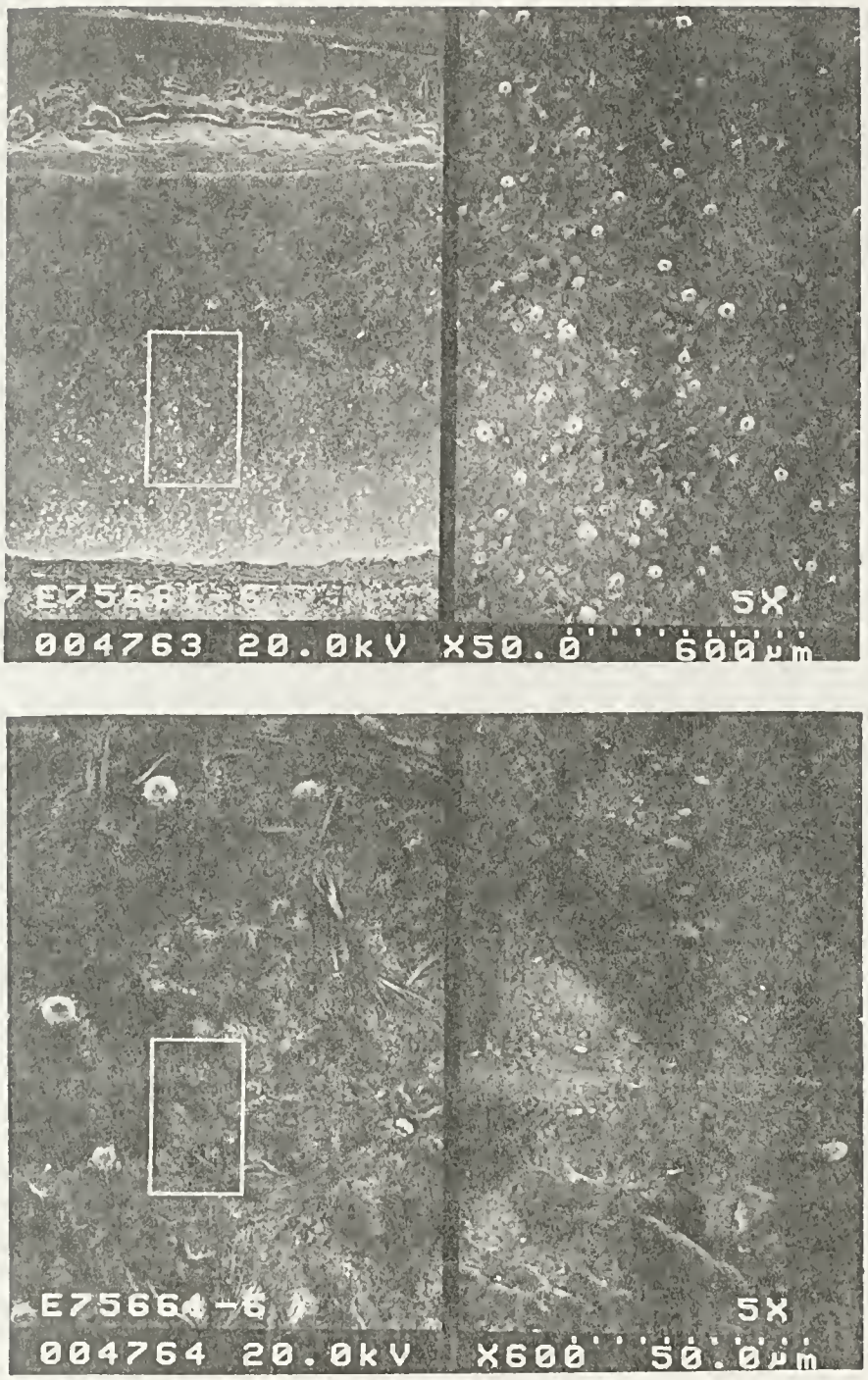

Figure 5-7 Surface morphology a heated target surface evaporated using KrF excimer laser at 2.5 J/cm^2. Number pulses: 3000. Atmosphere: 100 mtorr O_2. (a) magnification 50x and 250x , and (b) maginfication 600x and 3000x. Note the absence of surface morphology.

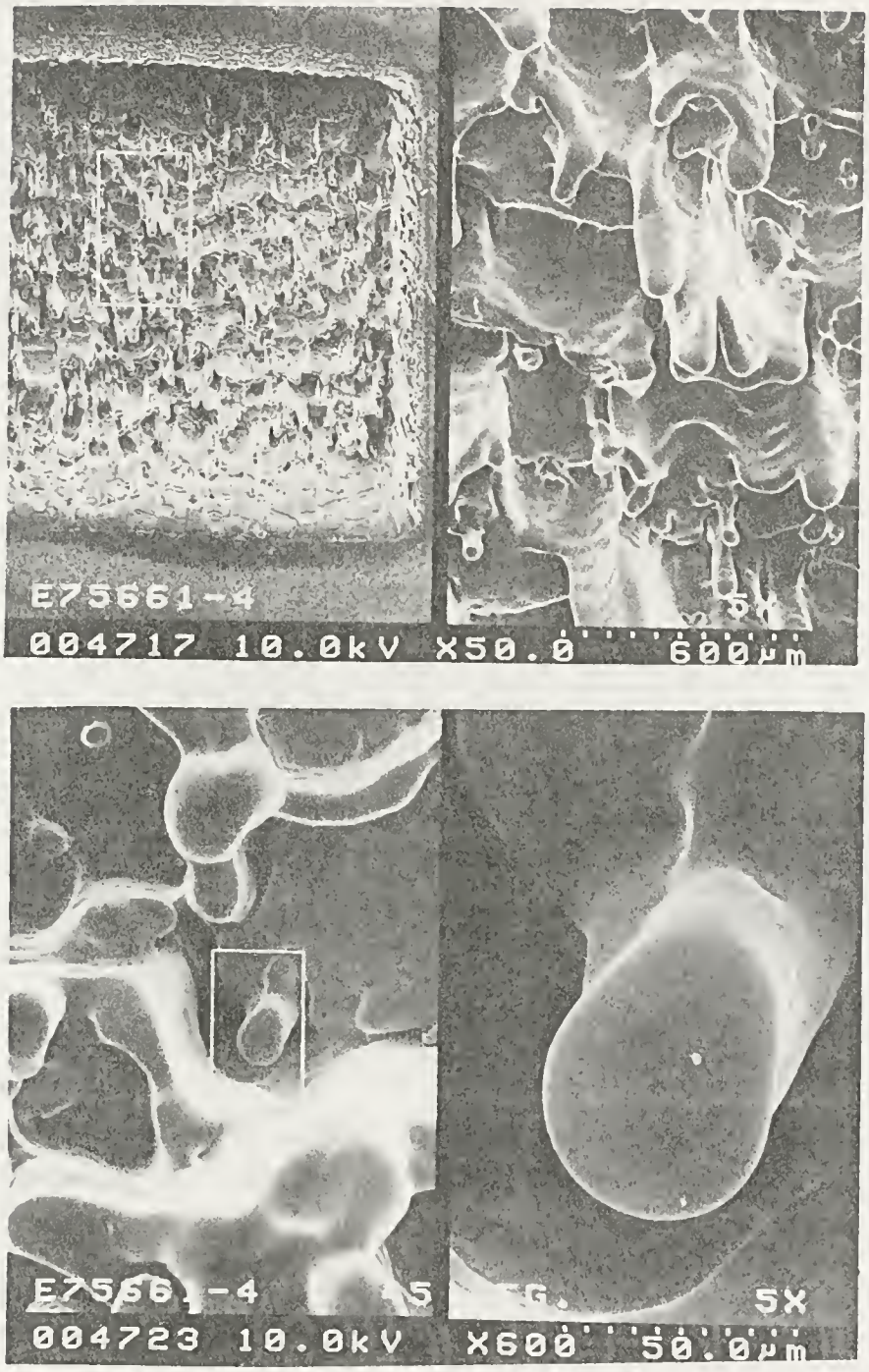

Figure 5-8 Surface morphology a target surface evaporated using KrF excimer laser at 2.5 J/cm^2. Number pulses: 3000. Atmosphere: 100 mtorr O_2. (a) magnification 50x and 250x , and (b) maginfication 600x and 3000x. Note the presence of surface morphology.

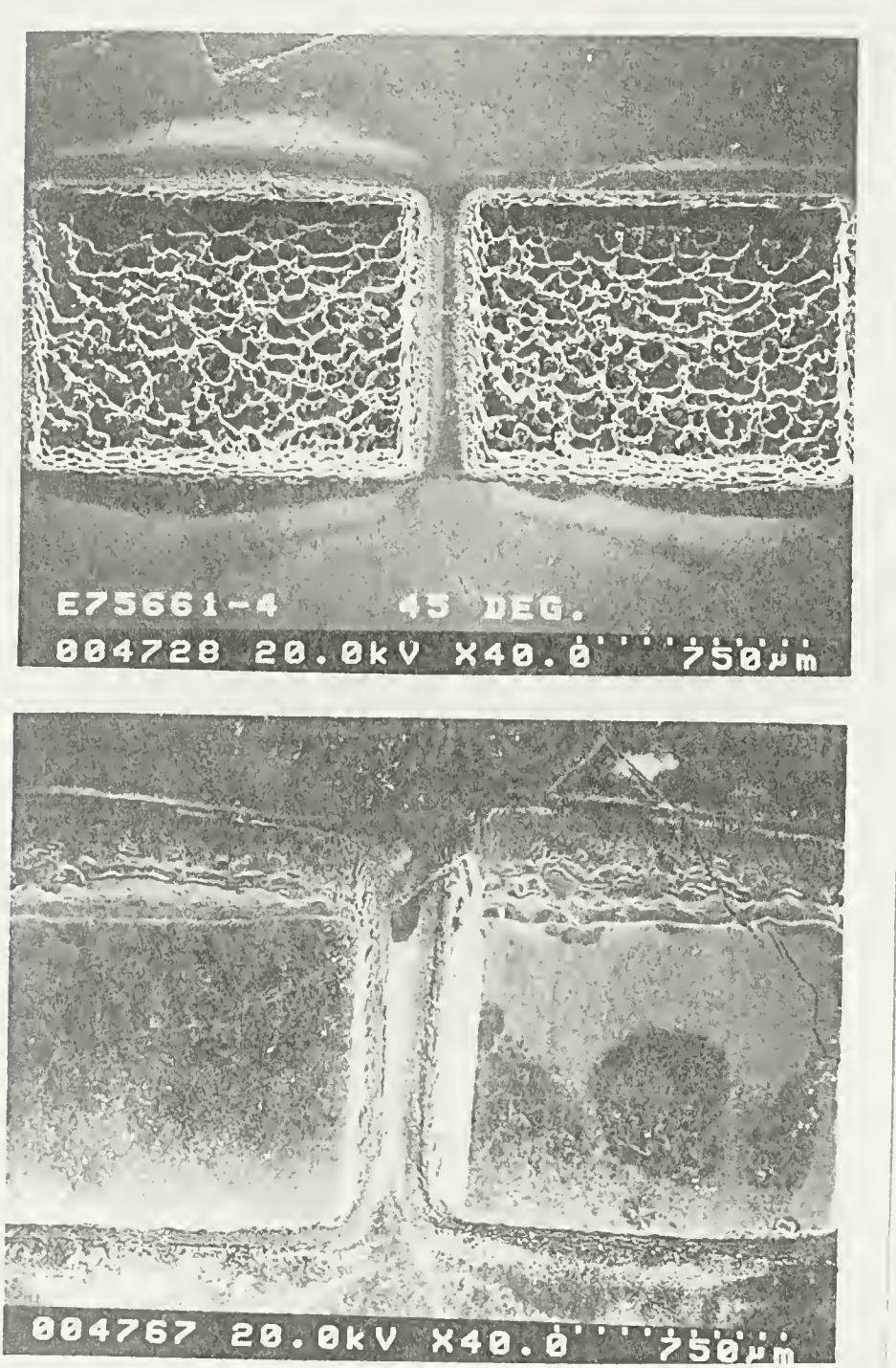

Figure 5-9 Surface morphology YBCO target surfaces evaporated using KrF excimer laser at 2.5 J/cm^2. Number pulses: 3000. Atmosphere: 100 mtorr O_2. Magnification: 40x. (a) target at 25 ^oC, and (b) target at 600 ^oC.

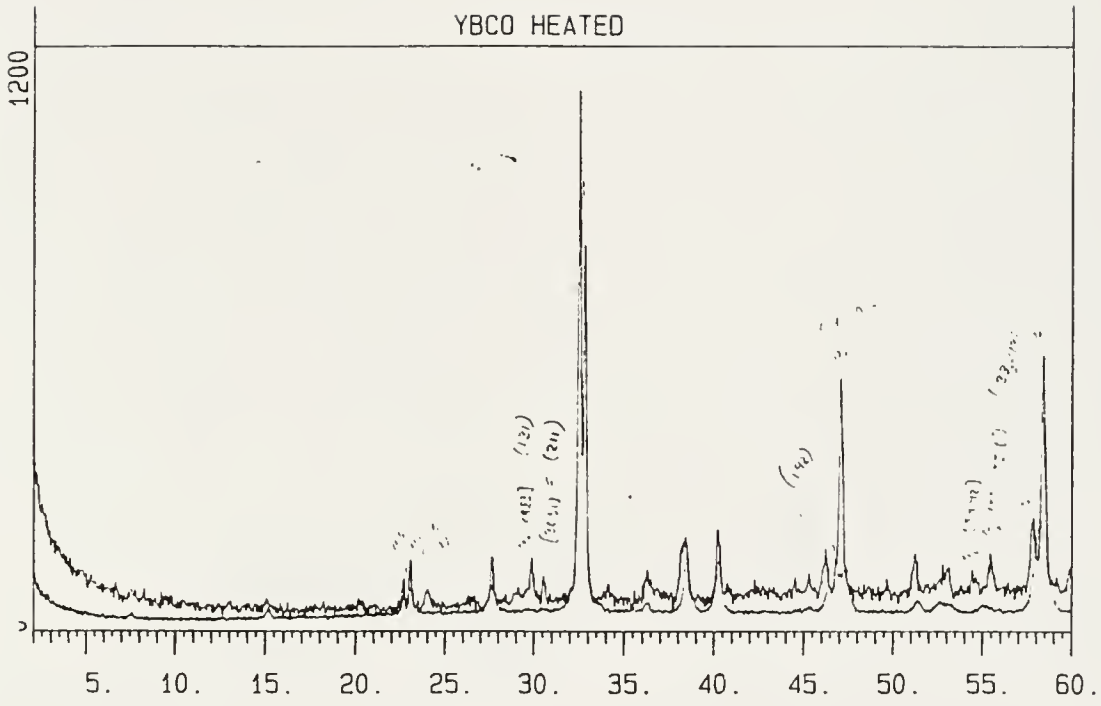

Figure 5-10 XRD YBCO target after heating at 600 °C for 2 hours. Loss of oxygen can be noticed.

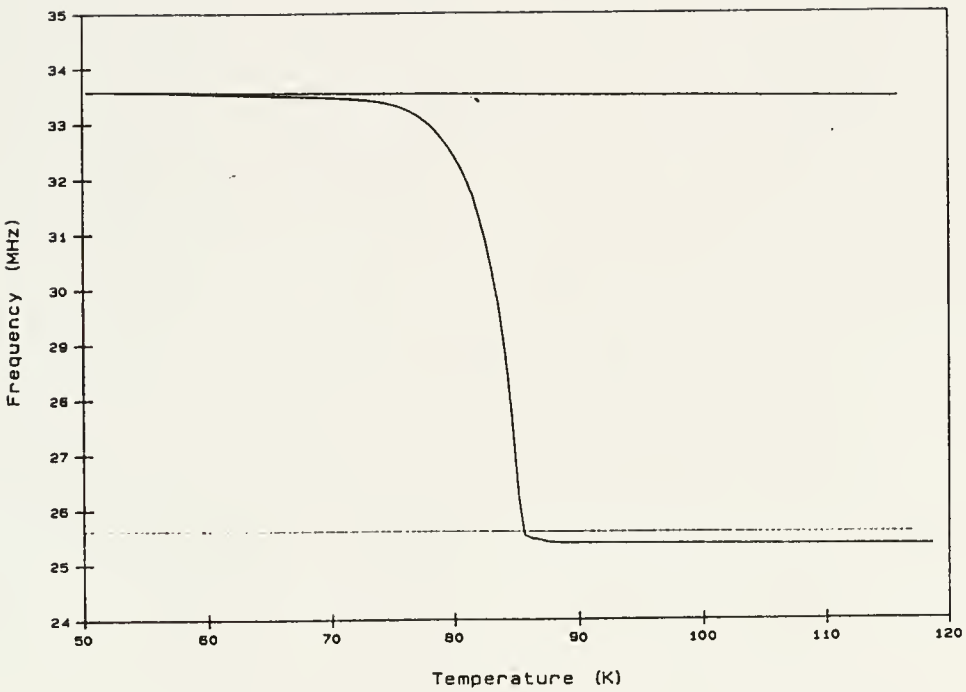

Figure 5-11 Typical temperature dependent surface resistivity.

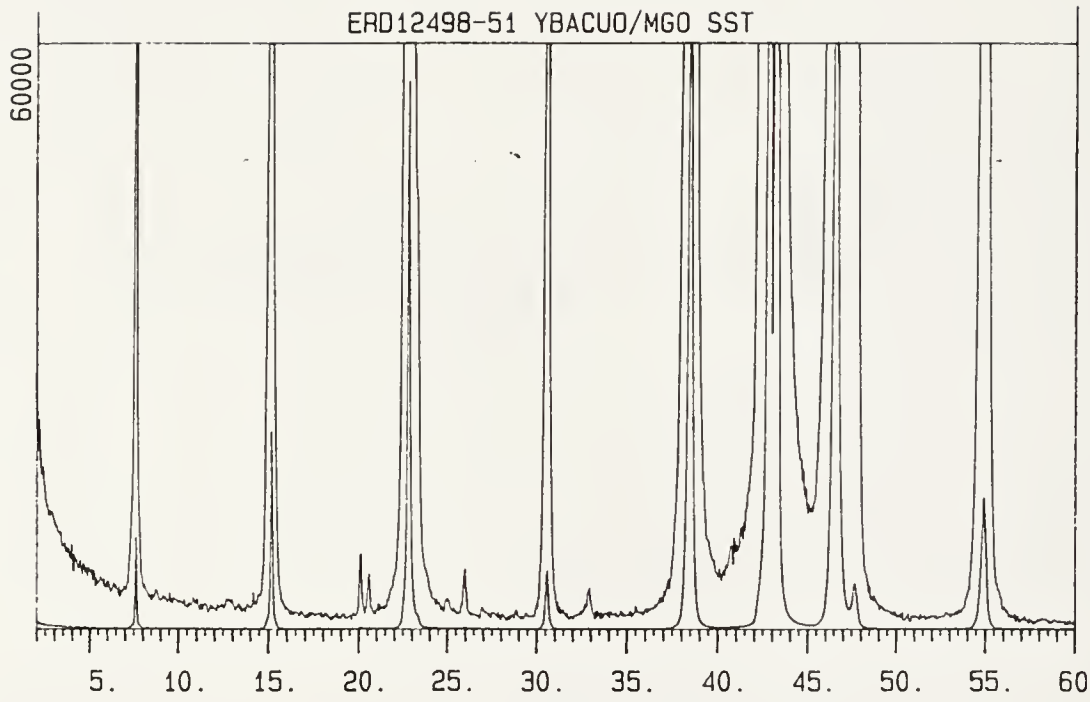

Figure 5-12 Typical XRD of laser deposited thin film on MgO substate, showing c-axis orientation.

the particulates are cooled by a forced convection. A previous calculation suggests that during an adiabatic expansion, the temperature of the plasma can drop to room temperature in a few microseconds. The maximum heat transfer coefficient of the spherical particulates can be calculated by assuming that the surrounding fluid flow is at room temperature. Using an equation for fluids flowing past a sphere, [193]

$$Nu = 2 + (0.4\ Re^{1/2} + 0.06\ Re^{2/3})\ Pr^{0.4}\ (\mu_\infty/\mu_w)^{1/4}s \qquad (5\text{-}1)$$

where Nu is the Nusselt number, hd/k, Re is the Reynolds number, $\rho vd/\mu$, Pr is the Prandtl number, $C\rho\mu/k$, h is heat transfer coefficient, μ is viscosity and d is the particulate diameter. Using the physical properties of the fluid at room temperature, [193] the values of Re, Nu, and h were calculated to be 0.006, 2, and 5.2×10^4 $W/m^2.{}^oC$ respectively. The minimum time required to cool a 1 μm particulate from the melting point to room temperature is therefore approximately 10 μs, longer than the time required for film deposition. It is possible that the temperature of the ejected particulate from a heated target is higher than the melting point during the droplet ejection, such as at 2000 ^oC, making it more likely that the droplet reached the substrate at a high temperature.

In comparison, in the cooling of a metal droplet, the typical cooling rate is about 10 ^oC/min, much slower than the time required to transport the droplet from the target to the substrate.[192] If the cooling rate of the YBCO is similar to that of metal, it may be suggested that in 5 μs, the temperature of the droplets drops by less than a degree, still in the order of melting point by the time the droplets reach the substrate. The calculation for a spherical powder melting in a plasma jet showed that the more alloyed particles have a higher rate of melting due to the higher melting path.[191] The heat transfer coefficient, h, for nickel particles reached a value of 3.5 cal/cm^2sec. If a more detailed analysis is required, a Biot modulus given by $Bi = hD_p/k_p$, where D_p and k_p are the diameter and thermal conductivity of the particles, respectively, could be used to test the condition of heat transfer. In a conduction-limited heat transfer, the Biot number has a value of 1.0.

The second possibility is likely, provided that a larger pool of molten layer is available. From the cross-sectional analysis, however, it can be seen that this layer is less than 0.2 μm thick. Although the result from the deposition of Ge seems to suggest that a liquid molten pool is desirable in the prevention of film particulate; [186] others suggest that the presence of a liquid molten pool, in fact, increases the formation of particulates.[145]

5.4.3.2 Surface morphology and droplet formations

The first possibility for the reduction of film particulates via target heating is associated with the formation of target morphology. As the target surface becomes rougher, more film particulates are formed. The initial formation of surface morphology itself, however, is related to the formation of surface cracking following rapid cooling after each laser pulse. By preventing the formation of this surface cracking, the evolution of target morphology, and therefore the formation of particulates, can be avoided. This concept is consistent with the absence of particulates observed on films made using a highly polished target.[53]

In the experiments using heated targets, the formation of surface cracks was eliminated. It was believed that if the cooling rate following each laser pulse is minimized that the surface has sufficient time to relax. The target heating can also be performed using other external radiation sources, for example, a CO_2 laser. Although it may be argued that, based on the premise that thermal heating of the target surface is desirable, longer wavelength alone may not work for the following reasons. First, the beam has to be energetic to vaporize the surface stoichiometrically. Various studies have shown that shortwave lasers produce better stoichiometric film. Second, a longer wavelength laser produces a higher penetration depth to give a thicker molten liquid pool during the evaporation. A high quantity of molten layer has a tendency to produce more molten droplets. A combination of a highly energetic excimer laser and external heat source, from either conduction heating or radiation, is desirable, since it produces both the residual target

temperature for slow cooling and highly energetic evaporation with a short penetration depth, which vaporizes the target stoichiometrically.

The effect of target temperature on the evolution of surface morphology was investigated. The results from a series of evaporations, at which the bulk temperature was varied to 25, 500, 600, 700, 800 and 900 °C, showed that the evolution of the surface morphology was surpressed when the target was heated above 600 °C. The target appeared smoothest when the target was heated to 900 °C. This surface smoothing may have been caused by the different cooling times at various target temperatures. At a temperature close to the melting temperature, the cooling rate is reduced, allowing sufficient time to reduce the surface stress and prevent the formation of cracks. The calculated relaxation time for this process at elevated temperature was on the order of microseconds, in contrast to the order of nanoseconds for the cooling with the target at room temperature. As previously indicated, the absence of cracks prevents the formation of the columnar structure.

5.4.3.3 Hydrodynamic sputtering and particle size

The formation of film particulates from the columns on a textured surface can be explained in terms of hydrodynamic sputtering. Hydrodynamic sputtering [44] refers to the process by which material is removed from a target as a consequence of transient melting due to photon pulses. This theory predicts the size of the particles as a function of thermal properties of the solid and liquid materials. A major condition for this model is that surface asperities, which produce surface temperture nonuniformities, must exist. These surface asperities may be caused by the nonuniformities in the solid phases, reflectivity, thermal properties, and surface defects. In a condition where the target surface is very flat, the target temperature will be heated uniformly and droplets will not form. On the other hand, if the target surface contains many pedestals or columns, it is likely that temperature nonuniformity exists and therefore more sites for particulate formation. Assuming that the surface contains surface asperities, there will be a temperature gradient on the surface. The

time scale of the laser exposure is so small that viscous dissipation can be ignored. The concept of detachment of the surface asperities as droplets requires that the momentum from the expanding solid due to thermal expansion is larger than the surface tension of the droplets,

$$4/3\ \pi\ r^3\ \rho\ (\Delta L/\Delta t)\ > 8\ \pi\ r\ \sigma\ \Delta t \qquad (5\text{-}2)$$

where $\Delta L = 2\ r\ \alpha\ \Delta T$ is the total height change of the droplet , r is the droplet radius, σ is the surface tension, α is the thermal expansion coefficient, ρ is the density, $\Delta T = T_m - T$, where T_m is the maximum surface temperature, T is the melt temperature, $\Delta t = \tau\ (1\text{-}T^2/T_m^2)$is the duration of surface melting, and τ is the laser pulse length. Rearranging the above equation yields

$$r = (3\sigma/\rho\alpha\Delta T\ \ \Delta t^2)^{1/3} \qquad (5\text{-}3)$$

Using a typical condition, where σ = 700 erg/cm^2 (for liquid oxides [194]) ρ = 6.3 g/cm^3, T_m = 3000 K, T = 1333 K, $\alpha = 11\text{x}10^{-6}$ K^{-1}, and t = $2\text{x}10^{-8}$ sec, the radius of the droplet was calculated to be 1.8 μm, in good agreement with the experimental value.

The relaxation during the pulses is important since it will determine whether surface morphology will develop. This phenomenon can be described in terms of Deborah number, which is the ratio of fluid response (or relaxation time) to process time.[195]

In addition to preventing the formation of cracks, target heating should also improves the etch-rate efficiency. First, if the target temperature is high, most of the photons are used in the material evaporation, instead of being used for target heating. Energy balance calculations for the evaporation at 2 J/cm^2 showed that 30 % of the photon energy is used in the conversion of solid phase at room temperature to vapor phase. Second, since the target remains smooth during the evaporation, photon loss due to surface reflection is minimized, resulting in higher photon efficiency. It is known that the etch rate for a smooth surface is higher than that for a rough surface.

5.5 Conclusion

The effect of target heating in the reduction of film particulates, especially the spherical particles, has been demonstrated. The best result was obtained when the target temperature was kept within 200 °C below the target melting point. The reduction of the number of particulates was improved by one or two orders of magnitude with target heating. The possible mechanism is that target heating allows the surface to relax following each laser evaporation pulse and therefore prevents the formation of target morphology.

CHAPTER 6
TARGET MORPHOLOGY OF YBCO SUPERCONDUCTOR

6.1 Review of Literature

In the deposition of thin film by PLD, the development of target surface morphology is undesirable because it affects the target evaporation efficiency and the deposited film quality. Fundamental understanding of the interaction between the target surface and the laser beam, leading to the formation of target surface morphology is therefore important to improve the performance of PLD.

6.1.1 Introduction

Energetic beams are commonly used to texture the surface of materials to improve bonding strength, radiative absorption, and heat transfer.[196] The development of surface morphology during laser irradiation of material has been observed on various materials including semiconductors,[197] polymers,[198] metals,[148, 199-201] ceramics,[202] and lately high-temperature superconductors.[53] The morphological developments of the laser-treated surface have been attributed to the optical and physical properties of the materials.[203]

During the pulsed laser deposition of thin films, however, surface texturing of the target material by the incident beam produces some undesirable effects due to the loss of deposition directional control and significant reduction in the etch rate. The development of surface morphology, most importantly, has been associated with the unwanted formation of film particulates.

Although the role of laser-target interaction is very important in the deposition process, especially to improve the evaporation efficiency and film quality, work in the area

of high-temperature superconductor is limited.[53, 54, 204-208] This chapter deals with the development of target morphologies and models that relate to this development for YBCO ablated with a KrF laser beam. For comparison, the developments of surface morphology for other systems such as ceramics, metals, and polymers were also studied.

6.1.2 Surface Modification

In general, surface modification can be understood in terms of sputtering and evaporation. The former involves direct kinetic energy transfer between the target surface and the impinging particles, such as in ion or electron bombardments. The surface morphological changes, in this case, depend on the sputtering yield as well as the angle of incidence. The latter is due to evaporation as the result of energy absorption, such as in a laser evaporation. This chapter will discuss only the laser-induced surface modification.

Unique microstructure developments during laser surface processing have been attributed to the optical properties and anisotropies of material,[203, 209] surface tension[200] and convective[199] forces on the molten film, and electric field interference.[202] Surface treatment using laser is unique because laser with different wavelength and intensity could be used to suit material need. Laser annealing on semiconductors showed that an amorphous film could be recrystallized at a high rate.[197] Excimer laser, in particular, is ideal because the high-energy, short laser pulse can rapidly melt metals, producing flat surface due to the high surface tension and low viscosity of molten metal.[201] In surface texturing, laser treatment has been used to increase the surface area for bonding and heat transfer.[196]

6.1.3 Target Morphology in YBCO

In the deposition of YBCO thin film by PLD, conditions affecting process efficiency and film quality have been linked to the interaction between the laser beam and the target. A subsurface explosion, loosely packed target, and the choice of laser

wavelength have been associated with film boulder formation.[41, 145, 151, 204] Target surface roughening correlates with the decrease in deposition efficiency[53, 208] and the shift of evaporation angle,[54] and laser fluence is known to affect the composition of the ablated target and the deposited film.[210]

The reduction in the evaporation efficiency is caused by the dilution of the laser energy over a larger surface area, giving a lower etch rate, or by the increase in the possibility that the plasma is redeposited on the target walls. The particulate formation is believed to have come from the fragmented target structure,[151] while the shift in the evaporation angle affects the quality of the deposited film because the optimum deposition rate and composition are at the center of the plume.[54]

Since target morphological development greatly affect the evaporation efficiency, it is important that this work is focused on laser target interaction. Fundamental work need to be done to address the formation of target surface morphology.

6.1.4 Statement of Purpose

Target morphology development needed to be studied to address the following issues: decrease in deposition rate, stoichiometry change, fundamental understanding of laser-target interactions, change in plume direction, and the increase in boulder formation. The present work concerns the development of target morphologies and their evaporation rates during evaporation of YBCO pellets with a KrF laser beam. The effects of fluence, repetition rate, pulse number, ambient pressure, and target density on the target morphology were studied in detail.

6.2 Target Morphology Studies of YBCO Systems

This section deals with the study of target surface morphology of YBCO superconductor evaporated using a KrF excimer laser. The experimental setup and the

effect of fluence, pulse number, phase impurities, repetition rate, geometry, background gas and target density are investigated.

6.2.1 Experimental Setup

Two different setups, a microfabrication workstation and a laser evaporation cell, were used to study the effect of fluence, pulse number, pulse repetition rate, and background pressure on the morphology and evaporation depth of superconducting YBCO pellets. The laser beam originated from a Questek model 2260 KrF excimer laser, at a wavelength of 248 nm, with a 17-ns pulse width. The targets used were both polished and nonpolished (Figure 6-1) and prepared using the procedure described at section 3.5.2.1

The laser beam at the microfabrication stage (Figure 6-2) was defined by an aperture and imaged through a 20-mm focal-length lens to give evaporation sizes of 100 x 100 μm, 200 x 200 μm and 400 x 400 μm. Fluence at the projection plane was typically varied from 0.1 to 2.0 J/cm^2 with attenuating filters. A 4-meter focal length convex lens was placed to minimize the beam divergence. The laser beam had a divergence of 2 and 3 milliradians at the vertical and horizontal axis. No beam homogenizer was used. For the high fluence studies, the aperture and the lens settings could be reconfigured to produce fluences as high as 30 J/cm^2. The fluence was calibrated using a Coherent light meter. The pulse number was varied from 1 to 2000 pulses at repetition rates of 1, 10, and 100 pps. Evaporation was done normal to the target in air at 760 Torr pressure. The target sample was placed on a Klinger translational stage, and the process was video-recorded for subsequent study.

The pressure inside the laser evaporation cell (Figure 1-1) was varied from 10^{-5} to 10^{-1} Torr in air or oxygen. The evaporation size was 1000 x 1000 μm, imaged from an aperture, focused with a 250-mm lens, and directed at 45 degrees to the target. The fluence at the evaporation plane was adjusted up to 3.7 J/cm^2.

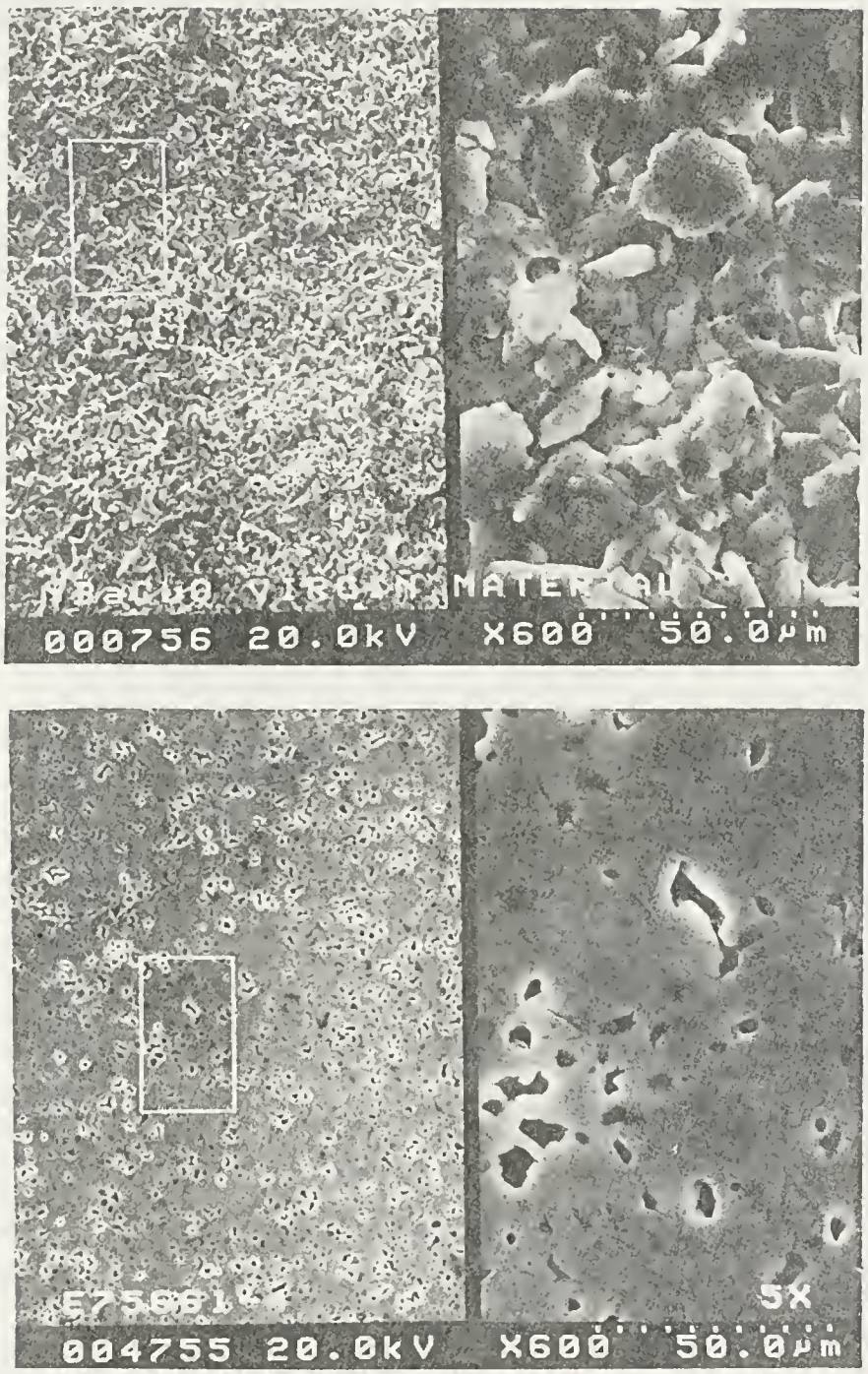

Figure 6-1 High density superconductor pellet target. (a) nonpolished surface, (b) polished surface.

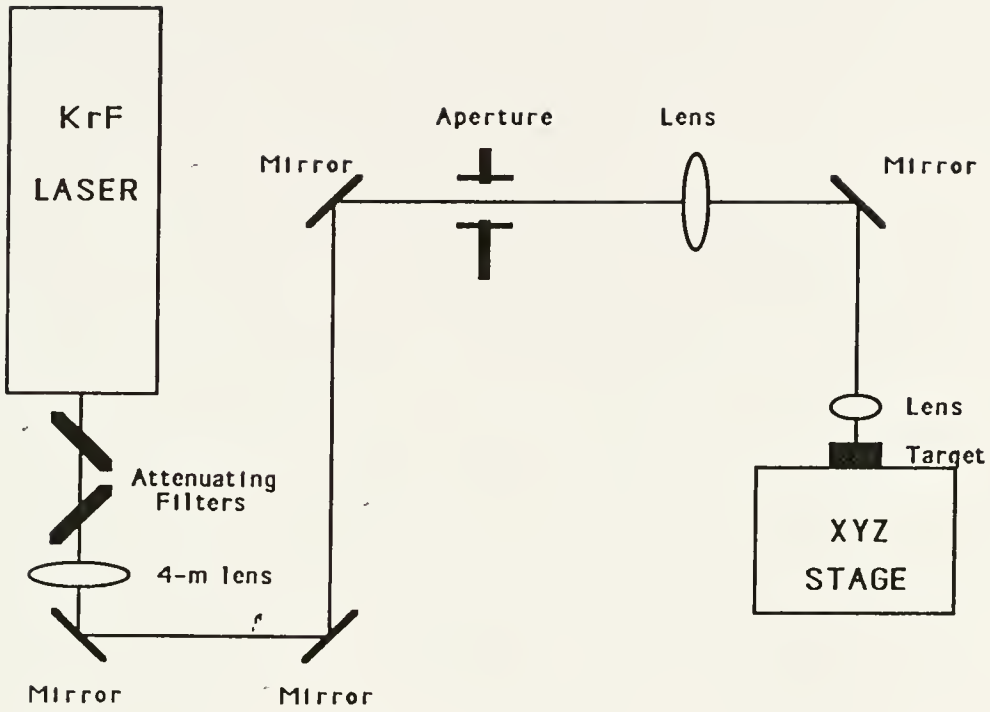

Figure 6-2 Schematic diagram of the microfabrication stage used in the evaporation YBCO target.

The resulting etch depths were measured with a Dektak 3030 surface profilometer and optical microscope. Evaporation depths at low fluence with cone and porous structures were measured with an optical microscope focused at the top and bottom of the evaporation area. The samples were analyzed by SEM, EDAX, EPMA and Auger spectroscopy. For the XRD analysis, the sample was prepared by scanning the beam to make a larger evaporated area on the target.

6.2.2 Effects of Laser Fluence

The morphology and composition of a YBCO superconducting target ablated with a KrF (248-nm) excimer laser were found to vary strongly with fluence and pulse number, and to a small degree with pulse repetition rate. Three different morphology types were identified: (1) a porous structure, created in evaporation at low fluence range, from 0.2 to 0.6 J/cm^2; (2) a cone structure at medium fluence range, between 0.6 and 1.1 J/cm^2; and (3) a melt structure at high fluence range, 1.1 J/cm^2 or higher. The transition stages between these structures were gradual, with each new structure evolving from the previous one. A comparison of the top and cross-sectional views of all three types is presented at Figure 6-3. The evolution of this morphology is described in Table 6-1. The etch depth per pulse increased asymtotically with increasing fluence; however, the etch depth per pulse decreased with increasing pulse number for the same fluence (Figure 6-4). Both the porous and cone morphology shared a similar characteristic in which an yttrium-rich phase was found on the top surfaces and shielded the underlying target surface from further radiation. The EDAX analysis of areas containing both peaks and valleys is presented in Figure 6-5. The overall composition at low fluence shows an increase in the yttrium concentration due to formation and growth of the yttrium-rich phase. Separate analysis of the peaks and valleys using Auger spectroscopy showed similar trends. Similar morphology was observed for both the high- and low-density targets, ablated at low and high background pressure. Microchemical analysis was used to determine the

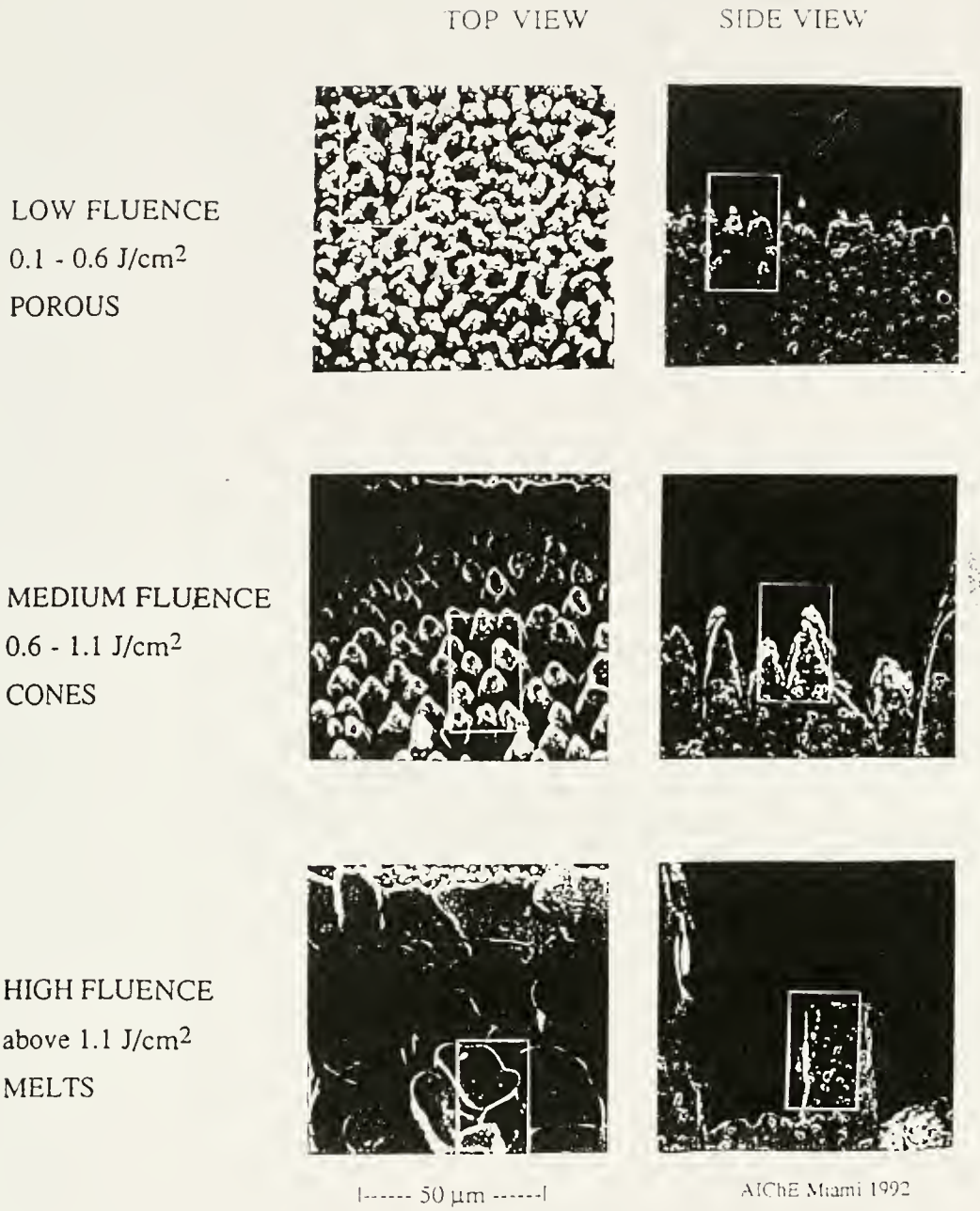

Figure 6-3 YBCO target evaporated at fluence (a) 0.1 to 0.6 J/cm^2, (b) 0.6 to 1.1 J/cm^2, and (c) above 1.1 J/cm^2. Corresponding to the formation of pores, cones and melts surface morphology.

Table 6-1 Morphology of YBCO target evaporated with a KrF laser at a fluence of 0.1 to 2.0 J/cm^2 for 2000 pulses in 1 atm air. Evaporation size of 100 x 100 μm.

Fluence	Structure	Observations
0.0	Crystalline	Sintered material with grain boundary of 1 x 3 μm
0.1	Crystalline	Grain edges melt, forming rough edges, but still no material removed
0.2	Porous	Begining of porous structure; grains melt and coalesce, forming a network typically 8–10 μm
0.4	Porous	Later stage of porous structure; well-defined (mazelike) network 4–5 μm wide and 15–20 μm long; top edge of maze is rough and irregular
0.5	Porous/cone	Begining of cone formation from the porous; starts to break off, forming individual cones typically 5–8 μm; cone tips are rough and irregular
0.6	Cone/porous	Cone shape more distinct,tips more pointed, base clearly visible; typical cone base is 5–8 μm; irregularly shaped material still seen at cone tips
0.8	Cone	Shape of cones clear, and each cone distinct, with 10–13-μm base; cone tips are smoother with typical size of 5 μm
0.9	Cone	Cones become fewer and increase in size; typical base 13–20 μm; irregular tips are more distinct
1.1	Cone	Last stage of cone formation; only a few left and size up to 40 μm at base; irregularly shaped 7-μm tips still visible
1.2	Melt	Beginning of melt structure; 2–18-μm droplets found at crater; surface is very smooth
1.3	Melt	Grain size at crater base increases typically to 10–30μm; surface very smooth
2.0	Melt	Grain size about 20–40 μm; smooth surface

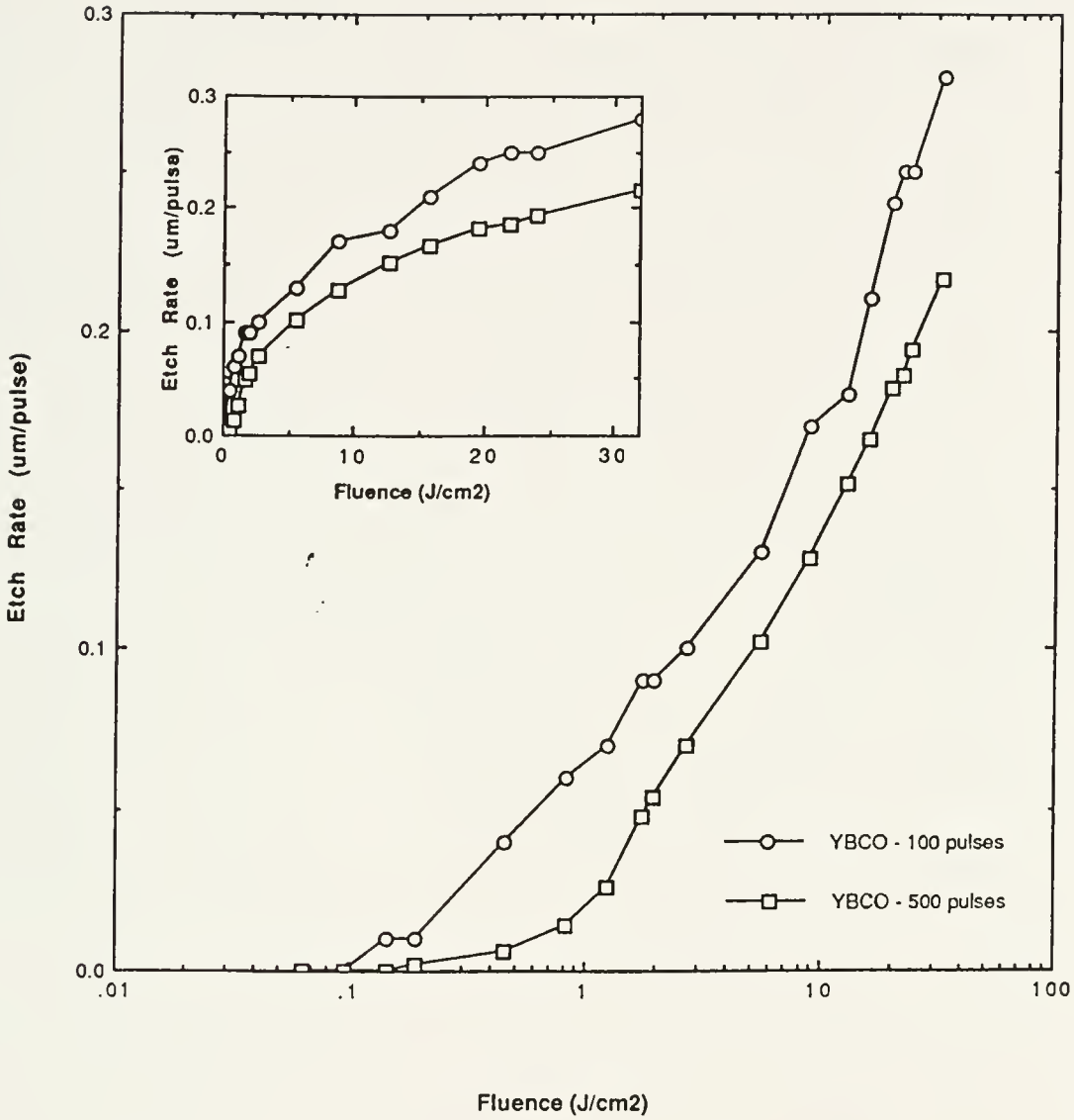

Figure 6-4 Etch rate YBCO as a function laser fluence. Inset graph is in linear scale.

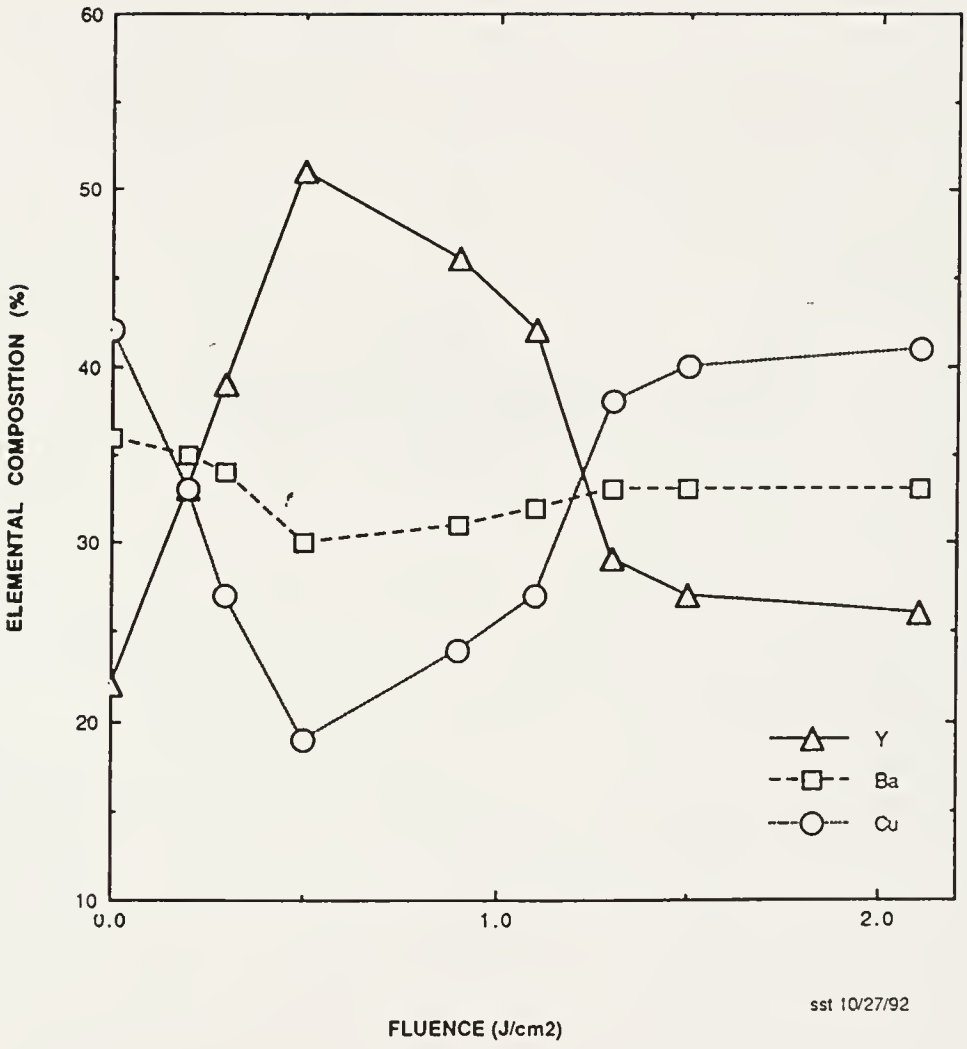

Figure 6-5 EDAX analysis YBCO target evaporated at fluence from 0.1 to 2.0 J/cm^2. The fraction of yttrium is high at fluence less than 1 J/cm^2.

compositions of the different morphologies observed on the target. The evaporation rate was also found to be strongly dependent on fluence.

6.2.2.1 Porous

Porous structures at fluences from 0.2 to 0.6 J/cm^2 were characterized by a network (or maze) morphology. Evaporation rates for this structure were low, with only surface texturing observed. A comparative development of the surface morphology at 50, 200, and 1000 pulses, together with the corresponding etch rate as a function of fluence is presented at Figure 6-6. Beyond 150 pulses, no more material removal was observed with a maximum measured depth was only about 12 μm. This structure appeared dark under visible light because of light trapped within the structure. The surface was found to be yttrium rich (stoichiometry of Y:Ba:Cu up to 10:1:1), as determined by EDAX, XRD, and Auger spectroscopy.

The porous surface morphology depends on fluence and pulse number. The threshold fluence was found to be 0.10 J/cm^2, below which no evaporation took place. A threshold of 11 mJ/cm^2 has been reported for thin-film evaporation.[43] Surface texturing of the porous structure was observed at 0.2 J/cm^2 from 2 to 2000 pulses, but without significant evaporation. At higher fluence, at 0.4 to 0.6 J/cm^2, surface melting was observed at the initial stage of evaporation. This surface was smooth and reflective under visible light with pulse numbers up to 10 pulses. At 50 pulses, the morphology began to change. Semidroplet structures, 5 μm in diameter, began to emerge from the smooth surface (Figure 6-7). Successive evaporations formed taller, densely packed, interconnecting semidroplets at 200 pulses (Figure 6-8), until clusters of irregular 5- to 6-μm particles appeared at the ridge of the structure at 500 pulses (Figure 6-9). These irregular particles acted as a bridge, joining the droplets and forming a mazelike or porous structure. Material removal at this fluence range was minimal, and plume production was not observed after 50 to 150 pulses. At 1000 pulses, the surface structure was practically unchanged (Figure 6-10).

50 PULSES

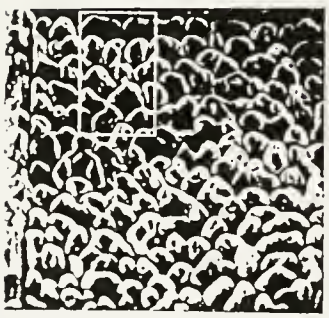

200 PULSES

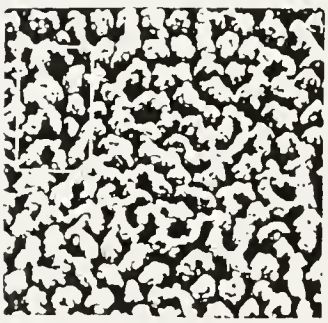

1000 PULSES

|------ 50 μm ------|

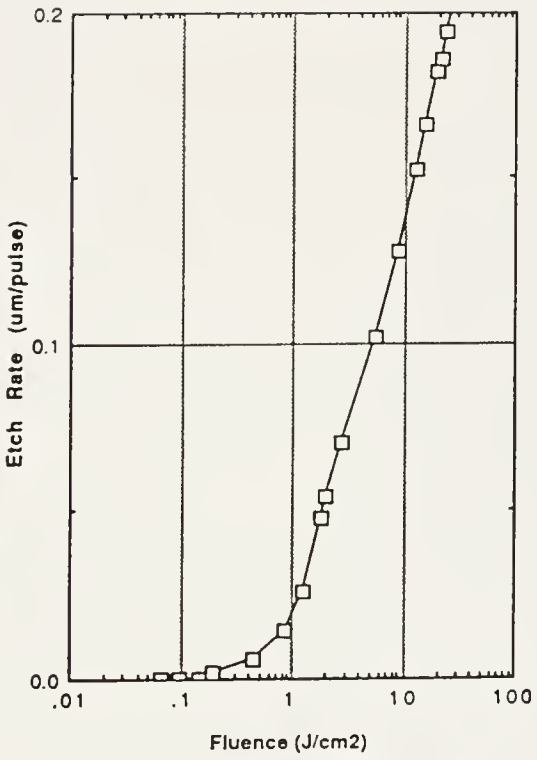

1000 PULSES

|------ 10 μm ------|

Figure 6-6 YBCO target evaporated using KrF laser at fluence between 0.1 to 0.6 J/cm^2. Formation of pores surface morphology. Atmosphere: air. Pulse number (a) 50 pulses; (b) 200 pulses; (c) 1000pulses.

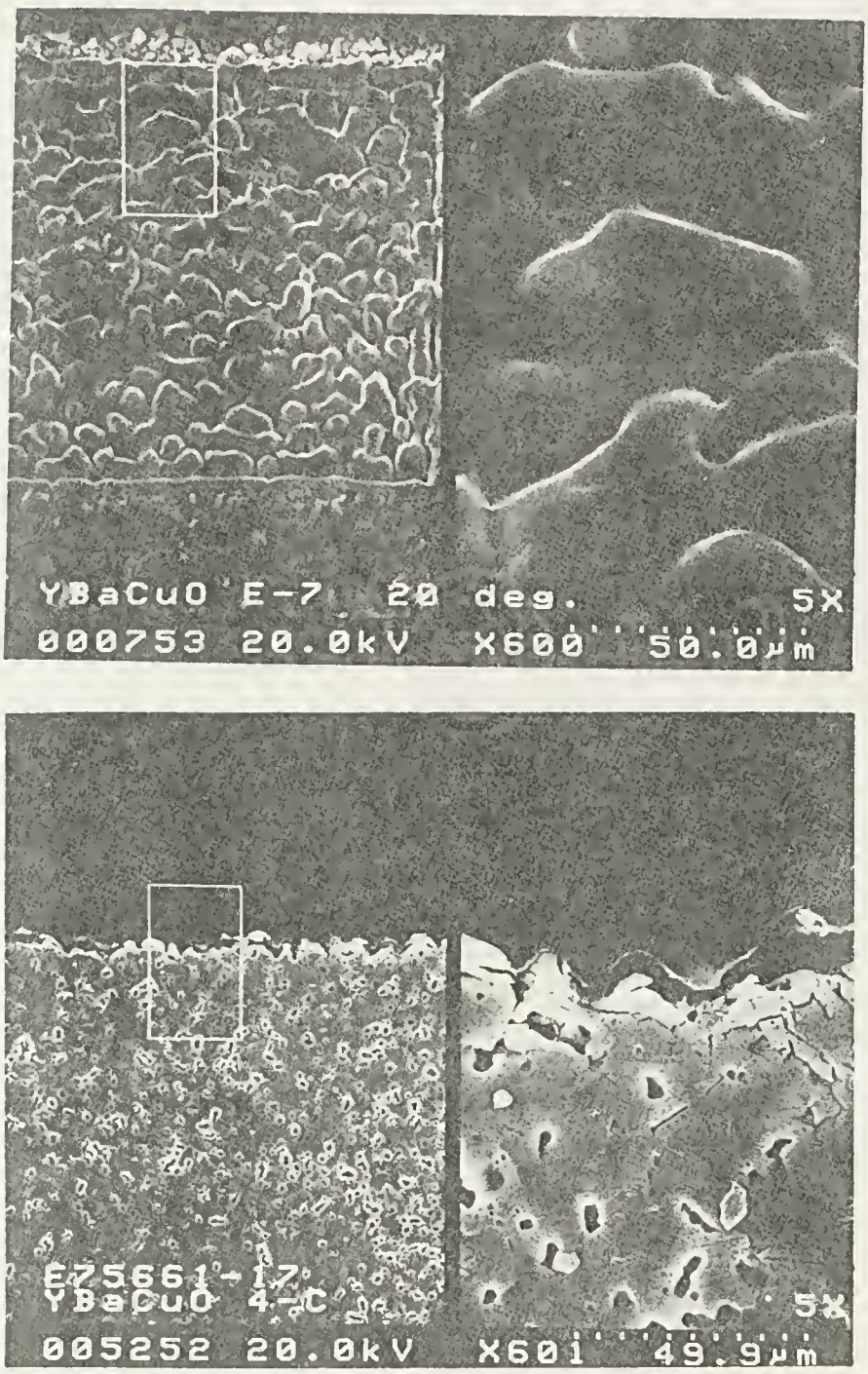

Figure 6-7 YBCO target evaporated using KrF laser. Atmosphere: air. Pulse number: 50 pulses. Fluence: 0.6 J/cm^2. Repetition rate: 10 pps. (a) top view; (b) cross-sectional view.

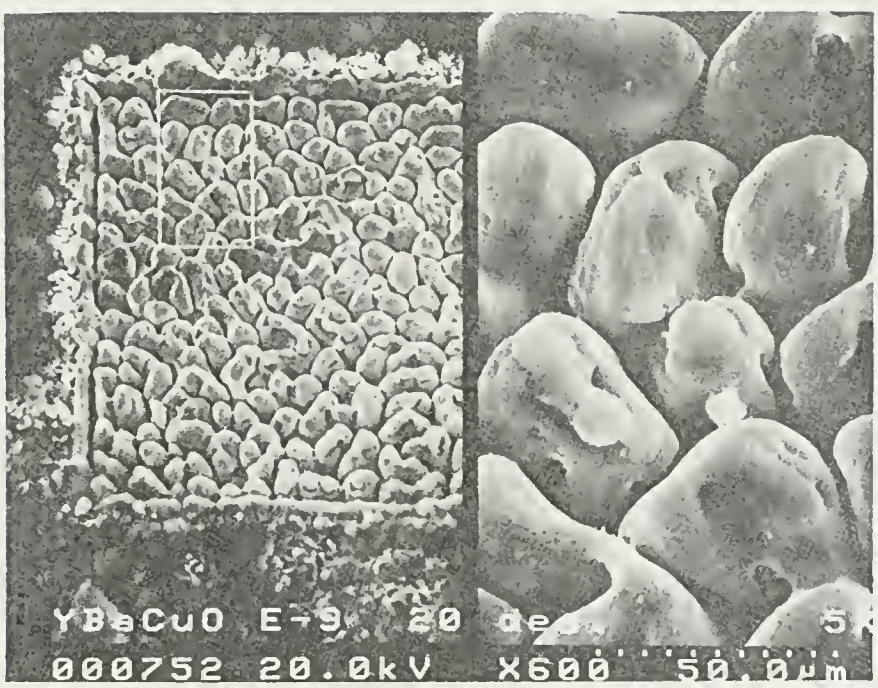

Figure 6-8 YBCO target evaporated using KrF laser. Atmosphere: air. Pulse number: 200 pulses. Fluence: 0.6 J/cm^2. Repetition rate: 10 pps. Top view.

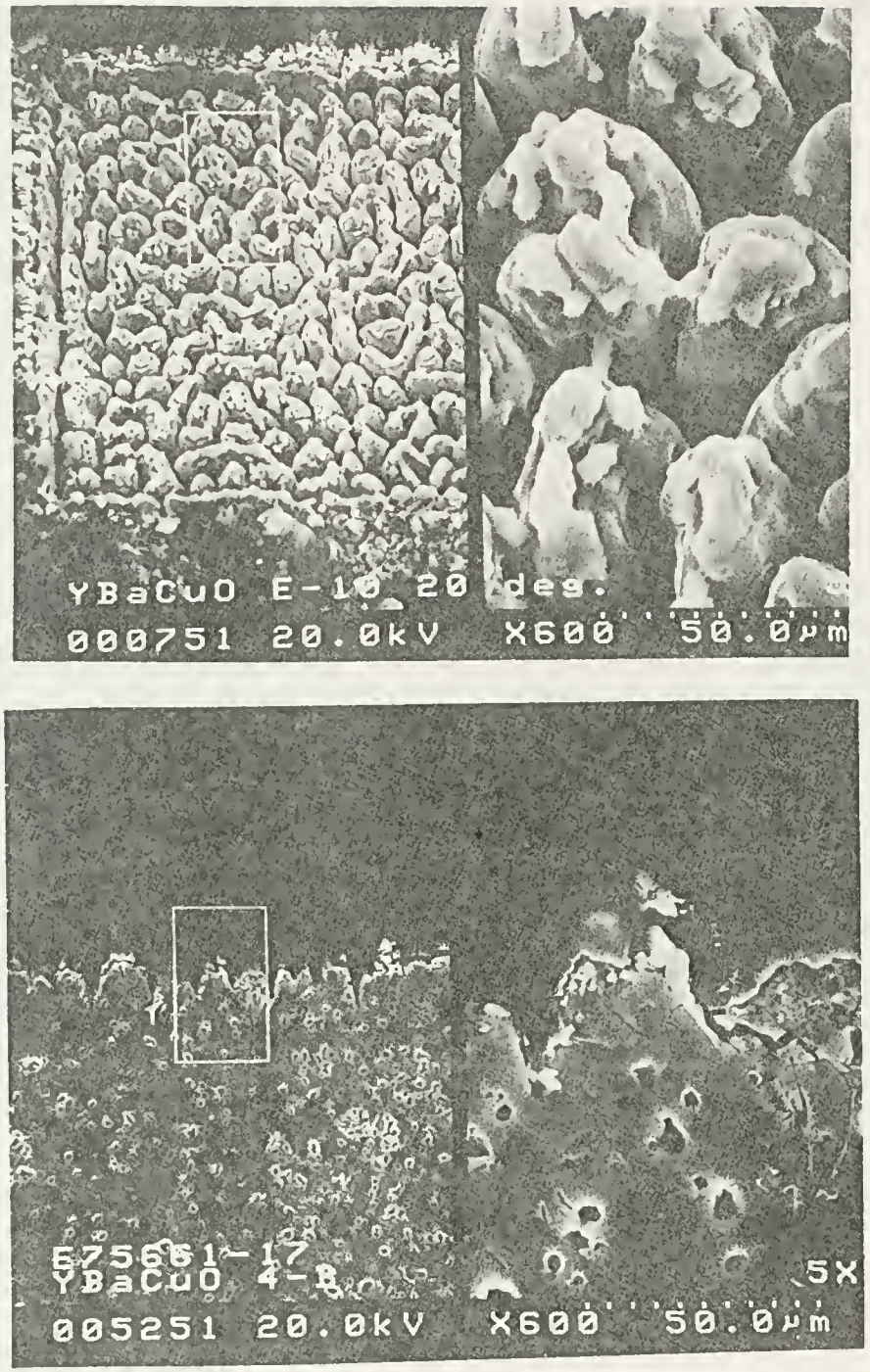

Figure 6-9 YBCO target evaporated using KrF laser. Atmosphere: air. Pulse number: 500 pulses. Fluence: 0.6 J/cm^2. Repetition rate: 10 pps. (a) top view; (b) cross-sectional view.

Figure 6-10 YBCO target evaporated using KrF laser. Atmosphere: air. Pulse number: 1000 pulses. Fluence: 0.6 J/cm^2. Repetition rate: 10 pps. (a) top view; (b) cross-sectional view.

The porous structure evolved from the formation of yttrium-rich phase particles, which probably shield the underlying material from incoming radiation. A pictorial representation of this process is presented at Figure 6-11. It is believed that these yttrium-rich phases have higher melting points and possibly higher evaporation thresholds than the bulk YBCO target, since they are stable even after 2000 pulses. The elemental ratio Y:Ba:Cu of 3:1:1 was determined using EDAX. These yttrium-rich particles were later determined to be Y_2O_3. The XRD analysis of the target surface is presented at Figure 6-12. The presence of Ba_2CO_3 could be attributed to the reaction with CO_2 during sample transfer. Solid phases of Y_2BaCuO_5 and Y_2O_3 were known to form as the product of $YBa_2Cu_3O_7$ quenching beyond the eutectic temperature of 900 ^oC,[84, 211] as shown in the phase diagram at Figure 6-13.[84] The etch rate of the Y_2BaCuO_5 phase was indeed much lower than that of the $YBa_2Cu_3O_7$ phase and the evaporation of this phase, in turn, yielded a Y_2O_3 phase. A detailed study of the evaporation of the Y_2BaCuO_5 phase is presented at Section 6.2.3.

The formation of the Y_2BaCuO_5 phase is possible because of the rapid heating and cooling associated with laser evaporation. Pulsed laser treatment is capable of rapidly heating and melting the surface of a target followed by rapid cooling and solidification at a rate of thousands of degrees per second. As a consequence, metastable phases are usually trapped or quenched-in. During the evaporation of a YBaCuO superconductor, a liquid phase is formed.[211] During the cooling, metastable phases, such as Y_2BaCuO_5, are likely to form.

Evidence from the SEM indicates that particle size increases with increasing pulse number, suggesting a crystal growth mechanism. The shape and number of these yttrium-rich particles depend strongly on fluence, and therefore surface temperature. At lower fluence, 0.2 J/cm^2 to 0.5 J/cm^2, the maximum surface temperature is sufficient to allow yttrium-rich particle formation and vaporization of the target surface, but not evaporation of the molten surface. Time-resolved optical measurements showed that, at 0.14 J/cm^2, the

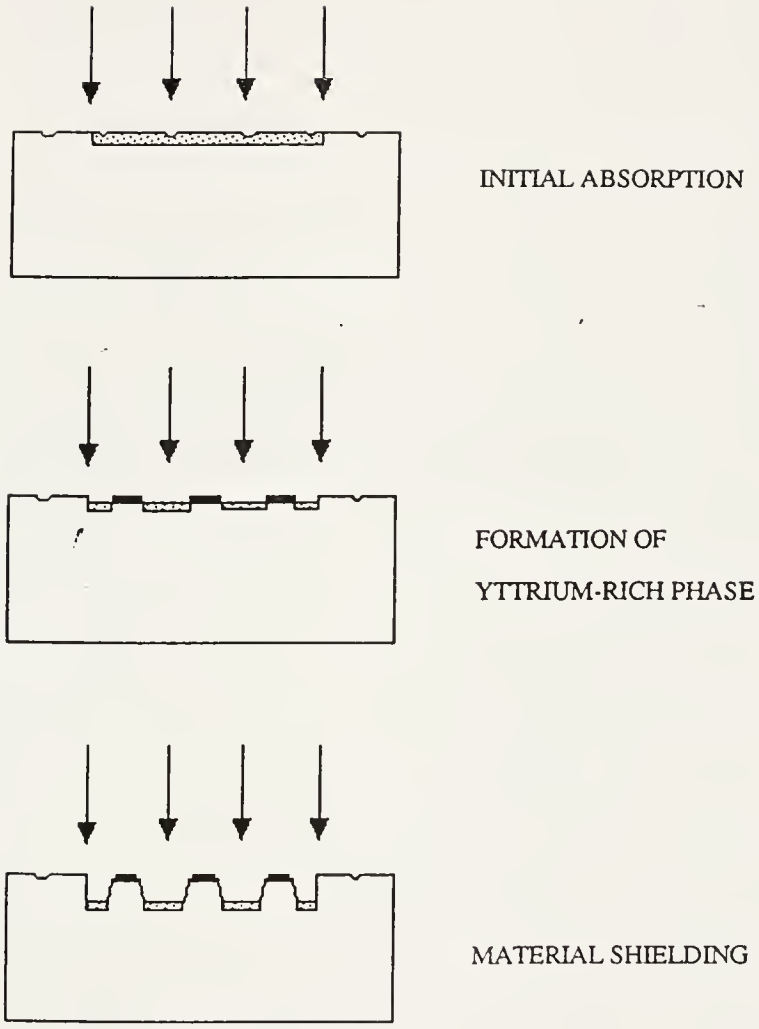

Figure 6-11 Cartoon for the evolution surface shielding due to formation yttrium rich phase. (a) initial absorption; (b) formation of yttrium-rich phase; (c) material shielding.

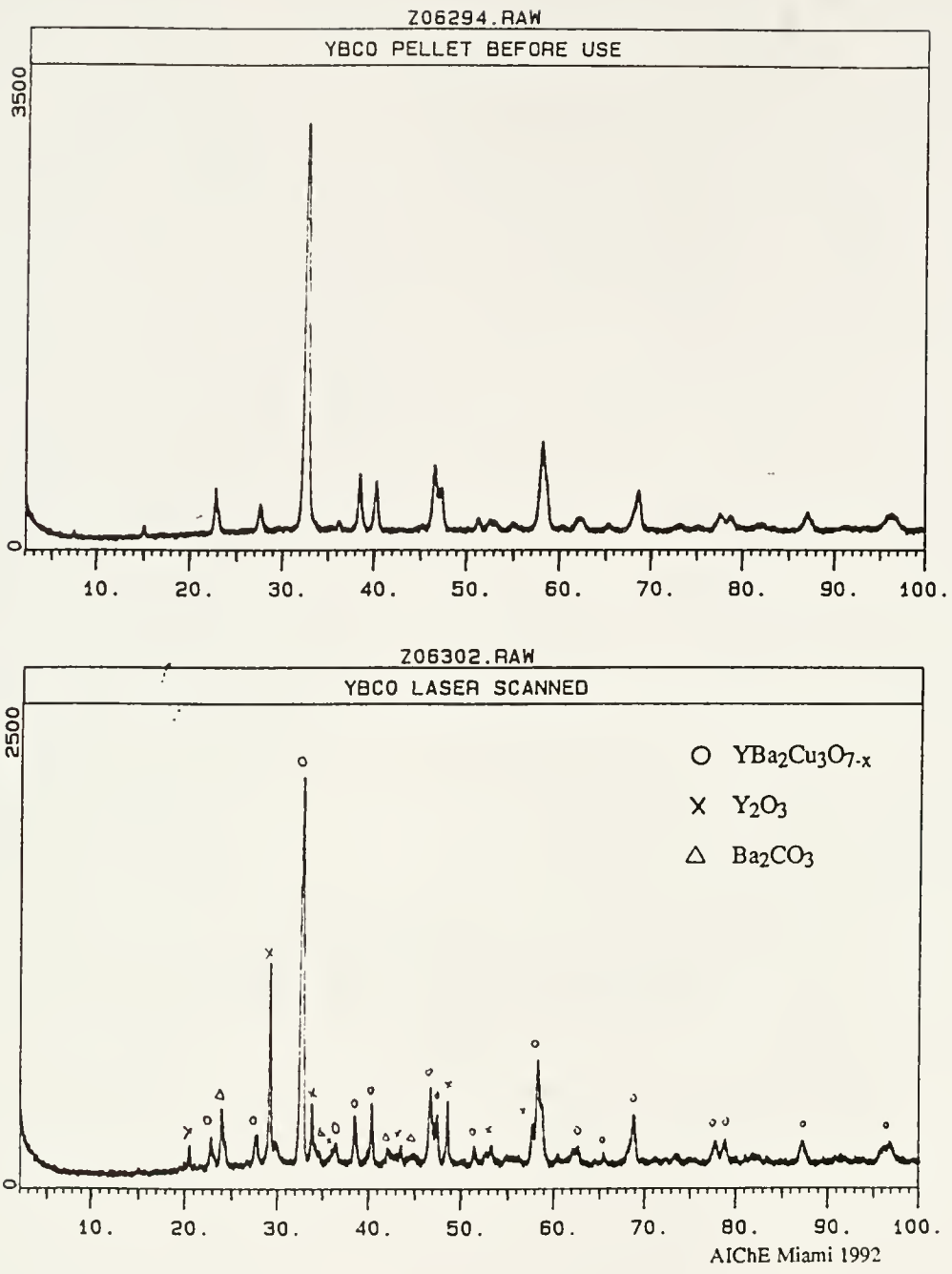

Figure 6-12 XRD YBCO (a) virgin material, (b) laser scanned at low fluence. Note the presence of Y_2O_3 phase.

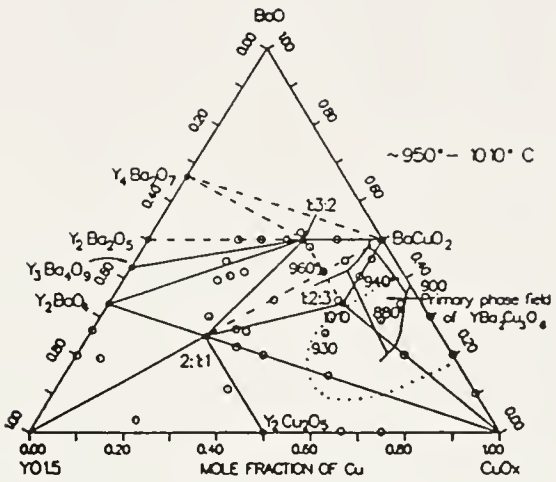

Fig. 7. Experimental phase diagram of $YO_{1.5}$–BaO–CuO, system.[6]

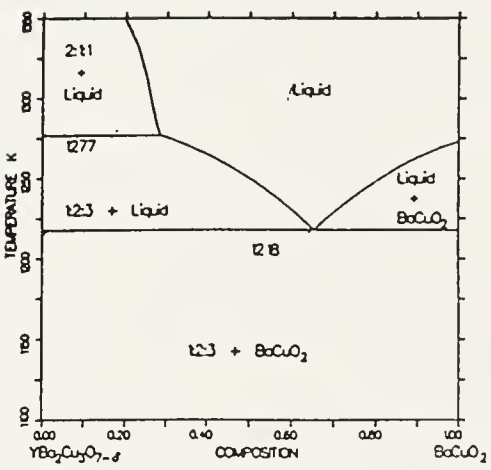

Fig. 14. Calculated phase diagram of $YO_{1.5}$–BaO–CuO, system (isopleth along *a–l* in Fig. 8).

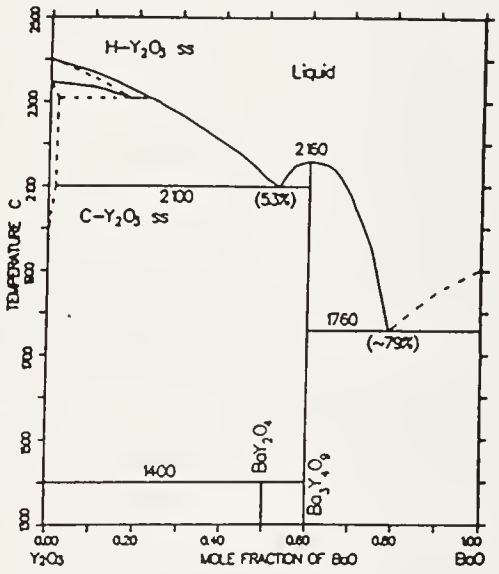

Fig. 1. Experimental phase diagram of $YO_{1.5}$–BaO system.[7]

Figure 6-13 Experimental and calculated phase diagrams for the Y-Ba-Cu-O system. Reference 84.

plume consisted only of high-velocity particles whereas, at 3.6 J/cm^2, both low- and high-velocity particles were observed,[12] suggesting two different types of evaporation mechanisms. At 0.6 J/cm^2, however, the temperature is high enough to allow yttrium-rich phase formation and the evaporation of material under the bridge. As a result, the connections in this network are weakened, leaving behind a partial network with a larger yttrium-rich phase, 3 μm in diameter, on the surface. This fluence marks the end of the porous structure and the beginning of the cone structure. The film deposited at low fluence is Ba- and Cu-rich; however, at higher fluence, the film is more stoichiometeric.[33]

6.2.2.2 Cones

The development of cones was first observed during glow discharge cathodes and was attributed to surface contamination with lower sputtering yield than the substrate.[212] The first systematic studies of cone formation were done by Wehner, who related the etch rate to incident angle.[213] In the laser evaporation of polymer material, the presence of ceramic impurities has been shown to produce cone formation as the result of beam shielding.[198]

In this study, the evaporation of a YBCO target at fluences of 0.6 to 1.1 J/cm^2 resulted in the formation of conelike structures (Figure 6-14). These structures were characterized by a forest-like morphology. The cones were normal to the target with dimensions of 8–10 μm, and a tip angle of 60 degrees. The cone tips appeared orange under visible light, probably because of reaction with moisture, [206] and were found to be yttrium rich. Material removal of this structure during evaporation was not efficient, with a maximum evaporation depth of only 20 μm at 2000 pulses. The true fluence on the surface was greatly attenuated, owing to the increase of surface area by the formation of cones. From simple geometry, the area ratio of a cone and a circle can be calculated as $(1+\tan^2(\theta/2))^{1/2}$, where θ is the cone angle. At a cone angle of 60 degrees, therefore, the fluence at the cone is only 50% that of a circle with the same diameter.

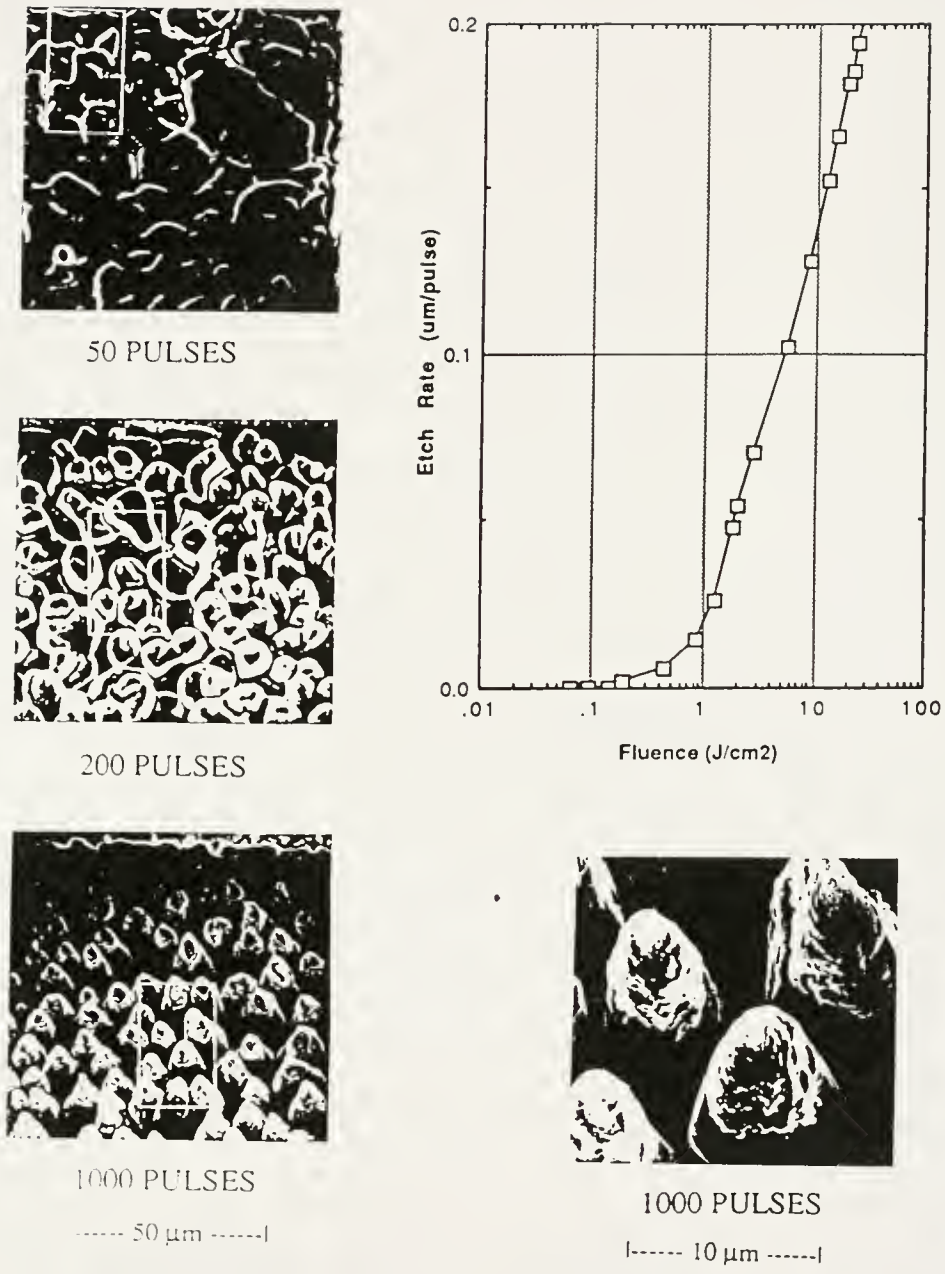

Figure 6-14 YBCO target evaporated using KrF laser at fluence between 0.6 to 1.1 J/cm^2. Formation of cones surface morphology. Atmosphere: air. Pulse number (a) 50 pulses; (b) 200 pulses; (c) 1000pulses.

The initial stages of cone formation, within the first 50 pulses, are similar to those of porous structure formation, where successive increases in the pulse number melt and smooth the surface (Figure 6-15). Further increase in pulse number cuts deeper into the target, forming columnar structures with base sizes up to 10 μm. At 200 pulses, the number of columns increases and "nipples" begin to form at the top of the column (Figure 6-16). These "nipples" shield the column from further irradiation. At 500 pulses, the cone shapes become more distinct (Figure 6-17). At 1000 pulses, the columns have completely changed to cones (Figure 6-18), and the evaporation depth levels off at 1000 pulses. The fluence of 1.1 J/cm^2 was the upper limit for cone formation, since at this condition, only a few large cones with a base of 30 μm were formed.

Cone structure evolution involves shielding the target with yttrium-rich particles, Y_2BaCuO_5 and Y_2O_3 from EDAX. These particles, typically 5 μm in diameter, may be formed during the cooling of the melted ablated surface area, as previously discussed, and may have an evaporation threshold higher than that of the bulk superconductor. Similar cone-shape morphology has been observed in the evaporation of polymer doped with ceramic particles that shield the laser beam,[198] and in sputtering of metal targets[214, 215] and semiconductors[216] from impurities. With each successive surface melting after each laser pulse, the particle size grows, forming larger cone tips. At low pulse numbers, the cone angle is approximately 50–60 degrees. At high pulse numbers, however, the cone becomes thinner, with an angle of 30–40 degrees. Beyond 1000 to 2000 pulses, no more evaporation is observed. At this stage the geometry of the cone is such that the beam is dispersed, and the true fluence falls below 0.6 J/cm^2, forming porous morphology on the cone shell with negligible evaporation rates. As an illustration, the fluence ratio of a 30% cone to a circle with the same diameter is 25%. The base of the cones also contains large grains with sizes of 10-20 μm, similar to the melted morphology observed at higher fluence. As the fluence increases, fewer cones are formed. The fluence of 1.1 J/cm^2 marks the end of the cone formation and the beginning of the melt structure.

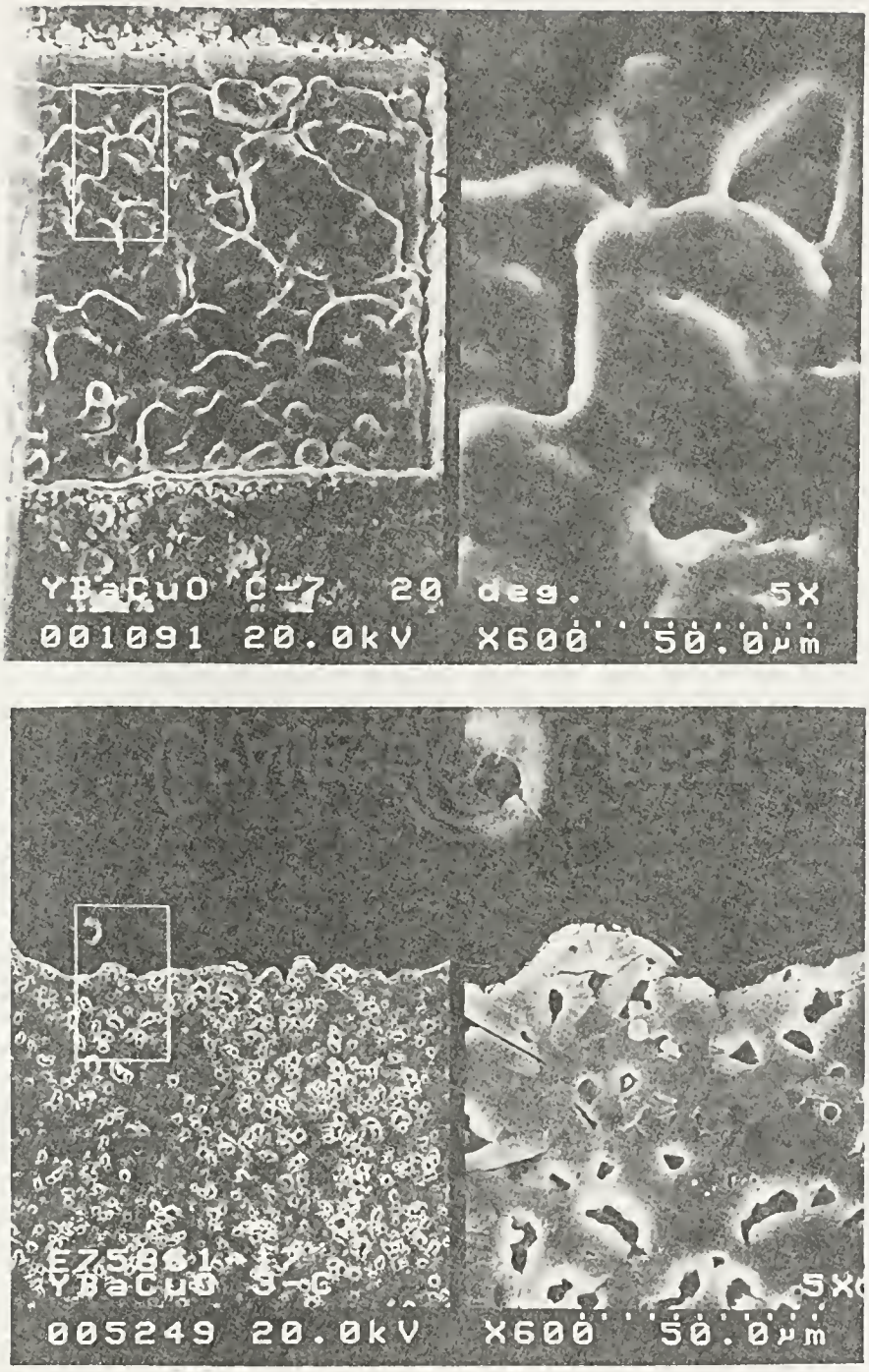

Figure 6-15 YBCO target evaporated using KrF laser. Atmosphere: air. Pulse number: 50 pulses. Fluence: 0.9 J/cm^2. Repetition rate: 10 pps. (a) top view; (b) cross-sectional view.

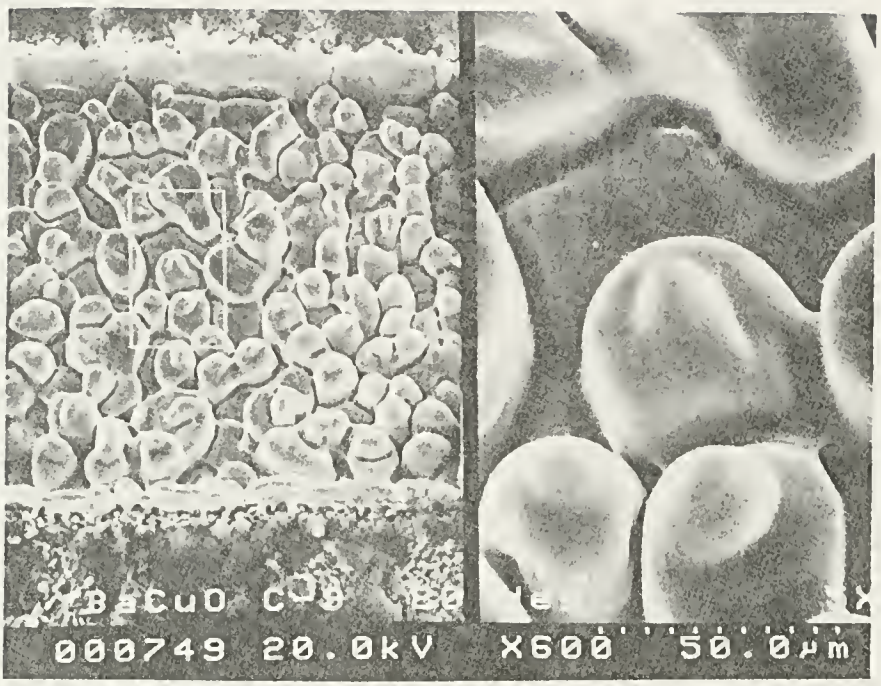

Figure 6-16 YBCO target evaporated using KrF laser. Atmosphere: air. Pulse number: 200 pulses. Fluence: 0.9 J/cm^2. Repetition rate: 10 pps. Top view. Note the formation of "nipples".

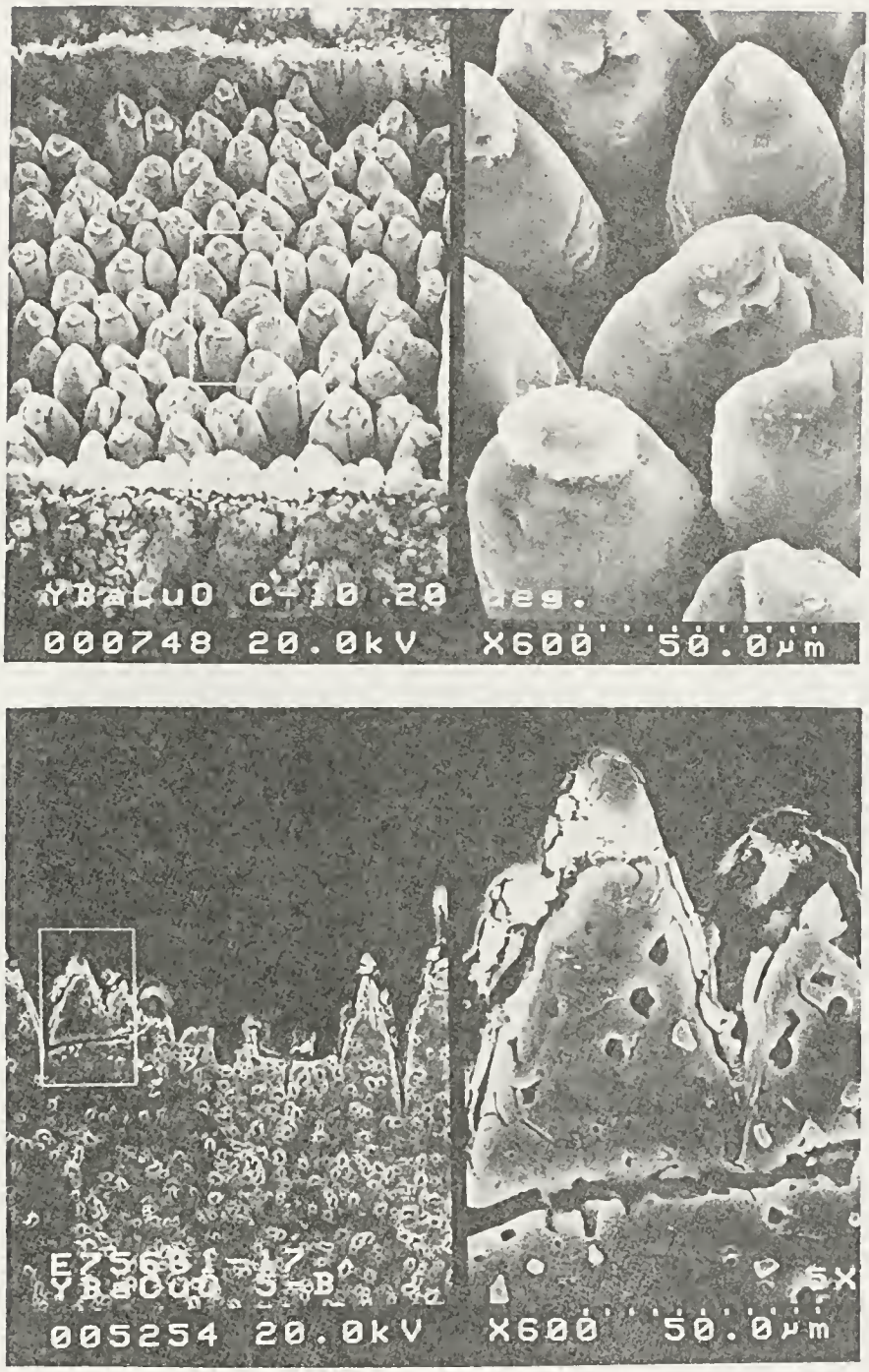

Figure 6-17 YBCO target evaporated using KrF laser. Atmosphere: air. Pulse number: 500 pulses. Fluence: 0.9 J/cm^2. Repetition rate: 10 pps. (a) top view; (b) cross-sectional view.

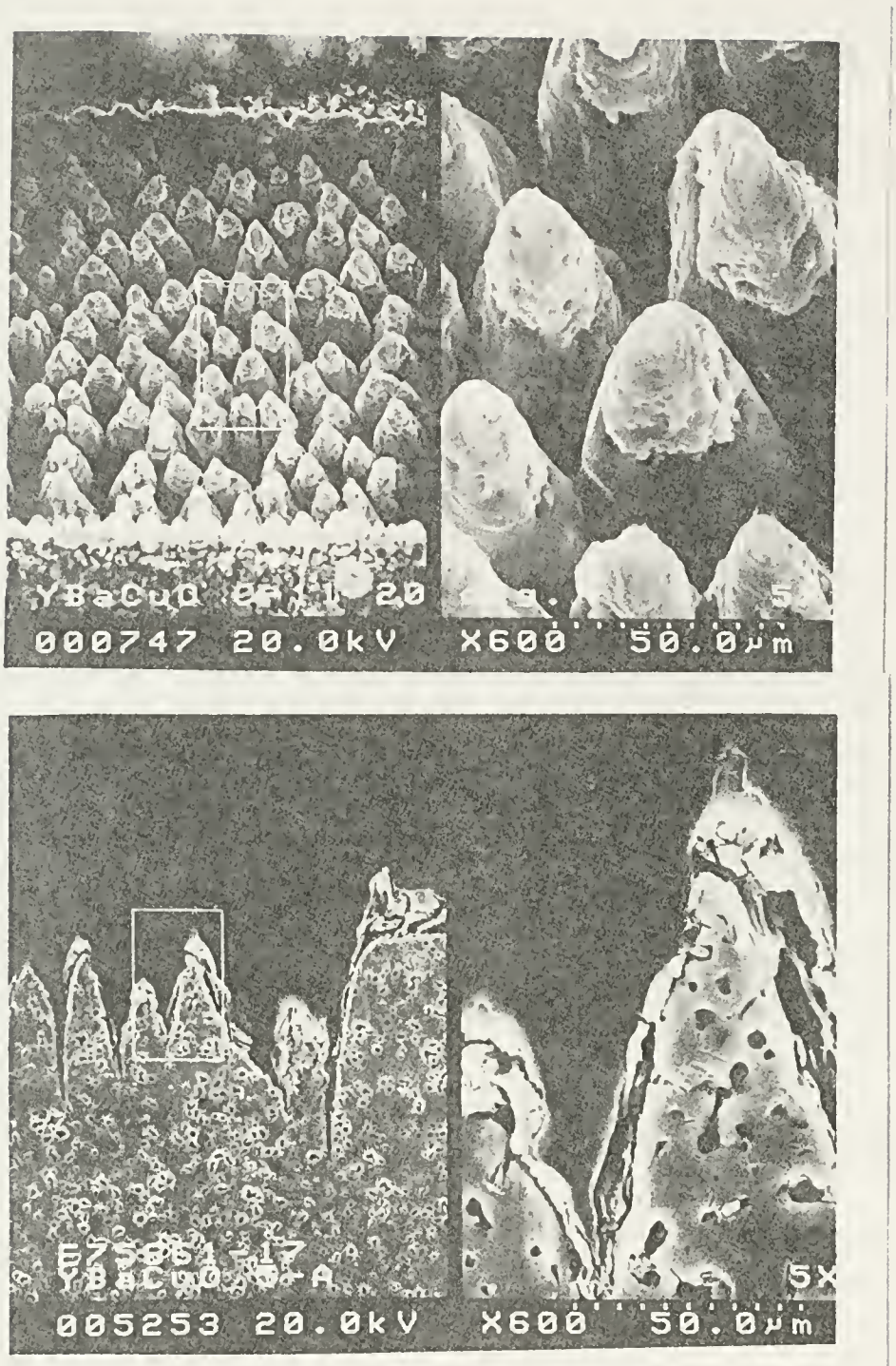

Figure 6-18 YBCO target evaporated using KrF laser. Atmosphere: air. Pulse number: 1000 pulses. Fluence: 0.9 J/cm^2. Repetition rate: 10 pps. (a) top view; (b) cross-sectional view.

Dyer observed the formation of stable, well-defined conical structures on the surface of excimer laser-etched polyimide.[198] These cones were found to be fluence related and were predominant near the evaporation threshold. At higher fluence, the cone formation can be induced by adding dopant impurities, such as alumina or rare earth compounds. The formation of cones, due to the shielding of the oxide with copper-rich surface, has been seen on CuO ablated with XeCl laser.[217] A semiquantitative explanation that provides a mechanism for this behavior can be given in terms of shielding effect. If the dopant is opaque, the shadowing will give cones with depth, d, approximately $d = r^2/\lambda$, where r = dopant radius and λ = laser wavelength. Upon successive evaporation, these cones will grow until they reach a limiting angle $\theta = 2 \sin^{-1}(E_t/E)$, where E is fluence and E_t is threshold fluence. Cone formation has also been observed during the sputtering of metal target due to shielding, resulting in low sputtering yield.[214]

In summary, the etch rate of the high-density pellet varied from 0.02 to 0.07 μm per pulse, depending on fluence and pulse number. Below 1 J/cm^2, in the fluence range for the cone formation, maximum evaporation depth was reached at 500 pulses. Additional pulses modified the cone geometry slightly, but the depth remained the same.[214] At a fluence higher than 1.1 J/cm^2, the fluence region for melt formation, the evaporation rate decreased linearly with increasing pulse numbers. In fact, during the evaporation at low pulse number, the evaporation rate was the most efficient at the first 100 pulses, consistent with the measured deposition rates.[53, 208]

6.2.2.3 Melts

Melted structure was found at fluence higher than 1.1 J/cm^2. This structure, generally observed during film deposition,[205-207] is characterized by the solidified-melt appearance, smooth and highly reflective, with frozen droplets (as distinguished from the cones) and grains at the base. The development of this structure at 50, 200 and 1000 pulses is presented in Figure 6-19. Droplet size varies from 10 to 20 μm, whereas grain size goes as high as 30 μm. This structure is the most favorable for the production of film,

50 PULSES

200 PULSES

1000 PULSES

|------ 50 μm ------|

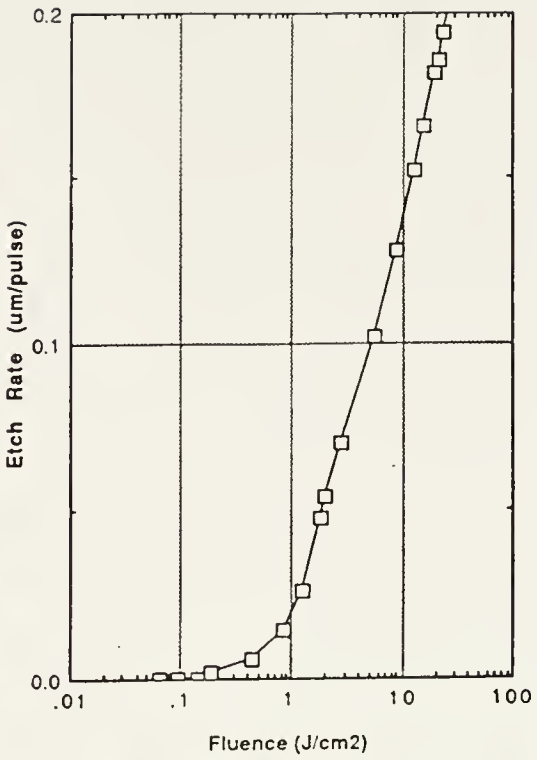

1000 PULSES

|------ 10 μm ------|

Figure 6-19 YBCO target evaporated using KrF laser at fluence above 1.1 J/cm^2. Formation of melts surface morphology. Atmosphere: air. Pulse number (a) 50 pulses; (b) 200 pulses; (c) 1000pulses.

since the etch rate is higher than those of the porous or cone structures, up to 70 nm/pulse at 2.0 J/cm^2. In addition, the surface can be ablated at a high pulse number. Texturing for this fluence range can occur with only 1 pulse.

The early stages of the melted morphology, up to 50 pulses, were similar to those of the porous and cone structures (Figure 6-20). As the pulse number increased, a "frozen droplet" structure was formed, with typical diameter up to 10 μm. As the pulse number increased, the droplets became more elongated until, at 500 pulses, the droplets became flatter. The size of the droplets, however, increased with increasing pulse number. At 100 pulses, frozen droplets of 10-15 μm formed. These droplet sizes gradually increased to 15–17 μm at 200 pulses (Figure 6-21), 17–20 μm at 500 pulses (Figure 6-22), 20–25 μm at 1000 pulses (Figure 6-23), and 25–30 μm at 2000 pulses. The grain size also increased with the increase in fluence. The evaporation depths at 2.0 J/cm^2 for 2000 pulses were 80 μm at the tip of the droplet and 130 μm at the deepest point. The tapering angle at the edge of the square was about 8 degrees. In the evaporation of Al_2O_3, a shorter pulse duration gave a more tapered hole.[111]

A characteristic of this melted structure was the formation of smooth-surfaced columns or grains. There are two possible mechanisms for the formation of the melted structure. First, as the surface evaporates from subsurface heating,[8, 138, 204] the molten target is ejected normal to the target and frozen, resulting in frozen column-type morphology. This formation is transient, since the column has melted and solidified after each pulse. In addition, it requires a large pool of molten material. The other mechanism involves crystal growth from the bottom of the melt. Following each pulse, the molten material cools down and starts to crystallize. If a single crystal exists at the base of the pools, crystal growth will start from those sites. The crystals will eventually grow upward and form columnar structures. From the cross-sectional view, however, it can be seen that the material under the column consists of virgin materials. Indicating that a mechanism based on the difference in the etch rate during the evaporation is the cause of the column

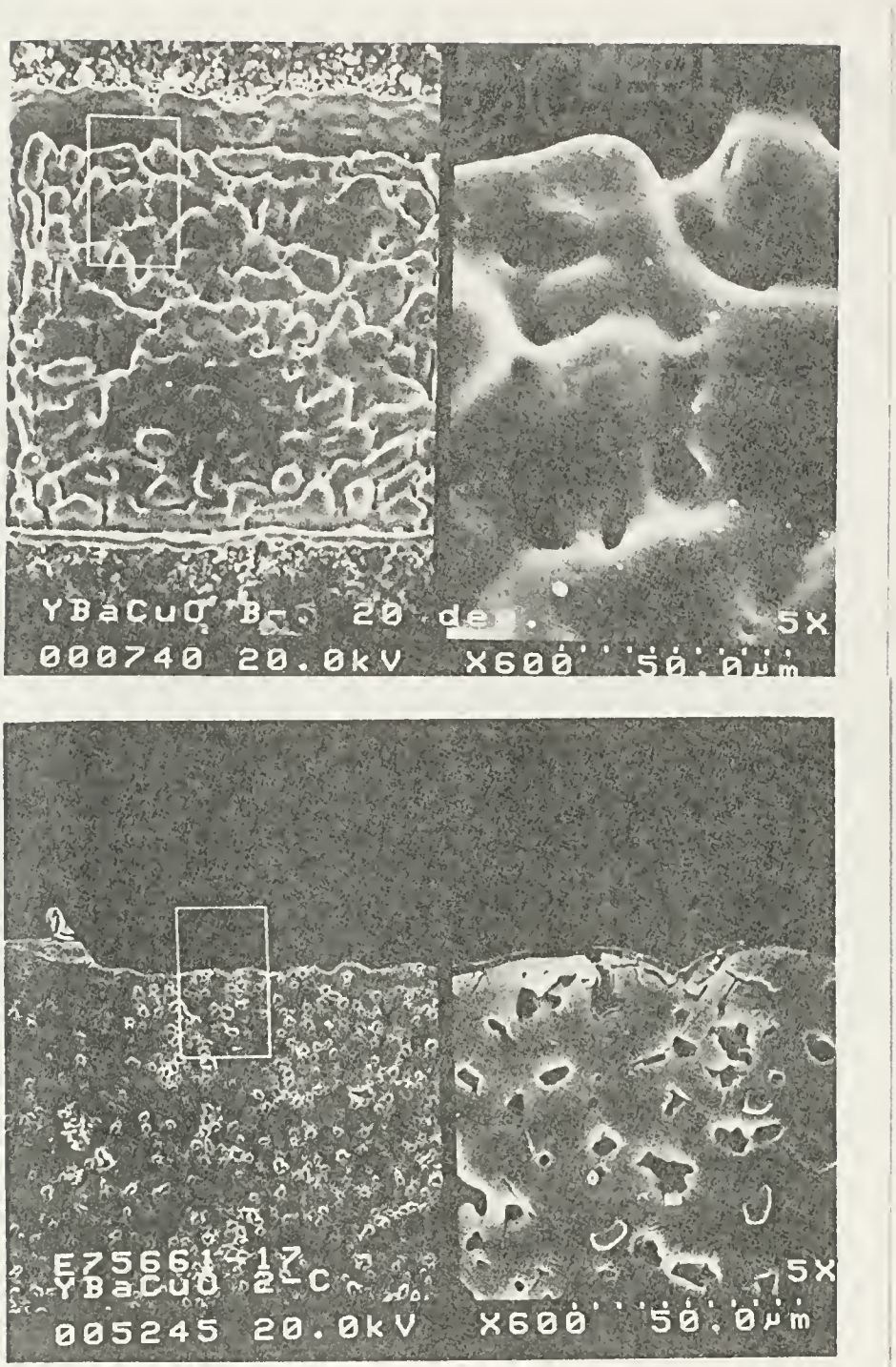

Figure 6-20 YBCO target evaporated using KrF laser. Atmosphere: air. Pulse number: 50 pulses. Fluence: 2.0 J/cm^2. Repetition rate: 10 pps. (a) top view; (b) cross-sectional view.

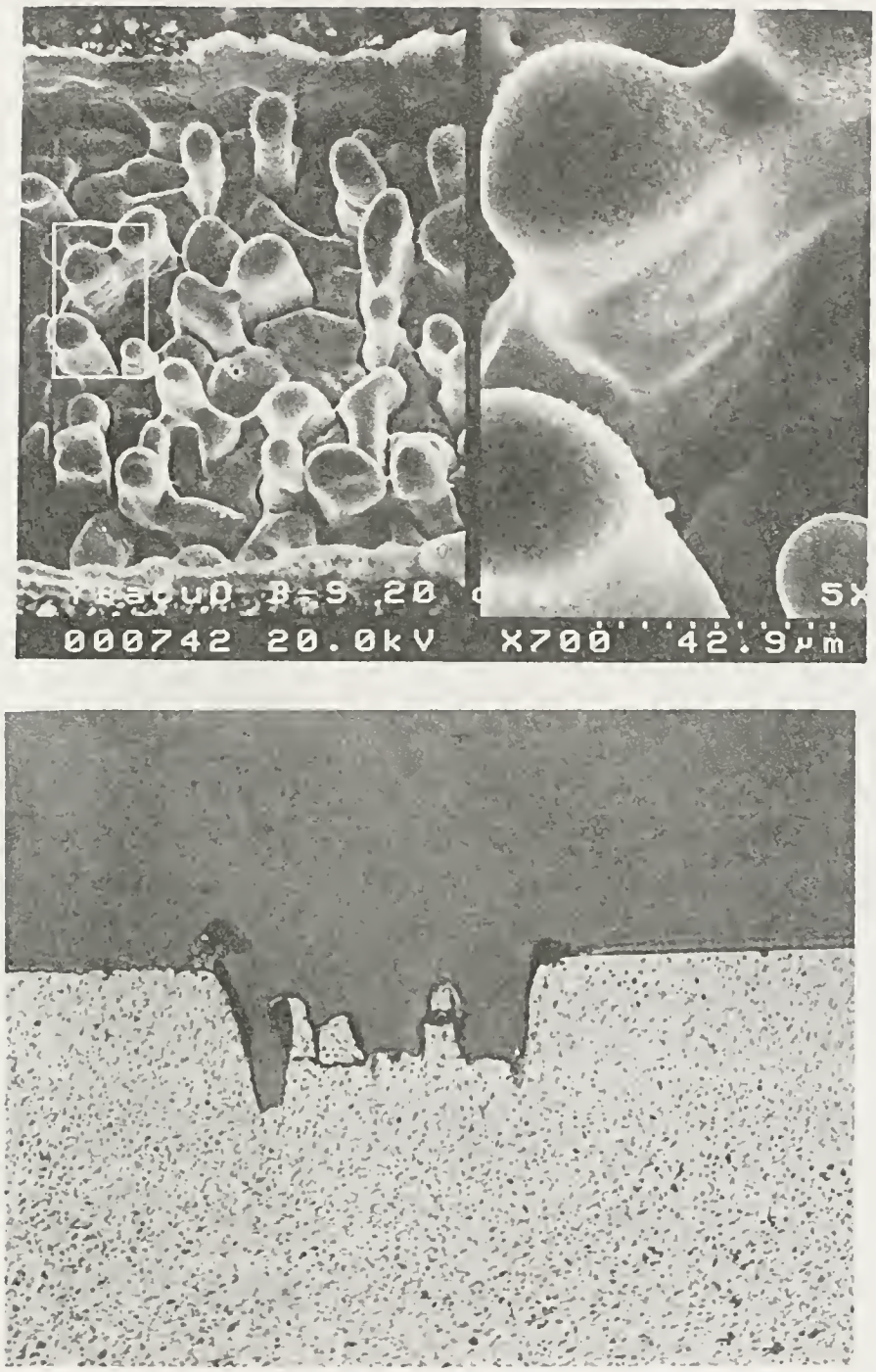

Figure 6-21 YBCO target evaporated using KrF laser. Atmosphere: air. Pulse number: 200 pulses. Fluence: 2.0 J/cm^2. Repetition rate: 10 pps. (a) top view; (b) cross-sectional view.

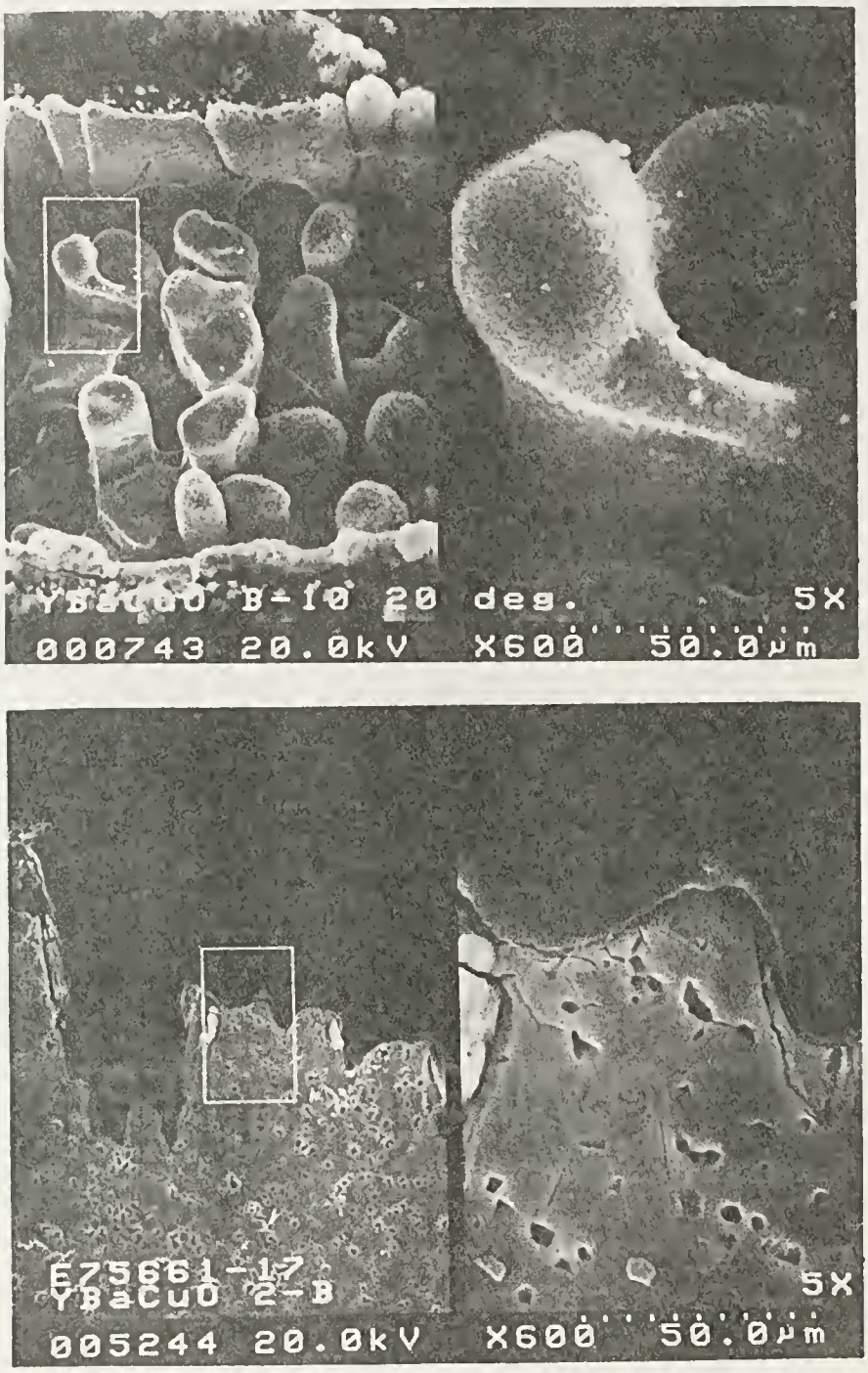

Figure 6-22 YBCO target evaporated using KrF laser. Atmosphere: air. Pulse number: 500 pulses. Fluence: 2.0 J/cm^2. Repetition rate: 10 pps. (a) top view; (b) cross-sectional view.

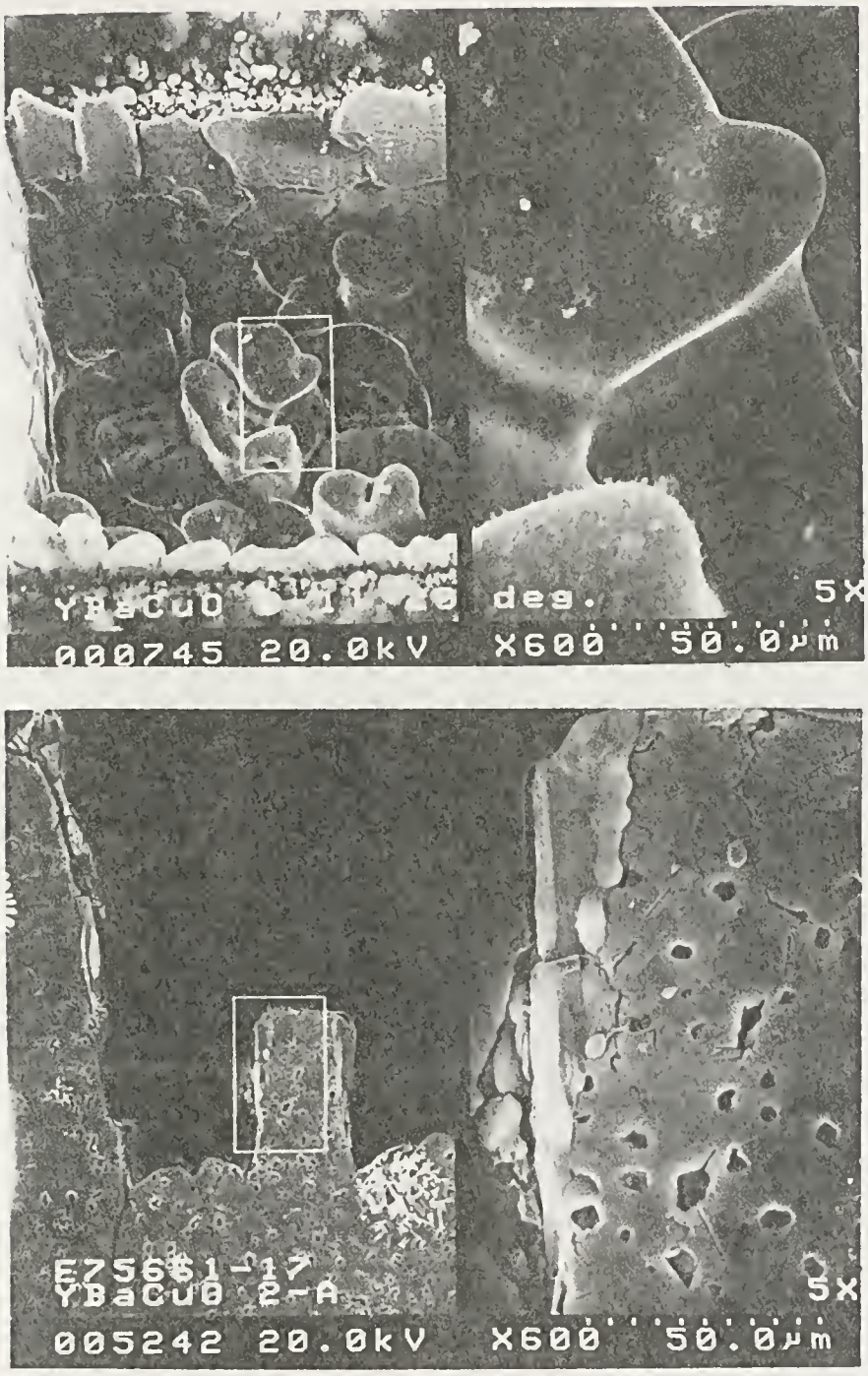

Figure 6-23 YBCO target evaporated using KrF laser. Atmosphere: air. Pulse number: 1000 pulses. Fluence: 2.0 J/cm^2. Repetition rate: 10 pps. (a) top view; (b) cross-sectional view.

formation. As seen in the recorded video tape of the evaporation process, the dynamics of this formation showed droplets that moved rapidly and had a lifetime of only 6 to 10 seconds, corresponding to 100 pulses at 10 pps.

The removal of material was more efficient at fluence higher than 1.1 J/cm^2 because of the formation of relatively flat and smooth ablated surfaces. Beam attenuation at this fluence range was minimal, and the average temperature of the ablated area was high. Thus material was removed instead of being allowed to cool down and form the yttrium-rich phase.

6.2.3 Effect of Pulse Number

The morphological development of the surface was studied in detail at the early stages of the development as a function of pulse number. At the fluence typically used for the deposition of thin film, 2 J/cm^2, there are three regions of morphology formation: 1) the formation of molten surface during the first 20 pulses; 2) the formation of column, between 20 and 200 pulses; and 3) the formation of table beyond 200 pulses. This result is analogous to the effect of fluence on morphology. The polished target material used in this study is presented in Figure 6-24. In this study, the evolution of the target morphology are monitored as a function of pulse number from the same evaporated area.

6.2.3.1 Melting of surface: less than 20 pulses

The first stage in the evolution of target surface mophology at fluence of 1.2 J/cm^2 was characterized by the formation of smooth molten surface. In this first 20 pulses, the photon energy is primarily used in the build up of molten layer, without significant material removal. Surface smoothing is performed by filling the pits and pores initially contained in the virgin material. At the initial 2 pulses, the top layer containing pits and holes formed by the porosity of the target material was melting and partially filled (Figure 6-25). The pit density was in the order of 25 pits/100 μm^2. The surface appeared relatively flat; however, the development of cracks can be seen. The cracks may be due to the rapid cooling of the

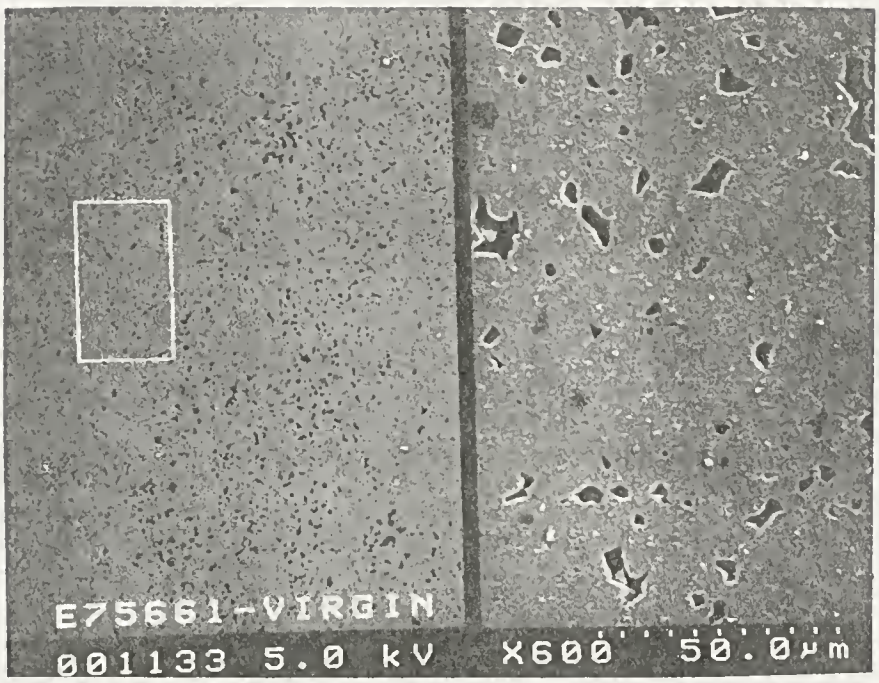

Figure 6-24 Polished YBCO surface.

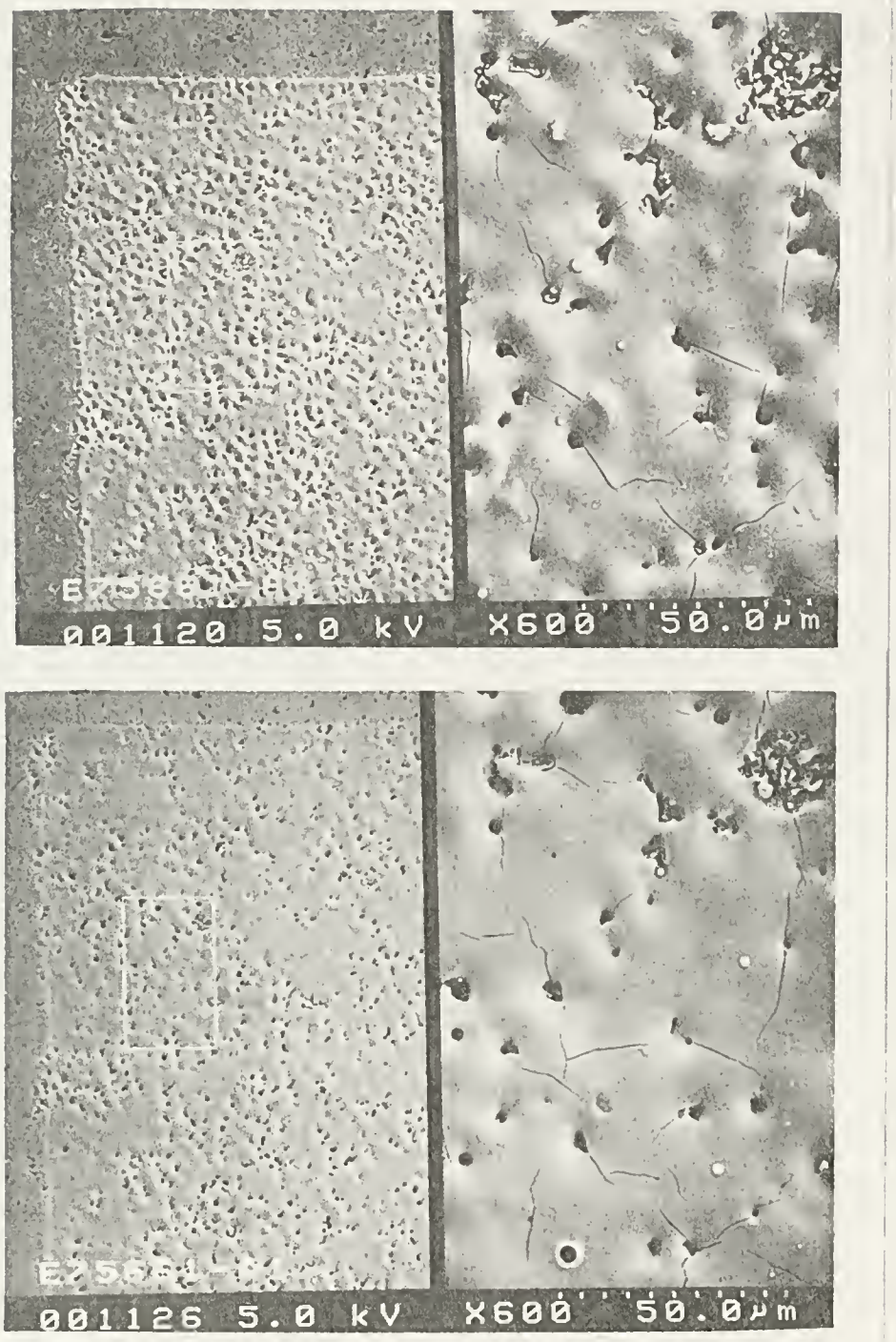

Figure 6-25 Polished YBCO target evaporated using KrF laser. Fluence: 2.0 J/cm^2. Atmosphere: air. Pulse number: (a) 1 pulse (b) 2 pulses. Note that at 2 pulses, some of the holes are filled.

molten target surface. At 5 pulses, some of the holes had been covered by the melt, and the material removal can be detected from the cross-sectional profile (Figure 6-26). The surface appeared to have been etched selectively. The melting also became more apparent, and the pit density dropped to 5 pits/100μm^2. Surface periodicity of smooth protusion were about 10 μm apart. At this stage, it appeared that the protusion was a product of droplet formation due to the formation of molten layer. However, the cross-sectional view showed that the material under the protusion is virgin, indicating that the mechanism of this protusion is selective evaporation. It is not known at this point how the protusion evolved. At 10 pulses, the surface periodicity can be clearly seen; the distance is approximately 10 μm from both the top and cross-sectional view (Figure 6-27a). In the evaporation of metal, it was suggested that the formation of protusion-like structure depends on the surface diffusivity of the molten layer. This idea, however, does not apply here due to the presence of virgin material under the protusion.

6.2.3.2 Formation of columns: 20 to 100 pulses

Once the molten surface is formed and morphology developed, further pulses will etch the crater deeper, forming taller columns. At 20 and 50 pulses, the shape and depth of the protusion became very apparent. This protusion was tall and appeared as a column (Figures 6-27b and 6-28a). This column formed as the result of rapid evaporation of the pits and initial cracks. The distance between the peaks was still 10 μm. The base of the column became deeper with increasing pulse numbers. At 80 pulses, the base became flatter and formed a table (Figure 6-28b).

6.2.3.3 Formation of tables: higher than 100 pulses.

At pulse number higher than 100 pulses, the columns began to disappear and were replaced by tables (Figure 6-29). These tables were very flat and contained a large number of pits and particulates (Figure 6-30).

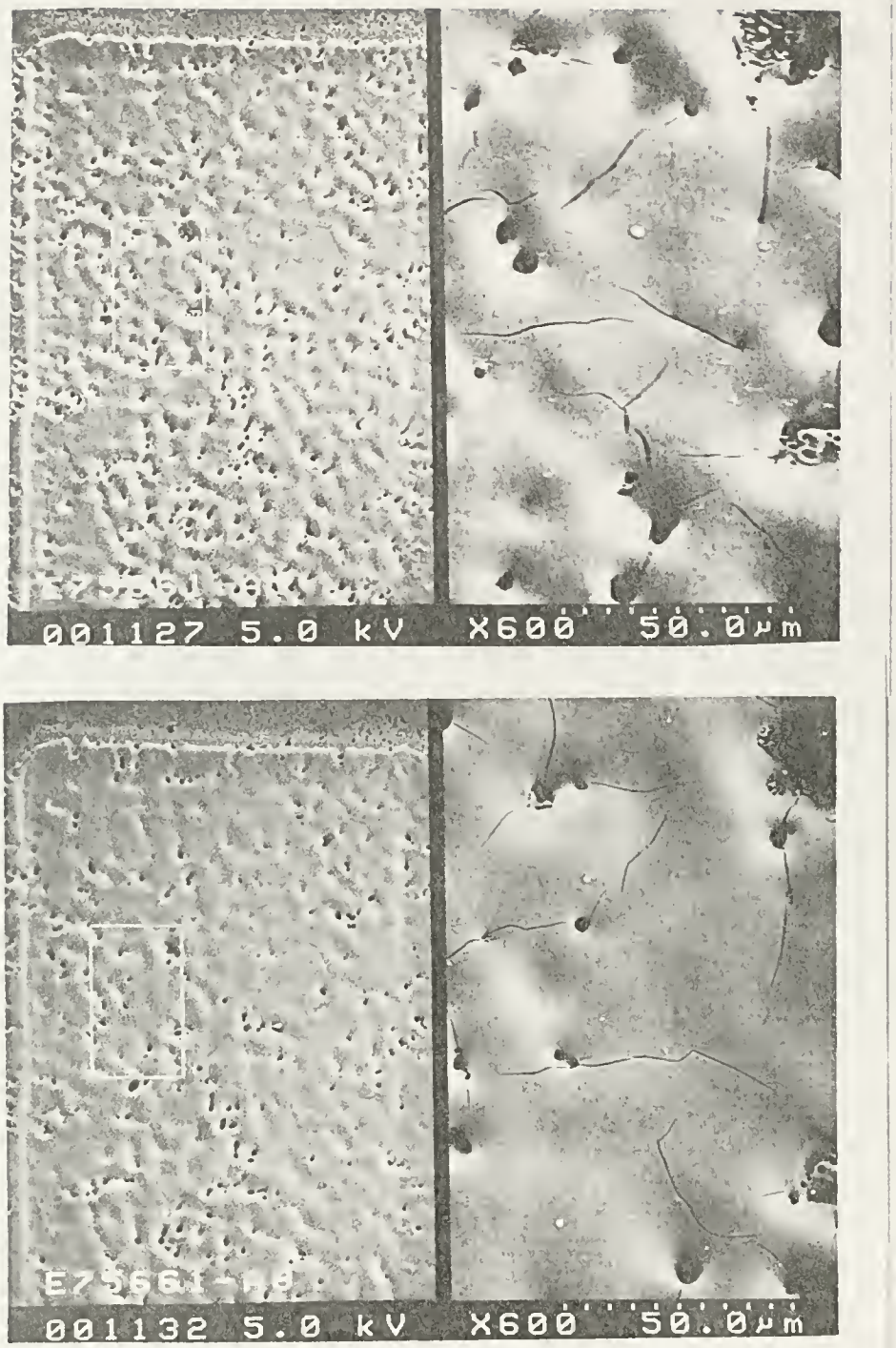

Figure 6-26 Polished YBCO target evaporated using KrF laser. The same surface area as Figure 6-25. Fluence: 2.0 J/cm^2. Atmosphere: air. Pulse number: (a) 5 pulses (b) 8 pulses.

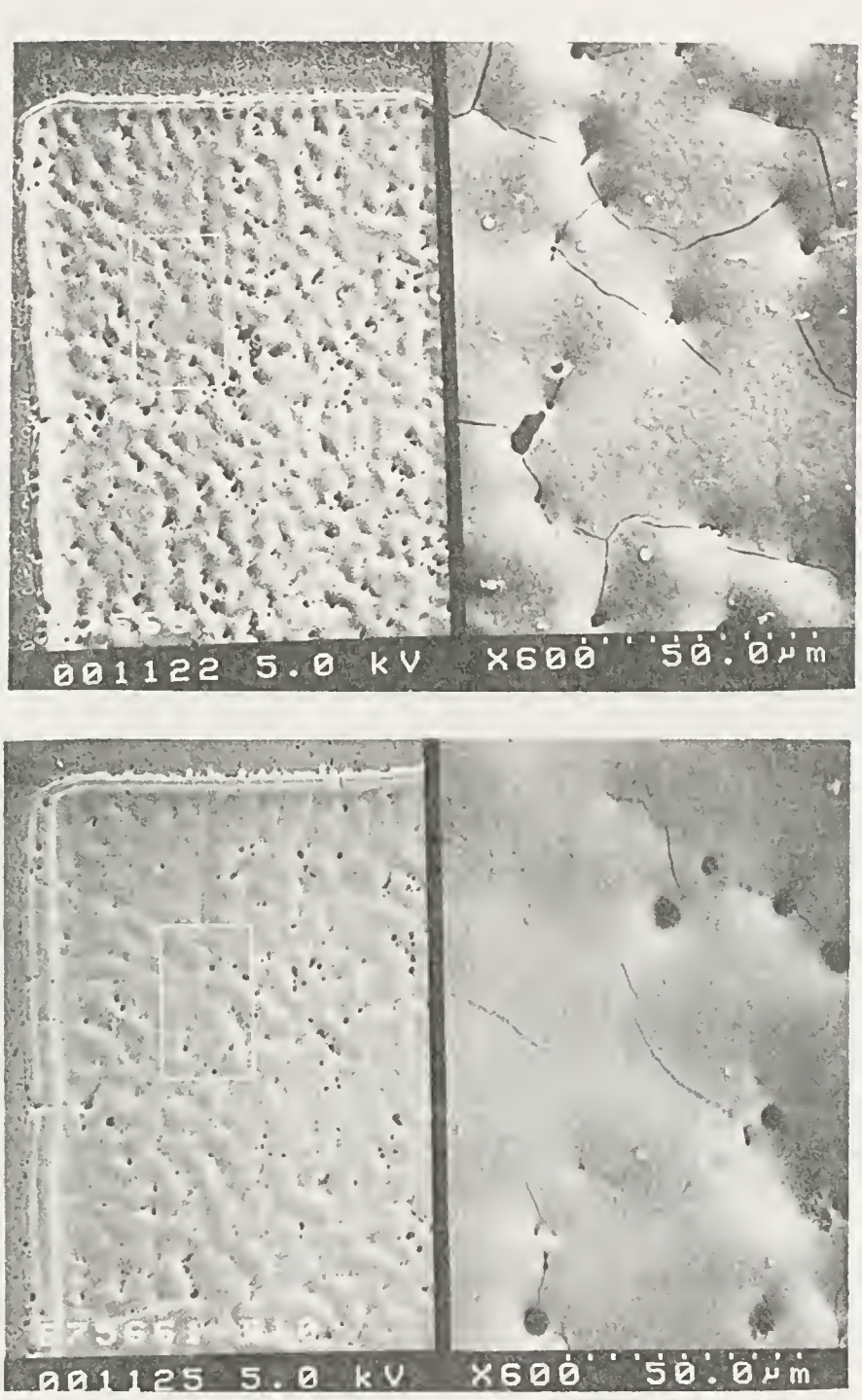

Figure 6-27 Polished YBCO target evaporated using KrF laser. Fluence: 2.0 J/cm^2. Atmosphere: air. Pulse number: (a) 10 pulses (b) 20 pulses.

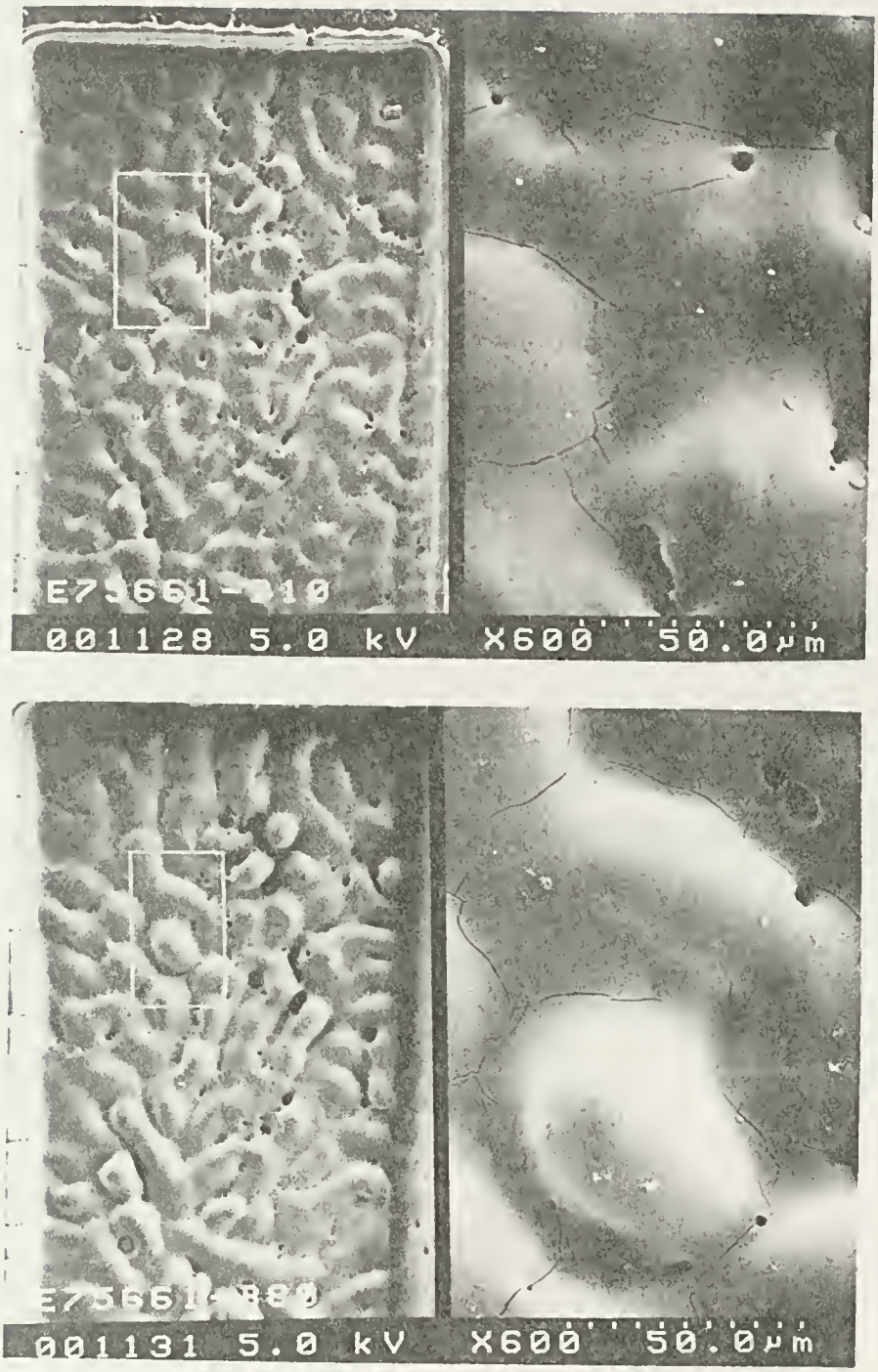

Figure 6-28 Polished YBCO target evaporated using KrF laser. The same surface area as Figure 6-27. Fluence: 2.0 J/cm^2. Atmosphere: air. Pulse number: (a) 50 pulses (b) 80 pulses.

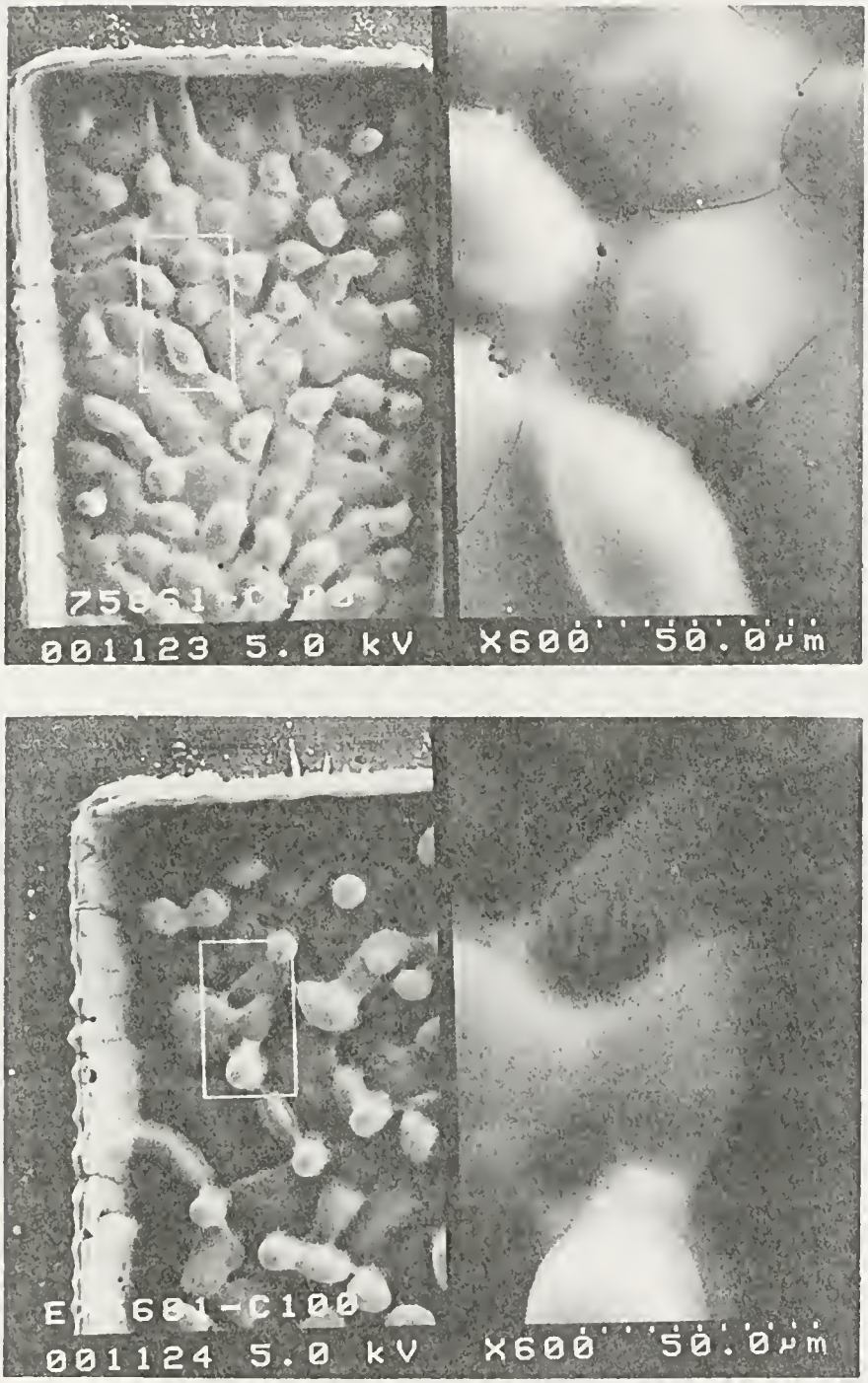

Figure 6-29 Polished YBCO target evaporated using KrF laser. Fluence: 2.0 J/cm^2. Atmosphere: air. Pulse number: (a) 100 pulses (b) 200 pulses.

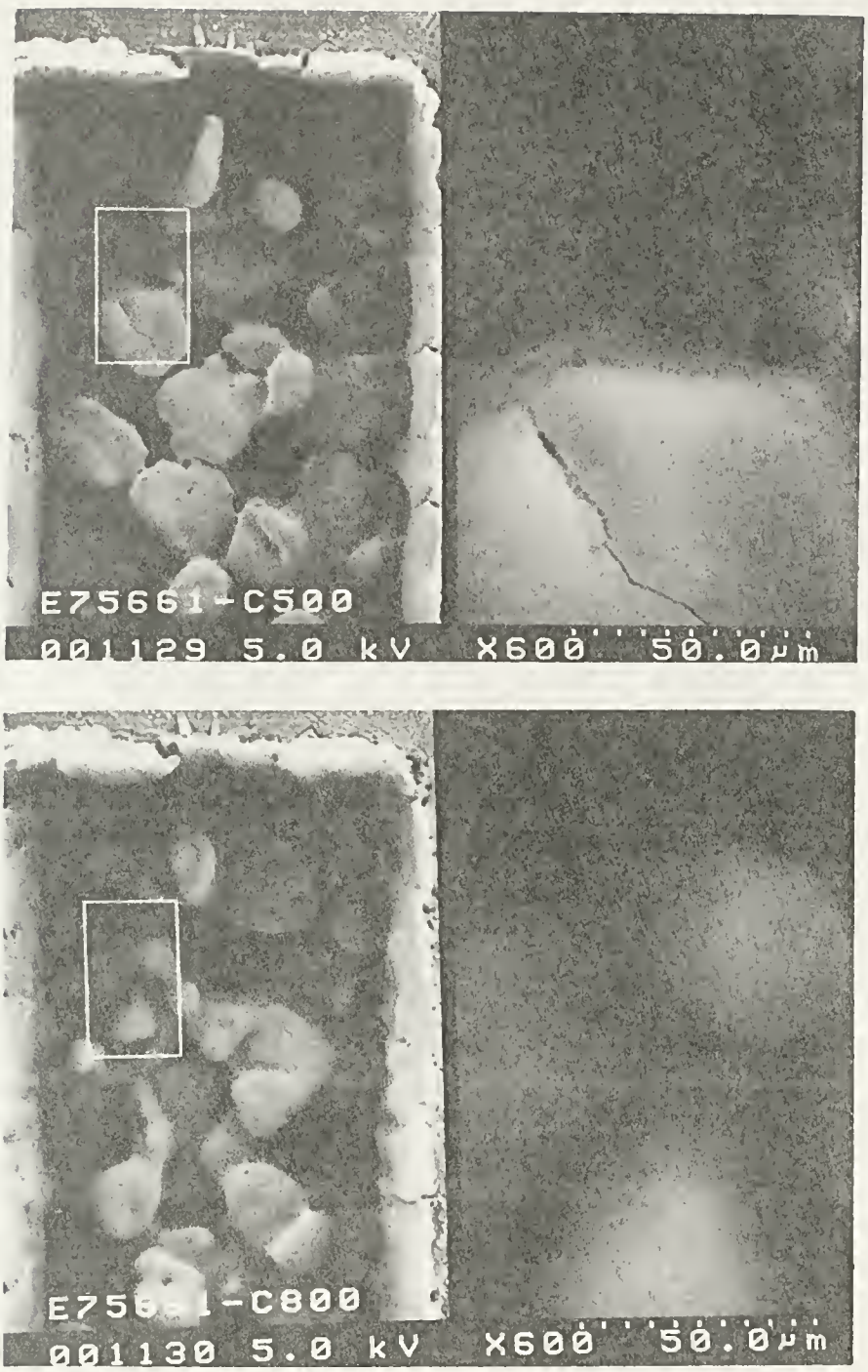

Figure 6-30 Polished YBCO target evaporated using KrF laser. The same surface area as Figure 6-29. Fluence: 2.0 J/cm^2. Atmosphere: air. Pulse number: (a) 500 pulses (b) 800 pulses.

6.2.4. Effect of Phase Impurities

Both the porous and cone morphology shared a similar characteristic in which a yttrium rich phase was found on the top surfaces and shielded the underlying target surface from further radiation. Porous structure occurred at low fluence because the yttrium-rich phase was thermally stable and the radiation did not raise the surface temperature sufficiently to evaporate this phase. Cone morphology, which is formed at higher fluences, is the result of the shielding of a few remaining yttrium-rich phase which becomes the tip of the cones. The etch rate and the morphology studies of the Y_2BaCuO_5 were conducted to test the hypothesis that beam shielding is indeed the mechanism associated with the formation of porous and cone structure.

A Y_2BaCuO_5 target was formed from a mixture of Y_2O_3, CuO, and BaO, which was repeatedly sintered and grounded to form a uniform phase. The sintering was performed in oxygen and kept at a temperature of 960 ^oC for 4 hours. This phase was finally formed into a pellet and used as a target. The surface morphology of the Y_2BaCuO_5 pellet is presented in Figure 6-31a.

The evaporation was performed in a microfabrication stage. The fluence was varied from 0.4 J/cm^2 to 3.5 J/cm^2, and the evaporation was performed in air at atmospheric pressure. The pulse frequency was maintained at 10 pps. Quantitative analysis of the sample was performed using an EDAX. The etch depth was done using a microscope focused at the surface and the bottom of the crater.

The observed surface morphology as a funtion of fluence was similar in characteristic to that of YBaCuO target, although the fluence required was higher. Porous and cone structures were seen at fluence between 0.4 and 2.1 J/cm^2. Characteristics similar to the melt morphology were found at fluence higher than 3.5 J.cm^2. At fluence of 0.4 J/cm^2, the surface morphology showed characteristics similar to the porous structure previously studied (Figure 6-31b). Particles, about 1 to 2 μm, with rough edges, were

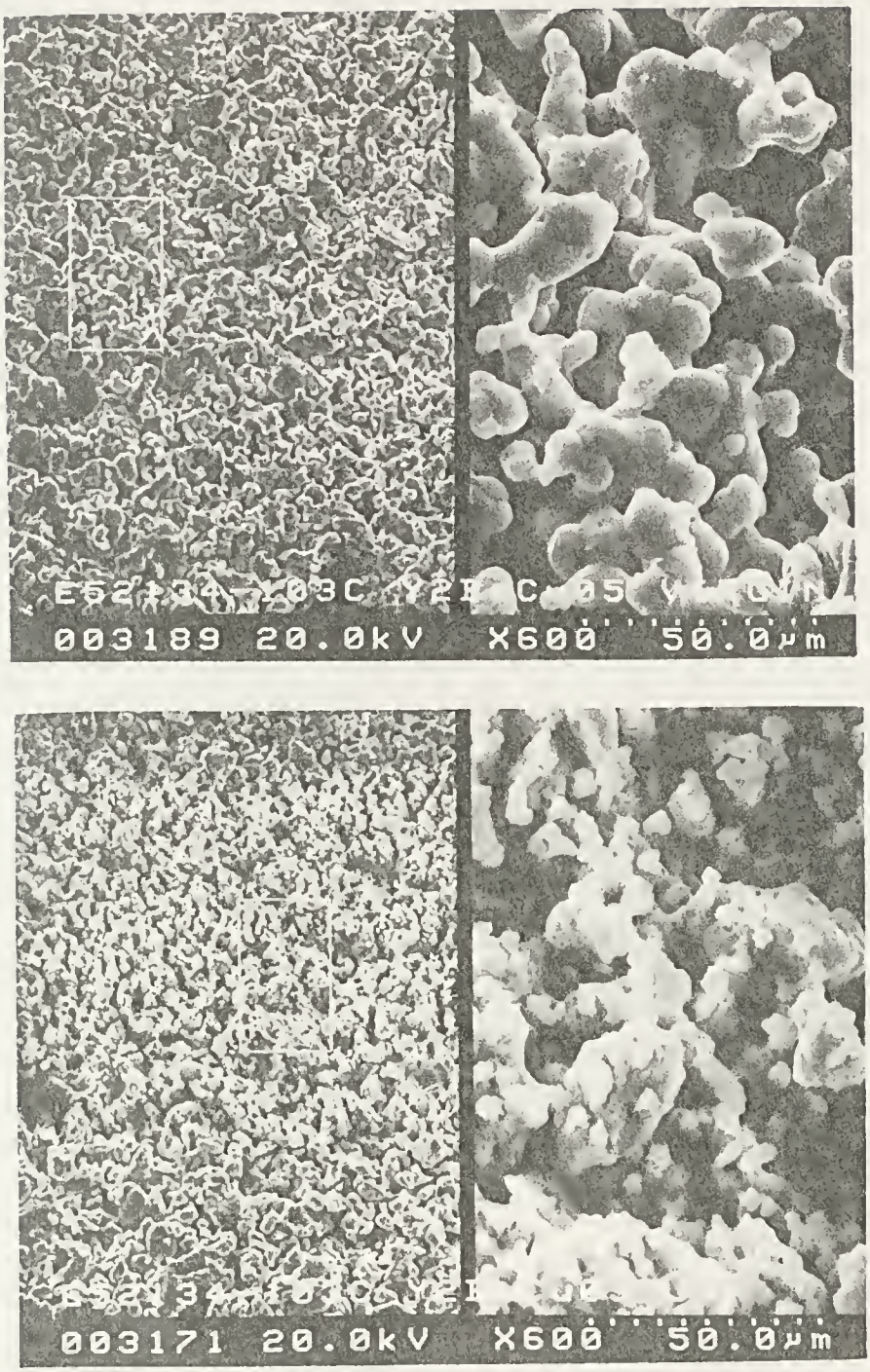

Figure 6-31 Y_2BaCuO_5 target evaporated using KrF laser. Atmosphere: air. Condition: (a) Virgin material; (b) 0.4 J/cm^2,1000 pulses

found at the surface. EDAX analysis showed that the particles were yttrium-rich (Y:Ba:Cu = 4:1:1). XRD showed that the surface contained both Y_2BaCuO_5 and Y_2O_3 phases. At fluence of 0.7 J/cm^2, the initial network seen in the porous structure is partially broken and individual clusters are beginning to form (Figure 6-32a). At 1.1 J/cm^2, cone morphology, as the result of the clusters formation, are clearly seen (Figure 6-32b). EDAX showed that the tip of the cones were mostly yttrium (Y:Ba:Cu = 10:1:1). The shape of the cones, however, was still rough even at 1000 pulses. At 1.4 J/cm^2, well-shaped cones were formed. The tips were smooth, indicating that melting of the yttrium rich phase has taken place. At fluence of 2.1 J/cm^2, very smooth cones were formed (Figure 6-33a). This trend continued until 2.7 J/cm^2, where the number of cones was decreasing, until at a fluence of 3.5 J/cm^2, where a melted surface was observed (Figure 6-33b). Although this surface did not have the same smoothness as that of the $YBa_2Cu_3O_7$ target, very likely because the target was not too dense, it had the high etch-rate characteristic of the melt structure. Also the droplet-like formation was absent, possibly due to the absence of liquid phase at this composition. EDAX analysis of the melted tips showed stoichiometric composition, indicating the presence of virgin material near the surface. As a comparison, the etch rates of the $YBa_2Cu_3O_7$ phase and the Y_2BaCuO_5 phase are presented at Figure 6-34. The etch depth as a function of fluence and pulse number for Y_2BaCuO_5 is presented at Figure 6-35. For comparison, the etch depth for YBCO is presented in Figure 6-36.

The evaporation of Y_2O_3 showed that the evaporation behavior was simple since no other possible phase could be present in the evaporated surface. If the fluence is too low, no evaporation takes place. At high fluence, the evaporation left a molten-type morphology behavior (Figure 6-37).

In conclusion, this study showed that the behavior of Y_2BaCuO_5 target ablated using KrF laser is similar to $YBa_2Cu_3O_7$, with the exception that the evaporation threshold occurs at 1.0 J/cm^2 instead of 0.1 J/cm^2. This result is consistent with the formation of

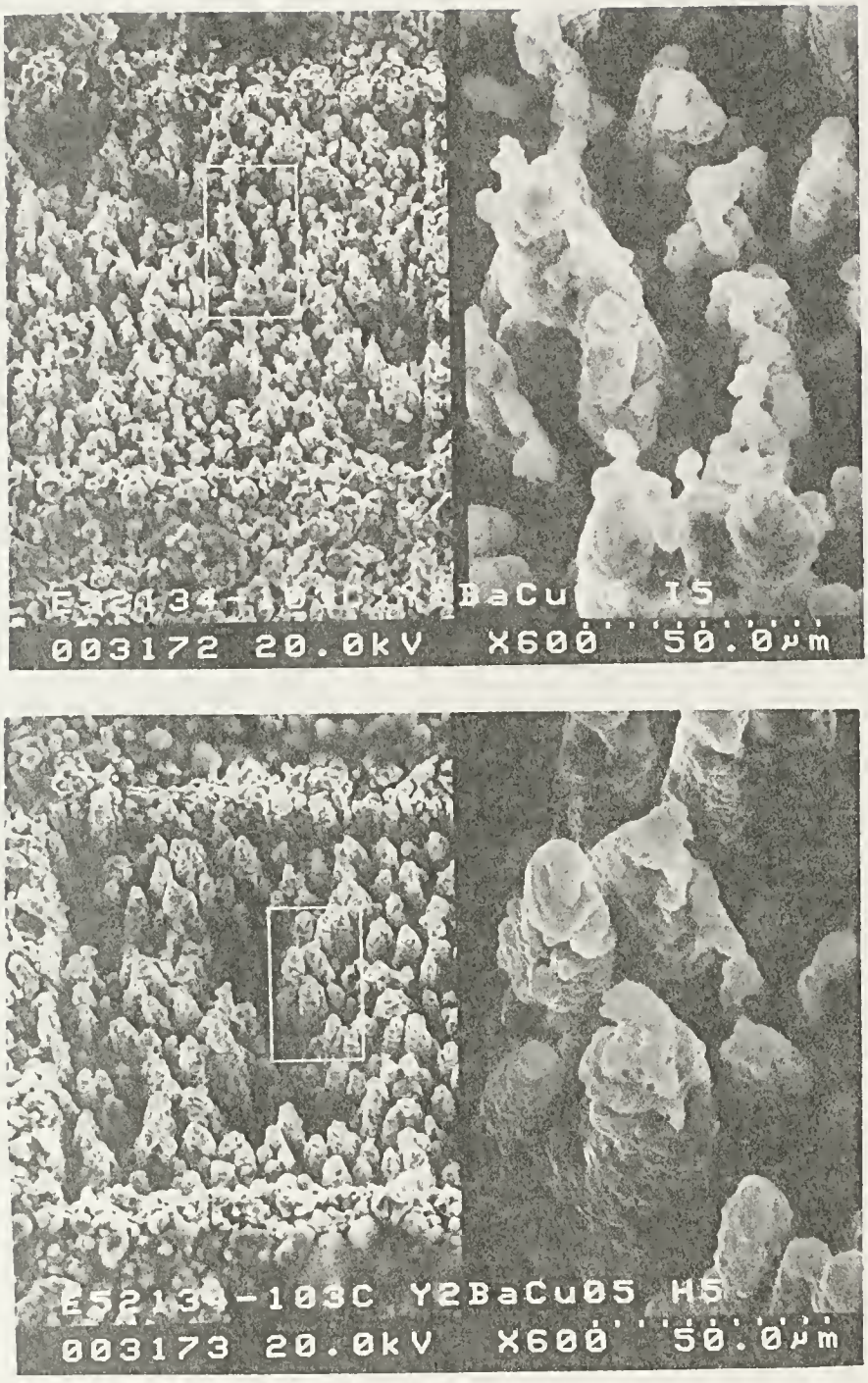

Figure 6-32 Y_2BaCuO_5 target evaporated using KrF laser. Atmosphere: air. Condition: (a) 0.7 J/cm^2, 1000 pulses, 10 pps; (b) 1.1 J/cm^2, 1000 pulses, 10 pps

Figure 6-33 Y_2BaCuO_5 target evaporated using KrF laser. Atmosphere: air. Condition: (a) 2.1 J/cm^2, 1000 pulses, 10 pps; (b) 3.5 J/cm^2, 1000 pulses, 10 pps

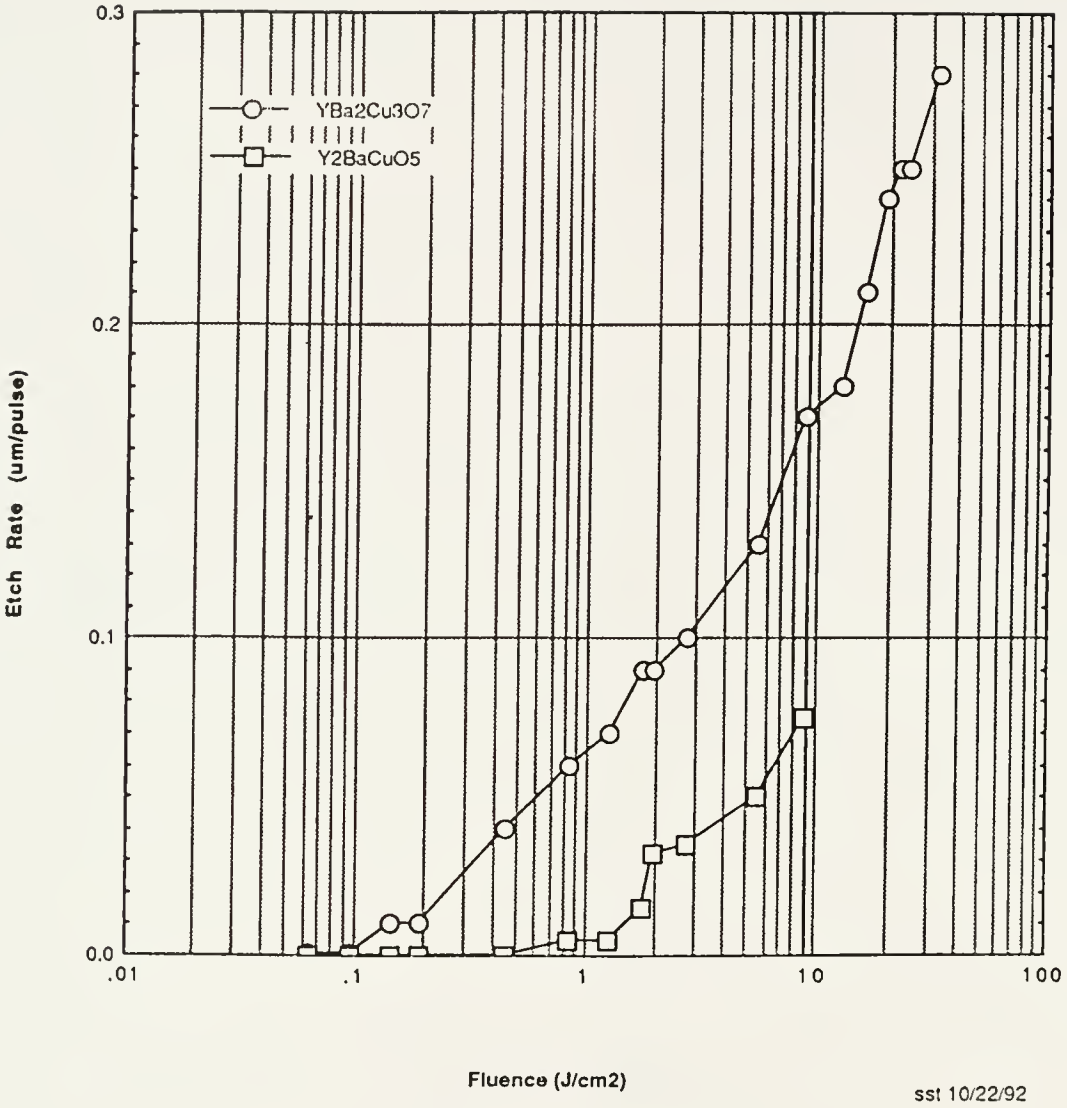

Figure 6-34 Comparison between the etch rates of $YBa_2Cu_3O_7$ and Y_2BaCuO_5 materials as a function fluence.

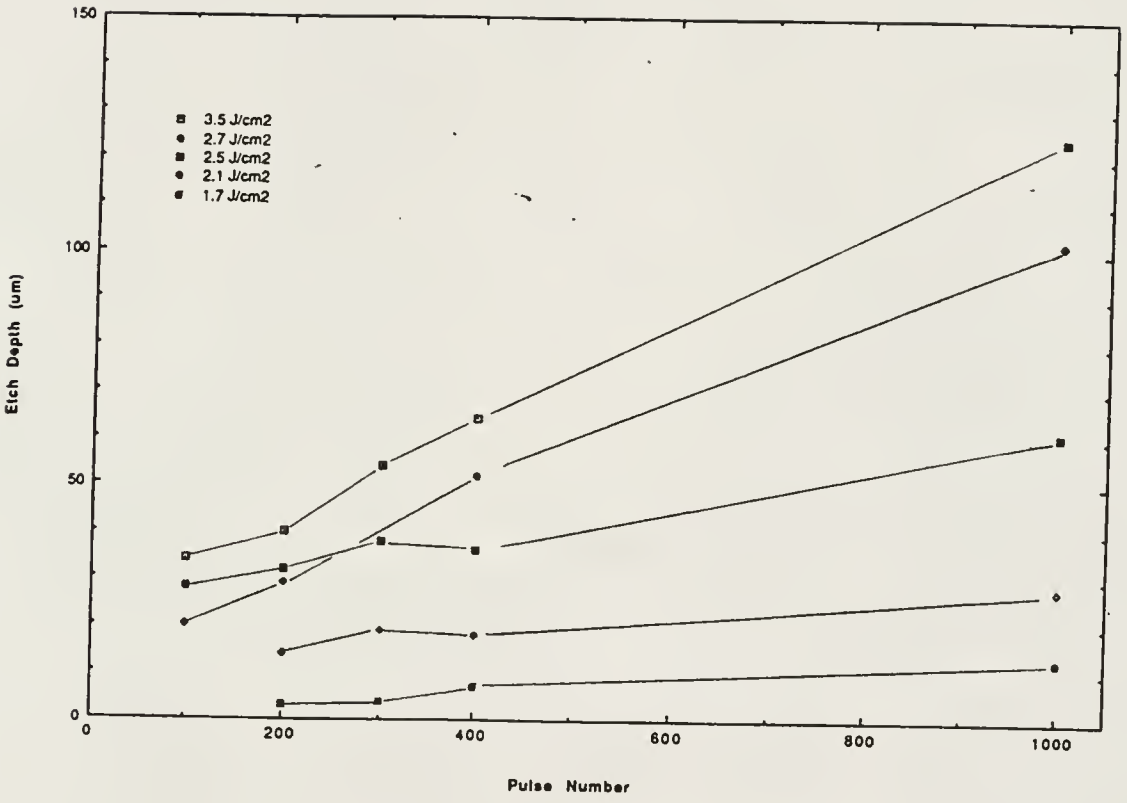

Figure 6-35 Etch depth Y_2BaCuO_5 as a function fluence and pulse number, evaluated at fluences from 1.7 to 3.5 J/cm^2.

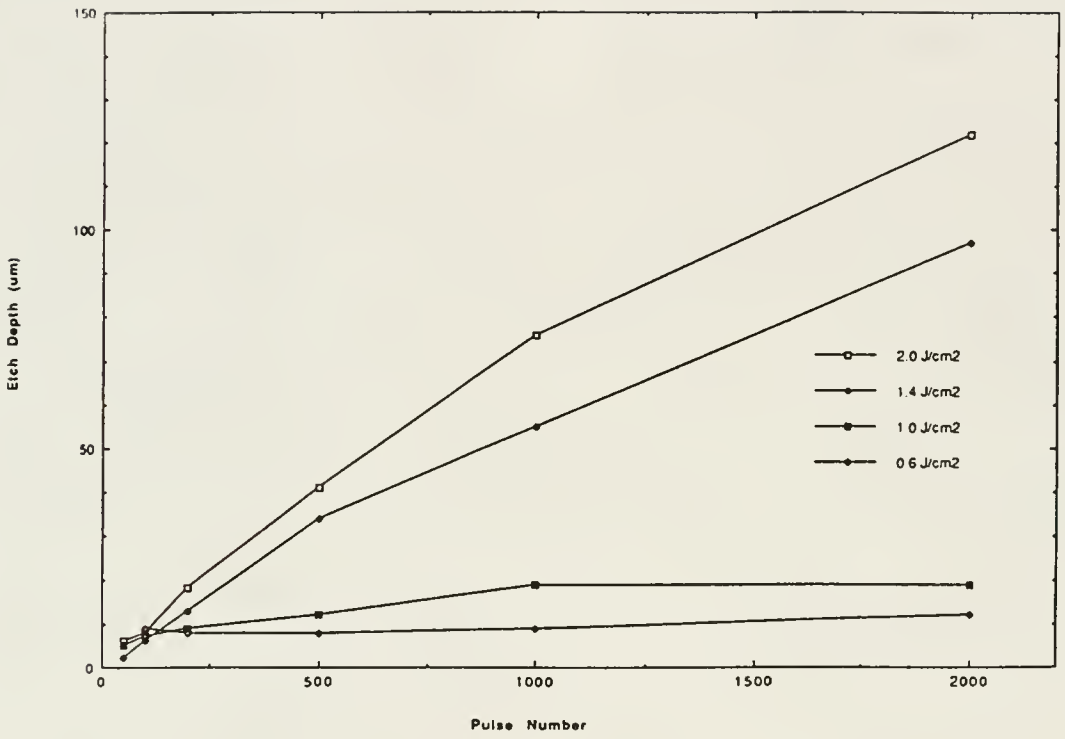

Figure 6-36 Etch depth of $YBa_2Cu_3O_7$ as a function fluence and pulse number.

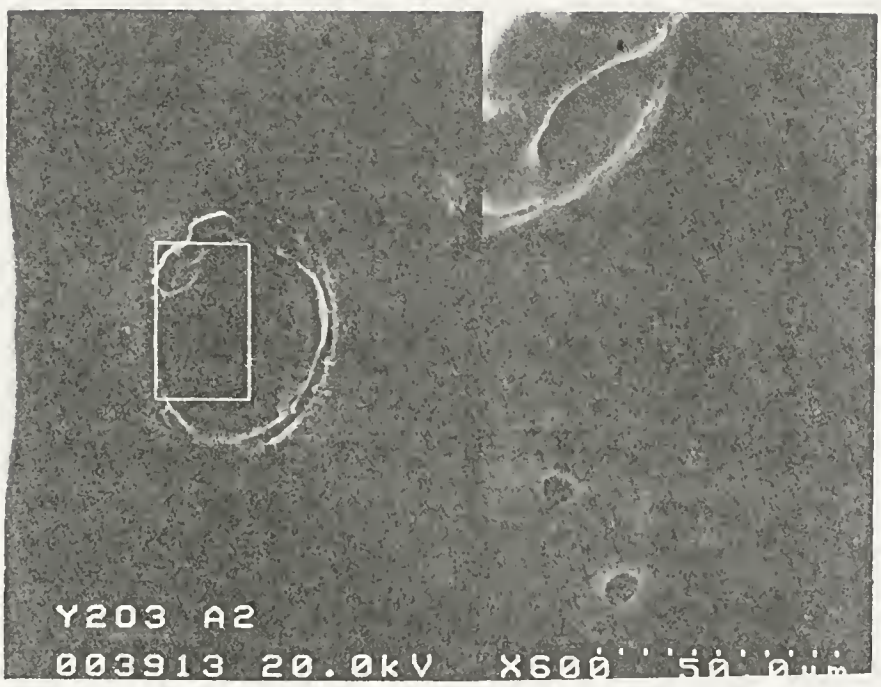

Figure 6-37 Y_2O_3 target evaporated using KrF laser. Atmosphere: air. Fluence: 3.0 J/cm^2. Pulse number: 200 pulses.

yttrium-rich phase in the evaporation of $YBa_2Cu_3O_7$ at fluence between 0.1 to 1.1 J/cm^2. The cause of the porous and cone formation in the Y_2BaCuO_5 target is the formation of Y_2O_3, a pure yttrium phase.

6.2.5 Effects of Repetition Rate and Beam Size

The morphology observed in the evaporation at high frequency showed characteristics similar to those ablated at low frequencies. The evaporation depths were also the same. The evaporation at 0.5 J/cm^2 and 10 or 100 pps are compared in Figure 6-38. Evaporation at 0.5 J/cm^2 and 100 pps is similar to evaporation at 0.8–0.9 J/cm^2 at 10 pps and 0.9–1.0 J/cm^2 at 1 pps. At 0.8 J/cm^2, a smoother surface is seen for the evaporation at 100 pps compared to the one at 5 pps (Figure 6-39). The presence of the irregular yttrium-rich phase is noticably reduced at 100 pps. A similar trend is observed for evaporation at high fluence, where the grain size at the ablated area increases with increase in frequency. At 1.1 J/cm^2, the grain boundary is 15–20 μm at 100 pps, compared with 10–15 μm at both 5 and 10 pps (Figure 6-40). It is possible that, at high repetition rates, the average temperature of the ablated area is higher,[218] providing additional driving force for grain growth. The transition from cone to melt is 0.85 J/cm^2 at 100 pps and 0.95 J/cm^2 at 5 and 10 pps.

The effect of beam size was investigated. The surface morphology of an area 200 μm x 200 μm at 0.9 and 1.4 J/cm^2 are presented in Figures 6-41 and 6-42. The result shows that beam size has no effect on the development of surface morphology.

6.2.6 Effects of Environments

Evaporation of a high-density target (90%) was done in vacuum at a pressure of 10^{-5} Torr air. The fluence was varied from 0.2 to 2.1 J/cm^2, and the evaporation size was 1 x 1 mm. At each fluence, 1000 evaporation pulses were done at 10 pps. The same type of morphologies, porous, cone, and melt, were observed. Little or no plume was observed

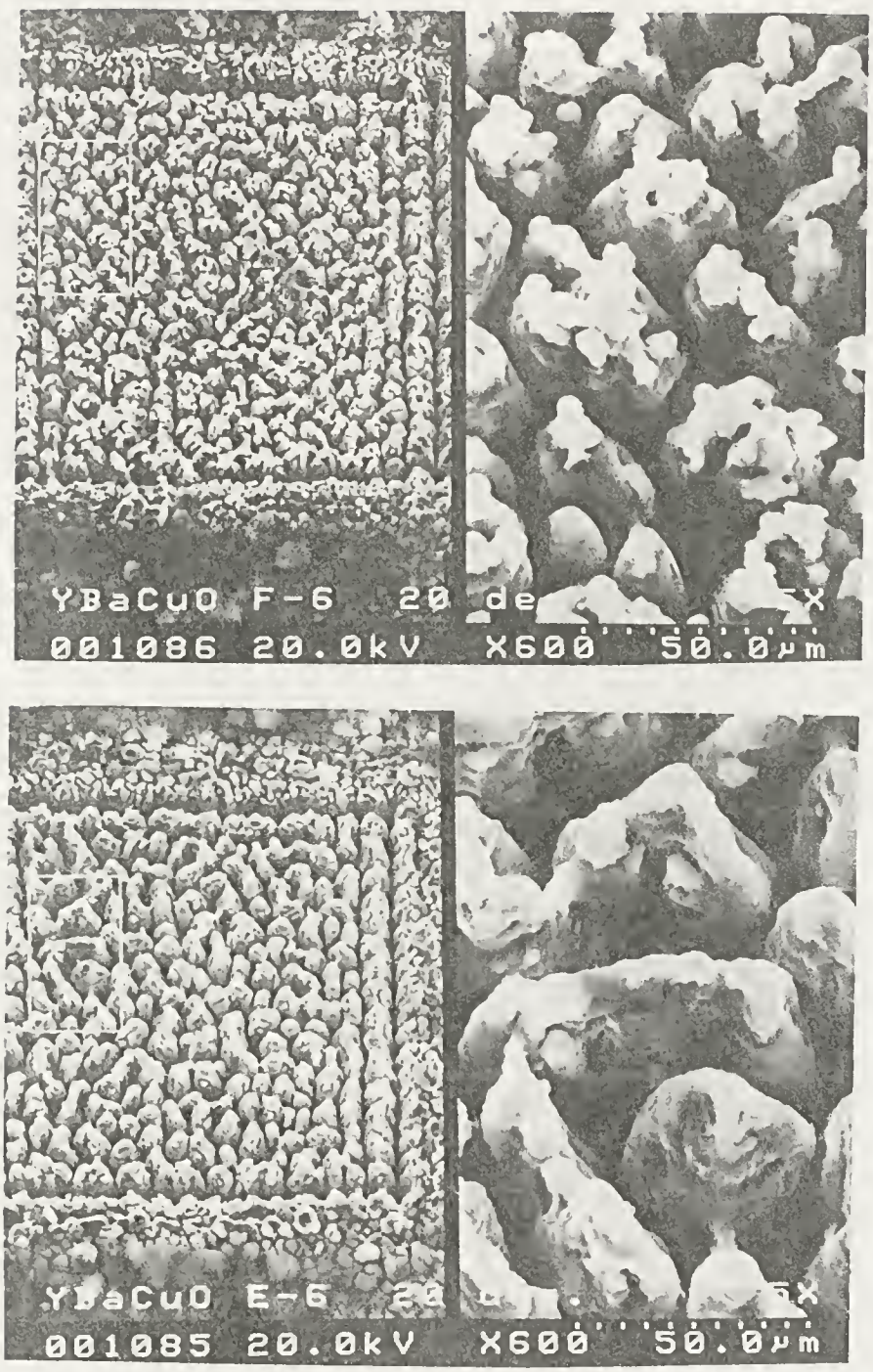

Figure 6-38 YBCO target evaporated using KrF laser. Atmosphere: air. Fluence: 0.5 J/cm^2. Repetition rates: (a) 10 pps (b) 100 pps.

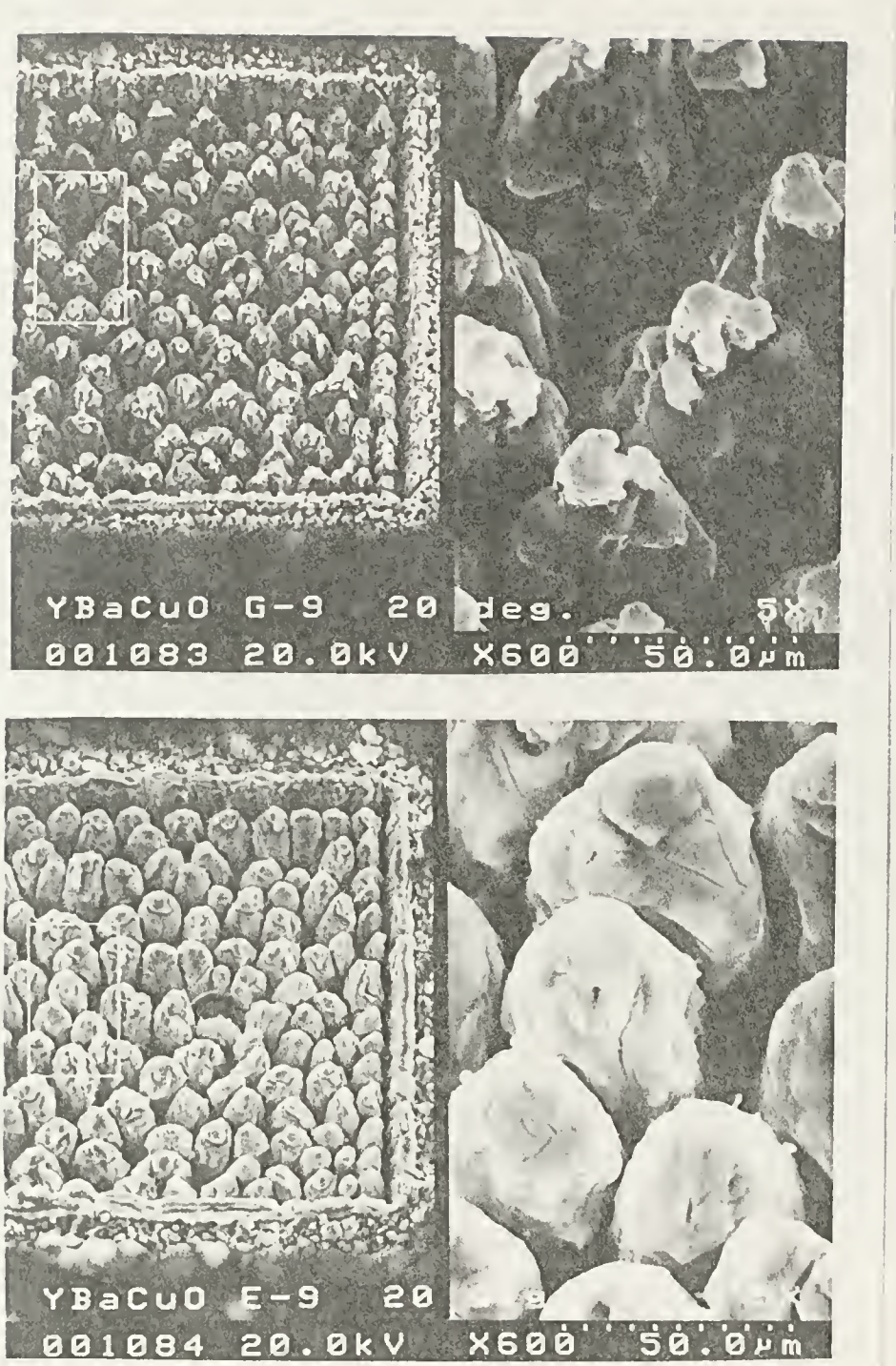

Figure 6-39 YBCO target evaporated using KrF laser. Atmosphere: air. Fluence: 0.8 J/cm^2. Repetition rates: (a) 5 pps (b) 100 pps. Note that surface (b) is smoother.

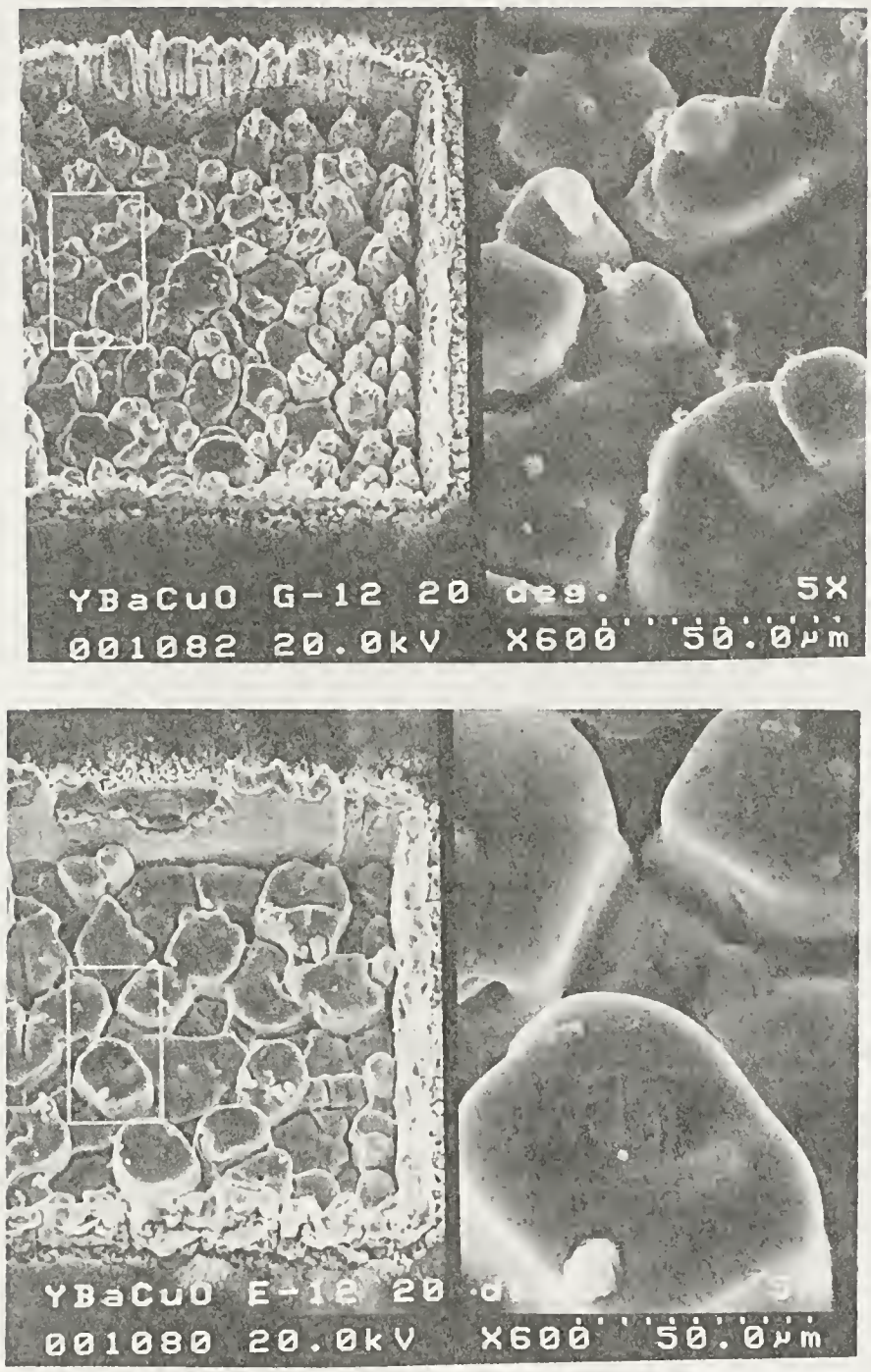

Figure 6-40 YBCO target evaporated using KrF laser. Atmosphere: air. Fluence: 1.1 J/cm^2. Pulse rates: (a) 5 pps (b) 10 pps.

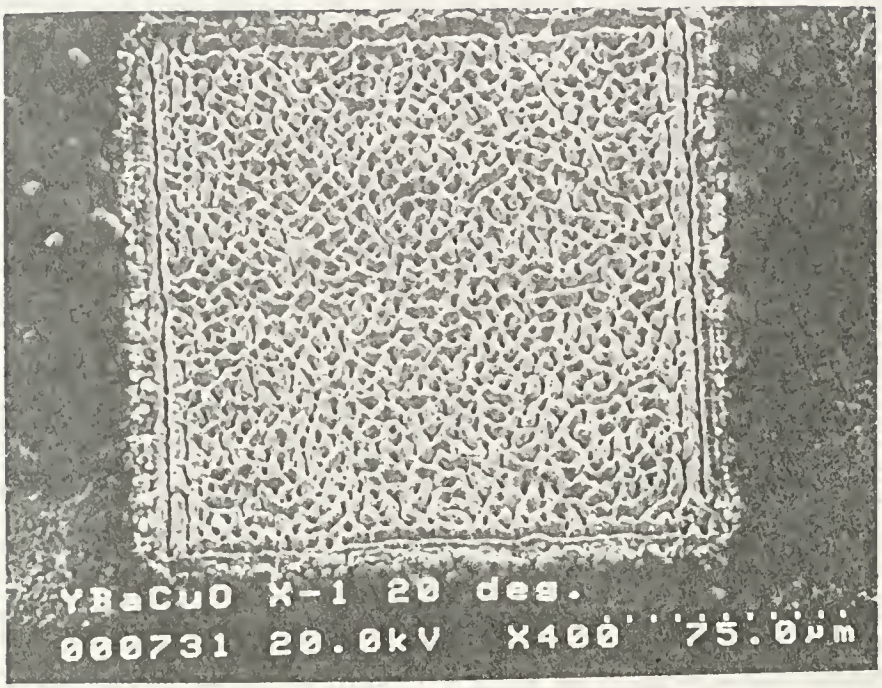

Figure 6-41 YBCO target evaporated using KrF laser. Atmosphere: air. Fluence: 0.4 J/cm^2 Size: 200 µm x 200 µm. Pulse number: 1000. Repetition rate: 10 pps. Top view.

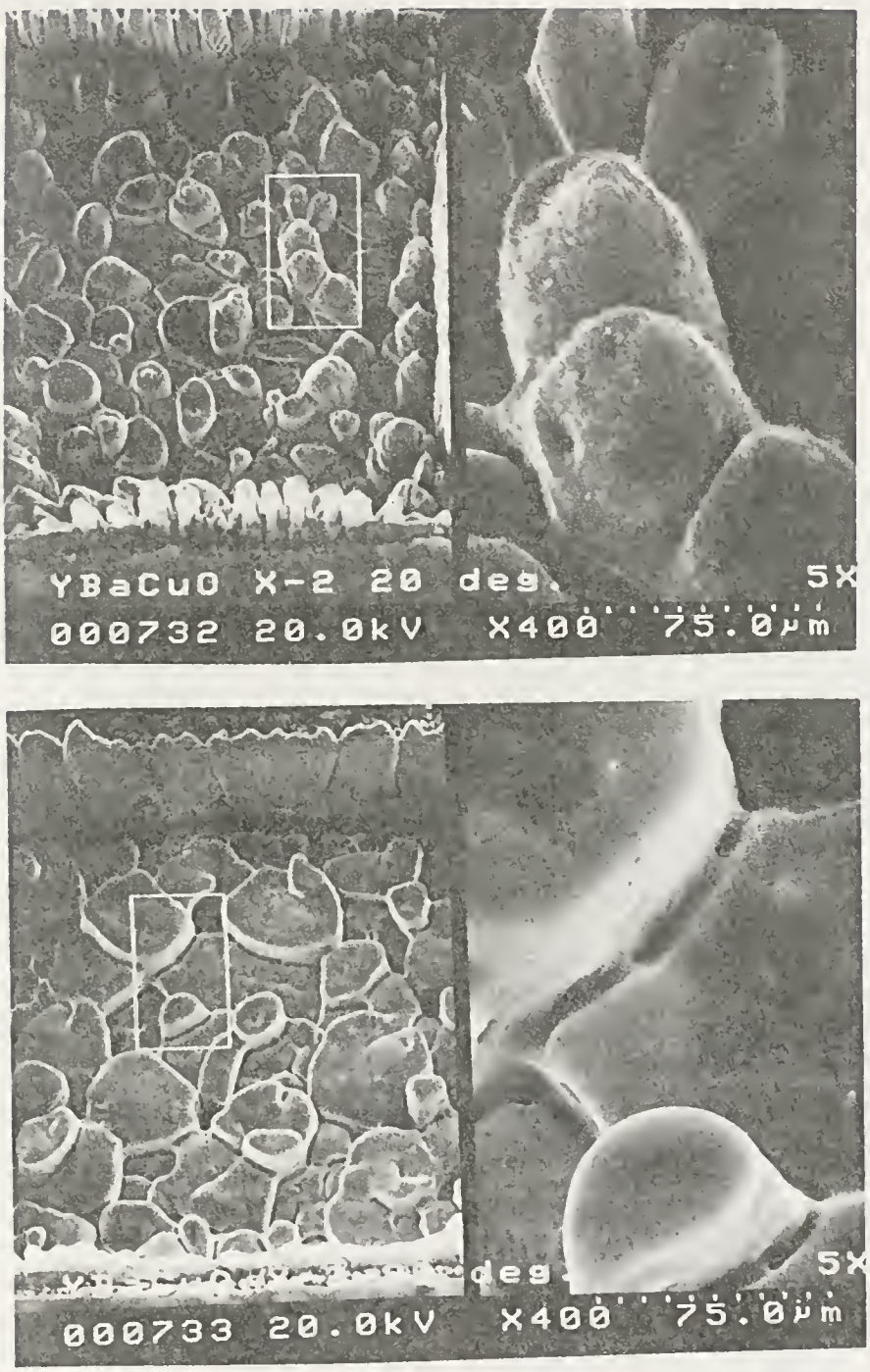

Figure 6-42 YBCO target evaporated using KrF laser. Atmosphere: air. Size: 200 µm x 200 µm. Pulse number: 1000. Repetition rate: 10 pps. Fluence: (a) 0.9 J/cm^2 (b) 1.4 J/cm^2.

at 0.2, 0.3, and 0.6 J/cm^2, consistent with the formation of porous structure previously studied. The cones were slightly thinner than the cones formed at higher pressure and were pointed in the direction of the laser beam.[53, 214]

In metal drillings, the presence of oxygen during the heating has increased the absorption of continuous wave laser and thus the processing speed. This advantage, however, was not observed in pulsed laser drilling, since duration of the pulsed laser is too short to allow significant formation of oxides.[111] The oxygen-initiated chemical reaction also changed the surface tension and affected the geometry of the melt by forming protusions and exothermic reactions by increasing surface heating and therefore higher drilling rates.[111] At low fluence, the evaporation can be described by conventional boiling; however, at high fluence, the evaporation has to be described by superheating of the underlying material due to high recoil pressure.[113]

6.2.7 Effects of Target Density

The evaporation of high- and low-density YBCO pellets was studied in 100 mTorr oxygen at fluences varying from 0.2 to 3.5 J/cm^2 for 100 and 1000 pulses. The repetition rates were 1 and 10 pps, and the evaporation size was 1 x 1 mm. Results showed that the ablated surface morphology was the same as that done in 760 Torr air, namely the porous, cone, and melt structures. The porous structure existed at fluence between 0.2 and 0.5 J/cm^2; the cone structure, at 0.5 to 1 J/cm^2; and the melted structure, at fluence above 1 J/cm^2 for both low- and high-density pellets. A comparison between the fluence required for the surface morphological transition for the low and high density pellets is presented at Table 6-2. Comparisons between the surface morphology of high and low density target evaporated at 2 J/cm^2 for 20, 50 and 100 pulses were made. The result showed that at low pulse number, a distiction can be made between the evaporated surface of a low- and high-density pellet (Figures 6-43 and 6-44). At high pulse number, the surface morphologies are identical (Figure 6-45).

Table 6-2 Surface morphological development of high- and low-density YBCO target evaporated using a KrF laser in 100 mTorr oxygen.

Fluence (J/cm^2)	Low Density		High Density	
	100 pulses	1000 pulses	100 pulses	1000 pulses
0.2	–	–	–	t
0.3	–	t	–	p
0.7	–	c	m	c
1.0	–	c	m	c/m
1.4	m	m	m	m
1.7	m	m	m	m
2.1	–	m	m	m
3.5	m	m	m	m

m-melted, c-cone, p-porous, t-textured

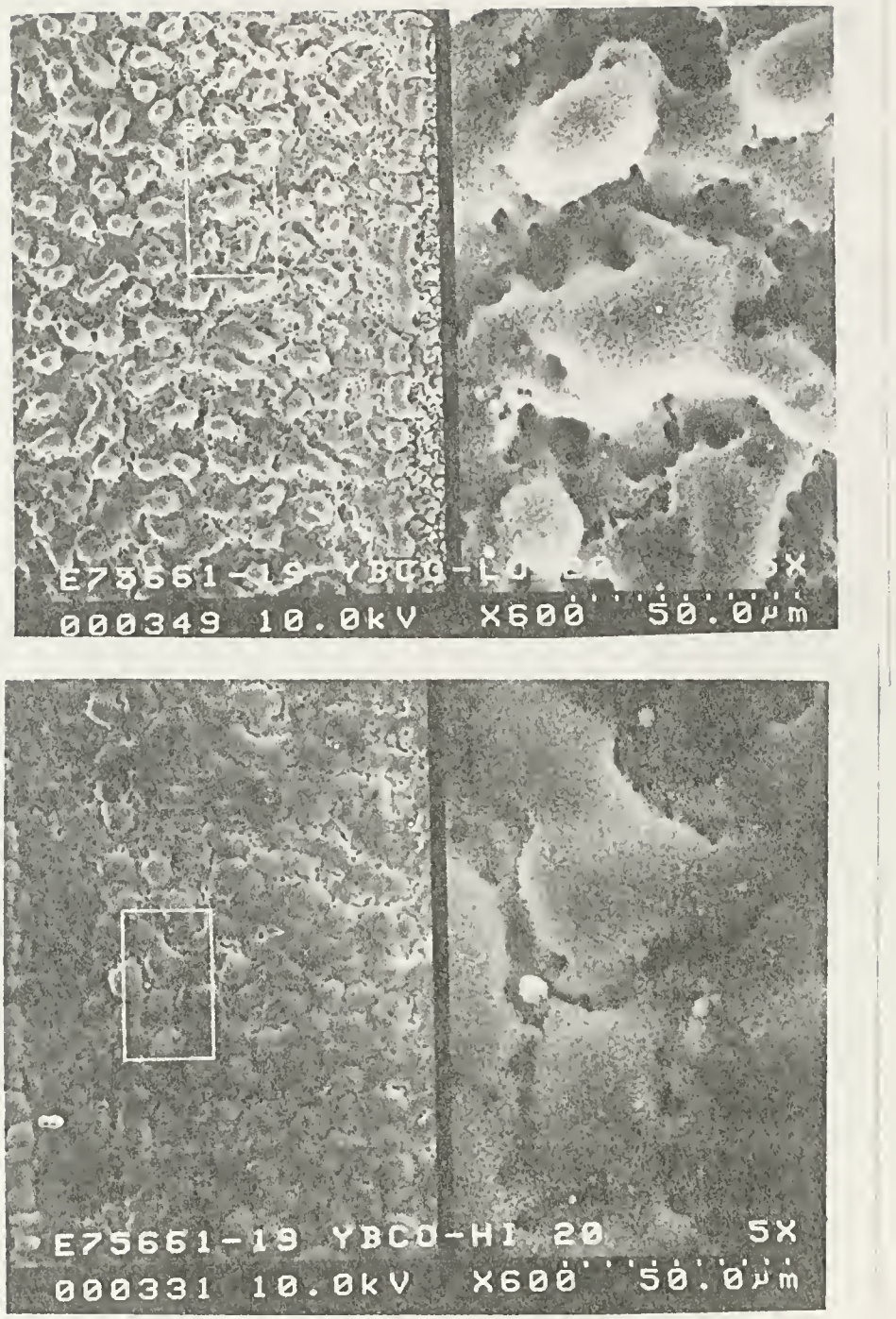

Figure 6-43 YBCO target evaporated using KrF laser. Atmosphere: air. Fluence: 2 J/cm^2. Pulse number: 20. Repetion rate: 1pps. Target density: (a) low density (b) high density.

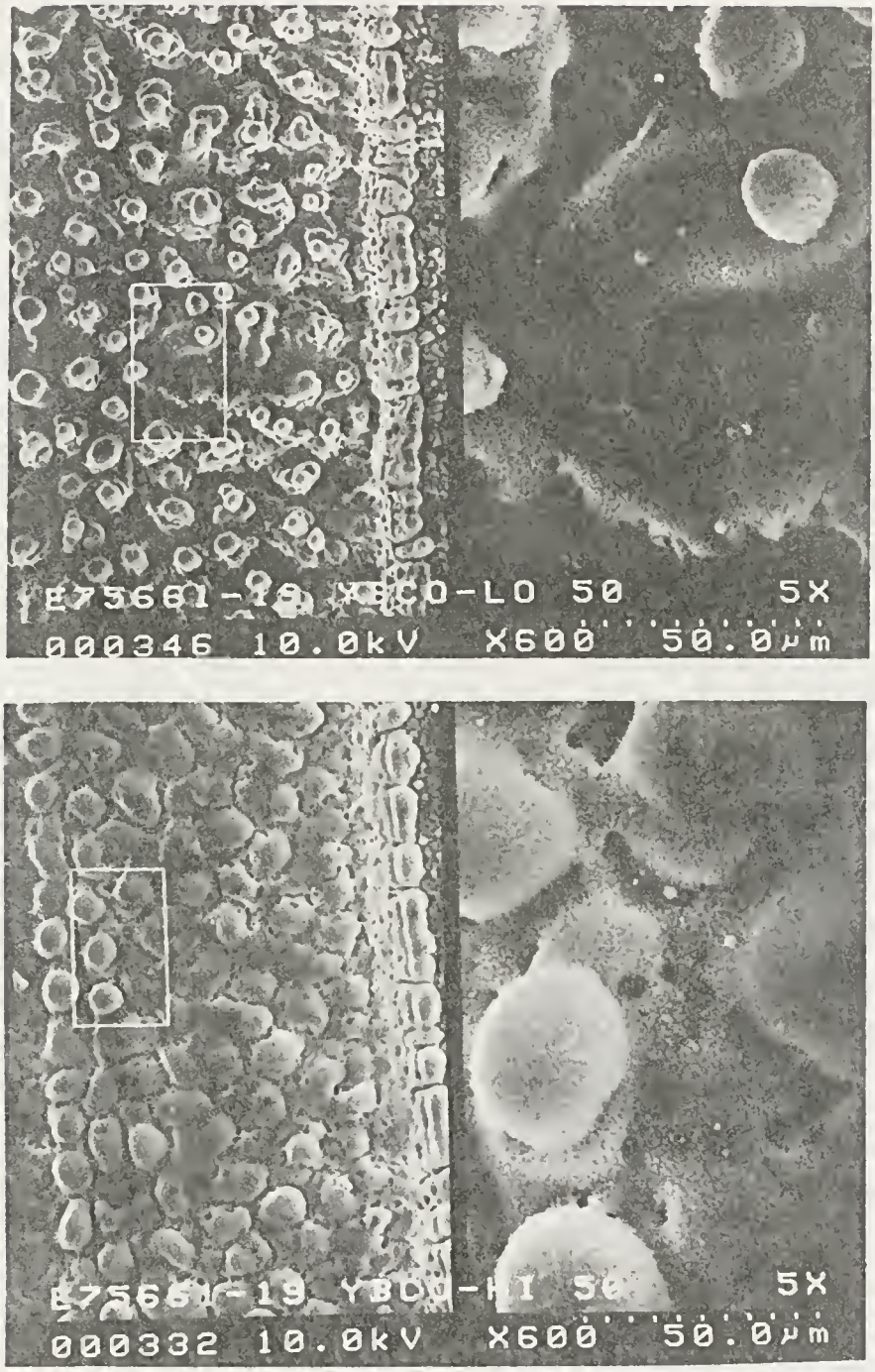

Figure 6-44 YBCO target evaporated using KrF laser. Atmosphere: air. Fluence: 2 J/cm^2. Pulse number: 50. Repetition rate: 1pps. Target density: (a) low density (b) high density.

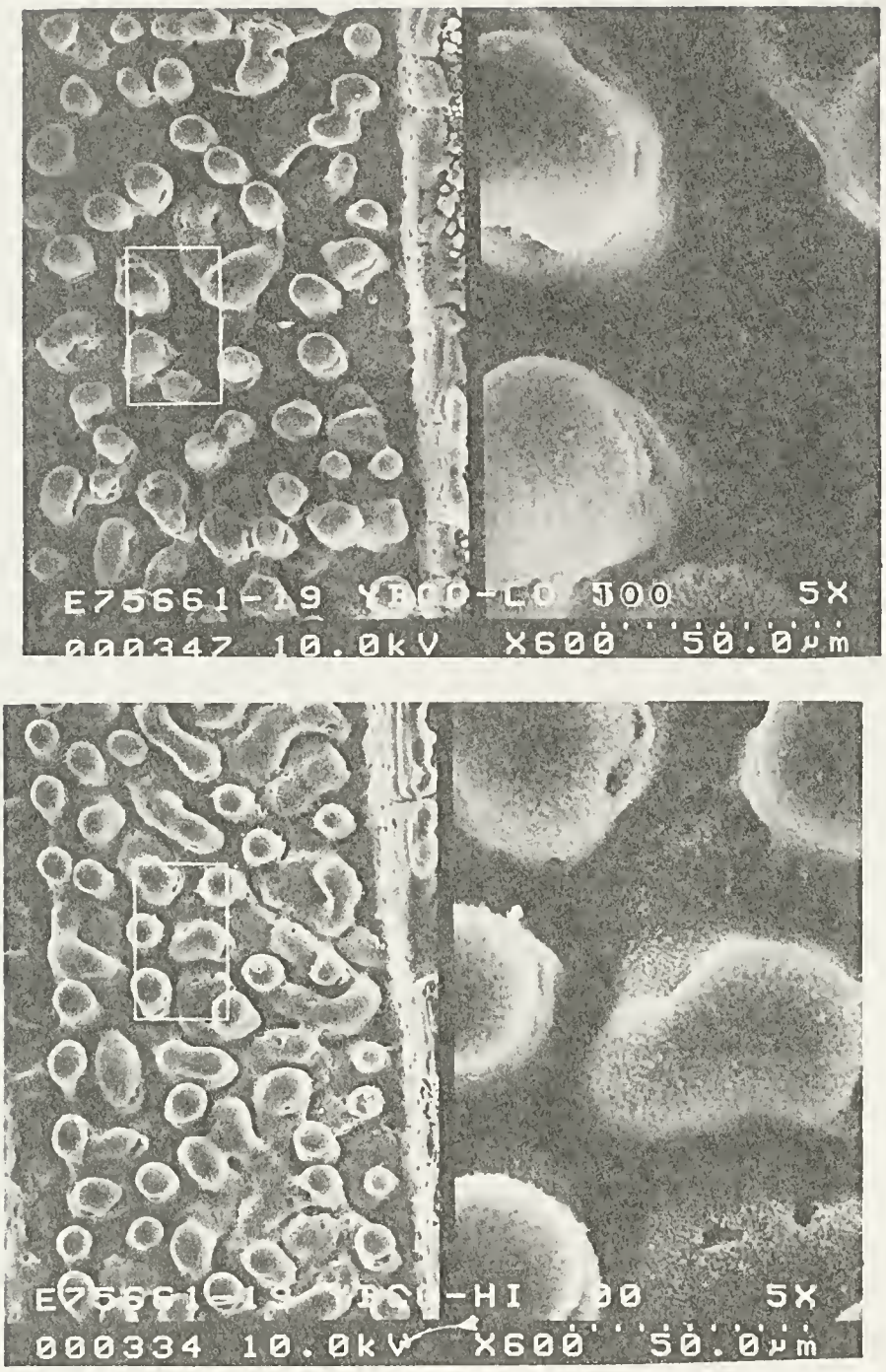

Figure 6-45 YBCO target evaporated using KrF laser. Atmosphere: air. Fluence: 2 J/cm^2. Pulse number: 100. Repetition rate: 1pps. Target density: (a) low density (b) high density.

Although the morphology for the low- and high-density pellets was similar, the etch rate for the low-density pellet was higher than that of the high-density pellet. The mass removed per pulse, however, was relatively the same. The similarity of the morphology suggests that the mechanism for this structure is determined by the properties of the ablated materials, not by initial density conditions.

6.3 Target Morphology Studies of Other Materials

The surface morphology of ceramic, metal and polymer material are studied for comparison.

6.3.1 Ceramics

The surface morphology of $LaAlO_3$ and Al_2O_3 are investigated. This material is ideal since they are single crystals.

6.3.1.1 $LaAlO_3$

The etch characteristic of a perovskite $LaAlO_3$ substrate using a KrF laser beam was studied. The etched $LaAlO_3$ could potentially be used as a substrate a simple SQUID. In addition, it may be used as a model for the evaporation of YBCO pellet, also having a perovskite structure.

A single crystal $LaAlO_3$ substrate was evaporated using a KrF excimer laser microfabrication stage at room temperature and atmospheric pressure. The evaporation was defined by an aperture setting to give an evaporation size of 100 x 100 μm, 200 x 200 μm, and 400 x 400 μm. The laser fluences were varied up to 2.2 J/cm^2 at pulse repetition rates of 1, 10 and 50 pps. The beam was at 90 degrees from the substrate surface.

No evaporation was observed at fluences of 0.44 J/cm^2 or lower. The evaporation between 0.6 and 1.6 J/cm^2 gave a granular-type morphology, whereas the evaporation at 2.2J/cm^2 or higher gave a clean evaporation. At fluence of 0.6 J/cm^2, minimal texturing was observed at the surface (Figure 6-46a). Small granular structures were formed along

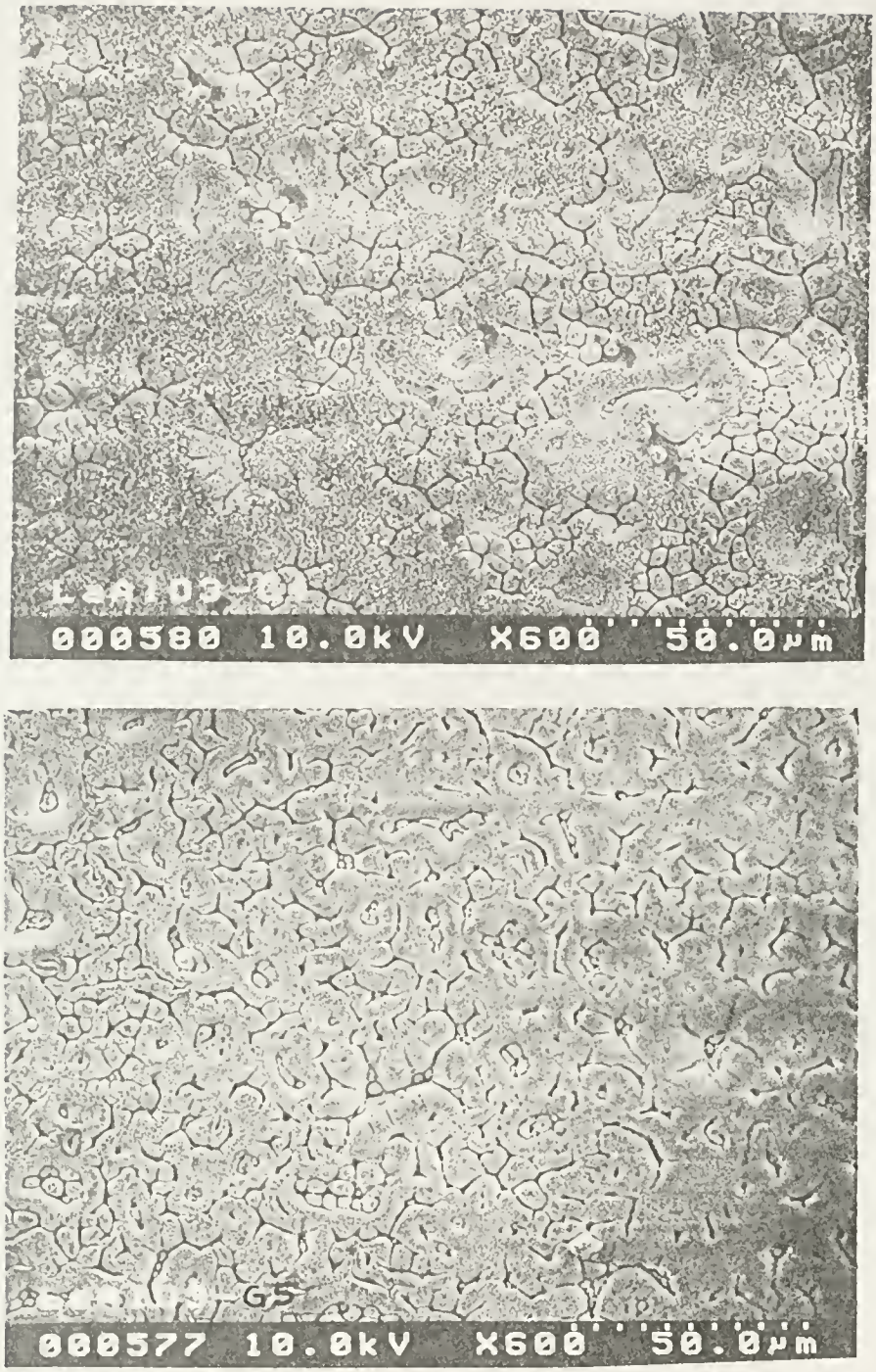

Figure 6-46 $LaAlO_3$ target evaporated using KrF laser. Atmosphere: air. Pulse number: 1000. Repetition rate: 10 pps. Fluence: (a) 0.6 J/cm^2 (b) 0.8 J/cm^2.

the side. At fluences of 0.8, 1.0 and 1.3 J/cm^2, the granules were noticeable, and the texturing became rougher (Figures 6-46b, 6-47a, and 6-47b). At 2.1 J/cm^2, a molten-like surface can be observed. The surface appears smooth at low pulse numbers (Figure 6-48a) and becomes rougher at higher pulse numbers (Figure 6-48b).

The surface morphology of the ablated $LaAlO_3$ was found to depend on the evaporation size. The morphologies of the ablated surface for 100 μm and 200 μm square size were similar. At 500 μm, a totally different morphology, corresponding to a lower fluence value, was observed. The formation of bubble may be caused by the coalesence of gas atoms within the film upon melting, and the surface froze before the surface tension smoothing action took place.[219] It is possible that nonthermal mechanisms, including dense carrier excitation, may be involved in the evaporation of a perovskite structure.[220]

6.3.1.2 Al_2O_3

A ceramic target consisting Al_2O_3 and small amount of Cr_2O_3 was drilled using a KrF excimer laser in a microfabrication stage. The effective fluence at the evaporation plane was 15 J/cm^2 at 100 pps. Up to 12,000 pulses were required to drill the target. The top and side view of the hole can be seen at Figure 6-49. The drilled hole tapers at 4 degree for a sample thickness of 1300 μm. The tapering was caused by the beams being reflected at the edge of the hole.

6.3.2 Metals

Metals were evaporated using a KrF laser to provide a comparison with the evaporation of ceramic materials. All these materials share a common evaporative behavior by having distinct surface morphologies as a function of fluence. The evaporations of titanium, gold, and copper were investigated.

6.3.2.1 Titanium

A titanium target was evaporated using a KrF laser. The fluence was varied from 0.1 J/cm^2 to 3.2 J/cm^2 at repetition rate of 50 pps. The evaporation threshold was found to

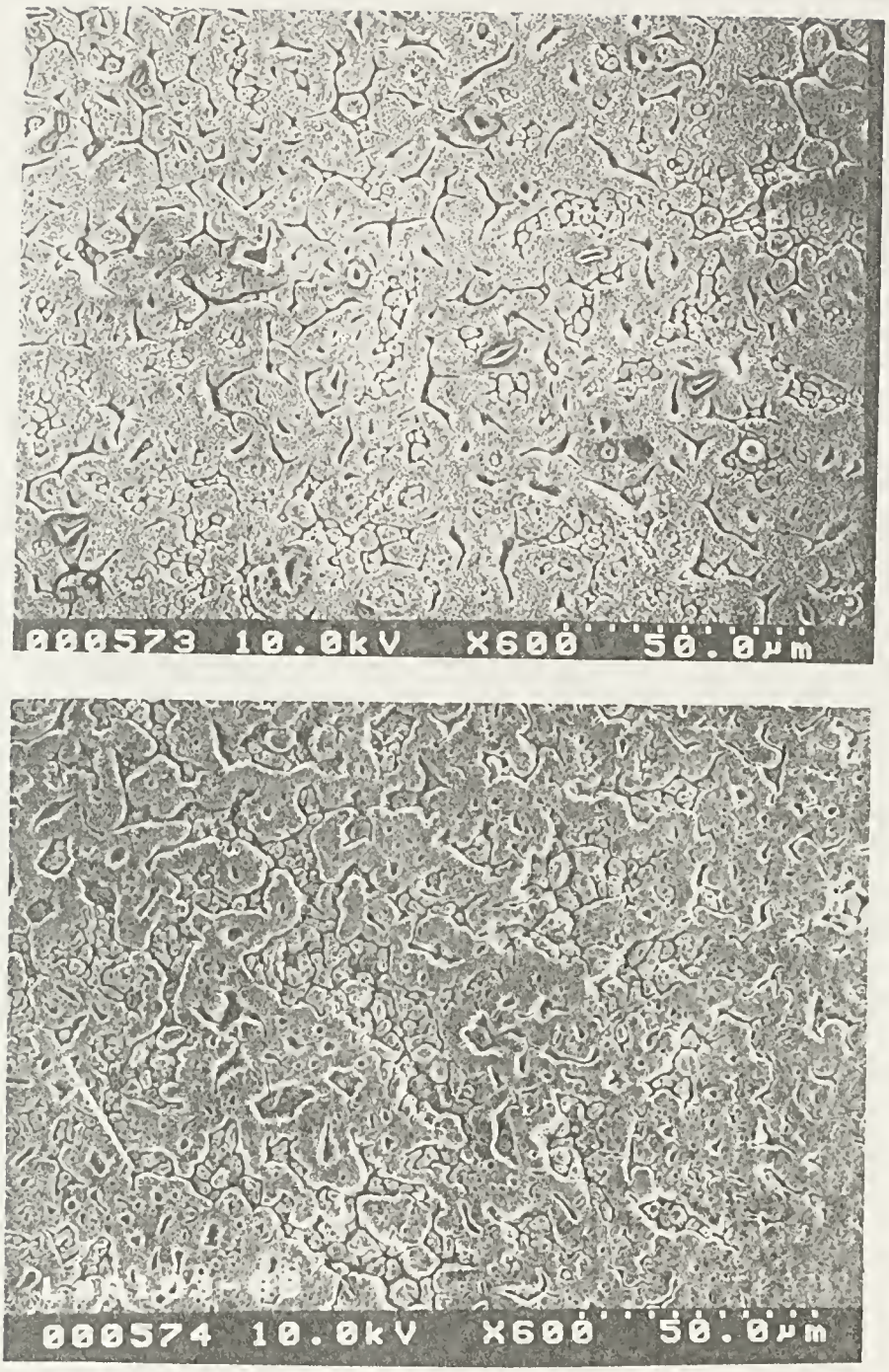

Figure 6-47 $LaAlO_3$ target evaporated using KrF laser. Atmosphere: air. Pulse number: 1000. Repetition rate: 10 pps. Fluence: (a) 1.0 J/cm^2 (b) 1.3 J/cm^2.

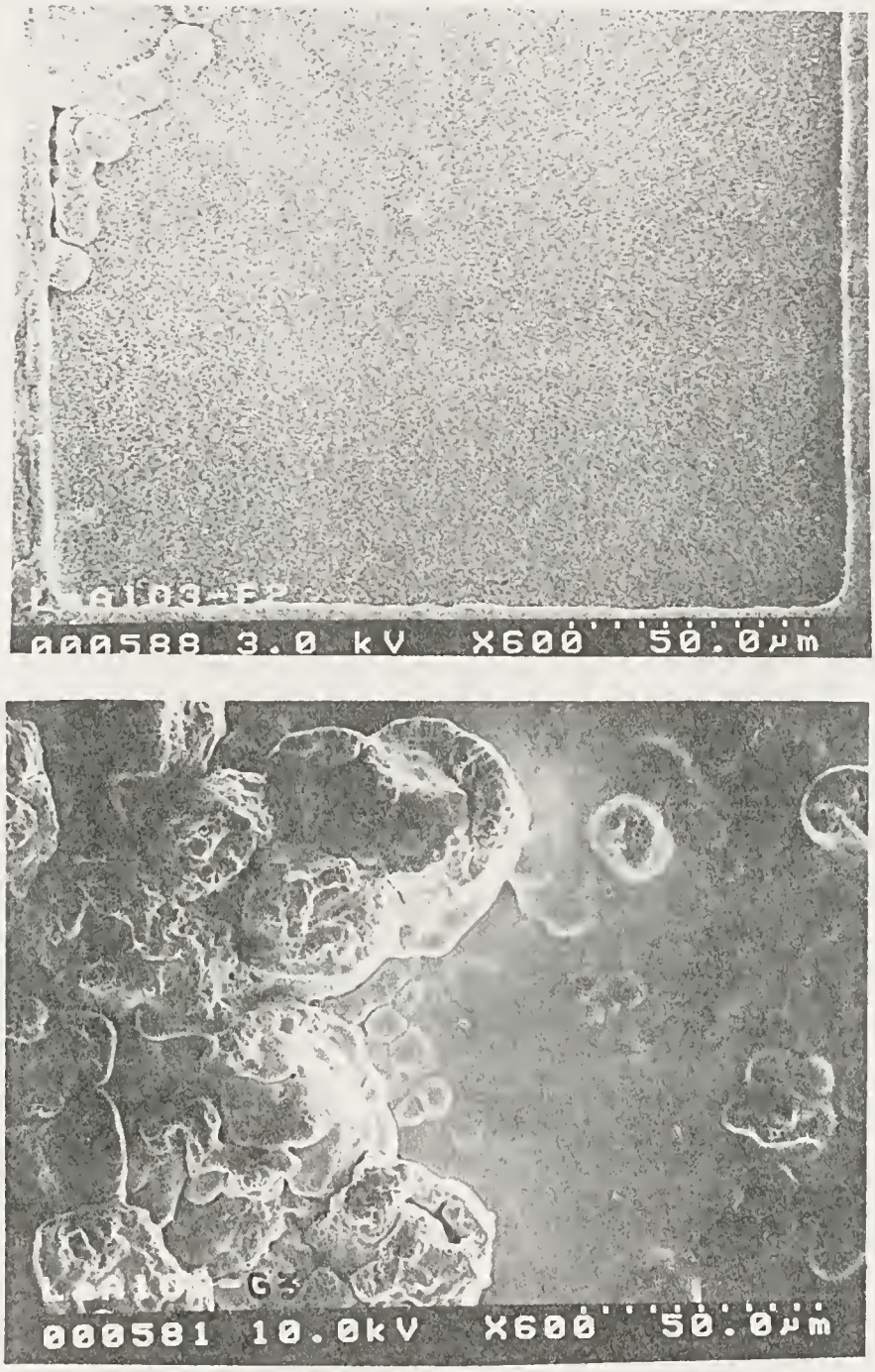

Figure 6-48 $LaAlO_3$ target evaporated using KrF laser. Atmosphere: air. Fluence: 2.1 J/cm^2. Repetition rate: 10 pps. Pulse number: (a) 200 (b) 1000.

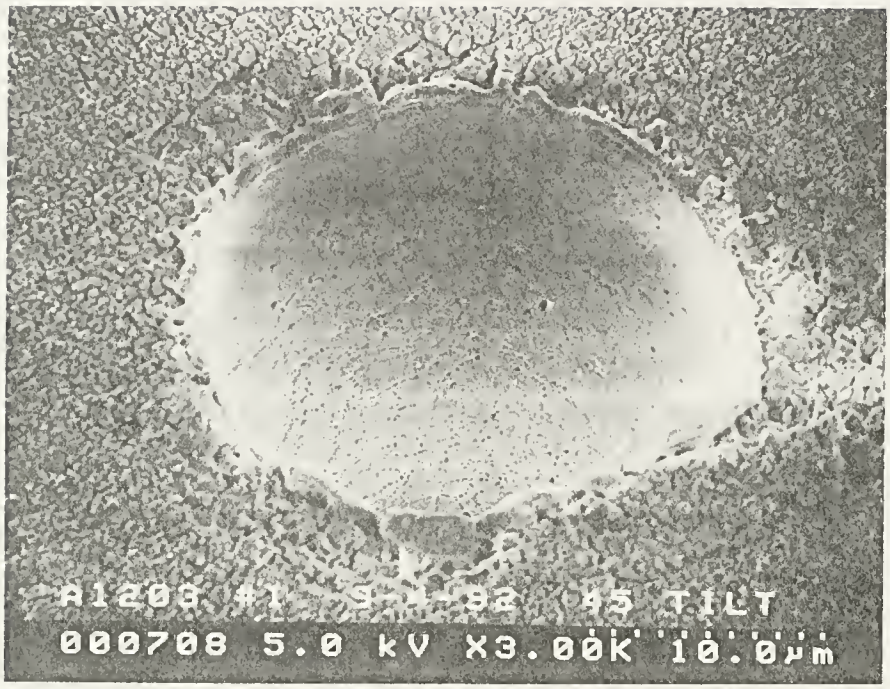

Figure 6-49 Al_2O_3 target evaporated using KrF laser. Atmosphere: air. Fluence: 15 J/cm^2.

be 0.2 J/cm^2. The evaporated surface showed a granular structure at 0.8 J/cm^2 and a molten structure at 1.6 J/cm^2.

The titanium target was 99.7% pure and was polished using 600A sandpaper. The original titanium surface was rough with grain boundary size of 30 microns. The evaporations were done on a microfabrication stage. The evaporation size was 100 μm x 100 μm, and the repetition rate was kept at 50 pps. The pulse numbers were varied from 50 to 1000. The sample was analyzed using SEM for the morphological changes.

The evaporation threshold was observed at 0.2 J/cm^2, at which surface texturing began to take place without altering the contours of the virgin material (Figure 6-50). At 0.4 J/cm^2, the surface became more textured, and the contours of the original surface had partly disappeared (Figure 6-50). At 0.8 J/cm^2, a granular surface morphology was formed. This structure may have been caused by the formation of surface grain boundaries. The molten surface appearance was formed at 1.6 J/cm^2 (Figure 6-51). The surface of the melt showed a cracking, possibly due to the formation of oxides, which have different thermal expansion coefficients than the titanium metal. Only 10^{-28} atm of oxygen was required to oxidize Ti at 1000 °C.[221]

6.3.2.2 Gold and copper

The evaporation of gold was similar to the evaporation of titanium metal. At fluence of 2 J/cm^2, a rippled molten surface was formed (Figure 6-52). A laser irradiation of iron using excimer laser showed surface damage caused by the displacement of molten surface layer by evaporation pressure.[222] These metals have the same reflectivity value of 0.3 at 248 nm. Copper metal also shows similar textured surface at low fluence and molten surface at higher fluences. Due to the absence of phase impurities, the surface texturing may have been caused by beam reflections or interferences instead of by phase impurity shielding as seen in the evaporation of the YBCO.

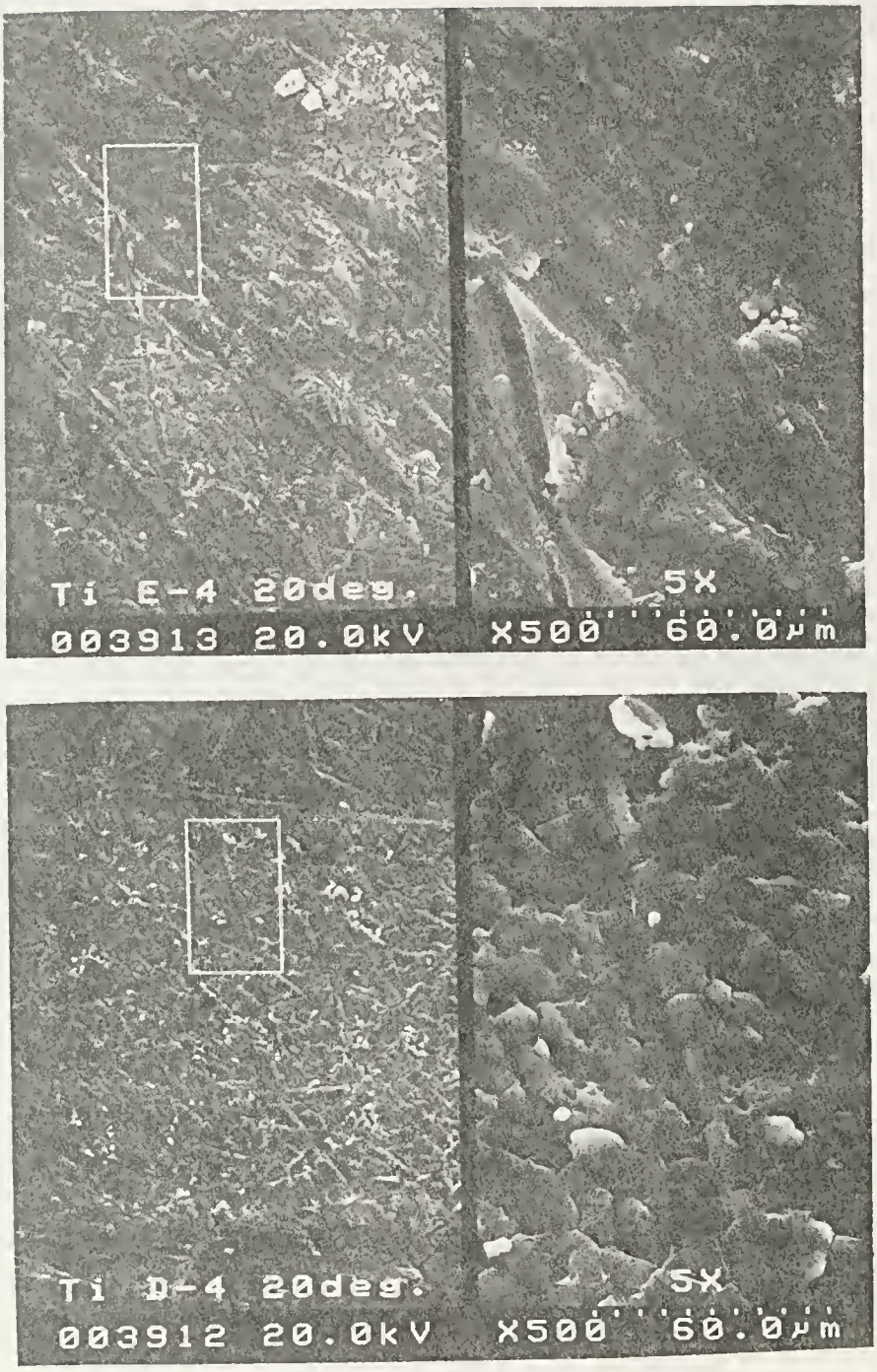

Figure 6-50 Titanium target evaporated using KrF laser. Atmosphere: air. Pulse number: 500 pulses. Repetition rate: 50 pps. Fluence: (a) 0.2 J/cm^2 (b) 0.4 J/cm^2.

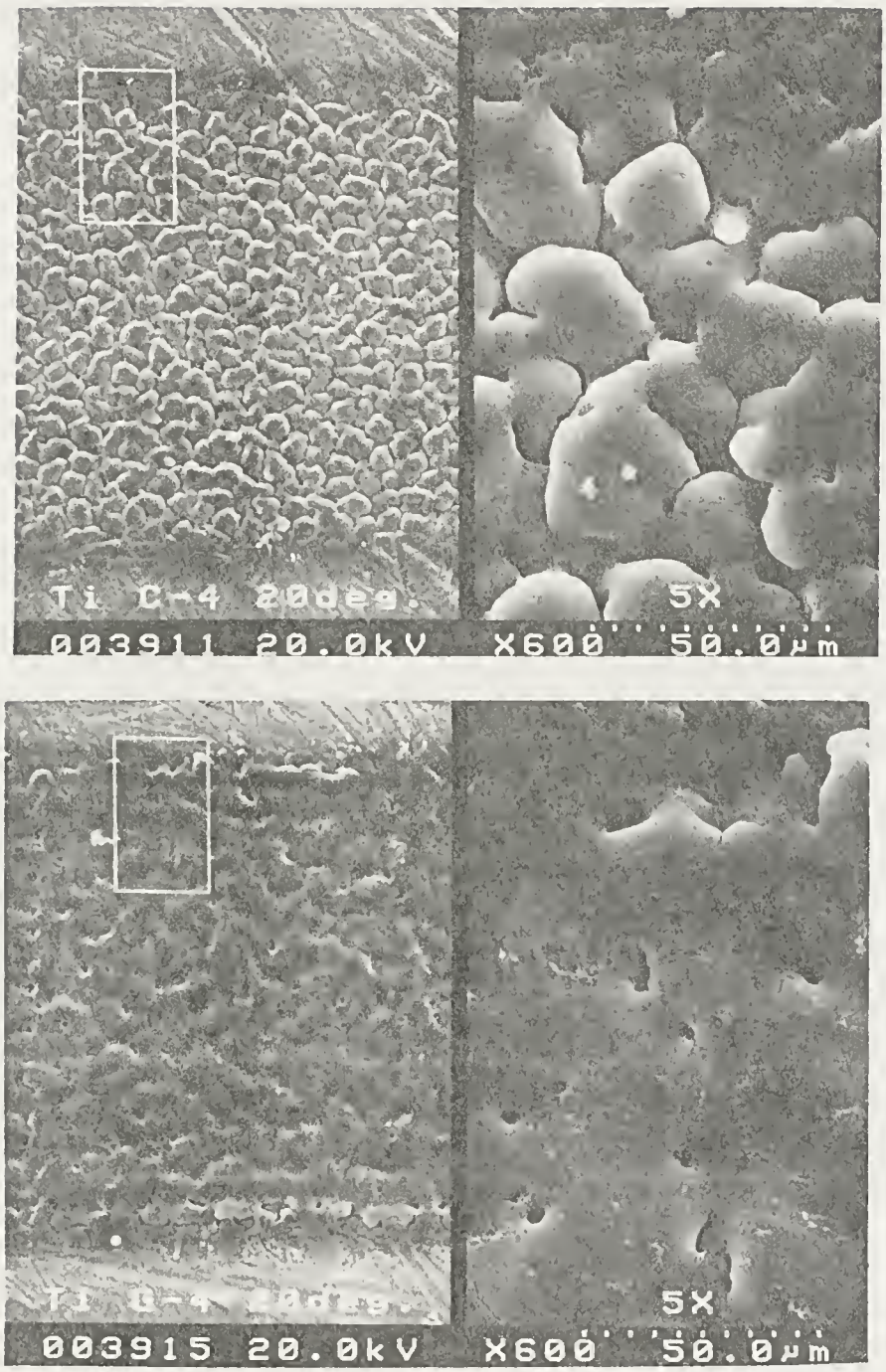

Figure 6-51 Titanium target evaporated using KrF laser. Atmosphere: air. Pulse number: 500 pulses. Repetition rate: 50 pps. Fluence: (a) 0.8 J/cm^2 (b) 1.6 J/cm^2.

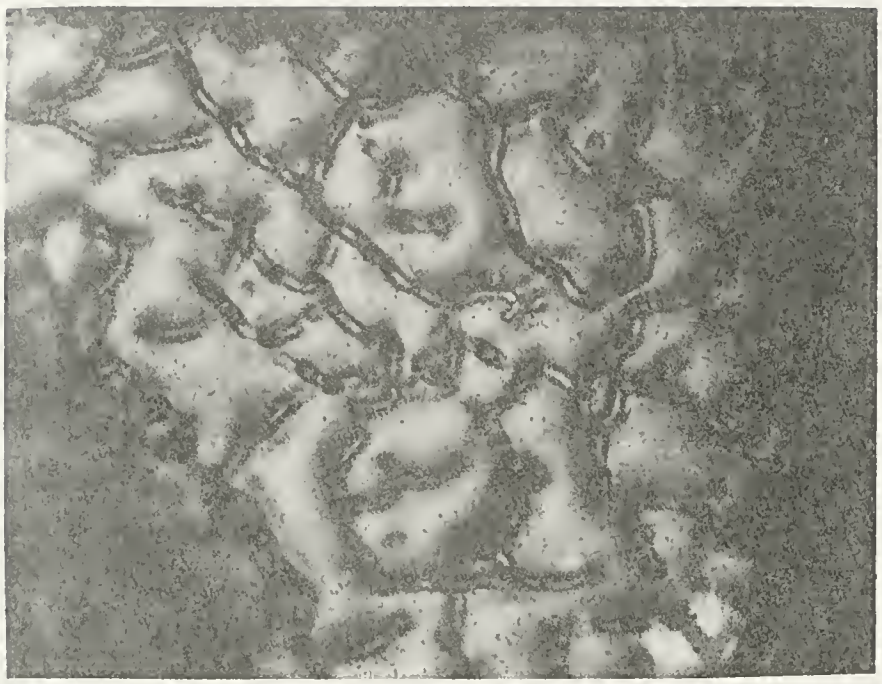

Figure 6-52 Gold target evaporated using KrF laser. Atmosphere: air. Fluence: 2.0 J/cm^2. Note the formation of surface ripples.

6.3.3 Polymers

The evaporation of polyimide polymer was performed. The evaporation threshold was found to be 0.03 J/cm^2. The surface morphology of a Kapton film evaporated at 25 mJ/cm^2 is shown in Figure 6-53. At higher fluences, up to 0.1 J/cm^2, a charred polymer surface could be seen. A semi-molten like surface, where partial evaporation was taking place could be seen on the surface evaporated at fluences between 0.1 to 0.2 J/cm^2. This condition is analogous to the cone formation range in the YBCO sample. At higher fluences, a molten morphology, the result of a complete evaporation, could be seen. This surface had a smooth, mirror-like finish. The etch depth at 1 J/cm^2 was 0.5 μm/pulse. In general, the characteristic evaporation of polymer was similar to those of ceramics and metals, with the threshold value approximately an order of magnitude lower. The theory of polymer evaporation has been discussed in the literature.[223]

6.4 Modelling on Target Morphology

The development of surface morphology during the pulsed laser evaporation of YBCO has an undesirable influence on the evaporation process. First, it reduces the evaporation efficiency by diluting the laser energy over a larger surface area or by increasing the plasma redeposition inside the target crater walls. Second, the formation of these surface features is linked to the formation of film particulates. A fundamental understanding of the formation of this surface morphology is therefore important in improving the performance of the PLD technique. This section will address some mechanisms related to the formation of surface morphology as presented at section 6.2 and 6.3.

Although there are numerous possible approaches to explain the formation of surface morphology, four mechanisms will be considered in this discussion. First, is the selective removal due to shielding of the target material with material that is nonabsorbing

Figure 6-53 Polyimide Kapton® target evaporated using KrF laser. Atmosphere: air. Fluence: 25 mJ/cm^2. The surface morphology showed the presence of debris.

or difficult to ablate, such as the formation of surface impurities. An example would be the shielding of a low etch rate, yttrium-rich phase on the YBCO. Second is the removal and redeposition of an evaporated material onto the columns or walls. Although a cross-sectional view of an evaporated target showed that the material under the evaporated surface is virgin, there is evidence of plasma redeposition (Figure 6-54). Third is the melting and resolidification mechanism by which a molten layer formed at the surface during the laser pulse is recystalized during target cooling due to seeding at the bottom of the crater. Experimentally it has been shown that the surface of a target evaporated at high fluence contains only a single phase. Last is melting and ejection in which the molten target solidified and formed the protusion. Although unlikely because of the requirement of a large molten pool, some cross-sectional views have shown that this mechanism is possible (Figure 6-55).

The formation of the surface morphology is, in fact, a combination of the above mechanisms, depending on the fluence and pulse number. At low fluence, the mechanism involving surface impurities and selective removal is the most likely. A mechanism for the initiation and development of cone surface impurities will be discussed. At high fluence and low pulse number where the surface morphology is still rather simple, melting and resolidification are possible. At high fluence and high pulse number, where the crater is deeper, condensation and melt ejection mechanisms are possible.

This chapter will discuss the physics for all the above mechanisms, including photon absorptions, effect of surface asperties, surface cracks due to rapid cooling, the effect of impurities shielding, surface tension effect on surface ripplings, and ray tracing mechanisms.

6.4.1 Surface Morphology at Low and Medium Fluences

At medium low and medium fluence, the mechanism for surface morphology formation is influenced by the surface asperties and material shielding. The effect of

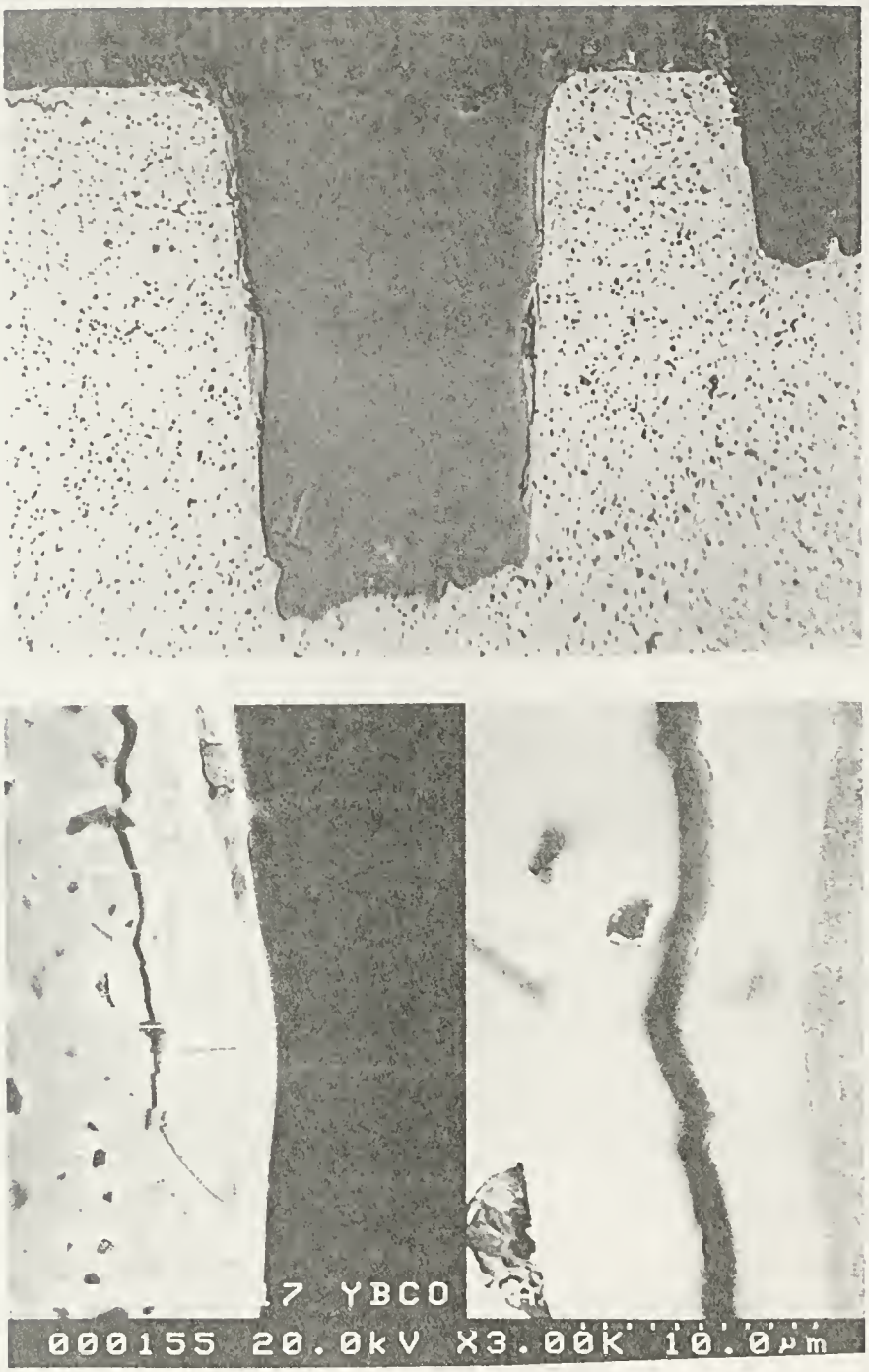

Figure 6-54 Cross sectional view YBCO target evaporated using KrF laser. Fluence: 2.0 J/cm2. Pulse number: 1000. Note the formation of melt on the crater wall. (a) cross sectional view of the crater (b) close up of the deposit on the left wall.

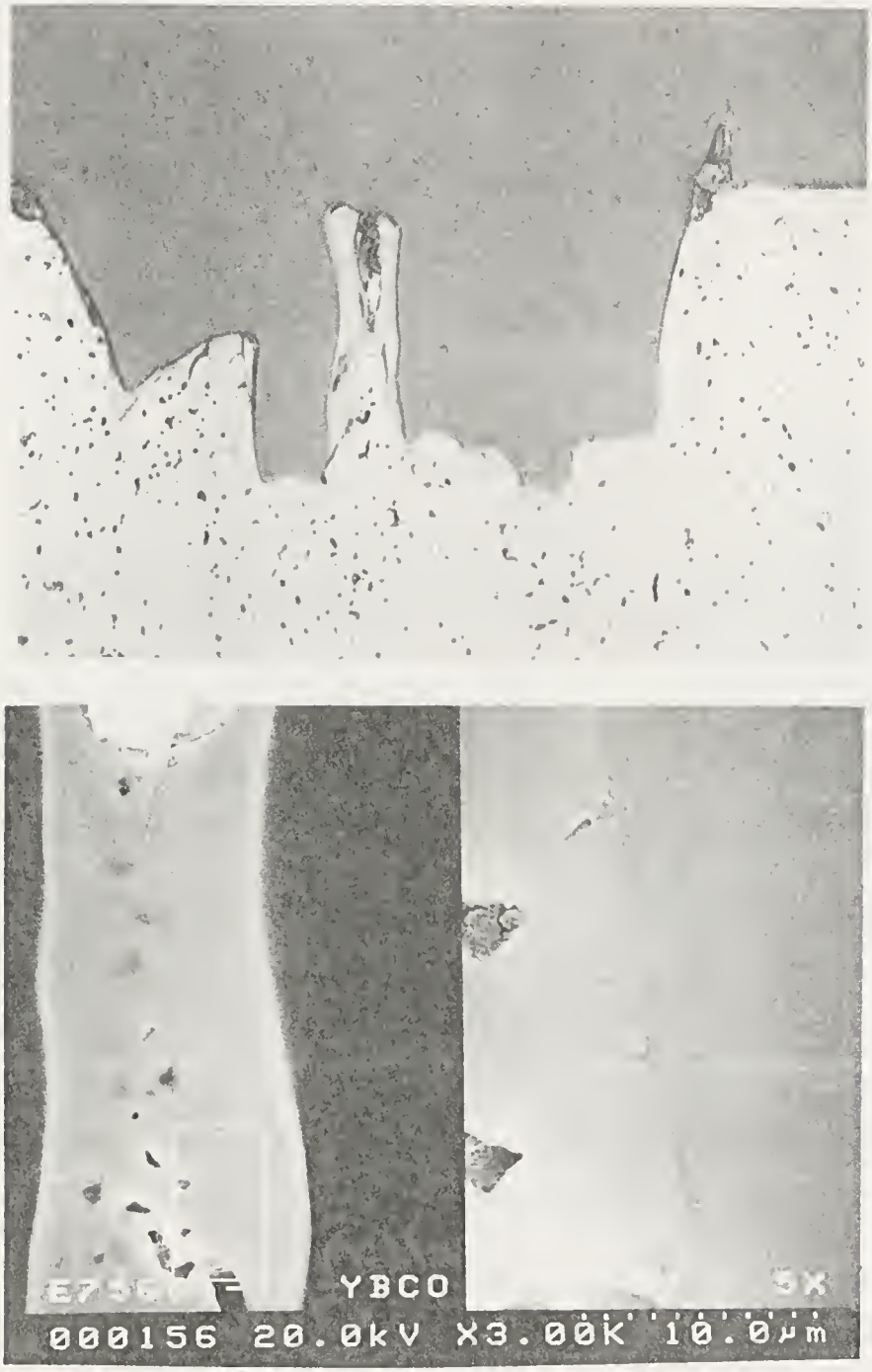

Figure 6-55 Cross sectional view YBCO target evaporated using KrF laser. Fluence: 1.5 J/cm2. Pulse number: 500. Note the formation of column on the crater bottom. (a) cross sectional view of the crater (b) close up of the deposit on the column.

surface nonuniformity and the formation of a yttrium rich phase on the irradiated surface are discussed below.

6.4.1.1 Radiation heating and suface asperties

In the treatment of radiative heat transfer, an assumption is made regarding whether the irradiated surface is diffuse or specular. A diffuse surface is a surface that reflects incoming radiation in all directions, such as a rough surface. A specular surface, on the other hand, reflects radiation to directions opposite to the normal, such as a polished or molten surface. In addition to the difference in their overall reflectivity values, a specular and a diffuse surface also have different reflectivities on their micoscopic scales. While the surface reflectivity varies with temperature for long wavelength,[224] it can be assumed constant for temperatures up to 1500 K.[225]

In the evaporation of highly absorbing surface, such as the YBCO using a highly energetic UV beam, the radiation is absorbed and confined to a thin surface layer. The thermal energy is transferred to the bulk material by thermal conduction, as described in Chapter 4. A small portion of the heat flux delivered to the surface is reflected. If the beam energy is low, the absorbed energy is primarily used to melt the surface without evaporation, resulting in the formation of a textured surface. At high energy, however, the process is accompanied by evaporation in the form of plasma plume and often by ejection of molten material. If the surface is not uniform and contains surface asperties, the surface temperature distribution and the evaporation rate across the irradiated surface may not be uniform. In sputtering, surface asperities, imperfections, impurities with low evaporation yield, and crystal grain orientation contribute to the formation of surface morphology.[196]

In a process that requires the interaction between a target surface and a laser radiation, the nonuniformity could be caused by target surface asperties or the nonuniformity of the beam itself. The surface asperties of a material are related to the material properties, which are thermal properties (conductivity, expansion, conductivity), optical properties (absorption, transmission, refraction) or thermodynamic properties

(density, phase separation). For example, a small pore or crack on an otherwise smooth surface will have different absorption properties than the surrounding material. A similar argument can be made with surface impurities on the surface. The surface absorptivity has been shown to decrease as the result of laser radiation , and mechanical polishing could introduce surface amorphization.[226] In sputtering, a different etching rate is expected for different crystalline orientation. The uniformity of the beam may be caused by the nonuniformity of the optics along the laser path, such as dust or a scratch on the optics.

6.4.1.2 Shielding of porous and cones

It has been shown in evaporation at low fluence that the formation of the yttrium-rich phase is responsible for the formation of pores and cone structures. The role of this yttrium-rich phase will be discussed, first in regard to the formation of the yttrium-rich phase, and second, in regard to the stability and growth of this phase with increasing pulse number and fluence.

The formation of the yttrium-rich phase, a combination of the Y_2BaCuO_5 and Y_2O_3 phases, is possible thermodynamically. From a phase diagram of a Y-Ba-Cu-O system, it can be shown that the Y_2BaCuO_5 phase is the stable solid phase in equilibrium with a liquid solution at high temperature. The evaporation of the Y_2BaCuO_5 phase, in turn, gives a Y_2O_3 phase. The etch-rate measurement showed that the Y_2O_3 phase is the most difficult to evaporate, consistent with the fact that this phase is found on the surface of pores and cones structures.

It is possible that the yttrium-rich phase forms as the result of a metastable phase entrapment, especially at a very high cooling rate. The solidification of the molten liquid takes place on the advancing solid-liquid interface. If the cooling proceeds slowly, crystallization will take place due to the presence of nuclei at the solid crystalline phase. If the cooling takes place rapidly, however, a metastable solid state may form by the rapid increase in the liquid viscosity. This metastable phase could later be transformed to a more stable state by forming a macroscopically a discontinuous phase,[227] which in this case is an

yttrium-rich phase. A thermodynamic treatment of a trapped solute on a crystal-solute interface has been discussed.[227]

Once the yrrtium-rich phase forms, a mechanism is needed to sustain its growth. The evidence on the evolution of cones and pores shows that this phase grows with increasing pulse number. A mechanism similar to that of sputtering, based on the surface diffusion, can be used. The principle is based on the random diffusion distance. If the distance between two cones is less than two random diffusion distances, the cones will coalesce; otherwise the cones remain separate. The average distance between the cones is therefore equal to two random diffusion distances. Since the diffusion coefficient increases with temperature, it can be expected that the random diffusion distance increases with increasing fluence. The random diffusion distance for the porous and cone structures are approximately 7 and 10 μm, respectively. The stability of the yttrium-rich phase depends on the balance between the rate of diffusion and the rate of evaporation. At high fluence or high temperature, the random diffusion distance increases; however the evaporation rate also increases causing the yttrium-rich phase to disappear at high fluence.

The growth mechanism of the impurities phase was confirmed during the evaporation of a superconducting target containing a finely dispersed 1-μm gold powder. During the evaporation, it can be seen that the gold powder migrates to the surface forming gold tip columnar structure (Figure 6-56). Since the sizes of these gold particles, 3 to 4 μm, is greater than in the original gold powder, it is concluded that the gold has migrated to the tip of the columns and finally coalesced.

6.4.2 Surface Morphology at High Fluence

At high fluence, a yttrium phase which result in pores and cones morphology does not form. The development of surface morphology, instead, is connected to the surface reflectivity and surface cracks formed due to the rapid cooling. The effects of surface cracks, surface ripples and the ray tracing are discussed below.

Figure 6-56 Cross sectional view YBCO-gold powder target evaporated using KrF laser. Notice the formation gold spheres at the tip of the columns.

6.4.2.1 Surface cracks due to self-stress

The formation of surface cracking during the laser evaporation of superconducting target can be attributed to the rapid cooling of the target surface following each laser pulse. These surface cracks are responsible for the development of surface morphology. Understanding crack evolution is fundamental to preventing the formation of film particulates.

The surface crack evolution was studied as a function of pulse number. The presence of surface cracking with a typical crack width of 0.1 μm can be seen from the evolution of the target morphology within the first 10 pulses (Figures 6-25, and 6-26). In this study, the same area was monitored with increasing pulse numbers (notice the presence of the defect on the top right-hand corner of each micrograph). Initially, the polished surface contained some pores with sizes in the order of 1 μm. As the number of laser pulses increased, the number of pores decreased. It can be observed that the surface melted and that some of the pores were filled. There are 10 pores per 100 μm^2 area on the polished virgin sample, and number of pores decreased approximately at the rate of one pore per pulse. It has been studied that the melt front velocity involves a balance between the rate of melting and recrystallization.[228] For a molten silicon irradiated using pulsed ruby laser, the crystallization velocity is 2-3 m/sec,[229] which can be translated to a distance of 0.06 μm for 20 nsec pulse.

The reduction of one pore per pulse is not unreasonable since a 1-μm diameter pore can be filled with the volume of a layer only 0.005 μm thick in an evaporation size of 100 μm^2, much smaller than the etch rate of approximately 0.1 μm per pulse. The pore filling can be either from the vapor condensation or surface melt flow if there is enough time for surface relaxation. It has been seen that a 1-μm pore can disappear in only one pulse. The disappearance of the pore may sometimes leave a surface depression due to partial pore filling. Occasionally, bubbles are seen, possibly due to the evaporation of volatile

impurities or trapped gas bubbles. If the pore has a high aspect ratio, however, the pores could be closed without filling them.[230]

Most cracks are terminated or initiated at a surface pore, with the exception of a few cracks that terminate at a pore underneath the surface. These cracks are caused by the thermal expansion mismatch between the molten layer and the bulk material during surface cooling. The origin of these cracks, which can be explained by stress intensity factor theory, are always initiated or terminated at the pores. It has been observed that some cracks grow or disappear in only one pulse, coinciding with the appearance or disappearance of the pore. The cracks near large surface imperfections or pores, however, can persist beyond 10 pulses. On average, the cracks grow or disappear at a rate of 2 μm per pulse. For cracks that are not completely healed, cracking can continue without the presence of a pore.

Materials that are subjected to temperature shock develop substantial surface stresses.[194] Since the stress level depends on many parameters, such as material ductility, porosity, pre-existing flaws and the stress duration, this value varies for different materials and conditions. For an ideal system, however, the surface-cracking phenomena can be explained using a thin film surface model (Figure 6-57). In laser evaporation, the surface temperature can be assumed to be instanteously changed without changing the bulk temperature, since the heating and cooling rates during laser evaporation are estimated to be 10^{10} ^{o}C/sec. Based on the difference in the thermal expansion coefficient of the molten thin layer and the bulk material, the surface of the thin molten layer can undergo tensile stress during the cooling cycle. The magnitude of the fracture stress, σ_f, can be described by the following relationship

$$\sigma_f = E \alpha \Delta T_f / (1-\mu) \qquad (6\text{-}1)$$

where E is Young modulus, α is thermal expansion coefficient, ΔT_f is fracture temperature difference, $T_s - T_a$, where T_s is the surface temperature or assumed to be equal to the melting point temperature, T_a is the average temperature, and μ is the Poisson ratio. If the

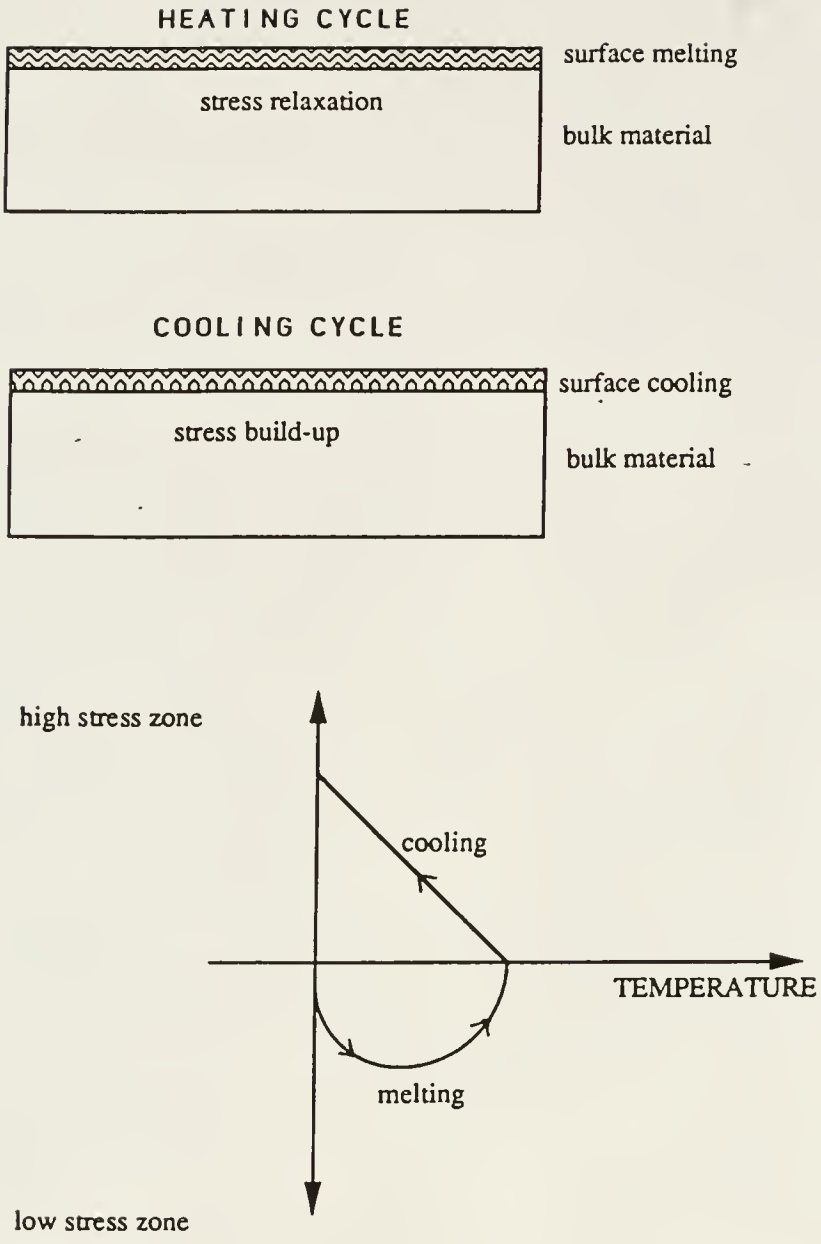

Figure 6-57 Cartoon of ultra thin surface crack model.

magniture of the stress, described by $(T_m-T_a) \alpha E d^{1/2} / (1-\mu)$ is larger than K_{IC}, where d is film thickness and K_{IC} is the stress intensity factor, then suface cracking takes place. In this context, the value of d is equal to the average pore diameter, which is 1-2 μm. The thermal expansion coefficient of YBCO is 11 x 10^{-6}/°C.[108] Assuming a Young modulus of $50x10^6$ psi, typical for ceramic materials, and a Poisson ratio of zero for polycrystalline target, the value of stress at 700 °C is calculated to be $200x10^3$ psi.

The hysterisis formed during the heating and cooling of the molten layer can be described as follows. Initially the surface of the target at temperature T_a is under residual stress from sintering. During the heating, assuming that the molten surface reaches a melting point of 1060 °C, the surface melts, and the stress is reduced to a minimum. After the surface cools, since it is restrained by the solid body, tensile surface stress develops, and surface cracking takes place.

The evolution of target morphology can be traced back to the formation of surface cracking. The initial formation of surface cracks seems to determine the location of the mountains and valleys associated with the surface morphology. The cracks are consistently located at the valleys, indicating that this is the most etched place. A simulation of the ray tracing, determined from the etched rate as a function and geometric factors, showed that surface cracks tend to deepen once they are formed. Successive evaporations deepened the cracking and produced columnar morphological developments.

During the evaporation of a polished surface at high fluence, small cracks have developed. The cooling and heating rate of a laser-heated surface can be estimated to be as high as 10^{10} °C/sec. Surface cracking of thin film due to self-stress has been observed during the heating of polycrystalline Al_2O_3.[231] Similar behavior is also observed during the evaporation of YBaCuO target using KrF laser. A series of micrographs taken on the target surface at one, two, five, and eight pulses revealed that surface cracking developed even as early as one pulse. This behavior can be explained in terms of stress development

during the cooling of the molten thin layer. The stress introduced during the cooling cycle can be expressed by

$$\sigma = (T_o - T_m)\alpha E/(1-\upsilon) \quad (6\text{-}2)$$

where σ = stress, T_o = bulk temperature, T_m = melting temperature, α = thermal expansion coefficient, E = Young modulus, and υ = Poisson ratio. Surface ripples that are formed during the evaporation are caused by the relaxation of the surface (not buckling since delamination does not occur). The wavelength is described by

$$\lambda = \pi G\gamma/\sigma^2 \quad (6\text{-}3)$$

where G = screw modulus, γ = surface energy and σ = stress.

The development of surface cracks seems to be crucial in the later development of target morphology. It appears from the micrographs presented at Figures 6-23 to 6-25, that the initial formation of surface cracks determines the location of the columns to be developed later. A successive evaporation of a target presented at Figure 6-24 and 6-27 showed that the location of the cracks remains the same. It is believed that heating the target surface to a temperature close to the target melting point prevents the development of these cracks, and therefore prevents the formation of surface morphology.

6.4.2.2 Surface tension induced ripples

Surface ripplings are also commonly seen on the surface of laser evaporated material. In the laser-treated metal, surface ripplings are caused by the depression of vapor pressure above the molten surface, surface tension gradient induced shear stress,[200, 232] and surface convection.[199]

The formation of the column can be induced by the surface tension of the molten surface. This surface tension gradient is caused by the temperature nonuniformity as a result of surface asperties or a nonuniform beam. If there is a localized high temperature area, corresponding to a low surface tension, the molten liquid will flow from the hot area to the surrounding area because of the force from the surface tension gradient. On the other hand, if a localized area is colder than the surrounding, corresponding to higher surface

tension, then the liquid will be accumulated from the surroundings. If the cooling rate is high, surface rippling due to surface tension is unlikely since the relaxation time is in milliseconds.[200]

The formation of surface induced ripples is best represented by the evaporation of gold shown in Figure 6-52.

6.4.2.3 Fluence-dependent optical analysis

While the concept of surface shielding by the yttrium-rich phase explains the development of porous and cone morphology satisfactorily, the development of the surface morphology at higher fluence remains unanswered. At this fluence range, the evaporation rate is high enough that a yttrium-rich phase does not form. Analysis of this surface using EDAX and Auger showed that the surface is stoichiometric, ruling out the possibility that selective evaporation of certain elements is taking place. In addition, the XRD analysis showed that no phases other than the 123 phase are present. The mechanism of liquid ejection is unlikely due to the rapid heating and cooling rates. It is intended, therefore, to develop a physical model based strictly on the optical behavior.

Several characteristics are present on the target surface evaporated at high fluence. First, is the formation of columns with steep edges. A cross-sectional view of the evaporated target showed that the material underneath the column is virgin material, therefore ruling out the possibility of frozen droplet formation. Second, the edge of the column has a deeper cut than the base. Since these edges appeared at the columns as well as at the edge of the evaporation area defined by the aperture, it is unlikely that this phenomena is caused by beam diffraction. Third, as the number of pulses increases, the columns become flatter. It appears that the curved surface is inherently unstable. A computer simulation based on ray tracing techinques will be used to explain the surface morphology observed in the evaporation of the YBCO at high fluence. This concept is based on the optical properties of a beam reflecting on a surface at oblique angles. This ray

tracing model, in principle, is similar to development of surface morphology and the sputtering yield dependence with angle for sputtering due to ion bombardments.

The development of surface morphology in sputtering has been studied.[196] The formation of surface texturing during sputtering has been attributed to different etch rates due to grain orientation, impurities, irregular surface, and selective removal of a certain constituent from an alloy.[196] Modelling of the angular dependence on the sputtering coefficients has been extensively studied.[233]

In this ray tracing simulation, the optical properties of the material need to be considered. Depending on the properties of the refractive index as a function of angle, the development of a column can be amplified or suppressed. The real part of the refractive index determines the optical transmission, whereas the imaginery part of the index determines the optical absorption.

The monochromatic reflectance of an optically smooth surface in the specular direction can be predicted.[114] This reflectance, which depends on the angle of incident and the complex index of refraction, is the average of the perpendicular and parallel components of polarization. For dielectric material (electric nonconductor), the index of refraction only has the real component. On the other hand, for a semiconductor, metal, and superconductor, the index of refraction has both the real and imaginary components. As the imaginary component value increases, the reflectance increases. Metallic surfaces are characterized by a high value of specular reflectance. The specular reflectance reaches a value of unity as the angle is closer to 90° (grazing incidence). For angle less than 80°, the value is essentially constant.

The development of the surface morphology at high fluence is demonstrated at Figure 6-58. This target surface was evaporated at fluence of 2.0 J/cm^2, higher than the range of porous and cone formation. This simulations is based on the fresnel reflections, and etch depth. Fresnel reflections[234] define the surface reflectivity as a function of incident angle and the index of refractions. For reflectivity of n=1.6, based on the surface

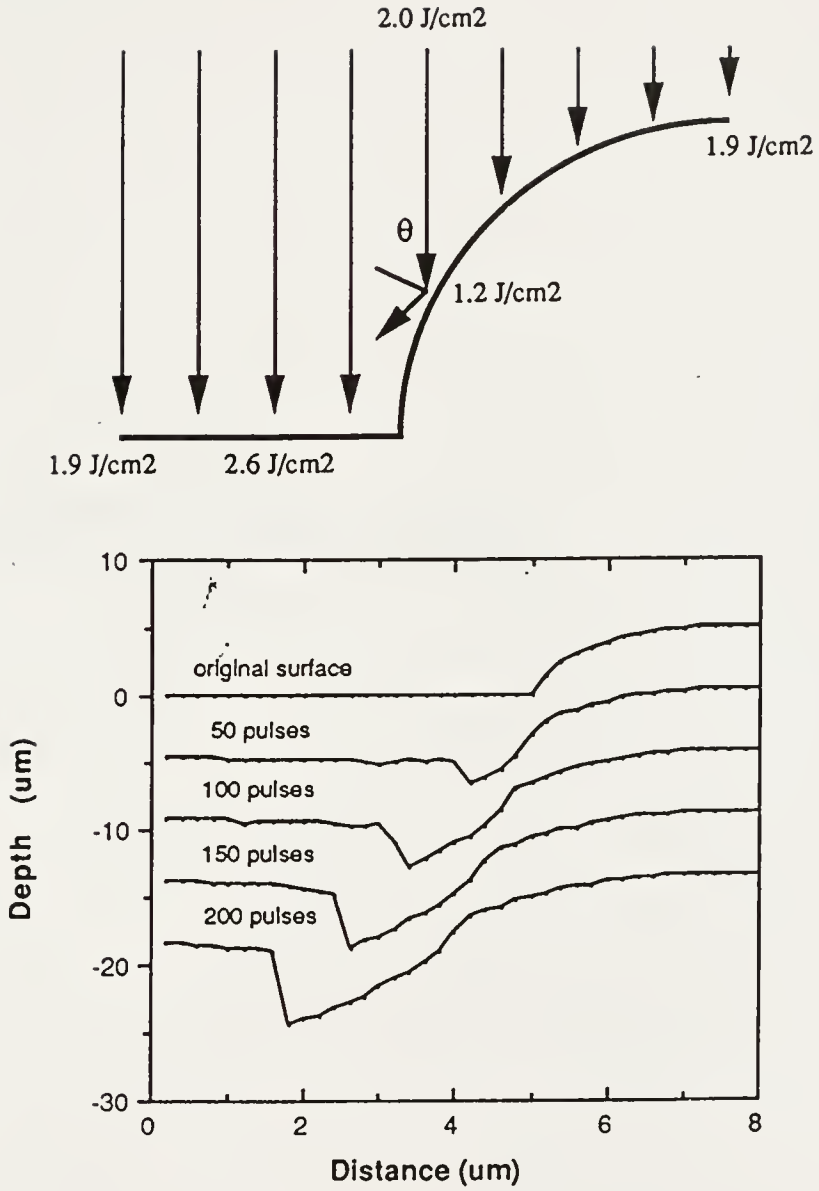

Figure 6-58 Ray tracing model used in the development surface morphology. As the pulse number increases, the etch depth becomes deeper and the broader.

reflectivity value of 5% at 0 degree at 248 nm (Figure 6-59), the value of surface reflectivity as a function of angle is presented in Figure 6-60. In comparison with sputtering, the probability of ion reflection increases from 0 at 60 degree to 1.0 at 90 degree. If the incident beam is equal to 0 degrees from the normal, then the reflectivity is equal to 0.05. At the edge of a column, the incident beam is at an angle from the normal, the reflectivity value is therefore higher, and the reflected beam is significantly high to add to the evaporation of the edge of the column. Since the edge of the column receives a higher fluence, the etch rate is also higher. As the result, the edge is getting deeper. Since the top of the column receives a higher radiation than the edge, the tendency is for the top to get flatter. The evolution of target surface morphology as a function of pulse number was compared for the high-density polished and non-polished targets (Figure 6-61). Unlike photonic process, the sputtering yield in a sputtering process reaches a maximum at the angle of incident of 80^{o} from normal.[235]

The computer simulations of the etched surface were performed for the following geometry : half circle, triangle, square, and random pit. This model sufficiently described the formation of the surface morphology seen on a target evaporated at high fluence. It is capable of explaining the transformation of the columnar structure to a flat surface. In addition, it also predicts the formation of deeper cuts around the edges.

6.5 Conclusions

The effect of laser evaporation on a superconducting YBa_2Cu3O_{7-x} target with a 248-nm KrF laser beam has been studied. The results show that the target exhibits three distinct morphologies as a function of evaporation fluences. At low fluence, between 0.2 and 0.6 J/cm^2, the ablated area results in a porous structure with minimal material removal. At fluences between 0.6 and 1.1 J/cm^2, a conical structure predominates. The conical structures are thought to be caused by shielding of the laser beam with low-evaporation, yttrium-rich phases, Y_2BaCuO_5 and Y_2O_3. The material removal was minimal and stopped

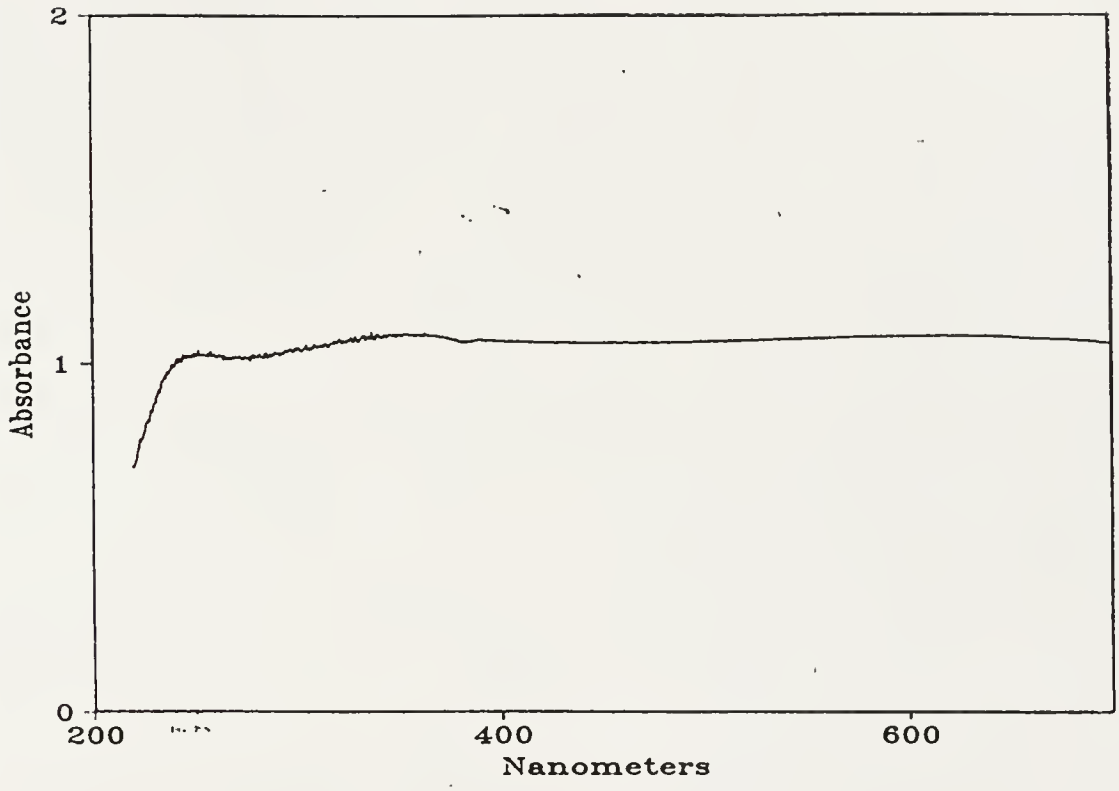

Figure 6-59 Surface absorbance as a function wavelength. Wavelength from 220 to 750 nm.

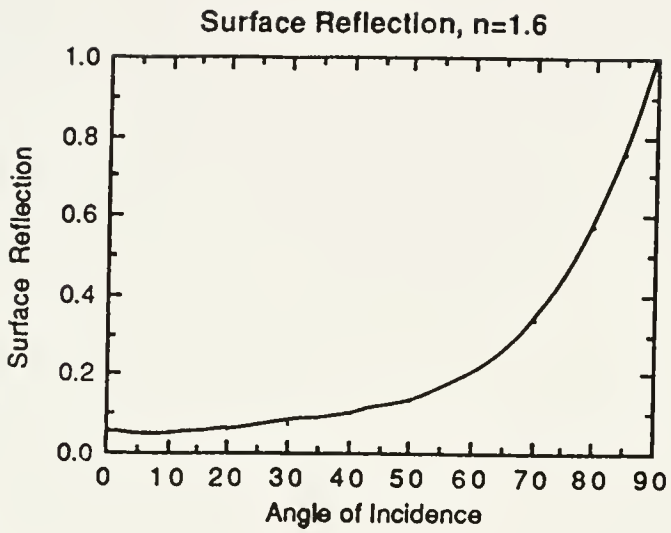

Figure 6-60 Surface reflectivity as a function of incident angles.

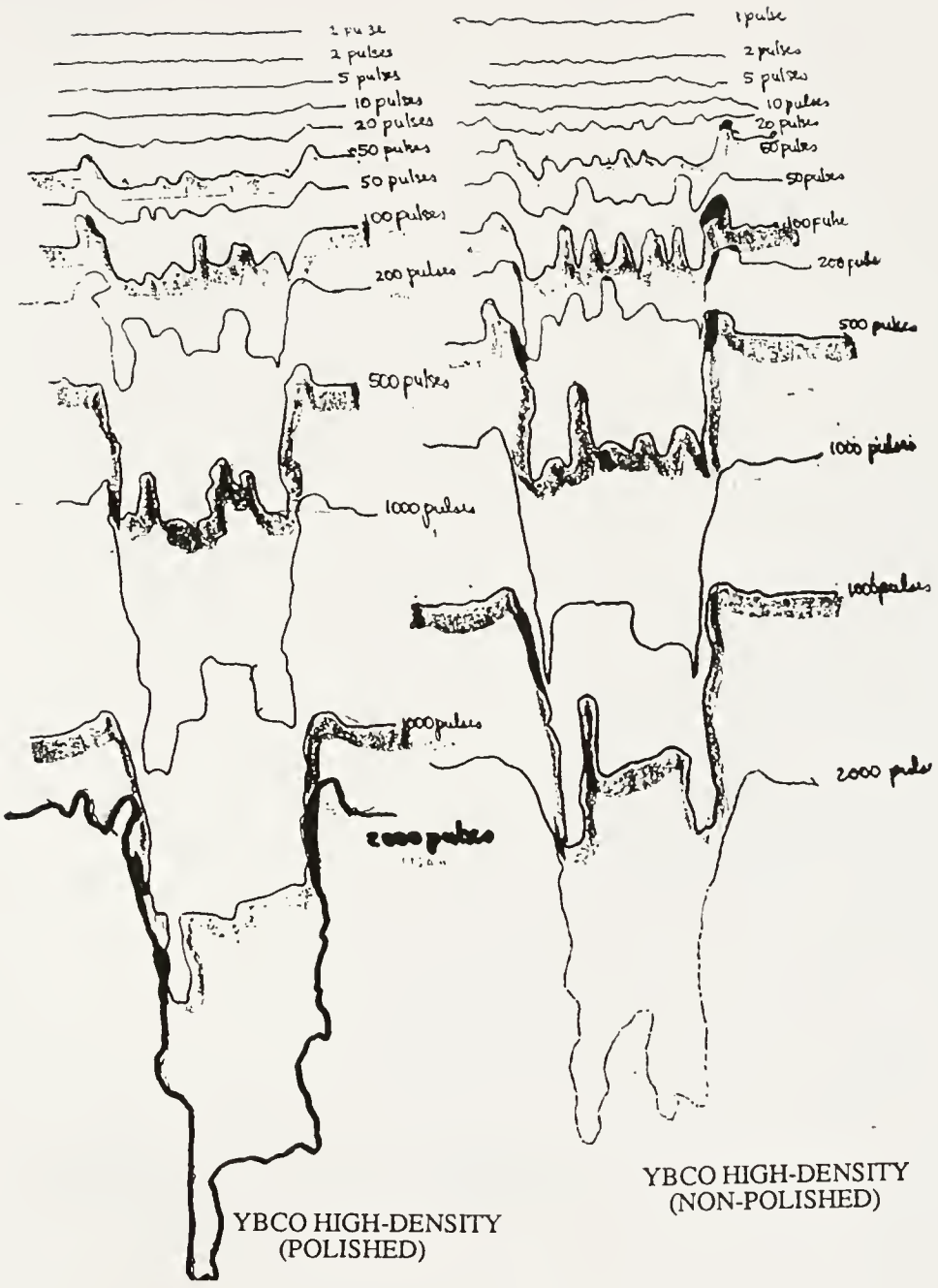

Figure 6-61 Evolution of YBCO suface morphology at fluence of 2J/cm^2 as a function of pulse number for both polished and non-polished targets.

after 1000 pulses owing to the shielding. At fluences higher than 1.1 J/cm^2, the evaporation is significant and is sustained for as long as the surface remains smooth. This melt structure is the most desirable condition for thin-film production, since evaporation rates up to 0.07 μm/pulse can be achieved. The fluence boundaries of these regions are affected only to a small degree by repetition rate.

CHAPTER 7
PLUME EXPANSION STUDIES

7.1. Overview of Laser Induced Shock Wave

There are three reaction regimes of interest in laser evaporation of material. First is the absorption of photon on the target surface. The absorbed photon energy is transferred to electronic and vibrational energy, causing thermal excitation and bond breaking. There is an incubation period between the beginning of photon absorption and the onset of material removal. Second is the evaporation of material as plasma plume. If the evaporation rate is high, a shock wave is formed as the result of the plasma expansion. Third is the deposition of the plasma either on the substrate at low background pressure, or if the background pressure is high, the plasma plume is redeposited at the target surface.

Despite its importance in the understanding of deposition characteristics, the physics of evaporation during the laser evaporation is not well understood. The study of plume dynamics, especially at high background pressure, can provide a better understanding of the evaporation process. This chapter deals with the redeposition of plume on the target surface during the evaporation of material at high pressure. In particular, it will discuss the process related to the shock wave formation at high background pressure. Two observations can be made from the patterns of the redeposited plume on various material. First, the plume size increases with increasing fluence, and second, the shape of the plume on a square aperture is rotated by 45 degrees.

7.1.1 Photon Absorption and Induction Period

The induction period between the time the first photon is absorbed and the time plasma evaporation takes place varies from nanoseconds to microseconds. At this stage, photon energy is absorbed by electronic to vibrational energy transfer, causing phase transformation, thermal excitation, and bond breaking. It has been demonstrated that melting silicon with a KrF laser can take place within 15 picoseconds.[236] The hot plasma containing molecular fragments with high pressure are then ejected from the surface. Time-resolved images from high speed photography during the evaporation of YBCO using a KrF laser showed that the duration required for material ejection depends on the ambient pressure,[174] which varies from 15 to 500 nsec at 0.3 Torr and from 100 and 900 nsec at 1 atm. During the evaporation of polymer using excimer lasers, the observed time delays varies from 200 to 800 nsec.[237] Based on the Knudsen flow, the evaporation time constant was estimated to be 20-60 nsec for metals.[44] During the evaporation of carbon using a 20 ns laser pulse, plume formation was observed at 25 ns, reached a maximum at 100 ns, and diminished at 1 ms after the laser pulse ended.[8] The formation of a shock wave requires the presence of high background pressure, otherwise free expansion is taking place. The maximum pressure allowed to avoid shock wave formation is 0.25 bar.[178]

7.1.2 Fundamental of Shock Wave Formation

The theory of shock wave is derived from the expansion of a high-pressure gas in a piston.[238] For a strong shock wave, the process is adiabatic and nonreversible. The energy balance shows that energy change is proportional to half of the initial and final pressure. Weak shock wave, on the other hand, is an isentropic process. The formation of a shock wave can be best represented in an explosion process, where exothermic reactions are proceeding very rapidly following an induction period, causing a rapid temperature

increase. The temperature increase further accelerates the rate at which the chemical reactions are taking place. If the energy liberated cannot be dissipated to the surroundings at a sufficiently fast rate, a thermal explosion takes place. A shock front is formed as the result of the rapid expansion of pressure during the explosion. Behind this shock front, the reaction products are gradually expanding.

The intensity of the shock wave depends on the rate at which the material is leaving the reaction zone. If the shock wave is produced as the result of evaporation, the intensity depends on the rate of evaporation. The evaporation theory of condensed material was developed by Hertz, Knudsen and Langmuir,[45] and involves the principles of kinetics, thermodynamics, and solid-state theory. The Hertz-Knudsen theory predicted that the evaporation rate of a liquid is proportional to the saturated vapor pressure and is expressed by

$$\text{Flux} = \alpha_v(2\pi mkT)^{1/2}p \qquad (7\text{-}1)$$

where p is the equilibrium pressure and α_v is the evaporation coefficient, with values equal to or less than unity. The values of α_v can be lowered by factors such as surface contamination and surface condensation. Surface contamination may affect the evaporation coefficient by increasing the activation energy of evaporation or by lowering the diffusion of the evaporant through the impurities. For a free solid surface, the evaporation flux was predicted by Langmuir by

$$\text{Flux} = 5.834\text{x}10^{-2}\,(M/T)^{1/2}p \qquad (7\text{-}2)$$

where flux in g $cm^{-2}sec^{-1}$, and p is in Torr.

In the evaporation of a compound or an alloy, the process is usually accompanied by a dissociation or an association. Although association rarely affects the overall stoichiometry of the deposited vapor, a dissociation may affect the composition, especially if the volatilities of the constituents are different. For a congruent evaporation of a complex molecule to take place, the molecule has to be either evaporated as a whole or the constituents must be equally volatile and have the same sticking coefficient.

The evaporation of a condensed phase, which is free-evaporating and has a Maxwellian speed distribution, follows a cosine distribution. This assumption is correct for surfaces that evaporate without restrictions, with α_v equal to unity.

In this analysis, two types of gas dynamic effects are considered: contact front and expansion front. Contact front is the spatial limit of the plume expanding in the background gas. Expansion front is similar except that the plume is expanding in a vacuum. The shock wave is the expanding boundary between the plume and the background gas. Similar to the evaporation of superconductor, the evaporation of polymer also produces high- and low-velocity components. If the contact front velocity is low, the low-velocity components are spread horizontally, resulting in the plume deposition observed with superconductor sample.

7.1.3 Laser-Induced Shock Wave

Laser-induced explosion, unlike a conventional explosion, is caused by the rapid evaporation and expansion of material. The process is endothermic, since it involves the phase transformation from the solid to the plasma state. The induction period is mainly determined by the time required to produce a sufficiently high temperature for evaporation.

Laser-induced plasma formation has been widely studied.[179, 239, 240] It is known that this plasma is highly directional and that dense plasma flux recombines during the adiabatic expansion. Various fluid models have been used to describe the expansion behavior of the plasma, including an axisymetric potential fluid model,[240] jet formation,[241] and adiabatic expansion.[239]

The temperature during laser evaporation was estimated to be as high as 9000 ^oK[242] and the pressure 10^3 to 10^4 atm.[243, 244] In the evaporation of YBCO, based on the maximum expansion velocity, the plasma temperature was estimated to be between 1400 and 4000 K; [174] however, if inverse Bremstrahlung absorption of the laser enegy by the plasma is possible, the plasma temperature could be higher than the target surface

temperature. The intensity of the shock wave depends on the evaporation rate that is taking place. Rapid evaporation of atomic and molecular species during surface irradiation leads to nonthermal velocity distribution.[30] Results from TOF mass spectroscopy, fluoresence spectroscopy, and streak camera showed that the velocity of this plasma is in the order of $1x10^6$ cm/sec. The velocity of the high-velocity components is equal to the Knudsen velocity if the evaporation is done in vacuum or proportional to the $m^{2/3}p$ where m is the ambient molecular weight and p is the ambient pressure.[237]

A model for material removal during laser drilling of copper using Nd:YAG laser was developed.[142] Based on the equilibrium between the energy absorbed by the laser and the energy carried away by the expulsed material, the rate of evaporation for the vapor can be expressed by

$$j_v = (1-\alpha)P_s(T_o)(m/2\pi kT_o)^{1/2} \tag{7-3}$$

and for the liquid by

$$j_l = ((2\kappa/r)\ln(T_o/T_m))^{1/2}P_s^{1/2}\rho^{3/4} \tag{7-4}$$

where P_s is the saturation pressure, κ us thermal diffusivity and α is reflectivity. The surface tension of the liquid metal must be greater than the tangential pressure force for the expulsion to take place.[142]

Laser-induced shock wave does not have spherical symmetry. At low ambient pressure, the plasma expands in a large volume. Shock wave models have a unit scale length, ε, defined as $\varepsilon = (E_b/P_o)^{1/3}$ and unit scale time, τ, defined as $\tau = \varepsilon/c_o$, where E_b is total blast energy and P_o is preshock sonic velocity.[245]

The shock front coordinate can be estimated depending on the ambient pressure and the shock wave geometry. The formation of a shock wave for a spherical plume can be described by $R(t) \propto (E/\rho_o)^{1/5}t^{2/5}$ and for planar $R(t) \propto (E/\rho_o)^{1/3}t^{2/3}$ where R(t) is the time-dependent shock radius, E is the shock energy released, ρ_o is the ambient gas density, and t is the time since explosion.[174, 246-248] In vacuum, the expansion of the shock wave is linearly dependent with time.[247] The numerical solution of a spherical blast wave has been

carried from pressure of 2000 atm to vacuum.[245] The calculation of a plasma that expands adiabatically in vacuum showed that the largest acceleration is greatest in the smallest dimension.[239]

7.1.4 Recoil Pressure and Plume Redeposition

In the expansion of a plasma in a high background pressure, a direct consequence of the shock wave formation is the redeposition of the plasma. The first idea of recoil pressure during laser evaporation was suggested Askaryan.[243] This theory is based on the concept that during plasma evaporation, the pressure front moves outward until a certain limit is achieved. As the result of this rapid expansion, a drastic pressure drop is formed behind the shock wave. If the pressure drop becomes very strong, the expanding plasma collapses. This pressure collapse is called the recoil pressure.

The evidence of recoil pressure was seen during the evaporation of polyimide.[249] The pressure was during the evaporation was estimated to be 150 atm.[249] The debris radius is proportional to pressure to the one-third power.[249] The effect of debris on the evaporation depth [250] and the shape of the side expansion [251] were studied.

7.2 Plume Expansion Studies of YBCO Systems

7.2.1 Statement of Problem

This chapter deals with the formation of plume and the redeposition of the debris during the evaporation of YBCO in atmospheric pressure. The correlation between the size of the debris and the laser fluence will be made. This process could be explained using the theory of shock wave formation. The other is the explanation on the effect of the aperture geometry on the shape of the expanding plume. In this case the process could be explained by the theory of adiabatic expansion and plasma cooling.

7.2.2 Experimental Details

The evaporation of YBCO target was performed in a microfabrication stage using a KrF laser. The fluence was varied from the 0.1 to 2 J/cm^2. The evaporation area was imaged from an aperture to give areas varying from 100 x 100 μm to 400 x 400 μm. The number of pulses was varied from 1 to 1000 pulses. The target area was later analyzed using SEM. The plume area was measured using graphical methods.

7.2.3 Effect of Fluence

The debris produced as the result of a redeposition of plasma plume during the evaporation of a YBCO target was found to vary with the fluence. As the fluence increases, the size of the plume increases (Figure 7-1). A plot of the debris size as a function of the fluence is presented in Figure 7-2, which shows that the debris area varies linearly with fluence. The linear dependency of the plume area as a function of fluence may be explained in terms of kinetic energy. An energy balance equation discussed in Chapter 4 has demonstrated that most of the photon energy is converted into kinetic energy. As a consequence, the fluence varies linearly with the square of the plume velocity. The linear dependency of plasma velocity with fluence has been observed from the evaporation of carbon[240] using a short laser pulse, where the lateral heat conduction is minimal.[252] If the evaporation period is constant, the velocity is proportional to distance, and the fluence therefore is a function of area, or square of the distance. The velocity of the elements in YBCO irradiated with KrF laser could be expressed in terms of $v \propto E^{0.3\text{-}0.4}$.[144]

7.2.4 Effect of Geometry

The shape of the deposited plume on the target was peculiar since it appeared to be rotated by 45 degree from the evaporation area. This effect was apparent at fluences less than 1 J/cm^2 (Figure 7-3). At higher fluence, the shape of the deposited plume was

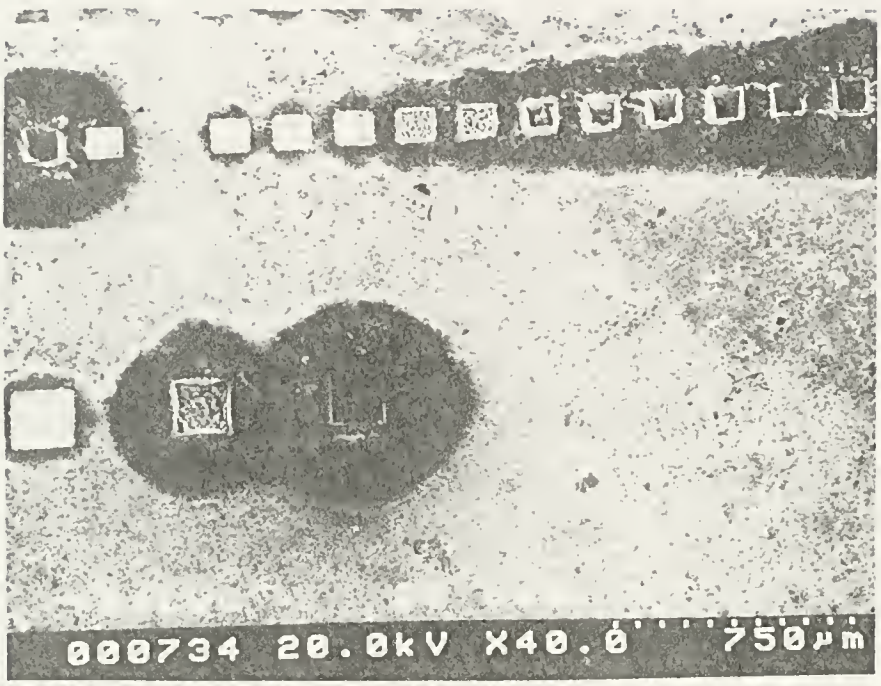

Figure 7-1 Redeposited YBCO plume as a function fluence.

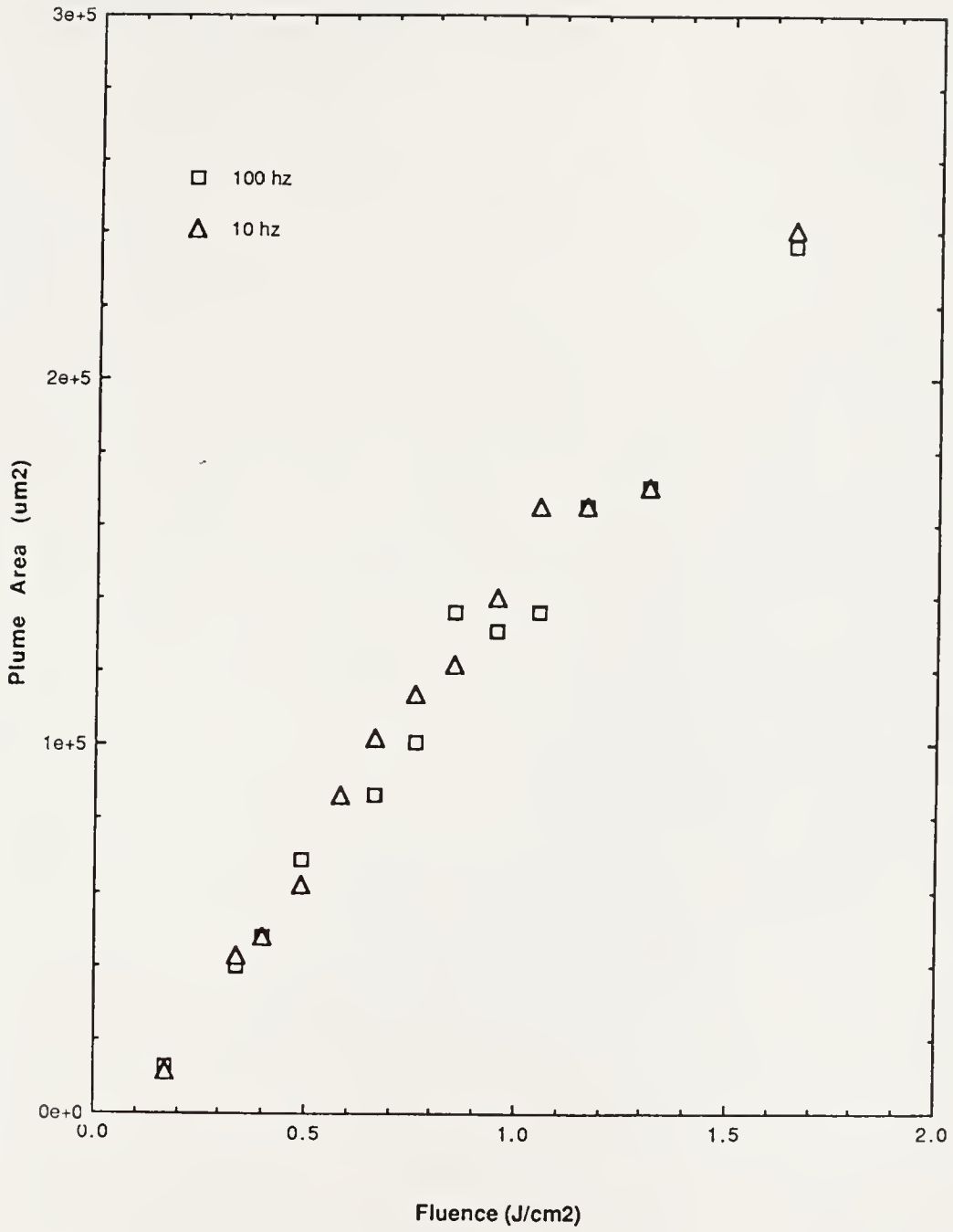

Figure 7-2 Redeposited plume area as a function of fluence. Linear dependency observed for both 10 pps and 100 pps.

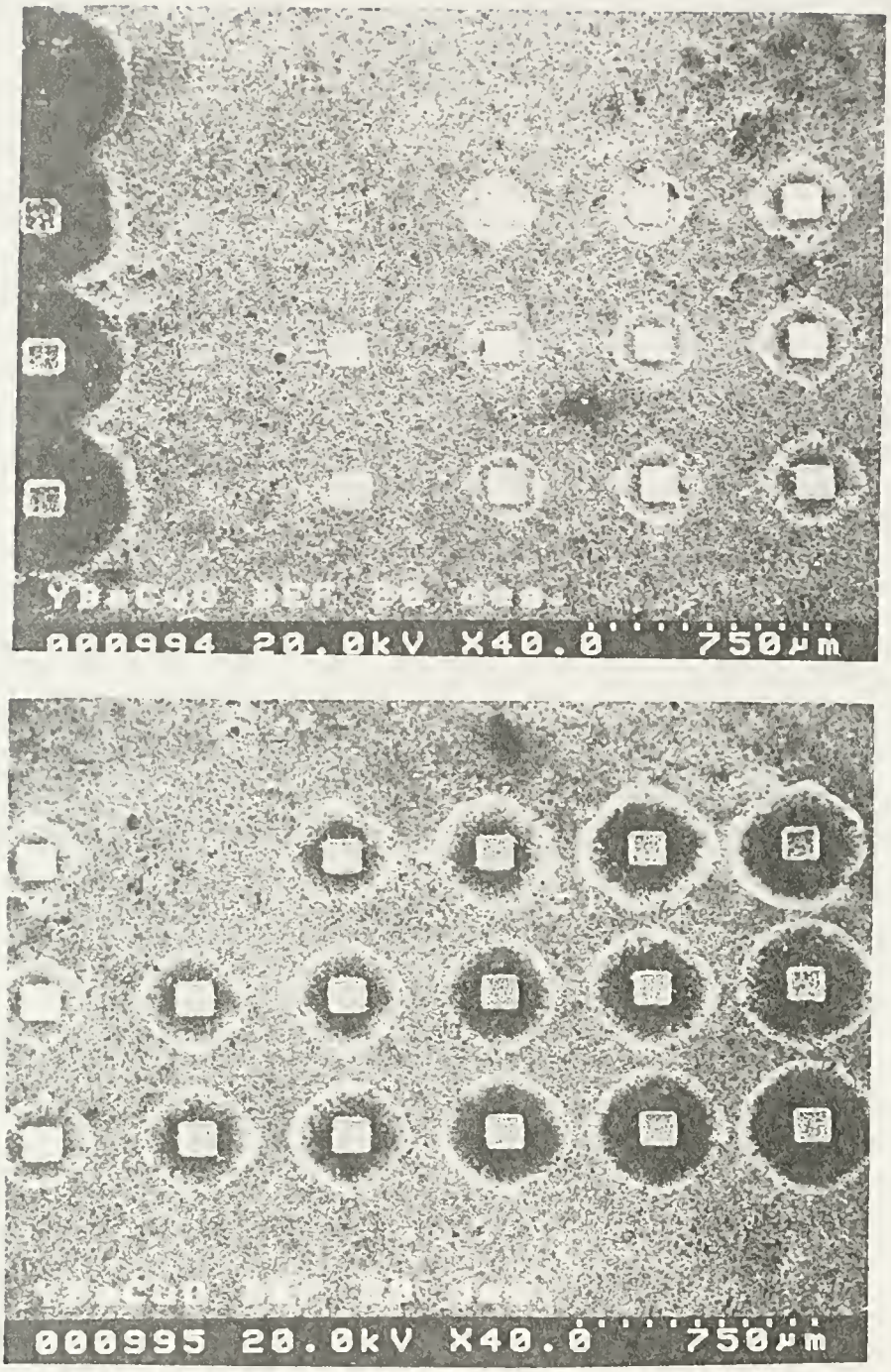

Figure 7-3 YBCO target evaporated using KrF laser. Pulse number: 500. Repetition rates (top to bottom): 100, 10 and 5 pps. Fluences: (a) 1.7, 0.1, 0.2, 0.3, 0.4, and 0.5 J/cm^2; (b) 0.5, 0.6, 0.7, 0.8, 0.9, and 1.0 J/cm^2.

rounder (Figure 7-4). Similar rotational effect was also seen in the debris formed during polymer evaporation.[251]

The shape of the deposited plume appeared to be consistent with increasing evaporation size. The debris area, however, increased linearly with fluence as presented in Figure 7-5. As a comparison, the redeposited plume pattern for titanium was presented at Figure 7-6. The pattern was similar to that of the YBCO material.

It should be noted that the trajectory developed in the begining stage of the evaporation and not as a result of shock wave. In separate experiments in vacuum where the shock waves do not form, the pattern of the deposited plume on the substrate also showed a 45 degree rotation.

There are two possible explanations for this phenomena. First is one strictly associated with the adiabatic expansion of plasma, and the second is related to the cooling at the corners of the aperture.

The rotation of the deposited debris may be explained in terms of the model of adiabatic expansion of plasma.[239] It shows that the highest acceleration takes place in the direction of the smallest dimension; namely, the direction normal to the target surface. The lateral acceleration, however, is higher at the edge of the square compared to the acceleration in the diagonal direction. The following argument may be used. For a particle that is located at the center of the evaporation area, it is closer to move to the edge than to move diagonally. As the result, the velocity to the edge is higher, producing a rotated shape debris. A similar approach is solving the gas dynamic effect. This method has been used to explain the debris shape observed on polymer.[251]

The other possible mechanism is the cooling of the corners of the aperture. If the cooling rate of the plasma is faster at the corners of the aperture compared to the bulk, and the velocity of the plasma is related to the temperature, the film trajectory is therefore slower at the corners. As a result, the debris deposited is closer. Based on the measurement of a debris pattern, the velocity at the corners is only 75% of the velocity at

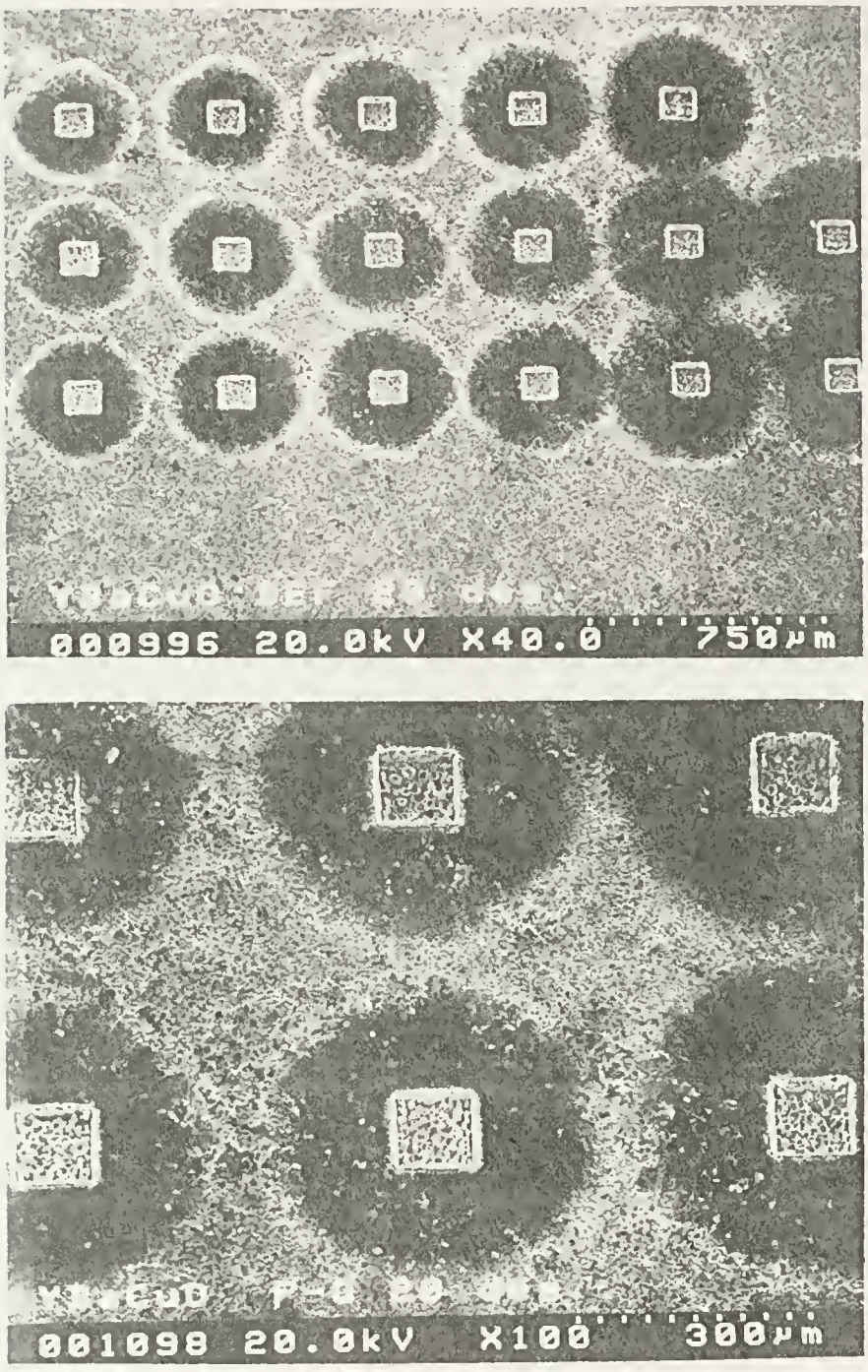

Figure 7-4 YBCO target evaporated using KrF laser. Pulse number: 500. Repetition rates (top to bottom): 100, 10 and 5 pps. Fluences: (a) 1.0, 1.1, 1.2, 1.3, 1.7 and 2.0 J/cm^2; (b) 1.0, 1.1 and 1.2 J/cm^2, 10 and 5 pps.

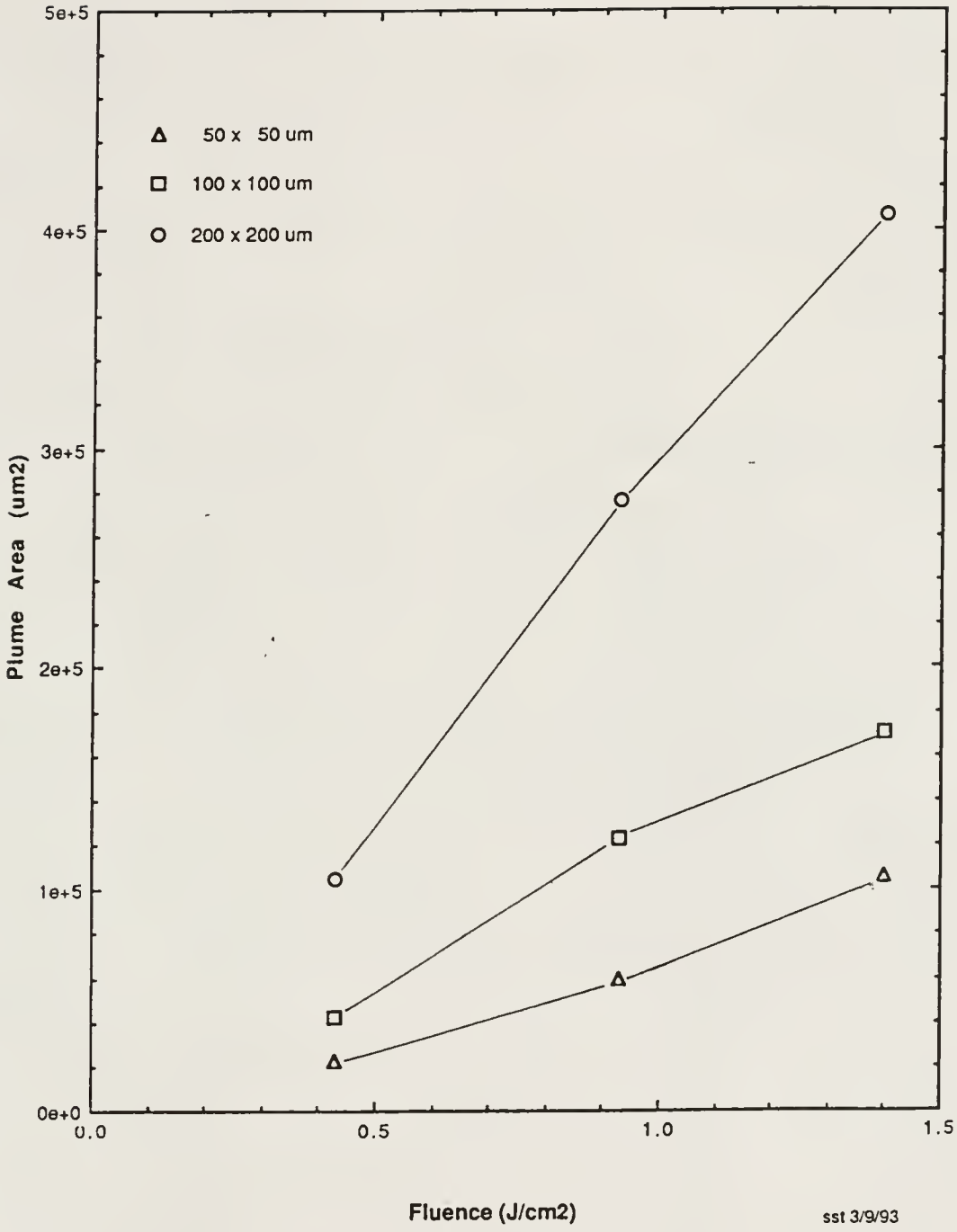

Figure 7-5 Redeposited plume as a function of fluence for different evaporation sizes for YBCO target.

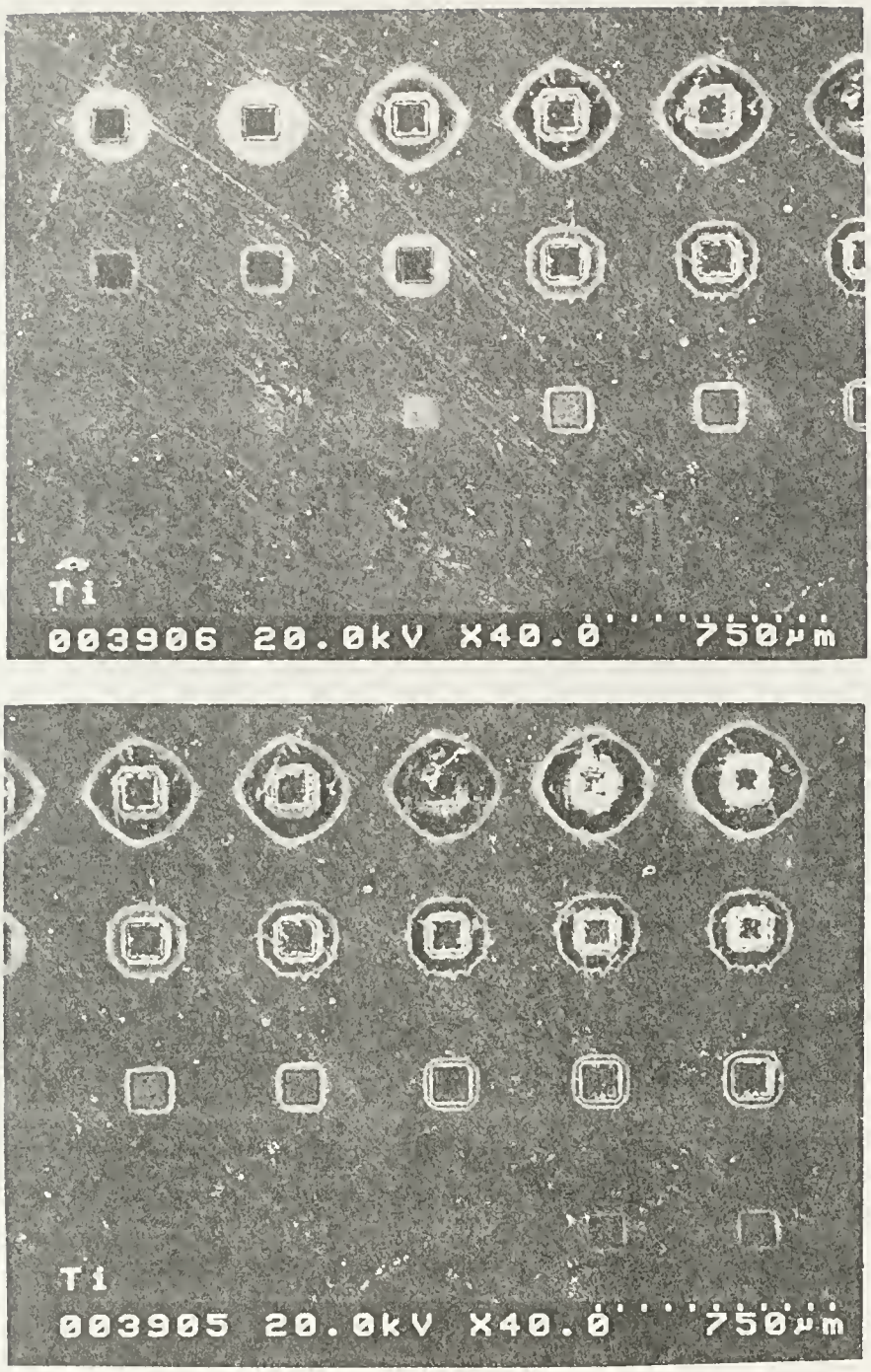

Figure 7-6 Titanium target evaporated using KrF laser. Fluence from 0.1 to 2.0 J/cm^2.

the edges. Therefore, if the temperature of the plasma at the corners can drop to 6000 K, assuming the rest of the surface is at 8000 K, within 5 to 20 nsec, then the plasma trajectory during the evaporation can be explained. A rough calculation on the heat transfer area, however, reveals that most of the heat transfer area is at the bottom of the plasma on the target and not at the corners. By including the edge effect, the heat transfer area is only improved by 2%, much less than the required 25% velocity loss described above.

7.2.5 Effect of Ambient Pressure

As anticipated from the theory, the plume size increases as the pressure decreases. At very low pressure, in the order of 10^{-4} Torr lower, the plasma plume spreads far beyond the substrate with no distinct shape. At pressure in the order of 0.1 Torr, the shape of the expanding plume is more confined, almost like the shape of hot air balloon. Similar rotated pattern is observed for the plume deposited on a substrate in vacuum.

7.3 Conclusions

The behavior of the deposited plume at high background pressure has been investigated. The results showed that the area of the debris is proportional to the fluence. This phenomena could be explained in terms of the plasma kinetic energy. The rotation of the debris relative to the evaporation area was explained in terms of an adiabatic expansion of plasma, where the highest acceleration is in the shortest dimension.

CHAPTER 8
MASS SPECTROSCOPIC INVESTIGATION

8.1 Review of Literature

8.1.1 Plasma Characterization

It is important to characterize the plasma species during laser evaporation in order to understand the underlying mechanism of laser target interactions. It has been known that target composition varies with increasing number of pulses as a result of target surface modification.[4] Changes in the deposition parameters, such as background pressure and fluence, have also been shown to alter plasma composition. The above evidence suggests that the plasma behavior is very dynamic, and the ability to directly monitor the plasma may provide better control of film stoichiometry. Various efforts have been made to better characterize the plasma produced during the evaporation of YBCO superconductor target. One of these techniques, mass spectroscopy, will be reviewed.

The evaporation phenomena resulting from the absorption of photon energy on the target surface during laser evaporation is very complex. During the evaporation, a brilliant, elongated plasma plume extends from the surface of the target. The plasma temperature is estimated to be as high as 15,000 K.[253] Many species are produced during the evaporation at such high temperature and pressure; in addition, the plasma also has a wide distribution of internal and kinetic energies. Hot, dense laser-generated plasmas are known to contain both x-rays and highly charged ions.[240] Early work suggested that the ablated material was in the form of molecular clusters, which were believed to be responsible for preserving the target and film stoichiometry.[4, 46] Further study, however, revealed that the plasma species consisted mainly of atoms and molecules, rather than clusters, and that

stoichiometry of the target and film changed during the evaporation process.[254, 255] This change in stoichiometry is undesirable since small deviations from the ideal film stoichiometry would significantly degrade the film quality.

In situ plasma diagnostics are useful tools for the characterization of the plasma during deposition. In a typical experiment, the deposition parameters, such as the fluence and background pressure, are adjusted to optimize the composition and the deposition of the plasma plume. Generally, the species ejected during laser evaporation can be divided into four major categories:[49] (1) excited atoms or molecules, which may produce emission spectra; (2) neutral atoms or molecules; (3) ions; and (4) clusters or particulates. All these species are mixed in the plasma phase and are eventually deposited as film on the substrate surface.

The studies of plasma produced during laser evaporation are divided into two main categories: those of plasma produced under the deposition conditions of fluence at 1 to 5 J/cm^2 and background pressure of 100 mTorr O_2, which includes all the species involved in film deposition; and those of the plasma produced in a vacuum at lower fluence, used to study part of the evaporation mechanism. Correspondingly, two classes of analytical techniques are available for plasma detection: optical spectroscopy and mass spectroscopy.

Both optical spectroscopy[31, 88, 143, 255-262] and mass spectroscopy at high vacuum, less than 10^{-6} Torr,[253, 255, 263-265] have been used in the characterization of a YBCO plasma. Since it provides the mass numbers of the individual species generated in the plasma as well as their isotopes, mass spectroscopy offers advantages over optical spectroscopy in the detection of plasma species. In addition, the ion current is linear to the deposition rate,[266] and the plasma can be studied at distances greater than a few millimeters from the target surface without decreasing sensitivity.[259] The optical spectroscopic technique, on the other hand, only detects the species that fluoresce or luminesce, which constitute only a small fraction of the total species close to the target surface.

Since the best film quality has been produced at pressures between 100 - 200 mTorr, mass spectroscopic analysis of the plasma composition during the evaporation process at the higher, more desirable pressures has been applied in this study.

8.1.2 Mass Spectroscopy Fundamentals

Mass spectroscopy works by resolving the charged compounds of a sample in the gas phase on the basis of mass-to-charge (m/e) ratio.[95] The resulting spectra contain ion currents as a function of m/e ratio. A typical mass spectroscopy setup contains an ion source, a mass analyzer, and a detector. The most common method used to produce ions from the sample is the electron impact source, which utilizes energetic electrons to induce collisions. Since some of the plasma produced during laser evaporation is ions, these charged species can be detected without additional ionization. Neutral species, however, need to be ionized before they can be detected. Following ionization, the charged species are separated based on the m/e ratios.

A time-of-flight (TOF) analyzer resolves the species based on the difference in velocities. Since all the species entering the analyzer have the same kinetic energy, the heavier species will have lower velocity, and therefore a longer time of flight. Time-of-flight is useful for resolving gas mixtures with wide energy distribution and for kinetic energy measurements. Since the plasma plume produced during laser evaporation contains a wide mass and energy distribution, a retardation grid is sometimes added to filter out a certain energy band.[181]

A quadrupole analyzer, in comparison, uses four parallel metal rods to resolve the species, based on their oscillation frequencies. When external voltage at a certain frequency is applied, only species with the corresponding mass range are affected. As a result, only those species with a certain m/e ratio can pass through the rods without colliding with one of the rods. A quadrupole analyzer is more accurate for resolving the

spectral peaks and more compact than the TOF analyzer; however, it cannot measure kinetic energy.

As a general configuration, two types of vacuum setups for mass spectroscopy are used in diagnostic techniques: plasma flux and partial pressure analysis. Plasma flux analysis requires a direct line-of-sight alignment of the emitted species to the mass detector. Therefore, this method is capable of detecting local composition of the plasma with a certain trajectory. Partial pressure analysis, on the other hand, uses a simpler vacuum system. The detection, however, is not selective and gives only the average gas composition. Early work on the mass spectrometer study of laser evaporation was done in 1974.[267]

8.1.3 Mass Spectroscopic Plasma Analysis

Mass spectroscopic techniques have been used to identify the species generated by the laser-target interaction on a YBCO compound.[47-49] The results showed that the overall composition of the vapor species consisted mostly of atomic neutral and charged species. All the atomic ions, Y^+, Ba^+, Cu^+, and O^+ were detected. The strongest signal detected[50] was that of Ba^+, followed by Y^+, and Cu^+. High Ba^+ concentration may be caused by its low ionization potential a.[49] Evaporation in vacuum using Nd:YAG,[264] XeCl,[49] KrF,[4] and ArF[181] lasers showed that YO^+ has an intensity higher than or comparable to that of BaO^+. However, no CuO^+ signals were observed,[49, 264] except during evaporation using an excimer laser.[4, 181] The BaO concentration is higher than those of Ba and Cu at low fluence.[49] Emission spectra showed that the Cu and CuO concentration decreases with increasing numbers of shots, possibly due to texturing.[4] YO^+ was believed to have come from peroxide or trapped oxygen molecules since the YO plane does not exist in the YBaCuO crystal.[264] Larger molecules, such as Y_2O_3, Y_2O, have been observed using fluorescence and mass spectroscopy.[255] The reactivity of La, which is similar to Y, with O_2 and O_3 was studied.[268] From the chemiluminescent spectrum, the dissociation energy

of lanthanum monoxide is 8.2 eV.[268] For Ba, the photon yield, the probability of emitting photons during reactions, was studied.[269]

8.1.3.1 Atoms and molecules

More neutral species than ions are emitted during the evaporation of YBCO.[49] The ratio of BaO to BaO^+ goes as high as 15 at 0.14 J/cm^2 and decreases to 6 at 0.23 J/cm^2.[49] Neutral Y and YO are not detected, but Y^+ and YO^+ are.[49] It is difficult to detect Y atoms due to the low ionization efficiency. At the near threshold of material evaporation, only ion species are observed[47] because the dynamic of material ejection is dominated by the electronic excitation in the solid. One study showed that minimum ion fraction is seen at 3.0 J/cm^2.[52] Compared to other systems, the fraction of species ionized during the evaporation of Ge using KrF laser is 30%.[30] Each laser pulse contains 10^7 ions.[181] During the evaporation of Si, ionized species up to Si^{4+} are formed at high fluence.[176] Quantitative mass spectra have shown that the composition of the charged particles in the plasma is less than 10%.[49]

8.1.3.2 Clusters

Evidence of cluster formation has been seen during the evaporation of YBCO at high fluence. Clusters with mass higher than 10^4 amu, believed to be the product of condensation, have been detected using mass spectroscopy.[50] The detection at this high mass is not highly efficient due to detector saturation at low-mass ions and inherent decline in the detector response at high-mass. A secondary laser beam focused on the plasma at 1 mm above the target has been shown to dissociate the clusters into smaller ions.[50] The production of clusters has been shown to increase as the crater becomes deeper. The removal of the crater also eliminates the cluster emissions. Smaller clusters, with molecular weights as high as 600 amu, such as BaCuO, $YBaO_2$, Ba_2O, Ba_2O_2, $YBaO_3$, and YBa_2O_6, can be seen during the evaporation at 5×10^9 W/cm^2 using Nd:YAG.[253] However, this fluence is higher than the normal deposition conditions. The formation of heavy-charged particles[50] and micron-sized particles[51] is observed under enhancement with

long wavelength irradiation during deposition. The absence of clusters in some measurements may be limitted by instrument insensitivity.

8.1.3.3 Quantitative determination.

Quantitative determination of the plasma using mass spectroscopy is difficult due to the different responses of various species and high inherent kinetic energies. Measurement at fluences higher than 1 J/cm^2 is difficult due to fast electron-ion combination.[49]

8.1.3.4 Kinetic energy

The dynamic behavior of the laser-ablated plume can be studied using the time-of-flight technique. This technique allows the investigation of both the temporal and angular dependence of the desorbed species. Slow velocity components in the plume, which arise from two different expansion regions, have been detected using TOF.[46] The plume velocities have been measured from 10^5 to 10^6 cm/sec with kinetic energies ranging from 0.1 to 100 eV,[48] and even as high as 200 eV for atomic ions.[181] Oxide ions and ionic clusters, having lower energies than atomic ions, are believed to be a product of plasma bombardment.[46, 181] In contrast, the high-velocity component is the leading edge of the expansion containing ions and electrons. The observed velocity distribution is complex, compared to the Maxwell-Boltzman thermal distribution, due to the nature of high-pressure expansion of gas in a low-pressure regime,[13, 270] formation of a collisional Knudsen layer,[271] and adiabatic expansion of high-temperature, high-pressure plasma.[272] From the plasma expansion velocity, the temperature of the plume was estimated to be 1400 K.[174] The plasma expansion velocity during the evaporation of Ge using a KrF laser has been measured to be 1.5x10^6 cm/sec.[30] The kinetic energy of metallic species has been shown to enhance their oxidation in oxygen background gas.[273]

8.1.3.5 Photochemistry

It is known that irradiation of a surface using a short-wavelength light causes instantaneous emissions from the surface. This phenomenon is known as the photoelectric effect. The

number of electrons emitted is proportional to the light intensity, while the kinetic energy of the electron is proportional to the frequency and independent of the intensity.[274]

8.2 Mass Spectroscopic Analysis of YBCO

8.2.1 Experimental

In order to utilize mass spectroscopy to analyze plasma at pressures higher than the mass spectrometer would tolerate, an evaporation cell, equipped with a differentially pumped mass spectrometer was constructed (Figure 8-1). The evaporation cell was connected to the mass spectrometer chamber through a 100-μm diameter, 100-μm long orifice (Figure 8-2). The pressure within the evaporation cell was varied between 10^{-3} Torr to $2x10^{-1}$ Torr by throttling a turbomolecular pump and introducing either oxygen, nitrogen or air into the system, at a flow rate of 50 sccm, through a dosing valve. This resulted in a pressure variation within the mass spectrometer chamber from $3x10^{-6}$ Torr to $1x10^{-7}$ Torr. The orifice, which connects the evaporation cell to the mass spectrometer chamber, was placed only 5-mm behind the heated substrate, thereby allowing representative sampling of the plasma deposited on the substrate.

The target, located 3 cm from the orifice, could be rotated at 10 rpm and was subjected to irradiation by a KrF pulsed excimer laser (Questek Model 2260, 248 nm, 20 ns). The target was prepared using conventional methods described at section 3.5.2.1 and had 96% theoretical density. The laser energy density was varied from 0.5 to 3.5 J/cm^2, and the beam was at 45 degree angle of incidence. The projected beam area on the target was 1mm x 1mm square, obtained from an aperture projection at a distance of 8 ft using a 250-mm lens. The energy density was calibrated using a Coherent power meter (Model 100E).

The mass spectrometer setup was a hybrid between plasma flux analysis and partial pressure analysis. The overall design was similar to partial pressure analysis,[275] except

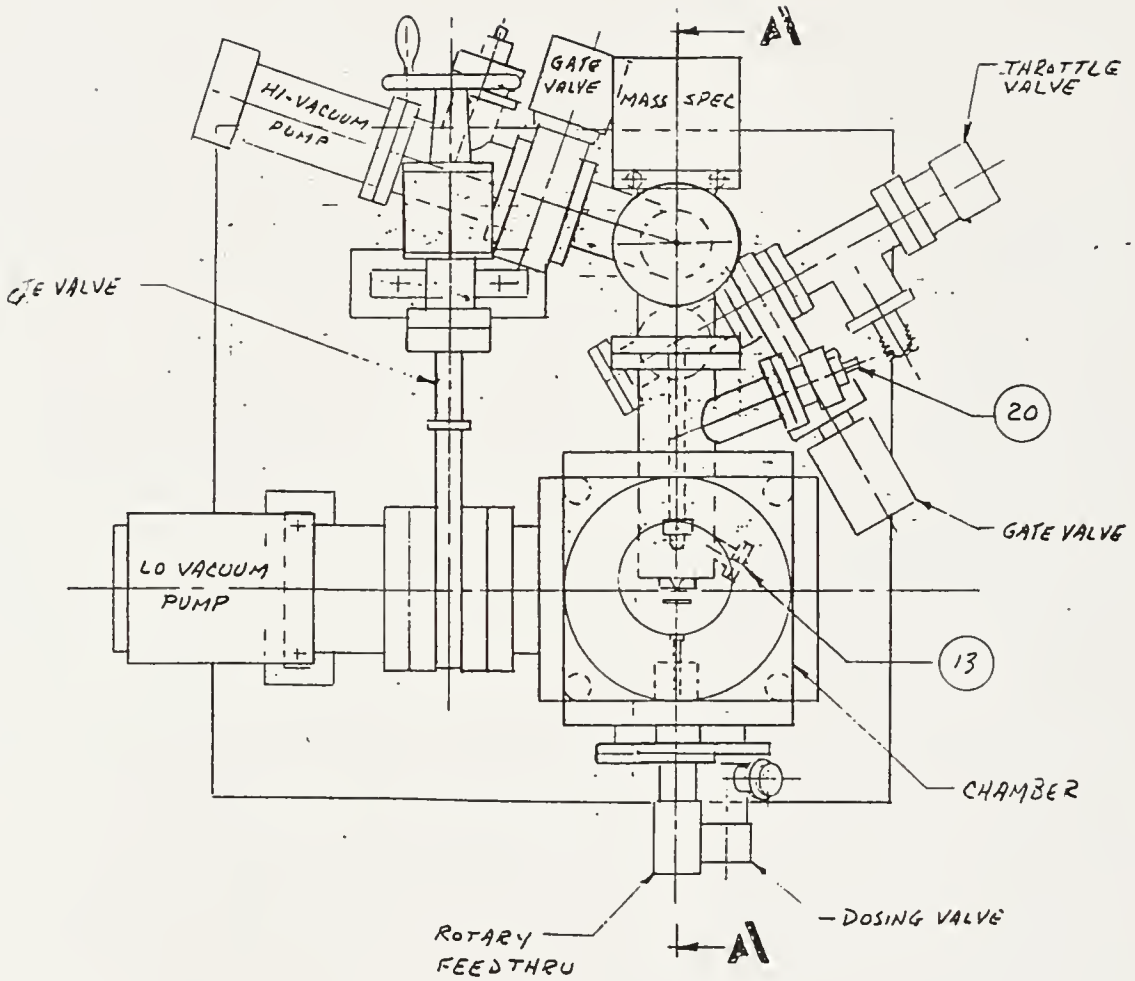

Figure 8-1 Schematic diagram a differentially pumped mass spectrometer.

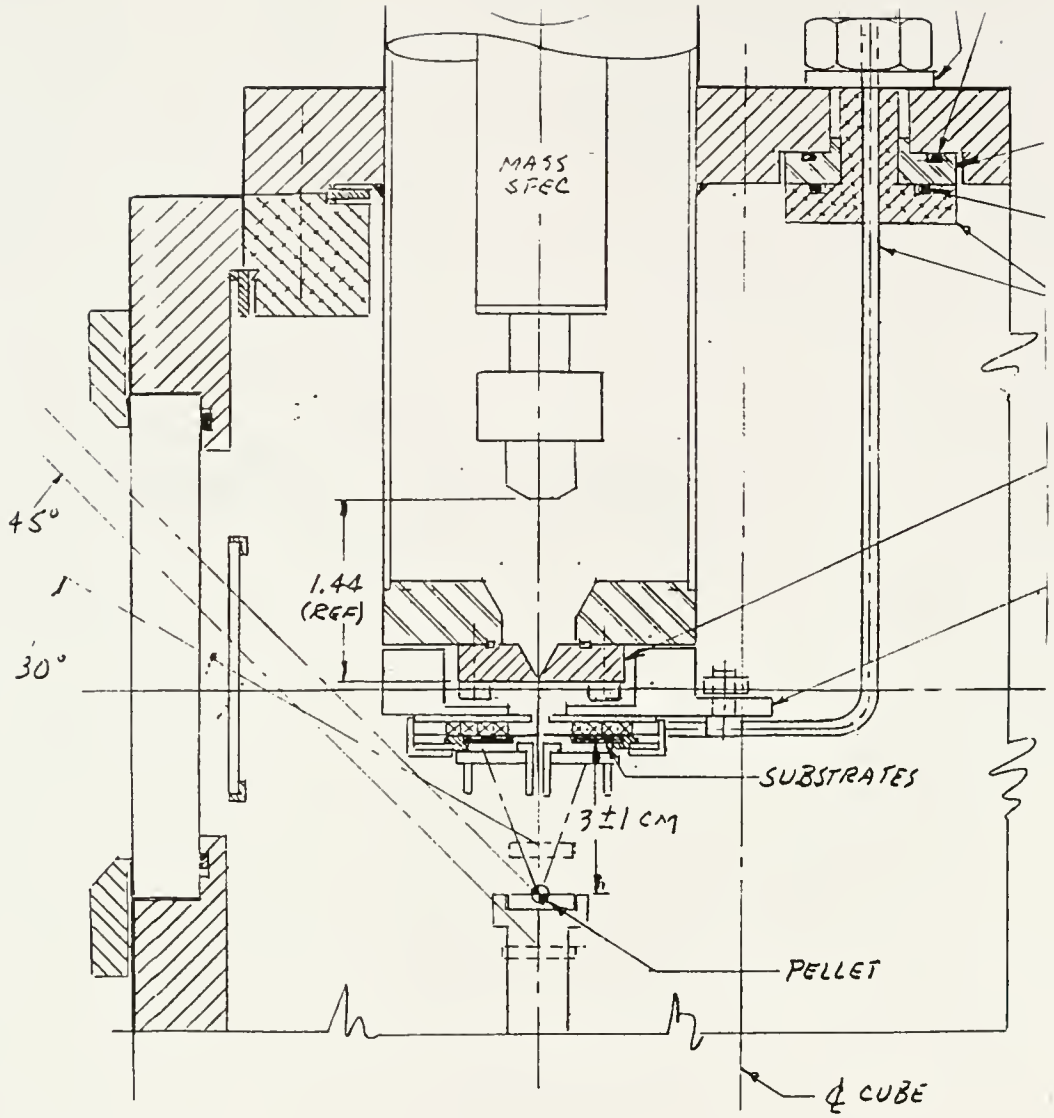

Figure 8-2 Detail the orifice design at the differentially pumped mass spectrometer. Orifice diameter: 100 μm. Orifice length: 100 μm.

that the target, orifice, and detector were in a direct line-of-sight alignmnent, allowing the study of ionic plasma species directly from the ablated target without thermalization. Since the mass spectrometer was not equipped with an energy analyzer, all the detected spectra peaks were representative of a plasma with a wide range of kinetic energy.

The Balzers QMA420 quadrupole mass spectrometer (QMS), used to analyze the plasma entering the orifice from the evaporation chamber, was equipped with a cross-beam ion source and a secondary electron multiplier (SEM) detector. The detection limit of the QMS was 512 amu with a current sensitivity of 10^{-12} amperes. The secondary electron spectra peaks higher than 44 amu were completely resolved. Below this value, the spectra peaks with a mass to charge(m/e) ratio of 15, 16, 18, 28, 32, and 44 were ignored since it was suspected that these were due to contributions from residual gases. The QMS was operated using the Balzers Quadstar™ software, providing spectra results in two different formats: Multiple Ion Detection (MID), which gives ion currents up to 16 mass numbers as a function of time, and Scan Bargraph (SCB), which gives the ion current intensity as a function of mass numbers.

To distinguish the ions from neutral particles within the plasma, the mass spectrometer could be operated with or without the cross-beam electron ionizer. Without the cross-beam electron ionizer, the operation is known as laser ionization mass spectroscopy (LIMS),[253] which detects the ions produced from the laser evaporations. Charged particles are suspected to have a major impact on the film morphology and quality.[260]

8.2.2 Effect of Fluence

The effect of laser fluences on the concentration of plasma elements and oxides species (Ba+, Ba^{++}, BaO^{+}, Cu^{+}, CuO^{+},Y^{+}, and $YO^{+)}$ was investigated. In order to detect small changes in concentration, the current intensities were collected as a function of time (MID mode), while laser pulses were introduced at various fluences (Figure 8-3).

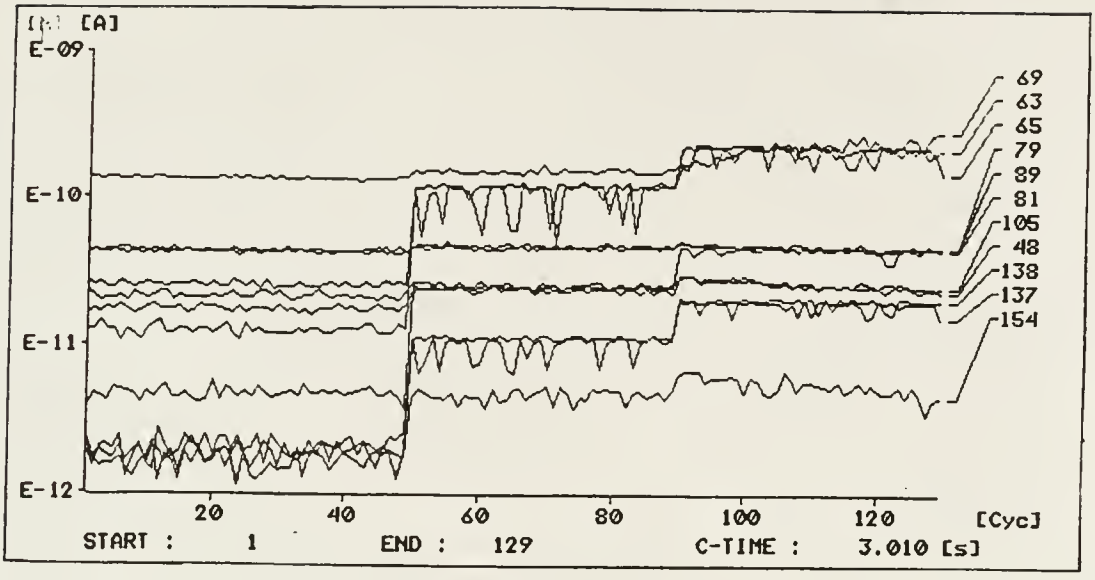

a

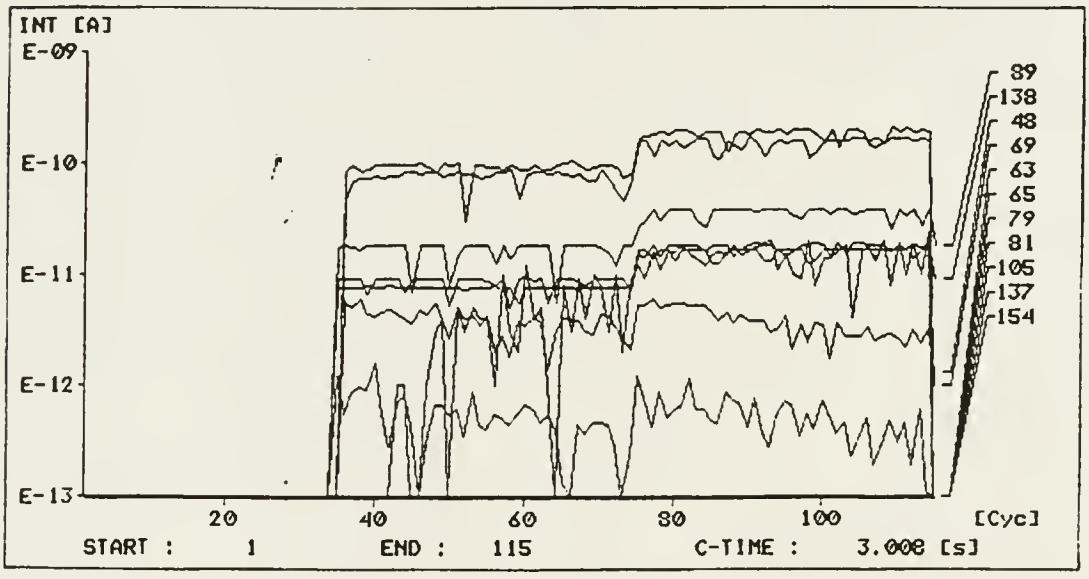

b

Figure 8-3 Mass spectrometer (MID) as a function fluence. (a) with ionizer, detecting both neutral and ionic species; (b) without ionizer, detecting only ionic species.

The results for fluences ranging from 0.3 J/cm^2 to 3.1 J/cm^2 at a pressure of 1x10^{-3} Torr in air are presented at Table 8-1. No species were detected at fluences below 1.1 J/cm^2. The reported threshold value derived from the emission spectra for evaporation of YBCO using ArF was 0.8 J/cm^2.[88] At fluence of 1.3 J/cm^2, major increases in the Y^+ and Ba^+ concentrations were observed, although the change in the oxide species concentration was almost negligible. At higher fluence, 3.1 J/cm^2, a significant increase in the BaO^+ concentration was observed. The concentrations of Y^+, Ba^+, and Cu^+ species in 10 mTorr and 30 mTorr oxygen increase with fluence, with a threshold fluence of 1.4 J/cm^2 and 1.9 J/cm^2, respectively. The linearity cannot be determined since the data points are too scattered at higher fluences. Emission spectra studies have shown that the concentrations of Y, Ba^+, and Cu plasma of YBaCuO ablated with an ArF laser increased linearly with fluence.[88] While no species higher than 153 amu were found at the fluence range studied here, large species, with molecular weights up to 400 amu, were reported during laser evaporation at fluence higher than 20 J/cm^2.[253]

One of the advantages of the mass spectrometer system described herein was the ability to study the charged species produced during the evaporation. Since the target, orifice, and mass spectrometer were aligned in a straight trajectory, some of the ions produced during the evaporation were allowed to enter the QMS chamber without colliding with the orifice.

The mass spectra of the plume produced during the evaporation of a YBCO pellet at 2.0 J/cm^2 in 10^{-3} Torr air were compared, with and without the cross-beam electron ionizer. It was observed that the currents obtained with the electron ionizer were equal to or higher than the currents obtained without the electron ionizer (LIMS), although the ratio of each element with respect to Y^+ remained essentially the same. This result is reasonable since only a small fraction of the plasma, typically 10^{-4}, is ionized by the cross-beam ionizer with the electron bombardments.[266] If it is assumed that the change in the measured ion currents constitutes 10^{-4} of the neutral atoms,[276] the fraction of the Y, Ba,

Table 8-1. Effect of laser fluence on the gas composition in 10^{-3} torr air

Fluence (J/cm^2)	Vapor Species MW	Species	Quantity
0.3	--	--	none
0.8	--	--	threshold
2.0	137	Ba^+	major
	153	BaO^+	major
	64	Cu^+	major
	80	CuO^+	minor
	89	Y^+	major
3.1	137	Ba^+	major
	153	BaO^+	major
	64	Cu^+	minor
	80	CuO^+	minor
	89	Y^+	major

Note : Ba^{2+} is absent in all runs

and Cu ions can be estimated to be 1.0 (Y), 10^{-3} (Ba), and $5x10^{-4}$ (Cu). The reported percentage value of ionic species in the plasma at higher pressure was measured using an ion probe was 4% at 5 cm in 200 mTorr oxygen.[260]

Quantitative determination of the plasma plume was difficult since the plasma dynamics, detector response and sensitivity, degree of ionization, and the plasma stability have to be considered. Calibrating the mass spectrometer with a standard gas mixture (He, Ne, Ar, Kr, SF_6) may solve this problem. A correction factor, assuming that the plasma gases behave like noble gases, could then be calculated to determine the quantity of the plasma.

8.2.3 Effect of Ambient Gas and Pressure

The composition of the species detected remained the same at different pressures. The pressure inside the evaporation chamber was varied from 10^{-4} to 10^{-1} Torr. The majority of the detected species were either atomic-neutral or single-charged. However, a very low concentration of oxide species was also detected. No other significant concentration of species existed between 150 - 512 amu. The mass spectra showed that individual isotopes are fully resolved. Representative spectra are provided in Figure 8-4.

Analysis without the electron ionization at pressures below 10^{-2} Torr in air, with a fluence of 2.0 J/cm^2, showed the presence of single-charged and ionic oxides species, including Y^+, Ba^+, Cu^+, Ba^{2+}, YO^+, and BaO^+. These species were the same as those detected using mass spectroscopy at high vacuum.[263, 264] The concentration of the oxide species was very low, similar to the measurement using emission spectroscopy[88, 257] and mass spectroscopy. Oxygen species were difficult to detect due to their interference with the high background oxygen. Plasma analysis at a higher current sensitivity, which was used to detect higher molecular weight species, only broadened the spectra peaks. It was considered that this broadening was caused by a distribution of kinetic energy in the

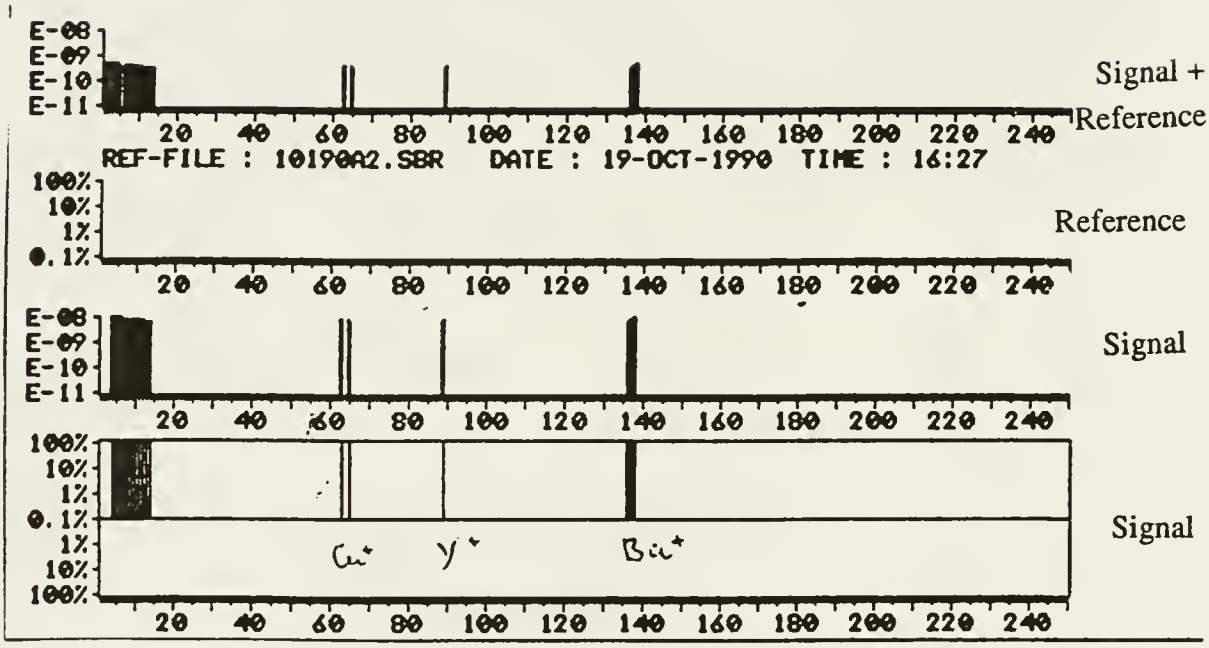

Figure 8-4 A representative mass spectra for YBCO plume. Note the presence of atomic species.

incoming species. The concentration of CuO was known to increase with the use of N_2O instead of O_2 due to the higher collisional rate.[277]

At pressures higher than 10^{-2} Torr in air, the ionic species were not detected. However, neutral species were still present and could be detected when the cross beam ionizer was activated. The absence of ionic species at higher pressure is presumed to be caused by the increased number of collisions between the ionic species and the background gases, resulting in neutralization of the ionic species before they reach the orifice. At higher pressure, the deceleration of the plasma lowers the collisional energy. As a result, the concentration of some species decreases.

Plasma temperatures were estimated from the mean free path and cut-off pressure of the ionic species. The mean free path for Y^+, Ba^+, and Cu^+ at 10^{-2} Torr varies from 1.7 to 3.4 mm at 300 K, and 4.6 to 9.1 cm at 8000 K (Table 8-2). This distance was significantly greater than the orifice diameter of 0.1 mm, which ensured that the ionic species did not collide with the orifice wall. In comparison, the distance between the target and the orifice was about 3 cm. Assuming a barium ion, which has the lowest mean free path, takes a direct path from the evaporation surface to the orifice without colliding with background gas, the average temperature of the barium ion would be at least 8000 K. This temperature is consistent with literature values of the plasma temperature based on the line intensity ratio in line emission spectroscopy, which ranged from 7000 to 9000 K.[143]

The barium concentration in the plasma was the highest for the observed species. Although the mean free path calculations suggest that barium atoms have the lowest mean free path, and are therefore less likely to reach the orifice, the experiment showed otherwise. A possible explanation is that the barium evaporates readily and predominates the plasma composition since the heat of vaporization of barium is the lowest (142 kJ/mole at STP), compared to yttrium (363 kJ/mole) and copper (300 kJ/mole). Another possibility is that barium ion is more stable since it has the lowest ionization potential.

Table 8-2 Theoretical mean free path of Y, Ba and Cu elements

Spec	Atom. Diam. (Å)	Calculated mean free path at given temperature and pressure[a] 300°K 10^{-1} torr	300°K 10^{-2} torr	300°K 10^{-3} torr	300 °K $2x10^{-2}$ torr	1000 °K $2x10^{-2}$ torr	8000 °K $2x10^{-2}$ torr
Y	4.5	350 µm	3.5 mm	3.5 cm	1.7 mm	5.6 mm	4.6 cm
Ba	5.6	220 µm	2.2 mm	2.2 cm	1.1 mm	3.7 mm	3.0 cm
Cu	3.2	680 µm	6.8 mm	6.8 cm	3.4 mm	1.1 cm	9.1 cm

a $\lambda = 2.33x10^{-6}\ T / P\ d^2$

where λ = mean free path (m)

T = temperature (K)

P = pressure (torr)

d = atomic diameter (Å)

More species were found during the evaporation in the oxygen environment than in nitrogen or air, although the number of oxide species was not as high as expected. The pressure was kept at 1.3×10^{-2} Torr, and the fluence was varied from 1.4 to 2.6 J/cm^2. Although it was expected that more oxidized plasma species would be found during the evaporation in oxygen than evaporation in nitrogen, the compositions of the plasmas were very similar (Table 8-3). The plasmas consisted mainly of Y^+, Ba^+, and Cu^+, except at 2.6 J/cm^2, where Y^+ and Ba^{2+} species were found in oxygen, but not in nitrogen. The photochemical process may be more exothermic in oxygen giving a higher reaction temperature and generating more species.

8.2.4 Effect of Repetition Rate

In general, as the repetition rate increased, the concentration of the plasma species also increased. At 1 pps, analysis without ionizing electrons detected only Ba^+ and Cu^+. However, as the frequency increased, other species such as Ba^{2+}, Y^+, and BaO^+ appeared, with the Cu^+ concentration among the highest. For the result at 1 pps, it was speculated that the reduction in the concentration of the species was due to the scanning cycles of the mass spectrometer. If the timing was not coordinated, a portion of the scan was accidently eliminated. The concentration of BaO^+ measured at 10 pps was higher than the concentration at 20 pps. Both YO^+ and CuO^+ were absent. Evidence on the presence of neutral species was found from the analysis with the electron ionizer. At 1 and 5 pps, results similar to those without the electron ionizer were found, where only Ba^+ and Cu^+ were detected. However, at higher frequencies, the species detected included O_3^+, Cu^+, Ba^{2+}, CuO^+, Y^+, YO^+, Ba^+, and BaO^+. All the oxide species were detected only at frequencies of 10 pps and 20 pps. The CuO^+ exhibited a maximum at 10 pps.

Table 8-3 Effect of background gases on plasma composition

Fluence (J/cm^2)	Species detected in nitrogen		in oxygen	
1.4	63	Cu^+		
	65	Cu^+		
	136	Ba^+		
	137	Ba^+		
	138	Ba^+		
1.7	63	Cu^+	65	Cu^+
	65	Cu^+	69	Ba^{2+}
	136	Ba^+	89	Y^+
	137	Ba^+	136	Ba^+
	138	Ba^+	137	Ba^+
2.6	63	Cu^+		
	65	Cu^+		
	89	Y^+		
	137	Ba^+		
	138	Ba^+		

Note : Scan Bargraph mode

Cell pressure : 1.3×10^{-2} torr

QMS pressure : 5.5×10^{-7} torr

Background gas : nitrogen and oxygen.

8.2.5 Effect of Pulse Number

The concentration of ozone increased as the number of pulses increased. Similar increases were seen on YO^+, BaO^+, and CuO^+, while the concentration of Y^+, Ba^+, and Cu^+ remained unchanged. The Cu and CuO emissions were reported to decrease with increasing numbers of shots, presumably because of target texturing.[4]

8.2.6 Effect of Target Density

No difference was found in the plasma composition when the evaporation was done using high-density or low-density targets.

8.3 Comparison with Complex Equilibrium Reactions

The result from the mass spectroscopic analysis and the equilibrium predicted from the thermodynamic calculations will be compared, which will show the actual condition of the plasma formed. The basic assumptions necessary to calculate plasma thermodynamic equilibrium are local thermodynamic equilibria, electric charge neutrality, and ideal gas. Several factors may affect the actual composition. First, the photochemistry effect, which may increase the production of the ions. Second, the plasma is undergoing a collision with the background gas. As the result, the composition of the oxides may be higher than the calculated value. In addition, since the mass spectrometer is located away from the target, it is possible that the charged species has been neutralized by the time it reaches the orifice. Third, the system pressure is hard to determine. In the calculations, an intermediate pressure around 1 atm was assumed. Despite the above uncertainty, the thermodynamic calculations can provide some valuable information, especially the trends on how the plasma reactions may proceed with changes in operational variables. The effects of temperature, pressure, and background gas are discussed below.

8.3.1 Effect of Temperature

The target surface and plasma temperatures are affected by the laser fluence and repetition rate. Detailed analysis on this physical phenomena is discussed at Chapters 5 and 6. As the fluence increased to 1.3 J/cm^2, it was found that the concentration of Y^+ and Ba^+ also increased. This result is consistent with the formation Y and Ba vapors at temperatures beyond 2500 K as shown in Figure 2-7. At higher fluence, BaO+ was formed. This result contradicts the prediction, since oxide formations are favorable at lower temperatures.

The mass spectrometer measurement showed that the increase in the repetition rate increases the number of Ba^{2+}, Y^+, and BaO^+ in the plasma. This result is consistent with the themodynamic prediction for the Ba^{2+} and Y^+, but not for the BaO^+, which was predicted to decrease with the increase in temperature. The absence of YO^+ and CuO^+ indicates that the temperature is higher than 5000 K. The increase in the repetition rate probably had more affect on the increase in the overall concentration than the increase in the plasma temperature.

The increase in the number of pulses increased the crater depth and was shown to increase the number of oxide formations detected using mass spectrometer. Two possible explanations from the thermodynamic calculations are the decrease on the plasma temperature and the increase on the plasma pressure, both of which increase the number of oxides.

8.3.2 Effect of Pressure

As the pressure decreases, the thermodynamics predict that the number of oxides and elemental species decreases at a fixed temperature. The mass spectroscopic measurements, indeed, showed the reduction of oxides at high vacuum. As an illustration,

Ba^+ formed at a temperature higher than 6000 K at 1 atm; however at 10^{-1} Torr, the temperature dropped to less than 3000 K.

8.3.3 Effect of Background Gas

The mass spectroscopic measurements showed that the plasma formed in the oxygen environment contains more species than the plasma formed in air or nitrogen. This result is consistent with the simulation with excess oxygen, presented at Table 2-6, which predicts the increase in ions and oxides by as much as 40% with 100% excess oxygen.

8.4 Conclusion

Mass spectroscopic investigation of the plasma plume created by the interaction of KrF excimer laser beam and an YBCO superconducting target indicates the presence of neutral and ionized species, Y, Y^+, Ba, Ba^+, Ba^{2+}, Cu, Cu^+, as well as diatomic species YO, BaO, CuO, YO^+, BaO^+, CuO^+. The plasma was studied at pressures up to $3x10^{-2}$ Torr using a differentially pumped mass spectrometer. The composition of the species detected remained the same at different pressures. More plasma species were detected at higher fluences. Reaction in oxygen produces more species compared to one in nitrogen and air. The concentration of the plasma increases with laser pulse frequency. Target density has no effect on the plasma composition. Based on the pressure cut-off of the ionic species at 10^{-2} Torr, the plasma temperature was determined to be 8000 K. The thermodynamic calculations gave a reasonably good prediction on the observed trend, especially the effect on the formation of oxides and ions.

CHAPTER 9
CONCLUSION

A detailed study of the interaction of a KrF beam with a Y-Ba-Cu-O high-temperature superconductor target was performed to address two principal problems associated with thin film deposition via pulsed laser evaporation: (1) formation of film surface particulates and (2) development of irregular target surface morphology. Thermodynamic chemical equilibrium and mass spectroscopic analysis were performed to determine the composition of the plasma generated by laser irradiation of Y-Ba-Cu-O during the formation and expansion stages.

9.1 Reduction of Film Particulate

The formation of film particulates was suppressed by maintaining the target bulk temperature greater than 700 °C (Chapter 5). Such target heating eliminated the formation of spherical film particulates greater than one micron and suppressed the evolution of target surface morphology. The number of particulates on the film formed by heating the target, in combination with fluence at 1.2 J/cm^2, produced a film with 5×10^3 particles/mm^2. Films produced from targets at room temperature had 10^5 particles/mm^2.

The formation of film particulates has been correlated with the formation of target surface morphology, such that a smooth target produced fewer film particulates. It is believed that by maintaining the target at high temperature, the surface tension developed at the target surface could be significantly reduced and that the target surface could relax after each pulse to form a smooth surface. Untreated targets cooled rapidly producing surface cracks which later contributed to the development of the target surface morphology

(Chapter 6). The size of the spherical particles was predicted from the momentum balance calculations. Under typical film deposition conditions, and using experimentally determined physical properties (Chapter 3), the particle size was calculated to be approximately 2 μm in diameter.

9.2 Development of Target Morphology

The development of surface morphology entailing the distribution of laser power via optical and conventional thermal analysis was investigated (Chapter 6). A detailed fluence-dependent optical analysis was used to describe the surface morphology evolution which was found to be a strong function of laser fluence and pulse number.

Studies of the evaporation of YBCO target material as a function of the fluence and pulse number identified the formation of porous (fluence 0.1 - 0.6 J/cm^2), cone (fluence 0.6 - 1.1 J/cm^2) and melt (fluence > 1.1 J/cm^2) morphology (Chapter 6). Below 0.1 J/cm^2, no surface texturing took place. At fluence below 1.1 J/cm^2, the evaporation rate was low. In addition, the textured target became yttrium rich making it unacceptable for film deposition. At fluence greater than 1.1 J/cm^2, the target remained stoichiometric and the evaporation rate increased with fluence. Because of the surface texturing, the optimum evaporation rate was at fluence between 2 to 3 J/cm^2.

The formation of pore and cone morphologies could be explained using the shielding model, whereas, the formation of the melt morphology at high fluence could be explained using fluence-dependent optical analysis. At low fluence, the evaporated target contains a high concentration of yttrium rich phase as determined using EDAX, auger and XRD analysis. XRD analysis revealed the presence of Y_2O_3 although the formation of Y_2BaCuO_5 was expected from the phase diagram. Evaporation of a Y_2BaCuO_5 at low fluence slowed the formation of Y_2O_3. The Y_2O_3 on the surface, which has a low evaporation rate, shielded the material underneath from the incoming radiation, producing a highly textured surface.

The formation of melt surface morphology at high fluence was explained with optical fluence-dependent analysis. It has been shown that once an initial development of surface morphology takes place, the development the evolution of coarser melt surface morphology can be predicted. The initial development of target morphology at low pulse number depends on the surface properties whereas at high pulse number, the material properties dominates. The development of the initial surface morphology at high fluence was attributed to the formation of surface cracks from thermal stress. If the target temperature was kept higher than 700 ^{o}C, the development of surface morphology could be suppressed. The effect of target density in the formation of surface morphology was minimal. By maintaining the target at elevated temperatures, a steady rate of evaporation could be sustained even at high pulse numbers.

9.3 Chemical Equilibrium Analysis

A thermodynamic equilibrium calculation based on stoichiometric algorithm was performed on a high-temperature, high-pressure, adiabatically expanding system to determine the chemical equilibrium as a function of temperature, pressure, and inert gas concentration (Chapter 2). The result from the equilibrium calculation was compared with the result obtained from mass spectrometer (Chapter 8). An overall energy balance calculation was also performed (Chapter 4).

The equilibrium calculations were performed by assuming that local equilibria exist, ideal gas applies and the absence of photochemical reactions. The results showed that the ion formation was favored at high temperatures, low pressures and high inert gas concentrations. The thermodynamic calculation is consistent with the Le Chatelier principle. Oxide formation was favored at high oxygen pressures and low temperatures. The concentration of ion increases with increasing temperature. The formation of CuO was not favorable due to its high heat of formation. At temperatures between 5000 to 10,000 K, the plasma consists mainly of neutral and ionic elemental species.

Chemical characterization of the plasma plume using a differentially pumped quadrupole mass spectrometer (P ≤30 mTorr) showed the presence of mainly neutral and ionic atomic species (Chapter 8). The result was qualitatively consistent with the thermodynamic equilibrium calculation. It showed the presence of neutral and ionic Y, Ba and Cu in the plasma phase. The concentration of BaO was higher than YO, and only a small concentration of CuO was detected. Based on the species detected, the temperature of the plasma can be estimated to be in the order of 7000 to 8000 K at fluence of 2 J/cm^2.

Because the composition of the plasma species can be estimated from thermodynamic calculation, the overall energy balance during laser evaporation was also performed (Chapter 4). An overall energy balance showed that the phase transformation, from solid of YBCO at room temperature to plasma with composition predicted from thermodynamic calculation at 8000 K and 1 atm showed that the phase transformation consumed one-third of the absorbed laser energy with the remainder converted to plasma kinetic energy. The total energy loss attributed to thermal conduction and radiation loss from the surface is less than one percent of the total energy. The thermal penetration depth was calculated using a one dimensional heat transfer model using thermal diffusivity determined using laser flash analysis (Chapter 3). This kinetic energy was manifested in the redeposited plume area formed during ambient pressure evaporation (Chapter 7). It was determined that the redeposited plume area was a linear function of fluence, consistent with the change in kinetic energy with increasing fluence. The physical properties used in calculations were determined using thermal methods (heat capacity, transition temperatures, and thermal expansion coefficient) and laser flash technique (thermal diffusivity) (Chapter 3).

9.4 Recommendations for Future Studies

In the area of surface morphology development, more work could be done to experimentally determining the temperature profile across the solid. The estimate of surface temperature from literature varied a great deal. It would be useful to compare the experimental value with the prediction from the thermal model. For the thermodynamic equilibrium calculation, a better prediction could be made if models other than the ideal gas model were used. Considering that the temperature and pressure of the plasma are high, a model such as Peng-Robinson would be adequate. A kinetic study of the plasma may provide a better answer whether the plasma has indeed achieve an equilibrium condition under the time frame considered in the evaporation process. A better way to determine the pressure of the plasma is also important. In the area of mass spectrometer, a better quantitative determination would be useful. Having a mass spectrometer which will resolve the plasma with certain kinetic energy would be advantageous. The study of film particulate reduction using target heating should be continued. A more accurate determination of the particle number to determine the histogram would be useful. A better correlation between the formation of column melt surface morphology with the number of film particulate can be made. Also the question whether the irregular particulate is caused by the target explosion or film outgrowth still need to be resolved. In the area of plume formation, further work on plasma expansion model can be done. In the area of process scale-up, a large area deposition can be made possible by incorporating the concept of target heating and optical scanning techniques to produce high quality films at a faster rate.

REFERENCE LIST

1. J. T. Cheung, H. Sankur, CRC Critical Reviews in Solid State and Materials Sciences. **15**, 63-109 (1988).

2. F. Beech, I. W. Boyd, "Photochemical Processing of Electronic Materials," (I. W. Boyd, R. B. Jackman, Eds.), Academic Press, New York, 1991, pp. 387-429.

3. G. K. Hubler, Mat. Res. Bull. **17**, 26-27 (1992).

4. D. Djikkamp, T. Venkatesan, X.D. Wu, S.A. Shaheen, N. Jisrawi, Y.H. Min-Lee, W.L. McLean, M. Croft, Appl. Phys. Lett. **51**, 619-621 (1987).

5. V. S. Ban, D. A. Kramer, J. Mater. Sci. **5**, 978-982 (1970).

6. C. M. Cotell, K. S. Grabowski, Mat. Res. Bull. **17**, 44-53 (1992).

7. J. Cheung, J. Horwitz, Mat. Res. Bull. **17**, 30-36 (1992).

8. J. F. Ready, Appl. Phys. Lett. **3**, 11 (1963).

9. B. A. Lengyel, Am. J. Phys. **34**, 903-913 (1966).

10. H. M. Smith, A. F. Turner, Appl. Opt. **4**, 147-148 (1965).

11. C. W. Chu, P.H. Hor, R.L. Meng, L. Gao, Z.J. Huang, Y.Q. Wang, Phys. Rev. Lett. **58**, 405 (1987).

12. O. Eryu, K. Murakami, K. Masuda, A. Kasuya, Y. Nishina, Appl. Phys. Lett. **54**, 2716 (1989).

13. H. S. Kwok, D.T. Shaw, Q.Y. Ying, J.P. Zheng, S. Witanachchi, E. Petrou, H.S. Kim, "Processing of Films for High Tc Superconducting Electronics" (T. Venkatesan, Ed.), Proc. SPIE, vol. 1187, Santa Clara, CA, 1989, pp. 161-171.

14. H. Schwartz, H. A. Tourtellotte, J. Vac. Sci. Technol. **6**, 373-378 (1969).

15. M. Kanai, T. Kawai, S. Kawai, H. Tabata, Appl. Phys. Lett. **54**, 1802 (1989).

16. R. Simon, A. Smith, "Superconductors Conquering Technology's New Frontier," Plenum Press, New York, 1988.

17. J. Narayan, R.K. Singh, A.K. Singh, J. Krishnaswamy, K. Jagannadham, C.B. Lee, R.K. Prasad, N.R. Parikh, "Microstructure and In-situ Processing of Epitaxial High-Tc Films" (S. H. Whang, A. DasGuptas, Eds.), High Temp. Supercond. Compd.: Process. Relat. Prop., Proc. Symp., Miner. Met. Mater. Soc., Warrendale, PA, 1989, pp. 337-58.

18. J. Narayan, Journal of Metals **1**, 18-23 (1989).

19. S. M. Schoenung, M. I. Flik, J. R. Hull, Mechanical Engineering **111**, 92-99 (1989).

20. R. Simon, Physics Today **6**, 64-70 (1991).

21. S. T. Ruggiero, D. A. Rudman, "Superconducting Devices," Academic Press, Boston, 1990.

22. D. Laubacher, Internal Report, DuPont Company, 1993.

23. R. H. Ono, Mat. Res. Bull. **17**, 34-38 (1992).

24. D. B. Chrisey, A. Inam, Mat. Res. Bull. **17**, 37-43 (1992).

25. T. Venkatesan, C.C. Chang, D. Dijkkamp, S.B. Ogale, E.W. Chase, L.A. Farrow, D.M. Hwang, P.F. Miceli, S.A. Schwarz, J.M. Tarascon, X.D. Wu, A. Inam, J. Appl. Phys. **63**, 4591-4598 (1988).

26. S. Miyazawa, Appl. Phys. Lett. **55**, 2230 (1989).

27. C. H. Mueller, PhD Dissertation, University of Florida, 1992.

28. R. D. McConnell, S. A. Wolf, Eds., "Science and Technology of Thin Film Superconductors," Plenum Press, New York, 1989.

29. R. F. Bunshah, "Deposition Technologies for Films and Coatings," Noyes Publications, Park Ridge, New Jersey, 1982.

30. D. Lubben, S. A. Barnett, K. Suzuki, S. Gorbatkin, J. E. Greene, J. Vac. Sci. Technol. B **3**, 968-974 (1985).

31. H. S. Kwok, P. Mattocks, L. Shi, X.W. Wang, S. Witanachchi, Q.Y. Ying, J.P. Zheng, D.T. Shaw, Appl. Phys. Lett. **52**, 1825 (1988).

32. S. Komuro, Y. Aoyagi, T. Morikawa, S. Namba, Jpn. J. Appl. Phys. **27**, L34 (1988).

33. O. Eryu, K. Murakami, K. Takita, K. Masuda, H. Uwe, H. Kudo, T. Sakudo, Jpn. J. Appl. Phys. **27**, L628 (1988).

34. A. Inam, M.S. Hedge, X.D. Wu, T. Venkatesan, P. England, P.F. Miceli, E.W. Chase, C.C. Chang, J.M. Tarascon, J.B. Wachtman, Appl. Phys. Lett. **53**, 908 (1988).

35. H.S. Kwok, P. Mattocks, D.T. Shaw, L. Shi, X.W. Wang, S. Witanachchi, Q.Y.Ying, J.P. Zheng, P. Bush, in "Materials Research Society Symposium Proceedings " (M. B. Brodsky, Ed.), Material Research Society, Pittsburgh, PA, 1988, vol. 99, p. 273.

36. J. Narayan, N. Biunno, R. Singh, O. H. Holland, O. Auciello, Appl. Phys. Lett. **51**, 1845 (1987).

37. H. S. Kim, H. S. Kwok, Appl. Phys. Lett. **61**, 2234-2236 (1992).

38. C. C. Chang, X.D. Wu, A. Inam, D.M. Hwang, T. Venkatesan, P. Barboux, J.M. Tarascon, Appl. Phys. Lett. **53**, 517-519 (1988).

39. F. A. Miranda, W. L. Gordon, K. B. Bhasin, J. D. Warner, Appl. Phys. Lett. **57**, 1058-1060 (1990).

40. T. E. Mitchell, D. R. Clarke, J. D. Embury, A. R. Cooper, Journal of Metals **1**, 6 (1989).

41. C. C. Chang, X.D. Wu, R. Ramesh, X.X. Xi, T.S. Ravi, T. Venkatesan, D.M. Hwang, R.E. Muenchausen, S. Foltyn, N.S. Nogar, Appl. Phys. Lett. **57**, 1814 (1990).

42. X. D. Wu, D. Djikkamp, S.B. Ogale, A. Inam, E.W. Chase, P.F. Miceli, C.C. Chang, J.M. Tarascon, T. Venkatesan, Appl. Phys. Lett. **51**, 861 (1987).

43. A. Inam, X.D. Wu, T. Venkatesan, S.B. Ogale,C.C. Chang, D. Djikkamp, Appl. Phys. Lett. **51**, 1112 (1987).

44. R. J. Kelly, J. E. Rothenburg, Nucl. Instrum. Methods B **7/8**, 755 (1985).

45. L. I. Maissel, R. Glang, "Handbook of Thin Film Technology," McGraw-Hill Book Company, New York, 1970.

46. T. Venkatesan, X. D. Wu, A. Inam, J. B. Wachtman, Appl. Phys. Lett. **52**, 1193-1195 (1988).

47. L. Wiedeman, H. Helvajian, J. Appl. Phys. **70**, 233 (1991).

48. D. B. Chrisey, J. S. Horwitz, R. E. Leuchtner, Thin Solid Films **1**, 1 (1992).

49. C. H. Chen, T. M. Murphy, R. C. Phillips, Appl. Phys. Lett. **57**, 937-939 (1990).

50. C. H. Becker, J. B. Pallix, J. Appl. Phys. **64**, 5152-5156 (1988).

51. H. Dupendant, J.P. Favigan, D. Fivord, A. Lienard, J.P. Rebouillat,Y. Souche, Appl. Surf. Sci. **43**, 369 (1989).

52. R. A. Neifled, E. Potenziani, W.R. Sinclair, W.T. Hill, B. Turner, A. Pinkas, Appl. Phys. Lett. **69**, 1107 (1991).

53. S.R. Foltyn, R.C Dye, K.C. Ott, E. Peterson, K.M. Hubbard, W. Hutchinson, R.E. Muenchausen, R.C. Estler, X.D. Wu, Appl. Phys. Lett. **59**, 594-596 (1991).

54. T. Venkatesan, X. D. Wu, R. Muenchausen, A. Pique, Mat. Res. Bull. **17**, 30-36 (1992).

55. H. V. Boenig, "Fundamentals of Plasma Chemistry and Technology," Technomic Publishing Co., Lancaster, PA, 1988.

56. T. K. Fowler, in "Advances in Plasma Physics" (A. Simon, W. B. Thompson, Eds.), Interscience Publishers, New York, 1968, vol. pp. 1-66.

57. J. M. Baldwin, Appl. Spec. **24**, 429-435 (1970).

58. M. Ottosson, A. Harsta, J. O. Carlsson, J. Electrochem. Soc. **138**, 778-783 (1991).

59. C. T. Alkemade, T. Hollander, W. Snelleman, P. J. Zeegers, "Metal Vapours in Flames," Pergamon Press, Oxford, 1982.

60. L. Spitzer, "Physics of Fully Ionized Gases," Interscience, New York, 1962.

61. I. P. Shkarofsky, T. W. Johnston, M. P. Bachynski, "The Particle Kinetics of Plasmas," Addison-Wesley Publishing, Reading, Massachusetts, 1966.

62. R. Roberts, "Applications of Photochemistry," Technomic, Lancaster, PA, 1984.

63. W. R. Smith, R. W. Missen, "Chemical Reaction Equilibrium Analysis: Theory and Algorithms, " John Wiley and Sons, New York, 1982.

64. D.J. Myers, Ph.D. Dissertation, University of Florida, 1984.

65. M. W. Chase, C.A. Davies, J.R Downey, D.J. Frurip, R.A. McDonald, A.N. Syverud, J. Phys. Chem. Ref. Data **14**, 315-1695 (1985).

66. M. W. Chase, C.A. Davies, J.R. Downey, D.J. Frurip, R.A. McDonald, A.N. Syverud, J. Phys. Chem. Ref. Data **3**, 372-375 (1974).

67. L. B. Pankratz, "Thermodynamic Properties of Elements and Oxides," United States Department of the Interior, Bureau of Mines, Washington, D.C., 1983.

68. R. Hultgren, P.D. Desai, D.T. Hawkins, M. Gleiser, K.K. Kelley, D.D. Wagman, "Selected Values of the Thermodynamic Properties of the Elements," American Society for Metals, Metals Park, OH, 1973.

69. R. C. Weast, M. J. Astle, "CRC Handbook of Chemistry and Physics," 63/e, CRC Press, Boca Raton, FL, 1982.

70. V. B. Parker, D. D. Wagman, W. H. Evans, "Selected Values of Chemical Thermodynamic Properties," United States Department of Commerce, National Bureau of Standards, Washington, D.C., 1971.

71. M. W. Chase, C.A Davies, J.R. Downey, D.J. Frurip, R.A. McDonald, A.N. Syverud, J. Phys. Chem. Ref. Data **4**, 31-132 (1975).

72. I. Barin, F. Sauert, E. Schultze-Rhonhof, W. S. Sheng, "Thermochemical Data of Pure Substances," VCH Press, Germany, 1989.

73. L. V. Gurvich, IVTANTHERMO software, 1993.

74. D. D. Wagman, W.H. Evans, V.B. Parker, R.H. Schumm, I. Halow, S.M. Bailey, K.L. Churney, R.L. Nutall, J. Phys. Chem. Ref. Data **11**, 7-391 (1982).

75. F. D. Rossini, D. D. Wagman, W. H. Evans, S. Levine, I. Jaffe, U.S. Department of Commerce, National Bureau of Standard, Selected Values of Chemical Thermodynamic Properties, 1952.

76. D. D. Wagman, W.H. Evans, V.B. Parker, I. Halow, S.M. Bailey, R.H. Schumm, "Selected Values of Chemical Thermodynamic Properties," United States Department of Commerce, National Bureau of Standards, Washington, D.C., 1969.

77. D. D. Wagman, W.H. Evans, V.B. Parker, I. Halow, S.M. Bailey, R.H. Schumm, "Selected Values of Chemical Thermodynamic Properties," United States Department of Commerce, National Bureau of Standards, Washihgton, D.C., 1968.

78. B. J. McBride, S. Heimel, J. G. Ehlers, S. Gordon, "Thermodynamic Properties to 6000 K for 210 Substances Involving the First 18 Elements," National Aeronautics and Space Administration, Washihgton, D.C., 1963.

79. R. Hultgren, R. L. Orr, P. D. Anderson, K. K. Kelley, "Selected Values of Thermodynamic Properties of Metals and Alloys," John Wiley & Sons, New York, 1960.

80. J. B. Pedley, E. M. Marshall, J. Phys. Chem. Ref. Data **12**, 967-1016 (1983).

81. E. G. Rauh, R. J. Ackermann, Journal of Chemical Physics **60**, 1396-1400 (1974).

82. L. V. Gurvich, I. V. Veyts, C. B. Alcock, "Thermodynamic Properties of Individual Substances," Hemisphere Publishing Corporation, New York, 1989.

83. R. S. Roth, K. L. Davis, J. R. Dennis, Adv. Cer. Matl. **2**, 303 (1987).

84. B. J. Lee, D. N. Lee, J. Amer. Ceram. Soc. **72**, 314-319 (1989).

85. G. Wang, S.J. Hwu, S.N. Song, J.B. Ketterson, L.D. Marks, R. Poeppelmeier, T.O. Mason, Adv. Cer. Matl. **2**, 313 (1987).

86. S. Kuharuangrong, J. Taylor, J. Amer. Ceram. Soc. **74**, 1964-1969 (1991).

87. H. F. Sakeek, T. Morrow, W. G. Graham, D. G. Walmsley, Appl. Phys. Lett. **59**, 3631-3633 (1991).

88. T. J. Geyer, W. A. Weimer, Appl. Phys. Lett. **54**, 469 (1989).

89. R. J. Ackermann, E. G. Rauh, J. Chem. Thermodynamics **5**, 331 (1973).

90. R. J. Ackermann, E. G. Rauh, R. J. Thorn, Journal of Chemical Physics **40**, 883 (1964).

91. R. S. Newberry, G. W. Barton, A. W. Searcy, Journal of Chemical Physics **48**, 793 (1968).

92. L. Wiedeman, H. Helvajian, J. Appl. Phys. **70**, 4513-4523 (1991).

93. S. I. Sandler, "Chemical and Engineering Thermodynamics," John Wiley and Sons, New York, 1989.

94. R. K. Bordia, H.S. Horowitz, M.A. Subramanian, J.B. Michel, E.M. McCaron, C.C. Torardi, J.D. Bolt, U. Chowdhry, E. Lopdrup, S.J. Poon, in "Materials Research Society Symposium Proceedings" (M. B. Brodsky, Ed.), Material Research Society, Pittsburgh, PA, 1988, vol. 99, p. 245.

95. D. A. Skoog, D. M. West, "Principles of Instrumental Analysis," Saunders College, Philadelphia, 1980.

96. T. S. Chin, T.W. Huang, W.T. Lin, N.C. Wu, Y.H. Chou, T.C. Wu, P.T. Wu, H.H. Yen, Mater. Res. Soc. Symp. Proc. **99**, 261-264 (1988).

97. J. V. Armstrong, M. McLoughlin, J. G. Lunney, J. M. Coey, Supercond. Sci. Technol. **4**, 89 (1991).

98. S. Otsubo, T. Minamikawa, Y. Yonezawa, A. Morimoto, T. Shimizu, Jpn. J. Appl. Phys. **29**, 73 (1990).

99. M. Nalfold, J. Birchall, in "Ceramic Superconductor II" (M. F. Yan, Ed.), American Chemical Society, 1988, pp. 428-435.

100. J. Heremans, D. T. Morelli, in "Materials Research Society Symposium Proceedings" (M. B. Brodsky, Ed.), Material Research Society, Pittsburgh, PA, 1988, vol. 99, pp. 761-764.

101. V. Bayot, F. Delannay, C. Dewitte, J.P. Erauw, X. Gonze, J.P. Issi, A. Jonas, M. Kinany-Alaoui, M. Lambricht, J.P. Michenaud, J.P. Minet, L. Piraux, Solid State Comm. **63**, 983-986 (1987).

102. R. C. Enck, R. D. Harris, in "Advanced Electronic Packaging Materials" Material Research Society Symposia Proceedings, Westerville, OH, 1989

103. R. C. Enck, R. D. Harris, R. A. Youngman, in "Advanced Characterization Techniques for Ceramics" (W. Young, Ed.), Ceramic Transactions, American Ceramic Society, Westerville, OH, 1989, vol. 5, pp. 214-222.

104. H. S. Carslaw, J. C. Jaeger, "Conduction of Heat in Solids," Clarendon Press, Oxford, 1984.

105. W. J. Parker, R. J. Jenkins, C. P. Butler, G. L. Abbott, J. Appl. Phys. **32**, 1679 (1961).

106. R. K. Williams, R. S. Graves, G. C. Kroeger, G. C. Marsh, J. O. Scarbrough, J. Appl. Phys. **66**, 6181 (1989).

107. C. Uher, A. B. Kaiser, Phys. Rev. B **36**, 5680-5683 (1987).

108. H. M. O'Bryan, P. K. Gallagher, Mater. Res. Soc. Symp. Proc. **169**, 1093-1096 (1990).

109. D. Taylor, British Ceramic Transactions and Journal **84**, 181 (1985).

110. C. L. Chan, J. Mazumder, J. Appl. Phys. **62**, 4579-4586 (1987).

111. M. I. Cohen, in "Laser Handbook" (F. R. Arecchi, E. O. Schultz-DuBois, Eds.), North-Holland, Amsterdam, 1972, vol. 2, pp. 1577-1647.

112. J. W. Shearer, J. J. Duderstadt, Nucl. Fusion **13**, 401 (1973).

113. J. R. Ready, J. Appl. Phys. **36**, 462-468 (1965).

114. E. M. Sparrow, R. D. Cess, "Radiation Heat Transfer," Brooks/Cole Publishing, Belmont, CA, 1966.

115. M. von Allmen, J. Appl. Phys. **47**, 5460-5463 (1976).

116. A. N. Pirri, Phys. Fluids **16**, 1435 (1973).

117. Y. V. Afanas'ev, O. N. Krokhin, Sov. Phys. JETP **25**, 639 (1967).

118. S. I. Anisimov, Sov. Phys. JETP **27**, 182-183 (1968).

119. Y. I. Nissim, A. Lietoila, R. B. Gold, J. F. Gibbons, J. Appl. Phys. **51**, 274-279 (1980).

120. J. Mazumder, W. M. Steen, J. Appl. Phys. **51**, 941-947 (1980).

121. M. K. El-Adawi, E. F. Elshehawey, J. Appl. Phys. **60**, 2250-2255 (1986).

122. R. K. Singh, J. Narayan, Mater. Sci. Eng. B **3**, 217-230 (1989).

123. W. G. Driscoll, W. Vaughn, "Handbook of Optics," McGraw-Hill Co., New York, 1978.

124. J. G. Andrews, D. R. Atthey, J. Inst. Math. Appl. **15**, 59-72 (1975).

125. C. J. Knight, AIAA Journal **17**, 519-523 (1979).

126. S. A. Kokorowski, G. L. Olson, L. D. Hess, in "Laser and Electron-Beam Solid Interactions and Material Processing" J. F. Gibbons, L. D. Hess, T. W. Sigmon, Eds., Material Research Society Symposia Proceedings, New York, 1981, vol. 1, p. 97.

127. A. A. Iranmanesh, R. F. Pease, J. Vac. Sci. Tech. B **1**, 91 (1983).

128. K. T. Yang, J. Appl. Mechanics **25**, 146-147 (1958).

129. R. B. Bird, W. E. Stewart, E. N. Lightfoot, "Transport Phenomena," John Wiley & Sons, New York, 1960.

130. M. Lax, Appl. Phys. Lett. **33**, 786 (1978).

131. M. Lax, J. Appl. Phys. **48**, 3919 (1977).

132. M. von Allmen, in "Physical Processes in Laser-Materials Interactions" (M. Bertolotti, Ed.), Plenum Press, New York, 1983, pp. 323-332.

133. G. Carter, Radiat. Effects Lett. **50**, 147 (1980).

134. M. Sparks, E. Loh, J. Opt. Soc. Am. **69**, 859 (1979).

135. A. Cohen, P. Allenspacher, M. M. Brieger, I. Jeuck, H. Opower, Appl. Phys. Lett. **59**, 2186-2188 (1991).

136. R. K. Singh, O. W. Holland, J. Narayan, J. Appl. Phys. **68**, 233-47 (1990).

137. J. F. Ready, J. Opt. Soc. Am. **53**, 514 (1963).

138. F. P. Gagliano, U. C. Paek, Appl. Opt. **13**, 274-279 (1974).

139. C. Hill, in "Laser and Electron-Beam Solid Interactions and Material Processing" (J. F. Gibbons, L. D. Hess, T. W. Sigmon, Eds.), Material Research Society Symposia Proceedings, New York, 1981, vol. 1, pp. 361-374.

140. T. Nakamiya, T. Ikegami, K. Ebihara, IEEE Trans. Appl Supercond **3**, 1057 (1993).

141. R. F. Wood, G. E. Giles, Phys. Rev. B **23**, 2923-2942 (1981).

142. M. Von Allmen, Springer-Verlag, Berlin, 1987, pp. 120-130.

143. W. A. Weimer, Appl. Phys. Lett. **52**, 2171 (1988).

144. J. P. Zheng, Z. Q. Huang, D. T. Shaw, H. S. Kwok, Appl. Phys. Lett. **54**, 280 (1989).

145. G. Koren, R. J. Baseman, A. Gupta, M. I. Lutwyche, R. B. Laibowitz, Appl. Phys. Lett. **56**, 2144 (1990).

146. M. Hanabusa, M. Suzuki, S. Nishigaki, Appl. Phys. Lett. **38**, 385-387 (1981).

147. G. Groh, J. Appl. Phys. **39**, 5804 (1968).

148. A. C. Tam, W. P. Leung, D. Krajnovich, J. Appl. Phys. **69**, 2072-2075 (1991).

149. D. L. Singleton, G. Paraskevopoulos, R. S. Irwin, J. Appl. Phys. **66**, 3324-3328 (1989).

150. T. Sato, S. Furono, S. Iguchi, M. Hanabusa, Jpn. J. Appl. Phys. **26**, L1487 (1987).

151. G. Koren, A. Gupta, R. J. Baseman, M. I. Lutwyche, R. B. Laibowitz, Appl. Phys. Lett. **55**, 2450 (1989).

152. W. Sankur, J. DeNatale, W. Gunning, J. G. Nelson, J. Vac. Sci. Technol. A **5**, 2869-2874 (1987).

153. D. Bhattacharya, R. K. Singh, P. H. Holloway, J. Appl. Phys. **70**, 5433-5439 (1991).

154. S. S. Thé, T.J. Anderson, K.B. Keating, R.K. Bordia, J.L. Hohman, S.L. Witman, "Target Morphology Studies in Excimer Laser Ablation of $YBa_2Cu_3O_7$," AIChE 1992 Annual Meeting, American Institute of Chemical Engineers, Miami Beach, Florida, 1992.

155. J. A. Greer, H. J. Van Hook, Mater. Res. Soc. Symp. Proc. **169**, 463-468 (1990).

156. S. Otsubo, T. Minamikawa, Y. Yonezawa, A. Morimoto, T. Shimizu, Jpn. J. Appl. Phys. **29**, 173 (1990).

157. R. K. Singh, K. Jagannadham, J. Narayan, Mater. Sci. Eng. B **7**, 287-296 (1991).

158. R. Ramesh, A. Inam, D.M. Hwang, T.D. Sands, C.C. Chang, D.L. Hart, Appl. Phys. Lett. **58**, 1557-1559 (1991).

159. A. Kaldor, Z. Phys. D **3**, 95 (1986).

160. A. O'Keefe, M. M. Ross, A. P. Baronavski, Chemical Physics Letters **130**, 17-19 (1986).

161. N. Furstenau, F. Hillenkamp, Intl. J. Mass. Spec. Ion. Phys. **37**, 135-151 (1981).

162. R. Pflaum, K. Sattler, E. Recknagel, Chemical Physics Letters **138**, 8 (1987).

163. E. W. Becker, Z. Phys. D **3**, 101-107 (1986).

164. E. W. Becker, K. Bier, W. Henkes, Z. Phys. **146**, 333-338 (1956).

165. T. D. Mark, Adv. Mass Spectrom., 379 (1986).

166. M. R. Hoare, Adv. Chem. Phys. **40**, 49 (1979).

167. P. Buffat, J. P. Borel, Phys. Rev. A **13**, 2289 (1976).

168. P. Scheier, T. D. Mark, Int. J. Mass Spectrom. Ion Processes **76**, R11-R15 (1987).

169. D. Kreisle, O. Echt, M. Knapp, E. Recknagel, K. Leiter, T. Mark, J.J. Saenz, J.M Soler, Phys. Rev. Lett. **56**, 1551-1554 (1986).

170. T. D. Mark, Int. J. Mass Spectrom. Ion Processes **79**, 1-59 (1987).

171. O. Echt, M. C. Cook, A. W. Castleman, Chemical Physics Letters **135**, 229-235 (1987).

172. C. G. Levi, R. Mehrabian, Metall. Trans. A **13A**, 221-234 (1982).

173. B. P. Bewlay, B. Cantor, J. Mater. Res. **6**, 1433-1454 (1991).

174. A. Gupta, B. Braren, K. G. Casey, B. W. Hussey, R. Kelly, Appl. Phys. Lett. **59**, 1302-1304 (1991).

175. J. F. Ready, Academic, Orlando, FL, 1971, pp. 95-115, 188.

176. H. Van Brug, K. Murakami, F. Bijkerk, M. J. van der Wiel, J. Appl. Phys. **60**, 3438-3443 (1986).

177. D. H. Blank, D. J. Adelerhof, J. Flokstra, H. Rogalla, Physica C **167**, 423-432 (1990).

178. K. Scott, J. M. Huntley, W. A. Phillips, J. Clarke, J. E. Field, Appl. Phys. Lett. **57**, 922-924 (1990).

179. P. E. Dyer, J. Sidhu, J. Appl. Phys. **64**, 4657 (1988).

180. A. Gupta, B. W. Hussey, Appl. Phys. Lett. **58**, 1211 (1990).

181. H. Izumi, K. Ohata, T. Sawada, T. Morishita, S. Tanaka, Appl. Phys. Lett. **59**, 2950-2952 (1991).

182. R. K. Singh, D. Bhattacharya, J. Narayan, Appl. Phys. Lett. **61**, 483 (1992).

183. R. Edwards, Research Disclosure, Neocera, Inc., 1992.

184. Anonymous, Method of Depositing Laser Ablated Films, 1991.

185. W. P. Barr, J. Phys. E **2**, 2 (1969).

186. H. Sankur, W. J. Bunning, J. DeNatale, J. F. Flintoff, J. Appl. Phys. **65**, 2475-2478 (1989).

187. B. Holzapfel, B. Roas, L. Schultz, P. Bauer, Saemann-Ischenko, Appl. Phys. Lett. **61**, 3178-3180 (1992).

188. S. S. Thé, K. B. Keating, E.I. du Pont de Nemours and Co. (Inc.), Improved Method of Depositing Superconducting Film via Pulsed Laser Ablation, 1992.

189. R. K. Singh, Appl. Phys. Lett. **55**, 2351 (1989).

190. R. A. Hughes, Y. Lu, T. Timusik, J. S. Preston, Appl. Phys. Lett. **58**, 762-764 (1991).

191. W. S. Smith, D. Apelian, in "Plasma Processing and Synthesis of Materials" (D. Apelian, J. Szekely, Eds.), Material Research Society Symposia Proceedings, Anaheim, CA, 1987, vol. 98, pp. 49-60.

192. E. Gutierrez-Miravete, E. J. Lavernia, G. M. Trapaga, J. Szekely, N. J. Grant, Metall. Trans. A **20A**, 71-85 (1982).

193. J. P. Holman, "Heat Transfer," McGraw-Hill Book Company, New York, 1986.

194. W. D. Kingery, H. K. Bowen, D. R. Uhlmann, "Introduction to Ceramics" John Wiley & Sons, New York, 1976.

195. M. M. Denn, "Process Fluid Mechanics," Prentice-Hall, Englewood Cliffs, New Jersey, 1980.

196. R. S. Robinson, S. M. Rossnagel, J. Vac. Sci. Technol. B **21**, 790-797 (1982).

197. R. T. Young, R. F. Wood, Ann. Rev. Mater. Sci. **12**, 323-350 (1982).

198. P. E. Dyer, Appl. Phys. Lett. **49**, 453 (1986).

199. G. J. Van Gurp, G. E. Eggermont, Y. Tamminga, W. T. Stacy, J. R. Gijsbers, Appl. Phys. Lett. **35**, 273-75 (1979).

200. T. R. Anthony, H. E. Cline, J. Appl. Phys. **48**, 3888-3894 (1977).

201. P. G. Carey, B. J. Woratschek, F. Bachmann, Appl. Phys. Lett. **57**, 1499-1501 (1990).

202. J. F. Figueira, S. J. Thomas, in "Surface Studies with Lasers-Proceedings of the International Conference" (F. R. Aussenegg, A. Leitner, M. E. Lippitsch, Eds.), Springer-Verlag, Mauterndorf, Austria, 1983, pp. 212-215.

203. D. J. Ehrlich, J. Y. Tsao, J. Vac. Sci. Technol. B **1**, 969-984 (1983).

204. R. K. Singh, D. Bhattacharya, J. Narayan, Appl. Phys. Lett. **57**, 2022-2024 (1990).

205. O. Auciello, A. R. Krauss, J. Santiago-Aviles, A. F. Schreiner, D. M. Gruen, Appl. Phys. Lett. **52**, 239 (1988).

206. A. Hoffman, Supercond. Sci. Technol. **3**, 118 (1990).

207. D. N. Mashburn, D.B. Geohegan, D. Eres, D.H. Lowndes, L.A. Boatner, B.C. Sales, S.J. Pennycook, R.J. Culbertson, E.Sonder, D.K. Christen, in "Materials Research Society Symposium Proceedings " (M. B. Brodsky, Ed.), Material Research Society, Pittsburgh, PA, 1988, vol. 99, p. 699.

208. S. R. Foltyn, R.E. Muenchausen, R.C. Estler, E. Peterson, W.B. Hutchinson, K.C. Ott, N.S. Nogar, K.M. Hubbard, R.C. Dye, X.D. Wu, "Influence of Beam and Target Properties on the Excimer Laser Deposition of $YBa_2Cu_3O_7$ Thin Films," Los Alamos Report, 1990.

209. Y. Rytz-Froidevaux, R. P. Salathe, H. H. Gilgen, Appl. Phys. A **37**, 121-138 (1985).

210. B. Roas, L. Schultz, G. Endres, Appl. Phys. Lett. **53**, 1557 (1988).

211. K. Oka, K. Nakane, M. Ito, M. Saito, H. Unoki, Jpn. J. Appl. Phys. **27**, L1065 (1988).

212. A. Gunterschultze, W. Tollmien, Z. Phys. **119**, 685 (1942).

213. A. Jagota. Internal Report, DuPont Company, 1992.

214. G. K. Wehner, D. J. Hajicek, J. Appl. Phys. **4**, 1145-1149 (1971).

215. R. Kelly, O. Auciello, Surf. Sci. **100**, 135-153 (1980).

216. J. E. Greene, B. R. Natarajan, F. Sequeda-Osorio, J. Appl. Phys. **49**, 417 (1978).

217. G. N. A. van Veen, W. Vrijmoeth, T. S. Baller, J. Dieleman, in "Material Research Society Symposia Proceedings" (M. J. Aziz, L. E. Rehn, B. Stritzker, Eds.), Material Research Society, Pittsburgh, 1988, vol. 100, pp. 641-645.

218. B. Haba, B. W. Hussey, A. Gupta, J. Appl. Phys. **69**, 2871-2876 (1991).

219. H. J. Leamy, W.L. Brown, G.K. Celler, G. Fott, G.H. Gilmer, J.C. Fan, in "Laser and Electron-Beam Solid Interactions and Material Processing" (J. F. Gibbons, L. D. Hess, T. W. Sigmon, Eds.), Material Research Society Symposia Proceedings, vol. 1, Boston, 1981, p. 89.

220. D. Bauerle, M. Eyett, U. Kolzer, R. Kullmer,P. Mogyorosi, K. Piglmayer, K., "Laser-Induced Surface Modification and Etching of Materials," vol. 101, Material Research Society Symposia Proceedings, Boston, 1988.

221. D. R. Gaskell, "Introduction to Metalurgical Thermodynamics," 1981.

222. A. J. Pedraza, Journal of Metals **2**, 14 (1987).

223. G. D. Mahan, H. S. Cole, Y. S. Liu, H. R. Phillip, Appl. Phys. Lett. **53**, 2377-2379 (1988).

224. M. Sparks, E. Loh, J. Opt. Soc. Am. **69**, 847 (1979).

225. B. T. Barnes, J. Opt. Soc. Am. **56**, 1546 (1966).

226. I. Ursu, I. Apostol, I.N. Mihailescu, L.C. Nistor, V.S. Teodorescu, A.M. Prokhorov, V.I. Konov, N.I. Chapliev, in "Surface Studies with Lasers - Proceedings of the International Conference" (F. R. Aussenegg, A. Leitner, M. E. Lippitsch, Eds.), Springer-Verlag, Mauterndorf, Austria, 1983, pp. 234-236.

227. D. Turnbull, in "Physical Processes in Laser-Materials Interactions" (M. Bertolotti, Ed.), Plenum Press, New York, 1983, pp. 117-142.

228. S. S. Cohen, J. Appl. Phys. **67**, 6694 (1990).

229. G. J. Galvin, M.O. Thompson, J.W. Mayer, R.B. Hammond, N. Paulter, P.S. Peercy, Phys. Rev. Lett. **48**, 33 (1982).

230. P. F. Marella, D. B. Tuckerman, R. F. Pease, Appl. Phys. Lett. **56**, 2625-2627 (1990).

231. A. Jagota, Private Communications, 1992.

232. G. E. Possin, H. G. Parks, S. W. Chiang, in "Laser and Electron-Beam Solid Interactions and Material Processing" (J. F. Gibbons, L. D. Hess, T. W. Sigmon, Eds.), Material Research Society Symposia Proceedings, vol. 1, New York, 1981, pp. 73-80.

233. G. Carter, J. S. Colligon, M. J. Nobes, J. Mater. Sci. **8**, 1473 (1973).

234. E. Hecht, A. Zajac, "Optics," Addison-Wesley Publishing, Menlo Park, CA, 1979.

235. A. Auciello, in "Ion Bombardment Modification of Surfaces" (A. Auciello, R. Kelly, Eds.), Elsevier, Amsterdam, 1984, vol. pp. 1-25.

236. P. H. Bucksbaum, J. Bokor, in "Laser-Solid Interactions and Transient Thermal Processing of Materials" (J. Narayan, W. L. Brown, R. A. Lemons, Eds.), vol. 13, North-Holland, New York, 1983, pp. 51-56.

237. R. Kelly, A. Miotello, B. Braren, C. E. Otis, Appl. Phys. Lett. **60**, 2980-2982 (1992).

238. I. B. Zeldovich, A. S. Kompaneets, "Theory of Detonation," Academic Press, New York, 1960.

239. J. Dawson, P. Kaw, B. Green, Phys. Fluids **12**, 875-882 (1969).

240. J. A. Waltham, J. Phys. D **22**, 766-769 (1989).

241. L. J. Dhareshwar, P. A. Naik, P. D. Nandwana, H. C. Pant, J. Appl. Phys. **61**, 4458-4463 (1987).

242. R. E. Honig, Appl. Phys. Lett. **3**, 8 (1963).

243. G. A. Askar'yan, E. M. Moroz, Sov. Phys. JETP **16**, 1638-1639 (1963).

244. R. W. Waniek, P. J. Jarmuz, Appl. Phys. Lett. **12**, 52-54 (1968).

245. H. Brode, J. Appl. Phys. **26**, 766 (1955).

246. Y. B. Zel'dovich, Y. P. Raizer, "Physics of Shock Waves and High Temperature Hydrodynamic Phenomena," Academic Press, New York, 1966.

247. D. A. Freiwald, J. Appl. Phys. **43**, 2224 (1972).

248. D. B. Geohegan, Appl. Phys. Lett. **60**, 2732 (1992).

249. S. Kuper, J. Brannon, Appl. Phys. Lett. **60**, 1633-1635 (1992).

250. G. Koren, U. P. Oppenheim, Applied Physics B **42**, 41-43 (1987).

251. A. Miotello, R. Kelly, B. Braren, C. E. Otis, Appl. Phys. Lett. **61**, 2784-2786 (1992).

252. R. H. Hughes, R.J. Anderson, C.K. Manka, M.R. Caruth, L.G. Gray, J.P. Rosenfeld, J. Appl. Phys. **51**, 4088-4093 (1980).

253. T. Venkatesan, X.D. Wu, A. Inam, Y. Jeon, M. Croft, E.W. Chase, C.C. Chang, J.B. Wachtman, R.W. Odom, F. Radicati di Brozolo, C.A. Magee, Appl. Phys. Lett. **53**, 1431 (1988).

254. B. Roas, L. Schultz, G. Endres, Unpublished Results, 1989.

255. L. Lynds, B. R. Weinberger, G. G. Peterson, H. A. Krasinski, Appl. Phys. Lett. **52**, 320 (1988).

256. O. Auciello, S. Athavale, O.E. Hankins, M. Sito, A.F. Schreiner, N. Biunno, Appl. Phys. Lett. **53**, 72-74 (1988).

257. P. E. Dyer, R. D. Greenough, A. Issa, P. H. Key, Appl. Phys. Lett. **53**, 534 (1988).

258. Q. Y. Ying, D. T. Shaw, H. S. Kwok, Appl. Phys. Lett. **53**, 1762 (1988).

259. C. Girault, D. Damiani, J. Aubreton, A. Catherinot, Appl. Phys. Lett. **55**, 182 (1989).

260. D. N. Mashburn, in "Processing of Films for High Tc Superconducting Electronics" (T. Venkatesan, Ed.), Proc. SPIE, Santa Clara, CA, 1989, vol. 1187, p. 172.

261. K. M. Yoo, Appl. Phys. Lett. **54**, 1278 (1989).

262. E. Narumi, Appl. Phys. Lett. **56**, 2684 (1990).

263. A. Cerezo, R. M. Grovenor, R. M. Hoyle, G. D. Smith, Appl. Phys. Lett. **52**, 1020 (1988).

264. C. H. Chen, M. P. McCann, R. C. Phillips, Appl. Phys. Lett. **53**, 2701 (1988).

265. H. B. Elswijk, Appl. Phys. Lett. **55**, 2667 (1989).

266. L. Stolt, J. Vac. Sci. Technol. A **3**, 403 (1985).

267. K. A. Lincoln, Intl. J. Mass. Spec. Ion. Phys. **13**, 45-53 (1974).

268. J. L. Gole, C. L. Chalek, Journal of Chemical Physics **65**, 4384-4395 (1976).

269. C. R. Dickson, S. M. George, R. N. Zare, Journal of Chemical Physics **67**, 1024-1030 (1977).

270. N. H. Cheung, Q. Y. Ying, J. P. Zheng, H. S. Kwok, J. Appl. Phys. **69**, 6349-6354 (1991).

271. R. Kelly, R. W. Dreyfus, Nucl. Instrum. Methods Phys. Res. B **32**, 314 (1988).

272. R. K. Singh, J. Narayan, Phys. Rev. B **41**, 8843-8859 (1990).

273. C. E. Otis, R. W. Dreyfus, Phys. Rev. Lett. **67**, 2102 (1991).

274. J. G. Calvert, J. N. Pitts, "Photochemistry," John Wiley & Sons, New York, 1966.

275. M. J. Vasile, H. F. Dylla, in "Plasma Diagnostics" (O. Auciello, D. L. Flamm, Eds.), Academic Press, Boston, 1989, vol. 1, pp. 185-237.

276. Balzers, Product Literature, 1990.

277. C. E. Otis, A. Gupta, B. Braren, Appl. Phys. Lett. **62**, 102-104 (1993).

BIOGRAPHICAL SKETCH

The author, born in Java, Indonesia, received his bachelor's degrees in chemical engineering and chemistry from the University of Wisconsin - Madison in 1986, and his master's degree in chemistry from Purdue University in 1989 where he was the recipient of Lily Teaching Fellowship. His master's thesis in analytical chemistry was entitled "Micelle Surface Potential and Light Scattering Studies of Polyion-Mixed Micelle Complexes." The work on his doctoral dissertation in chemical engineering was conducted under the supervision of Prof. Timothy J. Anderson. The experimental portion of the research was performed at the DuPont Experimental Station Central Research and Development Division under the supervision of Dr. Kenneth B. Keating.

I certify that I have read this study and that in my opinion it conforms to acceptable standards of scholarly presentation and is fully adequate, in scope and quality, as a dissertation for the degree of Doctor of Philosophy.

Timothy J. Anderson, Chairman
Professor of Chemical Engineering

I certify that I have read this study and that in my opinion it conforms to acceptable standards of scholarly presentation and is fully adequate, in scope and quality, as a dissertation for the degree of Doctor of Philosophy.

Kenneth B. Keating
Research Fellow, E.I. du Pont
de Nemours and Co. (Inc.)

I certify that I have read this study and that in my opinion it conforms to acceptable standards of scholarly presentation and is fully adequate, in scope and quality, as a dissertation for the degree of Doctor of Philosophy.

Dinesh O. Shah
Professor of Chemical Engineering

I certify that I have read this study and that in my opinion it conforms to acceptable standards of scholarly presentation and is fully adequate, in scope and quality, as a dissertation for the degree of Doctor of Philosophy.

Gar B. Hoflund
Professor of Chemical Engineering

I certify that I have read this study and that in my opinion it conforms to acceptable standards of scholarly presentation and is fully adequate, in scope and quality, as a dissertation for the degree of Doctor of Philosophy.

Paul H. Holloway
Professor of Material Science and
Engineering

This dissertation was submitted to the Graduate Faculty of the College of Engineering and to the Graduate School and was accepted as partial fulfillment of the requirements for the degree of Doctor of Philosophy.

August 1993

for Winfred M. Phillips
Dean, College of Engineering

Dean, Graduate School

UNIVERSITY OF FLORIDA
3 1262 08557 0736